Structural tailoring of graphene based materials for energy applications

Anurag Mohanty

To cite this version:

Anurag Mohanty. Structural tailoring of graphene based materials for energy applications. Material chemistry. Université de Strasbourg, 2020. English. NNT : 2020STRAF051 . tel-03934706

HAL Id: tel-03934706
https://theses.hal.science/tel-03934706

Submitted on 11 Jan 2023

UNIVERSITÉ DE STRASBOURG

ÉCOLE DOCTORALE DES SCIENCES CHIMIQUES (ED 222)
ICPEES, UMR 7515 CNRS

THÈSE présentée par :

Anurag MOHANTY

soutenue le : **18 Décembre 2020**

pour obtenir le grade de : **Docteur de l'Université de Strasbourg**
Discipline/ Spécialité : **Chimie / Chimie des Matériaux**

Structuration de matériaux à base de graphène pour l'énergie durable
[Structural Tailoring of Graphene Based Materials for Energy Applications]

THÈSE dirigée par :

Dr. Hab. JANOWSKA Izabela	Charge de Recherche, ICPEES,UMR-7515 du CNRS, France

RAPPORTEURS :

Dr. Hab. GIAMBASTIANI Giuliano	Directeur de Recherche, ICCOM-CNR, Italy
Prof. SERP Philippe	Professeur, Université de Toulouse, France

AUTRES MEMBRES DU JURY :

Dr. Hab. MATEI GHIMBEU Camélia	Directeur de Recherche, IS2M, UMR-7361 du CNRS, France

-Dedicated to my family.

Acknowledgement

I believe it's not the goal but the journey and the people that makes it worthwhile. Had it not been for the people and the opportunities, my PhD thesis would not have seen the light of the day. Proper guidance and support has made this thesis fruitful and the experience all the more enriching. Looking back to my journey, I remember a good number of humble souls who have helped me tackle through the issues and supported my ideas during my tenure at Institute of Chemistry and Processes for Energy, Environment and Health (ICPEES, UMR 7515) of the CNRS, University of Strasbourg. Let me take this opportunity to convey my heartfelt thanks to all of them.

First and foremost, I would like to express my sincere gratitude to my thesis advisor, Dr. Izabela Janowska for accepting me as a PhD student and providing me a chance to work alongside her. I am really thankful to her for her guidance to my project and patience to my mistakes. Her approach to keep pushing till we get the entire story of what is happening has made me realise various aspects of being an independent researcher. Her constant encouragement to not give up even when I hit a roadblock has prepared me for any challenge that might come. Her selfless help and continuous support in both scientific and daily life has made my PhD journey smooth and seamless. I learned a lot from her scientific experience in the field and how to be vigilant to the minute details. Words fall short if I carry on describing the impacts of her support during my PhD. Lastly, I would like to thank her again for being the perfect advisor one could wish for.

Next, I would like to thank Solvay and Fondation pour la Recherche en Chimie (FRC) for providing me the grant to carry out my PhD thesis at ICPEES. It is ideas and supports like these which bring out the best from the young enthusiastic talents.

I would like express my warmest regards and to Dr. Giuliano Giambastiani of Istituto di Chimica dei Composti OrganoMetallici - Consiglio Nazionale delle Ricerche (ICCOM-CNR), Italy, and Prof. Phillipe Serp of Université de Toulouse, France, for accepting to be part of the advisory committee for my thesis. Further, I would like to extend my gratefulness to Dr. Camelia Matei Ghimbeu of Institut de Science des Matériaux de Mulhouse (IS2M), UMR-7361 du CNRS, France, for accepting to be one of the jury members for my PhD defense without any hesitation.

Special thanks to Dr. Cuong Pham-Huu for sharing his scientific and life experiences and being there whenever needed. His anecdotes and zeal for research has inspired me to a great extent. I would like to thank him and Dr. Anne-Cecile Roger specially for providing me methanation setups. I would also like to thank Dr. Valerie Keller and Dr. Thomas Cottineau for their collaborations and constant inputs in various projects I ventured upon during my PhD journey.

Next, I would like to thank all members of ICPEES who have been there supporting me through the thick and thin of my PhD journey. The indulging discussions with Dr. Housseinou Ba, Dr. Jean-Mario Nhut, and Dr. Wei Wang has helped quite a few times in solving various roadblocks I faced during experiments and in improvement of my French language and cooking skills. Thanks to the continuous efforts of Dr. Sergey Pronkin, Dr. Cuong Duong-Viet and Fabrice Vigneron, I was able to handle all major equipments with ease and understand the underlying principles. I am also indebted to Dr. Jagadeesh, Dr. Mallikarjuna, Dr. Lai, Dr. Essyed, Dr. Zhenxin, Dr. Ait Khouiya, Lola, Liping, Franck, Bing and Xiong for their kind help and encouragement in accomplishing my PhD. Special mention to Dr. Walid Baaziz from the Institut de Physique et Chimie des Matériaux de Strasbourg (IPCMS, UMR 7504) for helping me out with the TEM imaging.

I also express my gratitude to all the administrative staffs: Catherine Kientz, Agnès Orb, Silviya Markova, Julien Bertrand, Michèle Thomas and technical referees: Dr. Ksenia Parkhomenko, Thierry Romero, Sécou Sall, Dr. Thierry Dintzer, Alain Rach, Christophe Mélart, and Christophe Sutter at ICPEES for their valuable guidance and unwavering support.

The last three and half years in Strasbourg has taught me a lot, courtesy some great people I have met. Life beyond the lab has been fascinating. The most important of all will be Jayash, who has been there since day one of my arrival. Innumerable memories and adventures together has helped me kick back every time I was homesick or not having a good day. Gopal joined us soon and took apartment hunting and cooking nights to a whole new level. I made some beautiful memories learning about the Persian culture and cuisine with some amazing people like Mahnoosh, Maryam and Pooya. Thanks to Sujju, Sandy, Sushil and Heman for coping up with hour long calls, and to Tathagata for making sure French-German borders can be crossed for household chores. Life during confinement and thesis writing was made easy by some Indian guys in the residence. Anshul kept tabs on the Parme register while Pulkit made sure food is always there for everyone and Ankush focused on converting the lows with the highs. Cheers to Ines, Sybille, Spyridoula, Abhishek, Joy and all those happy souls who touched my life with their great ideas and good memories during my PhD.

Last but not the least, I would like to thank my family back home in India for nurturing me into the individual I am today. The innumerable sacrifices my parents have given for me to be able to study here in France cannot be expressed with the entire English alphabet. I believe I am living the dream my brother had seen for me and I would feel blessed if I can fulfil even a tiny fragment of his expectations. A big thank you to my awesome sister-in-law who is always there with her superb pep-talks (also husky image shares) and cool new recipes. I also extend my thanks to all the relatives of my family and friends for their support to me during my study.

Table of Contents

RÉSUMÉ ix

1. INTRODUCTION ix

   1.1 *Stockage électrochimique de l'énergie* ..... *x*

   1.2 *Conversion et stockage de l'énergie chimique* ..... *xii*

2. RÉSULTATS ET DISCUSSION xiv

   2.1 *Adaptation des composites FLG pour le stockage électrochimique de l'énergie* ..... *xiv*

   2.2 *Utilisation du FLG comme modèle pour les nanoplaquettes métalliques plates* ..... *xvii*

   2.3 *Dépendance structurelle des nanofibres de carbone/graphène à faible couche décoré de Ni/NiO pour la méthanisation du CO_2 par chauffage inductif* ..... *xix*

3. CONCLUSION GÉNÉRALE XXI

4. PERSPECTIVES XXII

RÉFÉRENCES XXIII

CHAPTER 1 INTRODUCTION 1

1.1 ELECTROCHEMICAL ENERGY STORAGE 6

1.1.1 Why Supercapacitors ? *7*

1.1.2 Mechanism Guiding Supercapacitors *8*

1.1.3 Carbon Based Materials for Supercapacitors *16*

1.2 CHEMICAL ENERGY CONVERSION & STORAGE 31

1.2.1 Power-to-Gas *32*

1.2.2 Mechanism of CO_2 Methanation *34*

1.2.3 Catalysts for Methanation *36*

1.2.4 Reactors for CO_2 Methanation *45*

1.2.5 Inductive Heating (IH) Technology *48*

1.3 SCOPE AND OUTLINE OF THE THESIS 55

REFERENCES 57

CHAPTER 2 TAILORING FLG COMPOSITES FOR ELECTRO-CHEMICAL ENERGY STORAGE 73

2.1 TUNING THE STRUCTURE OF IN-SITU SYNTHESIZED FEW LAYER GRAPHENE/CARBON COMPOSITES INTO NANOPOROUS VERTICALLY ALIGNED GRAPHENE ELECTRODES WITH HIGH VOLUMETRIC CAPACITANCE. 79

2.1.1 Abstract *79*

2.1.2 Introduction *79*

2.1.3 Experimental *82*

2.1.4 Results and Discussion *85*

2.1.5 Conclusion *96*

REFERENCES 97

SUPPORTING INFORMATION 100

CHAPTER 3 USING FLG AS TEMPLATE FOR FLAT METAL BASED NANOPLATELETS ... 101

3.1 Few layer graphene as a template for Fe-based 2D nanoparticles ... 104

3.1.1 Abstract ... 104

3.1.2 Introduction ... 104

3.1.3 Material and Methods ... 105

3.1.4 Results and Discussion ... 107

3.1.5 Conclusion ... 113

References ... 114

Supporting Information ... 116

CHAPTER 4 DEVELOPING FLG BASED SUPPORTS FOR CO_2 METHANATION ... 117

4.1 Structural impact of Carbon Nanofibers/Few-Layer-Graphene decorated with Ni/NiO for CO_2 methanation via Inductive Heating ... 122

4.1.1 Introduction ... 122

4.1.2 Experimental Section ... 124

4.1.3 Results ... 127

4.1.4 Conclusion ... 140

References ... 142

Supporting Information ... 146

CHAPTER 5 CONCLUSION & PERSPECTIVES ... 151

5.1 Conclusions ... 153

5.1.1 FLG/C composites for supercapacitors ... 153

5.1.2 FLG as template for metal based nanoplatelets ... 154

5.1.3 FLG/CNF support for Ni based Methanation of CO_2 ... 155

5.2 Perspectives ... 156

References ... 157

PUBLICATIONS & COMMUNICATIONS ... 159

Publications ... 161

Communications ... 162

List of Figures

Figure 1.1 Total Primary Energy Sources compared between 1990 and 2015 [2]. 3

Figure 1.2 IEA forecasts for; a)Renewable electricity capacity additions, 2007-2021, b)Annual growth for renewable electricity generation by source, 2018-2020 [7]. 4

Figure 1.3 Energy-related carbon dioxide emissions as per IEO 2019 [23]. 5

Figure 1.4 (a) Ragone plot comparing the power and energy densities of various supercapacitors [43], (b) Applications of supercapacitors. 8

Figure 1.5 Classification and examples of different types of supercapacitors[49]. 8

Figure 1.6 Schematic of different charge storage mechanisms. (a) Charge storage mechanism of rechargeable battery. (b) Charge storage mechanism of supercapacitor [48]. 10

Figure 1.7 Redox mechanisms that guide pseudocapacitance. 11

Figure 1.8 (a, b, d, e, g, h) Schematic cyclic voltammograms and (c, f, i) corresponding galvanostatic discharge curves for various kinds of energy-storage materials [70]. 13

Figure 1.9 Schematics of different kinds of EDL model for charge storage at electrode-electrolyte interface, a) Helmholtz Model, b) Guoy-Chapman model, c) Stern Model 14

Figure 1.10 Circuit representation of supercapacitor. 16

Figure 1.11 Charging mechanisms for carbon pores initially filled with electrolyte. 17

Figure 1.12 Various carbon materials derived from graphene [113]. 20

Figure 1.13 DFT based 3D band structures and corresponding projections for, a) graphene, b) bi-layer graphene, c) few-layer graphene, d) graphite. The AB stacking is considered and fermi levels has been set to zero [119]. 21

Figure 1.14 SEM and optical images of different kinds of Graphene based materials. 23

Figure 1.15 Four typical methods of exfoliation for mass production of graphene[160]. 25

Figure 1.16 Perfect and defective graphene clusters. (a) Perfect graphene cluster, (b) Stone–Wales defect, (c) single vacancy, (d) double vacancy, (e) edge defect with pentagon ring at zigzag edge, octagon and fused pentagon carbon rings line [203]. 30

Figure 1.17 Schematic illustration of the described “power-to-X” technologies: (A) Power-to-Gas; (B) Power-to-Liquid; (C) Power-to-Ammonia; (D) All-electrochemical synthesis 32

Figure 1.18 Energy Distribution System Based on PtG Technology wherein energy from green sources are utilized to synthesize H_2 which can be directly used or for synthesis of CH_4. 33

Figure 1.19 Processes for methanation 34

Figure 1.20 CO_2 conversion mechanism, a) associative, b) dissociative 35

Figure 1.21 Snippet of Periodic Table with methanation active materials highlighted in grey.[232] 36

Figure 1.22 Ru based methanation mechanism, (a)CO_2 dissociated to CO_{ad} and O_{ad} on Ru sites. CO_{ad} then evolved to methane in an associative way, (b): Surface formate species accumulated rather than hydrogenated to CH_4. [229] 38

Figure 1.23 Methanation mechanism of Ni NPs supported on Ceria-Zircona........................40

Figure 1.24 Methanation mechanism on MSN substrate having metal NPs [275]. 41

Figure 1.25 Different types of defects observed in CNTs: a)isolated pentagon, b) isolated heptagon, c) a 5|7 hole along the tube, d)) a 5|7 hole of different orientation [287]. 43

Figure 1.26 Schematic diagram of various types of CNFs, a) hollow-center herring bone, b) solid core herring bone, c) ribbons, d) stacked-cup, e) platelets 44

Figure 1.27 Schematics of energy loss from renewable sources till it reaches power supply system 46

Figure 1.28 Structured micro-reactor setup [217]. 47

Figure 1.29 Schematic illustration of (a) exemplary hysteresis loop of an array of single domain FM NPs and (b) exemplary curve for a SPM sample. [308] 49

Figure 1.30 Different Types of relaxation losses 50

Figure 1.31 a) Schematic of Induction Heating based CNT synthesis, b) Temperature estimation along the reactor indicating heating of active material [315] 51

Figure 1.32 a) IH setup. (b) SEM image of as-grown monolayer graphene on copper foil substrate (Scale bar is 3 μm). (c) Raman spectrum of Graphene sheets. Insets are photograph and optical microscopic image (scale bar is 20 μm) of transferred graphene on a SiO_2/Si substrate.(d–f) Raman mapping of transferred graphene film with different intensity band ratios(Scale bars are 6 μm) [323] 52

Figure 1.33 SEM images of graphene domains grown on Cu at different growth temperatures and times. Scale bar: 10 μm; inset scale bar: 500 nm [323] 53

Figure 1.34 Percentage of CO_2 conversion, CH_4 and CO yields, and CH_4 selectivity as a function of μ_0 H_{rms} for, a) CFO/Ni/S and, b) CFO@FO2/Ni/S systems. Sketches in blue and in blue-brown represent the single $Co_{0.6}Fe_{2.4}O_4$ phase and the core–shell $Co_{0.6}Fe_{2.4}O_4$@ Fe_3O_4 cuboctahedron employed for the heating, respectively. Dashed lines indicate the 95 % level [267]. 55

Figure 2.1 Synthesis schematic: HLB stirring → EG addition with sonication & stirring → Drying → Carbonization 75

Figure 2.2 BET Isotherm plots and I-V characteristics of FLG-C samples under the freeze drying(FD) and oven drying(OD). 76

Figure 2.3 I-V characteristics of FLG/C samples under different gas and temperature conditions. 77

Figure 2.4 SEM images reflecting the structuration obtained from various HLB systems with initial EG:HLB ration of 0.5:4; A) FLG-Haemoglobin, B) FLG- Agar-Agar, C) FLG-Bovine Serum Albumin, D) FLG-Tannic Acid, E) FLG-Maltodextrin (Scale: 10 μm).78

Figure 2.5 Exemplary TGA curves of two FLG/A/M composites after carbonization, b,c) the exemplary XPS C1s and N1s spectra of FLG/A/M: 1.4/1 before and after carbonization under NH3 and Ar, d) Table 2 containing the % of C, N, O elements according to XPS and/or elementary analysis*, e) deconvoluted N1s spectrum of FLG/A: 1/2 , f) % contribution of N-containing groups (blue-pyridinic; red-pyrolic; green-quaternary; purple-N-X) in different composites (C1-FLG/A:1/2; C2-FLG/A/M:1/1.6; C3-FLG/A/M:1/1.2; C4-FLG/A/M:1.4/1; C5-FLG/A/M:1.4/1-Ar). 85

Figure 2.6 Representative TEM and SEM micrographs of FLG/C composites: a) few microns size FLG flakes, b) edge of FLG flakes containing 8 sheets, c) FLG surface covered by C with some mesopores, d) FLG-C composite after carbonization, e) FLG/A/M composite (before carbonization) with visible hHLB spheres...................................... 87

Figure 2.7 The representative SEM micrographs of FLG/A composite: a and b) before carbonization (side and top view), c) side view of FLG/C (FLG/A after carbonization, a.c.)), d and e) side-view of FLG/C (FLG/A a.c.) electrode, f) top-view of FLG/C (FLG/A a.c.) electrode. 88

Figure 2.8. a) Table 3 containing the total SBET and contribution of micropores SBET, b) exemplary isotherms, c) pore size distribution curves, inset: mesoporous region......... 89

Figure 2.9 a) CV curves of FLG/A/(M) composites at 20 mV/s, b) GCD curves of FLG/A/(M) composites at 1 A/g, c) a graph combining obtained specific gravimetric capacitance values, CGCD at different current densities, d) stability test for FLG/A composite at 20 A/g.. 90

Figure 2.10 a–c) CV and d-i) GCD curves of FLG/A:1/2, FLG/A/M:1/1.6, FLG/A/M:1/2.3 at different potential sweeps. 92

Figure 2.11 Estimations of DL/Ps capacitance contribution: a) dependence of q^{-1} vs. $\nu^{1/2}$, b) dependence of q vs. $\nu^{-1/2}$; c) table 4 regrouping the maximum total C from CV and DL, Ps contributions (C_T, C_{DL}, C_{Ps}, C_{Ps}/C_T, C_{DL}/C_T), capacitance from GCD (C_{GCD}), voltametric C (C_{CV}), packing density (d) and volumetric capacitance (Cvol); d and e) mass and volume normalized Ragone plots.. 94

Figure 3.1 a-e) TEM micrographs with different magnifications of flattened iron oxide NPs over FLG (after annealing at 800°C under H_2/Ar (FLG-Fe_xO_y-1), f) AFM image and profile of (FLG-Fe_xO_y-1) system. 107

Figure 3.2 a) TGA curves of iron oxide/FLG before and after annealing at 800°C under H_2/Ar, b,c) corresponding XPS C1s and Fe 2p spectra. 108

Figure 3.3 a, b) SEM micrographs and c-f) TEM micrographs of iron oxide hexagonal platelets over FLG (FLG-Fe_xO_y-2). 109
Figure 3.4 a, b) Fe 2p and C1s XPS spectra of iron oxide over FLG before and after µ-waves treatment, c, d) corresponding TGA and Raman spectra. 110
Figure 3.5 TEM micrographs of CNFs growth over iron-oxide/FLG catalysts. 111
Figure 3.6 Scheme of hexagonal platelet vs. spherical particle. 112
Figure 4.1 Freeze dried FLG-Agar-agar sample loaded with 10% Ni NPs via wetness impregnation, A) before reduction, B) after reduction. 119
Figure 4.2 STEM (1st column), HAADF (2nd column) and enlarged section(3rd column) of FC-800-10Ni(1st row), FC-800-20Ni (2nd row) and FC-800-40Ni (3rd row) respectively. 128
Figure 4.3 TEM images and Particle Size Distribution of FC-800-10Ni (a, b),C-800-20Ni (c, d), and FC-800-40Ni (e,f) 129
Figure 4.4 XRD spectra of, (a) FC-800-YY, (b) FC-700-YY & FC-900-YY. 131
Figure 4.5 CO_2-TPD profiles of FLG-CNFs composites. 133
Figure 4.6 Conversion and Selectivity of CO_2 and CH_4 respectively on FC samples. 134
Figure 4.7 FC-800-10Ni sample under, (a) different reaction mixture ratio and temperature, (b) under different GHSV (blue dot- conversion, red dot- selectivity for the same sampling). 135
Figure 4.8 FC-800-10Ni CO_2 methanation under, (a) Inductive Heating at 60,000 ml g_{cat}^{-1} h^{-1} GHSV and, (b) Joule Heating at 60,000 h^{-1} GHSV. 136
Figure 4.9 TPSR studies of some FLG-CNF samples. 137
Figure 4.10 (a) Thermodynamic stability under IH and, (b) kinetic stability under JH for methanation with FC-800-10Ni sample. 137
Figure 4.11 Particle size distribution (a),and TEM micrographs (b, c) of FC-800-10Ni catalyst after stability test. 138
Figure 4.12 SEM images of FC-700(a,d), FC-800 (b,e), and FC-900 (c,f) samples indicating the CNFs distribution and diameter 139

Abbreviations

A- Albumin
AC- Activated Carbon
BET- Brunauer, Emmett and Teller
BSA- Bovine Serum Albumin
CCU- Carbon capture and utilisation
CCS- Carbon capture and storage
CNFs- Carbon nano fibres
CNTs- Carbon Nano Tubes
CO_2-TPD- Carbon Dioxide- Temperature Programmed Desorption
CVD- Chemical Vapor Deposition
EDLC-Electrical Double Layer Capacitor
EES- Electrochemical energy storage
EV- Electronic vehicles
FLG- Few Layer Graphene
FM- Ferromagnetic
GHG- Greenhouse gas
GHSV- Gas Hourly Space Velocity
GWh- Gigawatt Hour
IEA- International Energy Agency
IH- Inductive Heating
IHP- Inner Helmholtz Plane
JH- Joule Heating
NPs- Nanoparticles
M- Maltodextrine
MSN- Mesostructured Silica Nanoparticle
NGQDs- Nitrogen Doped Graphene Quantum Dots
OECD- Organisation for Economic Co-operation and Development
OHP- Outer Helmholtz Plane
PC-Pseudo capacitor
Ps- Pseudocapacitance
PtG- Power-to-gas
PtX- Power-to-X
PV-Photovoltaics
PVA- Poly-Vinyl Alcohol
RE- Renewable Energy

SC- Supercapacitor

SPM- Superparamagnetic

TGA- Thermogravimetric Analysis

TPSR- Temperature Programmed Surface Reaction

XPS- X-ray Photoelectron Spectroscopy

XRD- X-ray Diffraction

Résumé

1. Introduction

Le stockage et la distribution de l'énergie ont été le fer de lance des grandes politiques mondiales. En 2018, les combustibles fossiles comme le charbon, l'essence et le gaz naturel représentent environ 81% des sources d'énergie [1]. Cet abus incessant des combustibles fossiles entraîne des problèmes mondiaux sur de multiples fronts. Il est essentiel d'avoir un aperçu immédiat de l'utilisation durable des sources d'énergie renouvelables. La Commission européenne envisage cela dans le cadre du Green Européen Deal qui vise à rendre le continent neutre en carbone d'ici 2050, en investissant dans des technologies respectueuses de l'environnement et en rendant le secteur énergétique moins dépendant des ressources carbonées [2]. De nombreux efforts sont déployés dans le seul but de récolter et de stocker les énergies renouvelables en raison de leur caractère intermittent. Les sources d'énergie renouvelables ont été introduites sur le marché mondial, mais leur mise en œuvre a été jusqu'à présent limitée car elles nécessitent un stockage approprié pour une utilisation tout au long de l'année. Le stockage électrochimique de l'énergie est l'une des voies de recherche qui visent à stocker l'énergie provenant de ces ressources énergétiques intermittentes et à pouvoir la fournir de manière continue en fonction des besoins. Une autre solution de ce type pour répondre à la demande d'énergie consiste à remplacer le réseau de gaz existant par celui du méthane (CH_4), qui est écologiquement viable. Cela a donné naissance au concept de captage, d'utilisation et de stockage du carbone, qui vise à réduire les niveaux de CO_2 dans l'atmosphère et à le convertir en même temps en d'autres formes utiles. Le CO_2 étant un gaz à effet de serre majeur, il a un impact important sur l'augmentation de la température mondiale. L'hydrogénation du dioxyde de carbone en méthane a donné lieu à des recherches dans le domaine de la conception de catalyseurs et de réacteurs qui peuvent offrir une bonne efficacité tout en utilisant moins de ressources. Le projet actuel porte sur l'adaptation des aspects physico-chimiques et structurels des matériaux à base de graphène, qui sont les plus prometteurs pour résoudre ces problèmes pour les générations futures. Depuis sa découverte au début des années 2000 par K. S. Novoselov [3], le graphène a été un élément clé de la recherche dans le domaine des applications énergétiques en raison de ses caractéristiques uniques telles qu'une grande surface, une conductivité électrique et thermique potentiellement très élevée, etc [4-7]. Depuis lors, il a été étudié sous diverses formes (comme les feuilles monocouches de graphène, le graphène à quelques couches) et avec les métaux et leurs dérivés pour les applications énergétiques [8-11].

1.1 Stockage électrochimique de l'énergie

Le stockage de l'énergie étant l'un des aspects les plus importants pour la réalisation d'un passage complet aux énergies renouvelables, les meilleurs systèmes de stockage de l'énergie comme les supercondensateurs sont basés sur le stockage de la charge électrochimique. Les supercondensateurs en eux-mêmes sont connus pour leur rôle de soutien et d'encouragement aux questions énergétiques, car ils utilisent généralement les meilleures batteries et condensateurs. Ils sont conçus pour utiliser la haute densité de puissance des condensateurs conventionnels et fournir simultanément une densité d'énergie équivalente à celle des batteries modernes. Un supercondensateur typique est constitué de deux électrodes (anode et cathode) avec un séparateur entre elles qui contient normalement l'électrolyte et forme un système de membrane semi-perméable qui permet le passage des ions tout en gardant les électrodes isolées. Il existe deux mécanismes de base qui commandent le stockage de l'énergie dans les supercondensateurs : la capacité électrique à double couche résultant de l'accumulation électrostatique des charges d'électrolyte sur l'électrode, et la pseudo-capacité résultant des réactions d'oxydoréduction à l'interface électrode-électrolyte [12,13]. Outre le condensateur électrique à double couche (EDLC~ Electrical double layer capacitor) idéale, il existe des supercondensateurs hybrides qui utilisent à la fois la capacité électrique à double couche et la pseudo-capacité. Les matériaux adaptés aux électrodes de supercondensateurs doivent donc avoir une surface et une porosité élevées et être stables dans la fenêtre de tension requise. Ces dernières années, la conception de matériaux pour les supercondensateurs s'est développée, mais avec certains inconvénients tels que l'extensibilité, la facilité d'utilisation, l'épaisseur, la flexibilité, etc. Pour la plupart, diverses formes de carbone (nanofibre, charbon actif, graphène) ont été utilisées comme matériau de base pour les supercondensateurs, bien qu'elles présentent divers inconvénients [14,15].

La forme de graphène la plus courante qui a été utilisée est l'oxyde de graphène, mais une alternative est nécessaire au long et difficile processus de synthèse de ce matériau. L'idée qui sous-tend l'utilisation du graphène à quelques couches est de produire un graphène à surface encore plus élevée, facile à préparer et à rendement élevé, ainsi qu'à densité suffisante, ce qui le rendrait adapté à une mise à l'échelle et à une application industrielle. Un stade de cricket entier peut être recouvert de feuilles de graphène qui ne pèseraient qu'un gramme environ. Le graphène est théoriquement censé avoir une grande surface de 2675 m^2 g^{-1} [16] mais la recherche à son stade actuel n'a pas encore atteint sa pleine utilisation. Il a également été constaté que la capacité théorique élevée (560 F g^{-1} de 25 µF m^{-2}) doit être corrigée en raison des apports de bord. En fait, il a été prouvé que la capacité observée sur les bords des paillettes de graphène est supérieure à celle du plan basal. Par exemple, la capacité « surfacique » des bords du graphite est supérieure de 4 ordres de grandeur à celle du plan de base [17]. En outre, l'empilement π-π entre les couches de graphène rend les plans de surface inaccessibles pour la plupart des applications. Pour éviter cela, de formidables recherches ont été menées pour synthétiser des aérogels et des hydrogels au graphène qui ont tendance à avoir une surface élevée, ce qui leur donne une supériorité en terme de capacité spécifique élevée, mais qui sont insuffisants pour la capacité volumétrique. L'exfoliation mécanique et en phase liquide est l'une des méthodes les plus utilisées pour la synthèse de graphène à quelques couches (FLG~ Few Layer Graphene). Selon la théorie des potentiels intercouches dépendant de la distance, l'énergie d'exfoliation nécessaire pour séparer une feuille de graphène du graphite empilé AB est d'environ 55,16 meV atome^{-1}, ce qui équivaut à la moitié de l'énergie de liaison intercouche [18]. Il est essentiel de comprendre comment utiliser les méthodes de synthèse pour tirer profit de la grande surface spécifique (SSA~Specific Surface Area) du FLG. La structuration du FLG peut être réalisée par, i) l'amélioration de la SSA et de la conductivité de la FLG, ii) l'augmentation de la densité de tassement et, iii) le contrôle des défauts. C'est pourquoi l'accent est mis sur des méthodes de synthèse appropriées basées sur l'exfoliation pour utiliser le véritable potentiel du graphène, qui est encore à l'étude. Ceci, combiné à de bonnes idées pour la structuration du FLG, peut aboutir à la solution de stockage d'énergie de prochaine génération dont le monde a besoin.

L'objectif principal du projet est de synthétiser des matériaux à base de graphène qui peuvent être utilisés pour des applications énergétiques telles que les supercondensateurs et les catalyseurs. L'idée de base est d'utiliser les propriétés inhérentes du graphène et de le rendre disponible de manière économique et écologique pour de telles applications. La première partie de mon projet consiste en une synthèse de quelques couches de graphène par l'intermédiaire de l'eau et de biosurfactants pour former des électrodes alignées à base de graphène qui peuvent fournir une capacité volumétrique élevée. Des matériaux à haut équilibre hydrophile et lipophile (h-HLB~ high hydrophilic lipophilic balance) sont généralement utilisés pour cette étude. Les tensioactifs sont utilisés non seulement pour l'exfoliation mais aussi comme partie du composite dans le produit final. Ainsi, ils sont ajoutés en grand excès au début et ensuite converti en carbone amorphe lors d'un traitement gazeux à haute température. Le carbone ainsi formé agirait comme un espaceur entre les plaquettes de graphène et aiderait également à la pseudocapacité résultant de réactions faradiques. Le traitement au gaz contribue également au dopage à l'azote des surfaces de carbone. En outre, les matériaux h-HLB contribuent également à rendre les électrodes ultra-microporeuses, augmentant ainsi la capacité de rétention de charge. Dans le cas des supercondensateurs, l'objectif est aussi de maintenir l'alignement vertical de la structure de graphène multi-couches avec une densité accrue de sorte qu'il puisse y avoir une plus grande accessibilité aux bords et une capacité volumétrique élevée.

1.2 Conversion et stockage de l'énergie chimique

Il est bien connu des communautés scientifiques, industrielles et politiques du monde entier que la modification des concentrations de gaz dans l'atmosphère, en particulier du CO_2, qui a commencé avec l'industrialisation, a des effets drastiques. De plus, avec les possibilités de stockage des énergies renouvelables qui ont évolué ces dernières années, il sera judicieux de convertir le surplus d'énergie en d'autres formes qui peuvent être facilement utilisées dans la société. La technologie Power-to-Gas est l'une des méthodes Power-to-X qui permet de formuler des idées pour l'utilisation de l'énergie provenant de ces sources d'énergies renouvelables et de les utiliser pour la conversion en combustibles gazeux, ce qui permet de diminuer la pression exercée sur les combustibles fossiles et de réduire la pollution atmosphérique qui en résulte [19]. Selon la technologie PtG, l'énergie excédentaire récoltée à partir de sources vertes telles que l'hydel, le solaire et le vent peut généralement être d'abord acheminée vers un électrolyseur à eau pour la production de H_2. Le CO_2 peut être utilisé comme matière première avec l’hydrogène produit pour la production de méthane qui peut ensuite être introduit dans l'infrastructure de distribution de gaz existante sous forme de gaz naturel synthétique. Cela facilitera les chaînes mondiales de captage, d'utilisation et de stockage du carbone (CCUS~ Carbon Capture Utilisation and Storage) et augmentera également la densité énergétique volumétrique du gaz stocké (35-40 MJ m^{-3} pour le CH_4 contre 12,75 MJ m^{-3} pour l'H_2) sans poser de problèmes de sécurité [20]. La méthanation catalytique est un procédé mature qui est basé sur la réaction de Sabatier:

$$4H_2 + CO_2 \leftrightarrow CH_4 + 2H_2O \; ; \qquad \Delta G^o = -165\ kJ\ mol^{-1} \qquad \text{(Eq. R1)}$$

Le taux de conversion et la sélectivité des produits revêtent une grande importance dans ces cas. On considère normalement que la méthanation du CO_2 suit un mécanisme associatif ou dissociatif [21]. Le mécanisme associatif propose la formation initiale d’intermédiaires oxygénés par adsorption avec l'adatome de H_{ad}, suivie d'une hydrogénation ultérieure en CH_4. Au contraire, le mécanisme dissociatif suggère que le CO_2 est d'abord dissocié en adatomes (CO_{ad}) et (O_{ad}), suivi de l'hydrogénation du carbonyle en CH_4.

Le nickel est l'un des éléments les plus couramment utilisés pour la méthanation du CO_2 en raison de son faible coût (par rapport aux métaux nobles), de sa disponibilité, de sa bonne activité et de sa très bonne sélectivité pour le méthane. Il est largement utilisé avec d'autres métaux, des supports d'oxyde et des promoteurs pour améliorer l'activité et la sélectivité [22, 23]. L'un des facteurs les plus importants favorisant la méthanation du CO_2 par le nickel est le type de support sur lequel les NP sont placés et la manière dont ils se comportent avec l'environnement de chauffage. La dispersion des métaux NP et leur stabilité dépendent en grande partie des propriétés de surface et de texture, tandis que l'activité et la sélectivité dépendent de la réductibilité de la surface et des interactions métal-support [24]. De la famille des carbones, les nanotubes de carbone et les matériaux à base de graphène se sont avérés être les supports les plus efficaces pour la méthanation [25, 26]. Quelques couches de graphène et d'autres structures de graphène ont également été récemment exposées comme une alternative possible au support métallique pour la méthanation du CO_2. La plupart des interactions métal-carbone pour les applications catalytiques sont basées sur des nanofibres 1D qui ont normalement tendance à avoir un arrangement réciproque de feuilles de graphène avec un rapport bord/plan différent [27]. Une étude récente a prouvé que l'utilisation du graphène comme support diminue la température de conversion du CO_2 dans une large mesure, tout en augmentant le taux de conversion [28]. Cette étude a indiqué une activité négligeable du graphène seul vers la méthanation du CO_2 et seulement à une température supérieure à 400°C, ce qui indique qu'il se comporte comme un support pour les plages de température inférieures à cette température.

La catalyse hétérogène actuelle implique l'utilisation de réactifs et de gaz multiphasiques, ce qui exige de meilleurs systèmes de gestion de la chaleur sur place. Le chauffage par induction électromagnétique (IH~ Inductive heating) ou par radiofréquence (RF) de catalyseurs magnétiques ou électroconducteurs a récemment été une nouvelle piste d'intérêt pour les chercheurs du monde entier [29, 30]. L'approche du chauffage par induction électromagnétique, qui consiste à chauffer directement les matières actives dans le réacteur, est particulièrement utile pour s'attaquer aux limites de chauffage rencontrées dans une installation conventionnelle. Le chauffage direct du cœur du catalyseur sans chauffer l'ensemble de l'installation à partir des parois extérieures permet également d'économiser de l'énergie. La chaleur générée dans les réacteurs basés sur un système d'induction magnétique provient de trois sources différentes : a) les pertes par hystérésis dans le cas de matériaux ferromagnétiques (FM) [31], b) les pertes par courants de Foucault dans le cas de matériaux électriquement conducteurs [32], c) les pertes par relaxation de Neel et brownienne dans le cas de nanoparticules superparamagnétiques (SPM) [33]. Il a été prouvé que l'IH assure un chauffage plus uniforme, ce qui permet d'obtenir des CNTs de meilleure qualité que les méthodes de chauffage conventionnelles utilisées auparavant [34]. L'IH a également joué un rôle important dans la production de graphène monocouche et multicouche de haute qualité sur divers substrats métalliques, car il nécessite une rampe rapide pour obtenir un temps de chauffage réduit, ce qui permet d'éviter la croissance imprévue de plusieurs couches [35]. La méthanation via l'IH en est encore à un stade très précoce, car très peu de travaux de recherche ont été consacrés à ce sujet depuis que l'idée de la "catalyse à froid" a été lancée [36, 37]. La méthanisation étant une réaction exothermique, l'IH est particulièrement utile pour éviter d'importantes variations de température dans le réacteur. Le nickel a été utilisé sur des supports comme l'alumine et le feutre de carbone oxydé (OCF~ Oxidised carbon felt) pour la méthanation à base d'IH, mais il faut encore explorer l'utilisation du graphène comme support.

La deuxième partie de mon projet est consacrée à la conception rationnelle de matériaux catalytiques à base de graphène à quelques couches qui peuvent aider à résoudre les problèmes énergétiques en vue d'une production plus écologique et durable. En vue de faire un pas en avant vers les technologies vertes, le projet envisage l'idée de remplacer les catalyseurs en carbone à base de métaux nobles par des catalyseurs en carbone à base de métaux non nobles pour des applications de conversion du CO_2. Il est nécessaire d'être attentif à la manipulation des formes métalliques supportées par les structures soutenues par le FLG, afin de rendre les sites actifs plus viables et plus accessibles pour les réactions catalytiques qui peuvent aider à la libération d'énergie. La fixation des nanoparticules métalliques et leur stabilité thermique sont bien facilitées par les défauts et les groupes fonctionnels des structures de support, ce qui a été le cas pour les systèmes utilisant des nanofibres de carbone et des oxydes de graphène. Le projet vise à éliminer la nature granulaire de ces substrats en utilisant des feuilles de graphène à quelques couches comme modèle pour adapter les nanoparticules métalliques de manière à améliorer leurs caractéristiques 2D, ce qui contribue à augmenter le nombre de sites actifs pour les réactions catalytiques. Cela peut être réalisé en modifiant les procédures de synthèse et les éventuels traitements thermiques/gaz. Dans le cas des catalyseurs, l'objectif est de concentrer les efforts sur la synthèse de meilleurs catalyseurs sans métaux nobles qui peuvent aider à la conversion/méthanation du CO_2 ainsi qu'à la séparation de l'eau. Le défi consiste donc à concevoir des catalyseurs dont les supports sont stables aux brusques hausses et baisses de température, ce qui est la caractéristique principale du chauffage inductif.

2. Résultats et discussion

2.1 Adaptation des composites FLG pour le stockage électrochimique de l'énergie

Afin de conserver l'alignement des structures de graphène pour les supercondensateurs, l'exfoliation du graphite expansé dans l'eau a été combinée avec un lyophilisation conséquente suivie d'un traitement au gaz à des températures élevées. Cela a permis non seulement d'éliminer les précurseurs tensioactifs (maltose(M) et albumine de sérum bovin(A)), mais aussi de les convertir en carbone amorphe, ce qui permet d'éviter le ré-empilage des couches et de fournir une pseudo-capacité, formant ainsi un supercondensateur hybride. Un excès important de tensioactif apporte des caractéristiques uniques d'ultramicroporosité dans le composite tout en gardant une densité élevée. Les échantillons sont désignés comme FLG/A ou FLG/A/M (selon qu'ils contiennent de l'albumine ou du maltose -albumine comme précurseurs initiaux), puis le rapport final entre le FLG et les carbones amorphes après traitement au gaz à haute température.

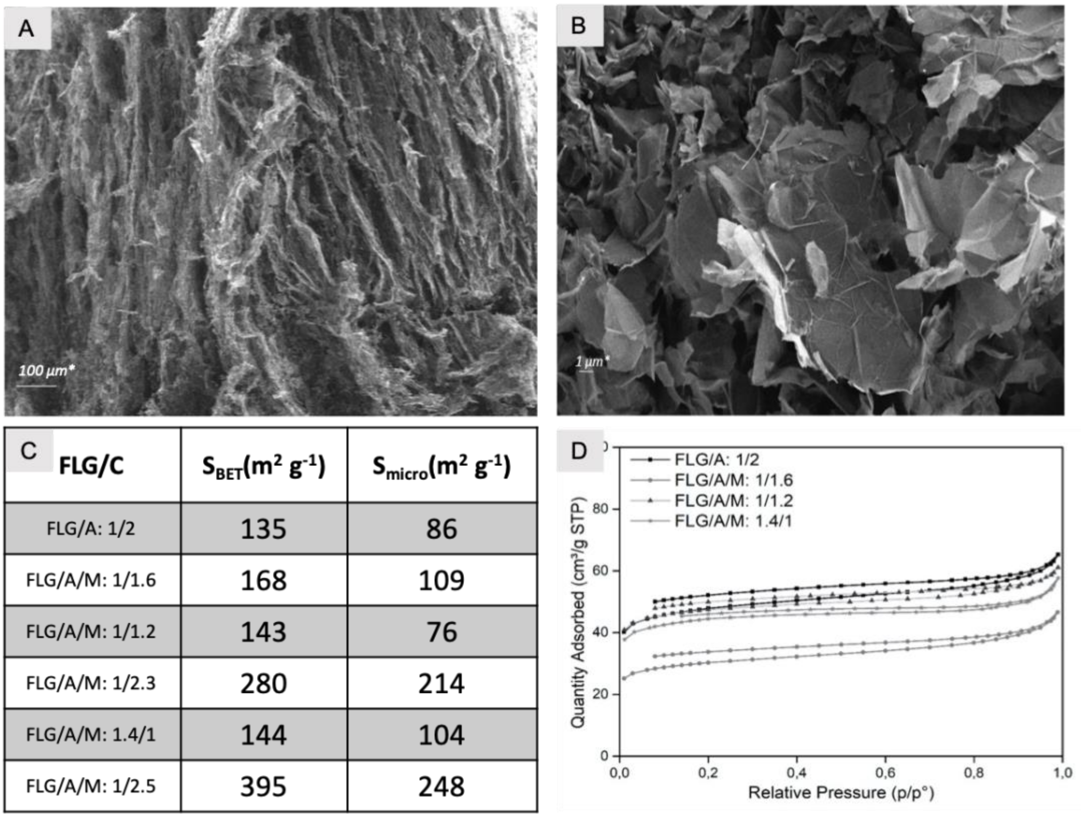

FLG/C	S_{BET}(m² g⁻¹)	S_{micro}(m² g⁻¹)
FLG/A: 1/2	135	86
FLG/A/M: 1/1.6	168	109
FLG/A/M: 1/1.2	143	76
FLG/A/M: 1/2.3	280	214
FLG/A/M: 1.4/1	144	104
FLG/A/M: 1/2.5	395	248

Figure R 1 a,b) Images MEB des échantillons FLG/C, c) Tableau contenant le S_{BET} total et la contribution des micropores, d) isothermes exemplaires de divers échantillons. [38]

Il a été constaté que les composites contenant uniquement de l'albumine ou son excès présentaient un degré d'alignement plus élevé, contrairement aux échantillons contenant des quantités plus élevées ou comparables de maltodextrine, qui présentaient une morphologie plus poreuse et plus mousseuse [38]. Le maintien de l'alignement même après la carbonisation, comme le montre la **Figure R 1 (a)**, peut être attribué à des liaison hydrogène renforcées localement par les interactions de Van der Waals. La **Figure R 1 (b)** montre les plus grandes feuilles de graphène intercalées avec des particules de carbone amorphe qui ont été formées suite à la dénaturation par un traitement d'ultrasons et ensuite à la carbonisation des précurseurs par un traitement gazeux à haute température. Les nouvelles liaisons hydrogène de l'albumine adsorbé sur FLG et l'eau ont joué un rôle dans l'alignement de FLG. Il est intéressant de noter qu'il n'y avait pas beaucoup de différence entre la capacité gravimétrique spécifique des électrodes fabriquées à partir d'échantillons directement après la carbonisation et celle des échantillons dispersés dans l'éthanol et déposés sur du carbone vitreux. Les mesures de surface ont montré que tous les échantillons présentaient une faible surface (**Figure R 1 (c)**), ce qui peut être attribué à l'épaisseur des couches de FLG et au ré-empilage partiel π-π inter-couches pendant le processus de dégazage. Tous les échantillons présentaient des isothermes de type I en analyse BET avec une prédominance de micropores. L'absence de chevauchement terminal des isothermes pour les pressions relatives plus faibles (**Figure R 1 (d)**) indique la présence de pores fendus dont la taille a augmenté en raison de l'interaction latérale des molécules adsorbées.

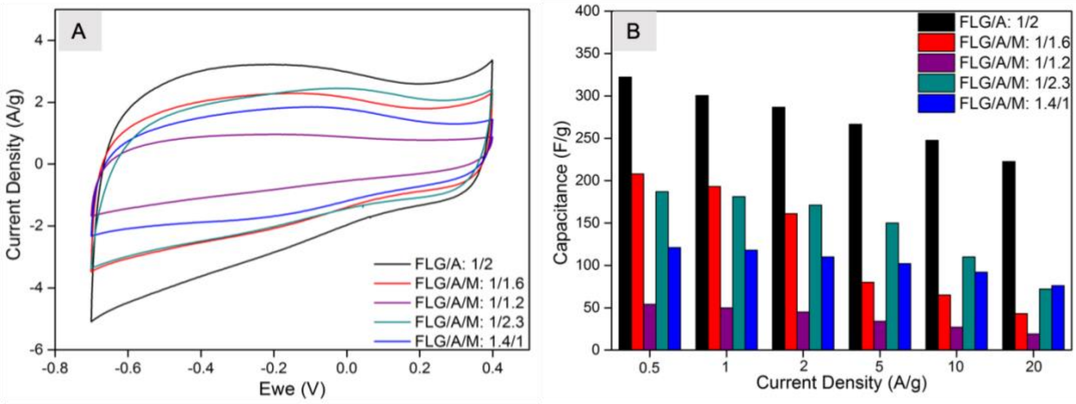

C

FLG/C (in. FLG/A/M)	C_T	C_{DL}	C_{PS}	C_{PS} / C_T (%)	C_{DL} / C_T(%)	C_{CV} (5 mV/s)	C_{GCD} (0.5 A/g)	d (g/cm³)	C_{Vol} (F/cm³)
FLG/A:1/2 (in. 0.5/4)	535	167	368	69	31	320	322	1.45	467
FLG/A/M: 1/1.6 (in. 0.5/3/1)	260	83	177	68	32	230	208	1.24	258
FLG/A/M: 1/1.2 (in. 1/1/3)	142	32	110	78	22	92	54	0.86	46
FLG/A/M: 1/2.3 (in. 0.5/1/3)	606	77	529	87	13	220	187	1.65	309
FLG/A/M: 1.4/1 (in. 1/3/1)	246	65	181	74	26	156	121	0.44	53

Figure R 2 a) Courbes CV des composites FLG/A/(M) à 20 mV/s, b) graphique combinant les valeurs de capacité gravimétrique spécifique obtenues, C_{GCD} à différentes densités de courant, c) tableau montrant les estimations de la contribution de la capacité DL/Ps, de la densité des échantillons et de la capacité volumétrique corr.[38]

Les performances électrochimiques des échantillons ont été étudiées dans une configuration à trois électrodes avec un électrolyte H_2SO_4 de 0,5 M dans une fenêtre de potentiel de 1,1 V. Cinq échantillons avec des proportions variées d'albumine et de maltodextrine ont été utilisés afin d'identifier le meilleur offrant une capacité supérieure. La **Figure R 2 (a)** montre les courbes de CV quasi rectangulaires symétriques des échantillons mesurés à 20 mV s-1, ce qui indique sa réversibilité et sa tendance à améliorer la supercapacité. On peut clairement voir que l'échantillon FLG/A:1/2 a la densité de courant maximale sur la même fenêtre de potentiel. L'écart de la forme par rapport à un rectangle parfait confirme la contribution pseudo-capacitive à la capacité nette. La **Figure R 2 (b)** représente la capacité obtenue par les mesures de charge/décharge galvanostatique (GCD) pour les cinq échantillons par application de différentes densités de courant. Elle montre également la rétention de capacité élevée (c'est-àdire une chute de 30%) du meilleur échantillon FLG/A:1/2 même à une densité de courant de 20 A g^{-1}. Une légère baisse a été observée pour le FLG/A/M:1.4/1 alors que de grandes baisses ont été observées pour les espèces riches en carbone amorphe telles que le FLG/A/M:1/1.6 et le FLG/A/M:1/2.3. Il n'a pas été possible de trouver une corrélation spécifique entre la capacité des composites et le S_{BET}. Les trois composites présentant les capacités les plus élevées mais différentes à 0,5 A g^{-1} ont des S_{BET} similaires. Le composite ayant la S_{BET} la plus élevée (FLG/A/M:1/2.5) présente une très faible capacité (22 F g^{-1} at 0,5 A g^{-1}). Simplement, toutes les valeurs de S_{BET} obtenues pour les composites FLG/C sont également extrêmement faibles compte tenu des très bonnes capacités démontrées par les composites. Cette incohérence vient du fait que la S_{BET} ne reflète pas nécessairement la surface effective accessible par les ions électrolytes (E-SSA) [39], surtout si les ultramicropores sont présents en excès.

Les contributions individuelles de la pseudo-capacité (C_{Ps}) et de la double-capacité (C_{DL}) ont été obtenues par une méthode récente adaptée aux supercondensateurs à base de carbone, dans laquelle la charge voltampérométrique totale Q_T est d'abord obtenue en traçant 1/q en fonction de $v^{1/2}$ et en extrapolant sa courbe de tendance à v=0, tandis que Q_{DL} est obtenue en traçant q en fonction de $v^{-1/2}$ et en extrapolant sa courbe de tendance à $v=\infty$ [40, 41]. Les capacités correspondantes C_T et C_{DL} peuvent être obtenues en divisant le Q_T et le Q_{DL} par la fenêtre de potentiel (1,1 V). D'après le tableau 3 de la **Figure R 2 (c)**, on peut voir que la tendance croissante du T_C calculé est en accord avec la C_{DL} obtenue, à l'exception d'un seul échantillon qui présente une pseudo-capacité énorme. Les valeurs de la capacité n'augmentent pas en tandem avec l'augmentation de la surface spécifique comme le suggère la théorie classique initiale des électrodes supercapacitives. Cela peut être attribué à une accumulation de charge supérieure par l'exposition différentielle des bords des feuilles FLG qui dépend à son tour de l'architecture des composites et non du rapport bords/plans. En outre, cette anomalie dans la dépendance de la surface à la capacité augmente également en raison des ultramicropores fendus entre les flocons qui maximisent la densité de stockage des ions, donnant lieu à une capacité volumétrique élevée [42]. L'alignement vertical amélioré et la nature compacte des composites les rendent plus denses que la plupart de leurs homologues, ce qui permet d'obtenir une capacité volumétrique élevée pour le meilleur échantillon FLG/A:1/2 jusqu'à 467 F cm^{-3}.

2.2 Utilisation du FLG comme modèle pour les nanoplaquettes métalliques plates

Les matériaux FLG sont également utiles pour obtenir des nanoparticules métalliques 2D, en vu par exemple de catalyse, potentiellement plus efficaces. La nature de la réaction catalytique est principalement déterminée par la nature du catalyseur utilisé qui se traduit entre autres par la taille et morphologie. Des feuilles de FLG décorées à l'oxyde de fer ont été synthétisées par deux méthodes différentes [43].

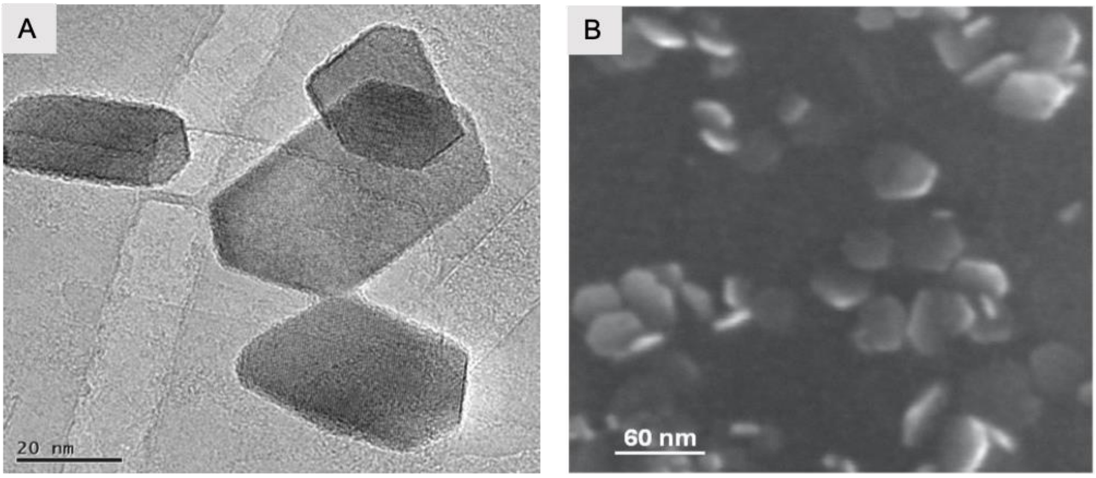

Figure R 3 (a) image MET de NP d'oxyde de fer sur un FLG préparé par addition de précurseur de Fe via in-situ suivie d'un recuit à 800°C sous H_2/Ar, (b) image MEB d'isalndes de particules métalliques plates formées sur du graphène par imprégnation par voie humide suivie d'un traitement aux microondes avec liq. NH_3. [43]

Dans la première méthode, le Fe NP a été synthétisé par une méthode solvothermique impliquant une exfoliation initiale du graphite en milieu liquide avec addition simultanée in situ de précurseurs du Fe NP. Après une réaction à haute température, le précipité final a été lavé et soumis à un processus de recuit en deux étapes à 400°C et 800°C sous des atmosphères Ar et Ar/H_2 correspondantes. Le traitement de réduction/recuit prolongé intentionnel vise à "purifier" la surface du FLG et à obtenir ainsi un réseau propre pouvant interagir davantage avec les NPs. Le principal résultat du processus de recuit est la formation de NPs de Fe à deux facettes aplaties (**Figure R 3 (a)**) avec une coalescence mineure. La cause la plus probable de cette géométrie unique peut être considérée comme le processus de stabilisation des NP le long des bords [44] et aussi de leur interaction avec les surfaces des terrasses de FLG à des températures aussi élevées.

La deuxième méthode a utilisé l'imprégnation avec de précurseurs du fer dissous sur les FLG obtenus par ablation mécanique du graphite. Le produit obtenu a d'abord été préréduit à 350°C sous atmosphère H_2/Ar pendant 2h avant d'être soumis à un traitement par microondes à une puissance de 800W avec de l'ammoniac liquide comme solvant. Ce traitement devrait générer des points chauds locaux (microplasmes) sur le FLG [45]. L'imprégnation ainsi que la pré-réduction provoquent la formation d'îlots d'oxydes métalliques sur les surfaces du FLG. Le traitement par microondes qui en résulte transforme ces îlots en structures plaquettaires polygonales bien formées, comme le montre la **Figure R 3 (b)**, d'une épaisseur d'environ 10 nm et d'une taille latérale de 60 nm. Les deux échantillons indiquent l'idée que le FLG sert de modèle pour des nanoplaquettes métalliques bien définies, en particulier dans le cas d'un échantillon traité par microondes. Le traitement de recuit à haute température provoque une graphitisation, ce qui réduit les défauts de la surface du FLG. Ces sites de défauts se transforment ensuite en centres de stabilisation pour les NP métalliques. Lors de la graphitisation, les défauts se rétablissent, ce qui entraîne la séparation partielle et la remontée des NP métalliques du plan FLG, formant ainsi des nanoplaquettes à deux facettes. La nature émergente des plaquettes du support FLG indique la diminution de l'énergie libre en surface. [46-48]. L'inclinaison des Fe NPs sur le FLG offre un avantage particulier car non seulement une mais deux surfaces actives peuvent être utilisées pour les réactions. L'affaiblissement des réactions entre le support du FLG et les NP métalliques a également été confirmé par le mécanisme de croissance de nanofibres de carbone (CNF) perpendiculaires aux plans du FLG [27]. Les CNF se sont formées sur les deux côtés des NP métalliques, ce qui prouve leur double face active. L'inclinaison des NP de Fe sur les plans FLG offre un avantage particulier car non seulement une mais deux surfaces actives peuvent être utilisées pour les réactions. Il peut donc être utilisé pour diverses applications catalytiques.

2.3 Dépendance structurelle des nanofibres de carbone/graphène à faible couche décoré de Ni/NiO pour la méthanisation du CO_2 par chauffage inductif

En ce qui concerne la possibilité d'agir comme support pour la conversion de l'énergie chimique par méthanation, différents supports de graphène ont été synthétisés. Un groupe de supports à base de FLG sur lesquels des nanofibres de carbone (CNF) ont été cultivées à trois températures différentes, suivies de charges multiples de nickel en tant que phase métallique active, a permis d'identifier les meilleurs paramètres pour l'utilisation d'un tel catalyseur dans un dispositif de chauffage inductif. Les catalyseurs ont été désignés par le sigle FC-XXX-YY, où XXX correspond à la température de croissance des CNF sur le FLG et YY au pourcentage de charge en nickel sur le FC. L'épaisseur des CNF cultivés à différentes températures suit la tendance : FC-800< FC-700< FC-900. La capacité de chauffage et de l’activité catalytique change en fonction de la morphologie de NFCs et le pourcentage de Ni déposé (10-40%). Une charge élevée d'environ 40% de Ni a donné lieu à la formation de plaquettes plates semblables à celles observées avec le Fe NP [43]. Les nanofibres de carbone, comme le montre la **Figure R 4 (a, b)**, se forment sous la forme de structures osseuses en hareng inhérentes à la croissance du CNF sur du graphène dopé au Ni. Il a été remarqué que la plupart des Ni NP étaient ancrées sur le CNF qui possède une grande quantité de bords accessibles pour stabiliser les NPs. De plus, parmi ceux qui étaient attachés aux flocons de graphène, la plupart étaient reliés au bord et étaient de plus grande taille que ceux déposés sur le CNF.

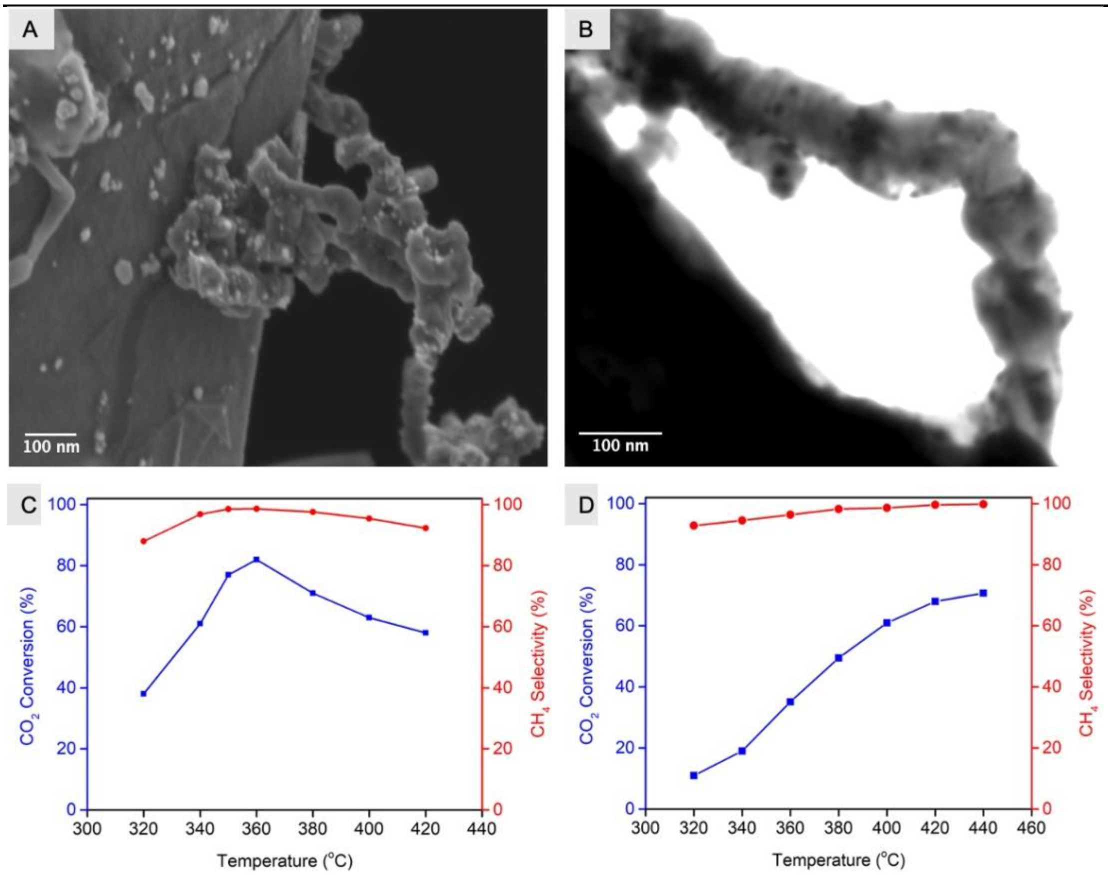

Figure R 4 Images MEB de catalyseurs FC-900-10Ni, (c) Réactivité de méthanisation du FC-800-10Ni sous chauffage inductif, (d) Réactivité de méthanisation du FC-800-10Ni sous chauffage Joule

Les performances catalytiques des catalyseurs ont été mesurées sur une plage de température de 280-440°C en quantifiant la conversion du CO_2 et la sélectivité du CH_4 dans deux installations de chauffage différentes, comme le montre la **Figure R 4 (c, d)**. Le chauffage inductif a récemment été reconnu pour la méthanation du CO_2 en raison de sa facilité à former des points chauds de phase active et à réduire ainsi la perte d'énergie due au chauffage de l'ensemble du réacteur [20, 21]. La méthanation du CO_2 réalisée avec le catalyseur FC-800-10Ni dans des installations IH et JH à 60,000 ml $gcat^{-1}$ h^{-1} (108 000 h^{-1}) et 60 000 h^{-1} (33 333 ml $gcat^{-1}$ h^{-1}) GHSV respectivement avec un rapport de gaz maintenu comme CO_2:H_2:gaz inerte (He/Ar) = 1:4:5. On peut clairement voir sur les deux courbes que la réaction démarre à une température plus élevée dans une installation JH par rapport à une installation IH. Un X_{CO_2} de 61% et un S_{CH_4} de 98% peuvent être obtenus à 340°C dans un dispositif IH (**Figure R 4 (c)**), alors que des résultats similaires dans un dispositif JH nécessitent une température pouvant atteindre 400°C (**Figure R 4 (d)**). La différence de 60°C pour une telle conversion, qui se prolonge avec l'augmentation de la conversion, prouve que l'IH est effectivement une meilleure approche pour le chauffage que le JH pour les réactions de méthanation avec des échantillons à faible charge. Les tests de stabilité effectués dans les deux installations indiquent une perte de 5-7% de réactivité après 60-80h de flux continu du mélange réactionnel.

Un test de stabilité et de réactivité (comme le montre la **Figure R 5**) a également été effectué, qui a prouvé que l'augmentation du rapport H_2 dans le mélange réactionnel augmente la conversion nette jusqu'à ~96%, tout en maintenant une sélectivité de ~99%. Un changement stoechiométrique du mélange réactionnel et une rampe de température alternative n'affectent pas le taux de conversion au bout de 60 heures, ce qui indique la stabilité du composite même dans des conditions changeant continuellement. Cela prouve donc que de tels supports sont des candidats viables pour la méthanation du CO_2.

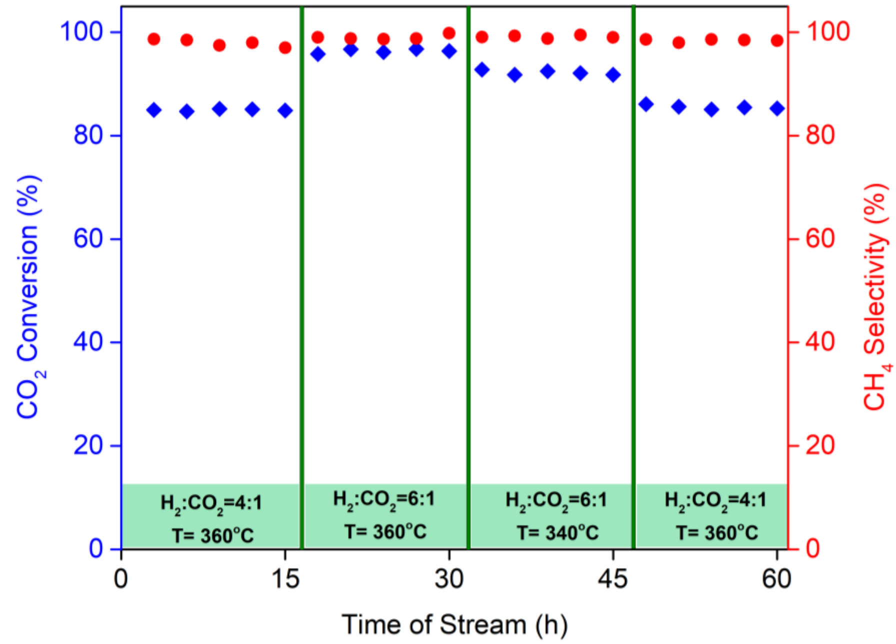

Figure R 5 Cohérence de la réactivité et de la sélectivité du catalyseur lors du changement de la stœchiométrie des gaz de réaction et de la température.

3. Conclusion générale

Au départ, des composites de carbone contenant graphène en quelques couches alignées verticalement ont été obtenus par exfoliation de graphite expansé en présence d'un excès important de précurseurs de h-HLB tels que la maltodextrine et la sérum-albumine bovine. Les composites obtenus se sont révélés être des candidats prometteurs pour les applications de supercondensateurs, même s'ils présentent une faible surface S_{BET}. Cela s'explique par le fait que la capacité dans le FLG est en grande partie due aux bords des écailles de graphène qui sont plus exposés en raison de l'alignement. De plus, l'ultramicroporosité et la densité élevée a permis l'obtention de capacités gravimétrique et volumétrique élevées.

On a tenté de comprendre la source et la contribution des deux types de capacité qui peuvent être responsables d'une telle capacité élevée. Il a été constaté que ces composites FLG ont une pseudo-capacité assez importante.

De plus, le FLG peut être utilisé comme modèle pour la synthèse de NPs métalliques plats avec un rapport surface/volume amélioré. Le procédé de synthèse conserve en grande partie la dispersion homogène élevée des NP métalliques même après un traitement à haute température, ce qui le rend avantageux pour diverses applications catalytiques. L'accès aux doubles faces permet d'obtenir une activité plus élevée de ces NPs.

Enfin, le FLG-CNF s'est révélé être un bon support de phase active (Ni) pour la méthanation par chauffage inductif. La température de croissance du CNF définit l'épaisseur de CNF et guide la dispersion des NPs formés. Les CNFs ayant une grande quantité de bords stabilisent de NPs et le FLG augment la conductivité thermique. La charge de Ni domine la taille des NPs formés et leur agglomération conséquente. On a constaté que le chauffage inductif permettait de réduire la température requise pour une conversion élevée du CO_2 par la formation de points chauds locaux. En outre, il a également été prouvé que l'efficacité maximale était obtenue pour une charge de Ni plus faible. Le CNF cultivé sur FLG à 800°C s'est avéré le plus mince, donnant ainsi naissance à des NPs de Ni de taille 5-10 nm qui peuvent assurer une conversion allant jusqu'à 85% à 360°C à une GHSV de 60 000 h^{-1}.

4. Perspectives

Les études suivantes sont envisagées pour l'optimisation nécessaire des systèmes étudiées.

- Les NPs métalliques plates de Fe seront étudiées pour les applications de méthanisation.
- Synthèse et étude des NPs plats de Ni pour les applications de méthanation et de supercondensateurs.
- Synthèse de NPs bimétalliques en alliage Fe-Ni pour la méthanation afin d'affiner la sélectivité et la conversion simultanément à une valeur >90 % avec une diminution de la température de réaction.

Références

[1] Total primary energy supply by fuel, 1971 and 2017, IEA, Paris https://www.iea.org/data-and-statistics/charts/total-primary-energy-supply-by-fuel-1971-and-2017, (accessed: September, 2020)

[2] European Commission, A European Green Deal, https://ec.europa.eu/info/strategy/priorities-2019-2024/european-green-deal_en, (accessed: September, 2020)

[3] K. S. Novoselov, A. K. Geim, S. V. Morozov, D. Jiang, Y. Zhang, S. V. Dubonos, I. V. Grigorieva, A. A. Firsov, *Science*, 2004, Vol. 306, 666-669

[4] Z. Niu, L. Liu, L. Zhang, Q. Shao, W. Zhou, X. Chen, S. Xie, *Adv. Mat.*, 2014, Vol. 26, 3681-3687

[5] Y. W. Tan, Y. Zhang, K. Bolotin, Y. Zhao, S. Adam, E. H. Hwang, S. Das Sarma, H. L. Stormer, P. Kim, *Phys. Rev. Lett.*, 2007, Vol. 99, 246803

[6] P. M. Ostrovsky, I. V. Gornyi, A. D. Mirlin, *Phy. Rev. B*, 2006, Vol. 74, 235443

[7] A. A. Balandin, S. Ghosh, W. Bao, I. Calizo, D. Teweldebrhan, F. Miao, C. N. Lau, *Nano Lett.*, 2008, Vol. 8, 902-907

[8] L. Qu, Y. Liu, J.-B. Baek, L. Dai, *ACS Nano*, 2010, Vol. 4, 1321-1326

[9] Y. Zhu, S. Murali, M. D. Stoller, K. J. Ganesh, W. Cai, P. J. Ferreira, A. Pirkle, R. M. Wallace, K. A. Cychosz, M. Thommes, D. Su, E. A. Stach, R. S. Ruoff, *Science*, 2011, Vol. 332, 1537-1541.

[10] Y. Xue, J. Liu, H. Chen, R. Wang, D. Li, J. Qu, L. Dai, *Angew. Chem. Int. Ed.*, 2012, Vol. 51, 12124-12127

[11] Y. Shi, L. Wen, G. Zhou, J. Chen, S. Pei, K. Huang, H.-M. Cheng, F. Li, *2D Materials*, 2015, Vol. 2, 024004

[12] Y. Wang, Y. Song, Y. Xia, *Chem. Soc. Rev.*, 2016, Vol. 45, 21, 5925-5950

[13] J. R. Miller, P. Simon, *Science*, 2008, Vol. 321, 5889, 651-652

[14] E. Frąckowiak, P. Ratajczak, F. Béguin, Electrochemical capacitors based on carbon electrodes in aqueous electrolytes, *Electrochemistry of Carbon Electrodes*, 2016, 285-312.

[15] P. Simon, Y. Gogotsi, *Materials for electrochemical capacitors, in: Nanoscience And Technology: A Collection of Reviews from Nature Journals*, World Scientific, 2010, 320-329

[16] M. Pumera, *Chem. Rec.*, 2009, Vol. 9, 211-223

[17] W. Yuan, Y. Zhou, Y. Li, C. Li, H. Peng, J. Zhang, Z. Liu, L. Dai, G. Shi, *Sci. Rep.*, 2013, Vol. 3, 2248

[18] X. Chen, F. Tian, C. Persson, W. Duan, N. Chen, *Sci. Rep.*,2013, Vol. 3, 3046

[19] M. Thema, F. Bauer, M. Sterner, *Renew. Sust. Energ. Rev.*, 2019, Vol. 112, 775-787

[20] H. Blanco, A. Faaij, *Renew. Sust. Energ. Rev.*, 2018, Vol. 81, 1, 1049-1086

[21] B. Miao, S. S. K. Ma, X. Wang, H. Su, S. H. Chan, *Catal. Sci. Technol.*, 2016, Vol. 6, 4048-4058

[22] M. A. A. Aziz, A. A. Jalil, S. Triwahyono, A. Ahmad, *Green Chem.*, 2015, Vol. 17, 5, 2647-2663

[23] C. Lv, L. Xu, M. Chen, Y. Cui, X. Wen, Y. Li, C. Wu, B. Yang, Z. Miao, X. Hu, Q. Shou, *Front. Chem.*, 2020, Vol. 8, 269

[24] M. Younas, L. L. Kong, M. J. K. Bashir, H. Nadeem, A. Shehzad, S. Sethupathi, *Energy Fuels*, 2016, Vol. 30, 11, 8815-8831

[25] J. Li, Y. Zhou, X. Xiao, W. Wang, N. Wang, W. Qian, W. Chu, *ACS Appl. Mater. Interfaces*, 2018, Vol. 10, 48, 41224-41236

[26] J. Wu, C. Wen, X. Zou, J. Jimenez, J. Sun, Y. Xia, M.-T. F. Rodrigues, S. Vinod, J. Zhong, N. Chopra, I. N. Odeh, G. Ding, J. Lauterbach, P. M. Ajayan, *ACS Catal.*, 2017,Vol. 7, 4497-4503

[27] I. M.-Gullon, J. Vera, J. A. Conesa, J. L. González, C. Merino, *Carbon*, 2006, Vol. 44, 8, 1572-1580

[28] A. Primo, J. He, B. Jurca, B. Cojocaru, C. Bucur, V. I. Parvulescu, H. Garcia, *Appl. Catal. B*, 2019, Vol. 245, 351-359

[29] S. Ceylan, L. Coutable, J. Wegner, A. Kirschning, *Chem. Eur. J.*, 2011, Vol. 17, 1884-1893

[30] W. Wang, G. Tuci, C. D.-Viet, Y. Liu, A. Rossin, L. Luconi, J. M. Nhut, L. N.-Dinh, C. P.-Huu, G. Giambastiani. *ACS Catal.*, 2019, Vol. 9, 7921-7935

[31] S. Ruta, R. Chantrell, O. Hovorka, *Sci. Rep.*, 2015, Vol. 5, 9090

[32] C. Appino, O. De La Barrière, F. Fiorillo, M. Lobue, F. Mazaleyrat, C. Ragusa, *J. Appl. Phys.*, 2013, Vol. 113, 17, 17A322

[33] J. Pearce, A. Giustini, R. Stigliano, P. J. Hoopes, *J. Nanotechnol. Eng. Med.*, 2013, Vol. 4, 1, 011005

[34] S. Sato, A. Kawabata, M. Nihei, Y. Awano. *Chem. Phys. Lett.*, 2003, Vol. 382, 3-4, 361-366

[35] R. Muñoz, C. G.-Aleixandre, *Chem. Vap. Deposition*, 2013, Vol. 19, 297-322

[36] B. R.-Murias, J. M. Asensio, N. Mille, B. R.-González, P.-F. Fazzini, , J. Carrey, B. Chaudret, V. Salgueiriño, *Angew. Chem. Int. Ed.*, 2020, Vol. 59, 15537

[37] A. Bordet, L.-M. Lacroix, P.-F. Fazzini, J. Carrey, K. Soulantica, B. Chaudret, *Angew. Chem. Int. Ed.*, 2016, Vol. 55, 15894

[38] A. Mohanty, I. Janowska, *Electrochim. Acta*, 2019, Vol. 308, 206-216

[39] L. Zhang, X. Yang, F. Zhang, G. Long, T. Zhang, K. Leng, Y. Zhang, Y. Huang, Y. Ma, M. Zhang, Y. Chen, *J. Am. Chem. Soc.*, 2013, Vol. 135, 5921-5929

[40] Y.-H. Lee, K.-H. Chang, C.-C. Hu, *J. Power Sources*, 2013, Vol. 227, 300-308

[41] J.-S. M. Lee, M.E. Briggs, C.-C. Hu, A. I. Cooper, *Nano Energy*, 2018, Vol. 46, 277-289

[42] J. Chmiola, G. Yushin, Y. Gogotsi, C. Portet, P. Simon, P. L. Taberna, *Science*, 2006, Vol. 313, 1760-1763

[43] A. Mohanty, W. Baaziz, M. Lafjah, V. D. Costa, I. Janowska, *FlatChem*, 2018, Vol. 9, 15-20

[44] I. Janowska, M.-S. Moldovan, O. Ersen, H. Bulou, K. Chizari, M. J. Ledoux, C. P.-Huu, *Nano Res.*, 2011, Vol. 4, 511-521

[45] J. A. Menéndez, A. Arenillas, B. Fidalgo, Y. Fernández, L. Zubizarreta, E.G. Calvo, J.M. Bermúdez, *Fuel Proc. Technol.*, 2010, Vol. 91, 1-8

[46] F. Banhart, J. Kotakoski, A. V. Krasheninnikov, *ACS Nano*, 2011, Vol. 5, 26-41

[47] S. S. Datta, D. R. Strachan, S. M. Khamis, A. T. C. Johnson, *Nano Lett.*, 2008, Vol. 8, 1912-1915

[48] F. Banhart, *Nanoscale*, 2009, Vol. 1, 201-213

Chapter 1

Introduction

The development of an ecosystem needs various resources. One of the most important being energy, it is imperative that we should have easy access to sustainable energy sources and supply methods for a better future. The latter half of 20th century and early 21st century has witnessed some major technical advances and global population explosion thereby creating a gap between sustainable energy supply and demand. According to the reports published by U.S. Energy Information Administration, there will be a 50% growth in energy demand by 2050 [1]. As seen from **Figure 1.1**, fossil fuels still dominates a larger part of the primary energy sources (close to 80 % of the total of world consumption)[2] with its overcompensating disadvantages. Burning of fossil fuels has been the prime factor for increase in global warming, increased level of pollution and climate change as a whole [3, 4]. The last year has witnessed some of the most tragic environmental disasters on the face of earth like the Amazon Rainforest fire 2019 [5], Australian Bushfire 2019-20 (also known as the Black Summer), California Wildfires and Cyclone Idai etc. Before moving ahead, the year 2020 is itself worth mentioning, not only because of the COVID-19 global pandemic but also about how humans have dealt with it. Each nation has implemented new strategies to tackle and come out this. An interesting outcome of the global lockdown is the decrease in the rate of depletion of resources thereby defying the global predictions of last year. The International Energy Agency (IEA) has reported that the global energy demand declined by 3.8% in the first four months of 2020, with coal sustaining the biggest hit of 8% decline among all the sources [6]. Electricity demands have taken a big dip of up to 20% during the time of global lockdown. The only source that posted a growth in demand are the renewables. With continuously evolving technologies, we have been introduced to renewable energy (RE) sources which are greener in nature and help in the sustainable development. They utilise the naturally available resources in a process to obtain energy that doesn't harm the well-being of the future.

RE sources like hydropower and solar photovoltaics have been the forerunners among all for the last decade. The market investment for RE is increasing globally with new stated policies.

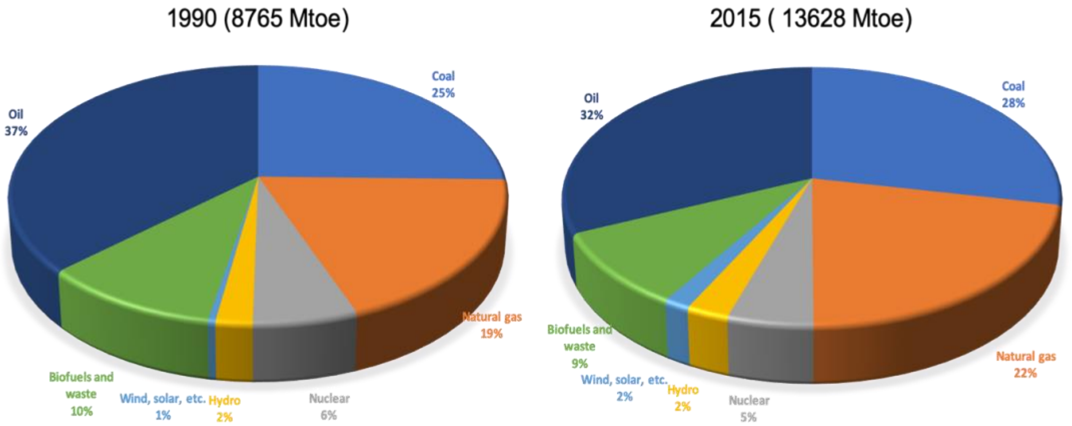

Figure 1.1 Total Primary Energy Sources compared between 1990 and 2015 [2].

As per the International Energy Agency(IEA), the REs have a share of 26% in 2018 for global electricity generation [7] and are expected to rise to 45% by 2040. A dip in the addition of new RE addition capacity as per **Figure 1.2 (a)** for the current year because of the pandemic but the next year forecasts are hopeful for a brighter comeback. The European Commission envisions this through The Green European Deal which aims at a carbon-neutral continent by 2050 by investing in environmentally-friendly technologies and decarbonising the energy sector [8]. Besides, the global electronic vehicles (EV) market has noticed a boom in terms of technology aiming for a zero emission approaches. With major players like Tesla and Nikola kicking in for the EV segment, it's a matter of time the world witnesses a makeover of the fastest vehicles on the road running on electricity. According to projections by Mckinsey & Company, by 2040, the EV market in Europe will create a battery demand as high as 1200 GWh year^{-1} which can be compensated by 80 gigafactories with an average capacity of 15 GWh year^{-1} [9]. But, the primary issue of using renewable energy sources is their ease of harvest and access for substantial implementation [10]. Solar photovoltaics (PV) and wind power being the most feasible candidates (as seen in **Figure 1.2 (b)**) are largely climate dependent which makes them all the more vulnerable for consistency [11,12]. The location for harnessing such energy sources are not always logistically facile which gives rises to issues needing further investments emphasizing on proper electricity storage and transmission from source to end-user [13,14]. The incoherent nature of the sources also makes it difficult for inclusion into full-scale dependencies [15]. As of now, they are backed by conventional sources which make sure the load on REs is low, but a carbon neutral source in future requires a consistent energy source to ease up the grid-management [16, 17]. Renewable energy is also being considered to have a positive impact on the economic growth of countries [18,19].

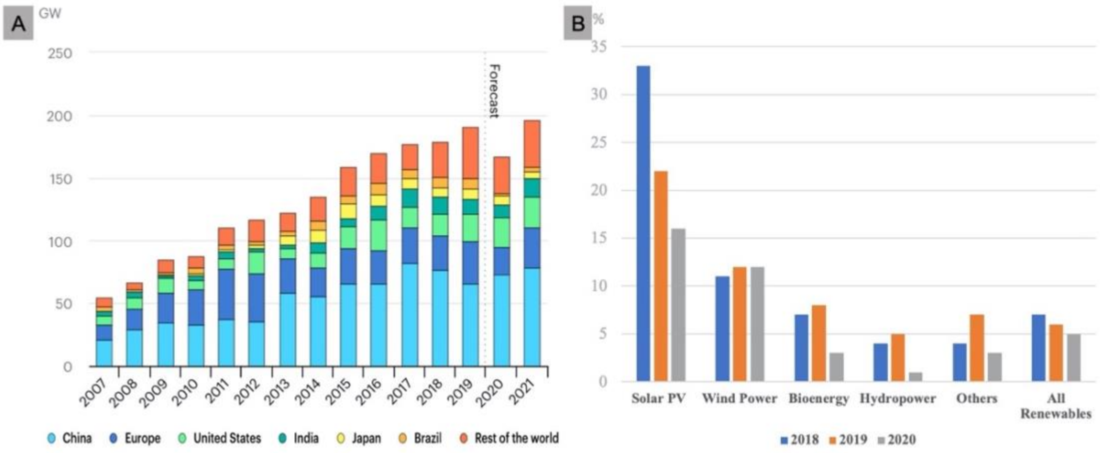

Figure 1.2 IEA forecasts for; a)Renewable electricity capacity additions, 2007-2021, b)Annual growth for renewable electricity generation by source, 2018-2020 [7].

One of the prime motivations for searching such REs are the huge amount of CO_2 emissions during the generation and end-user applications processes [20]. Right from burning of coal in industries to generate electricity to every vehicle giving out a bulk of exhaust when we dab the accelerator, CO_2 emissions have been growing exponentially with the population explosion and rapid deforestation. A part of it also arises from the urban constructions [21] and indirectly from some renewables also [22]. The continuous use of such techniques has made the CO_2 concentrations in the atmosphere to reach as high as 412 ppm as of July, 2020 which is highly alarming. According to the International Energy Outlook 2019 (**Figure 1.3**), the rate of growth of energy related CO_2 emissions is expected to follow a decreasing trend from 2018 to 2050, albeit the fact that it will still be around 1.6% per year from the non-OECD (Organisation for Economic Co-operation and Development) countries [23]. It being one of the major greenhouse gases (GHGs) impacts largely to the global temperature increase causing multi-prong issues [3]. Carbon capture, storage and utilization (CCS/CCU) have been major methods to combat with such huge concentrations of CO_2 in the atmosphere [24, 25]. A large amount of innovations around the globe have been focusing on CO_2 sequestration [26]. Conversion of CO_2 into variable usable forms efficiently in a cost effective and ecological manner has given rise to various technical innovations in this domain [27, 28]. All these have shortened the gap for the future requirements but we still have a long way to go to achieve a carbon neutral climate.

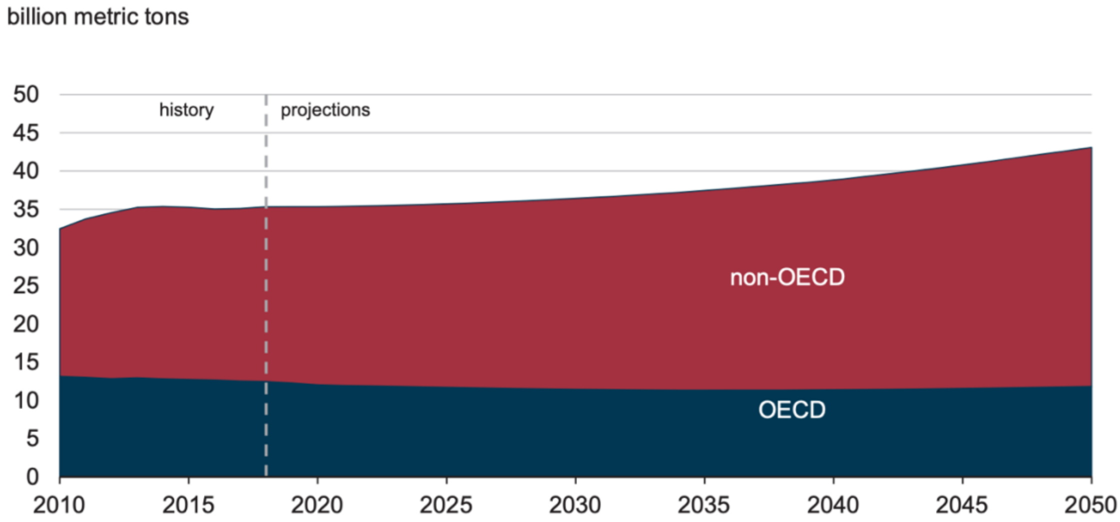

Figure 1.3 Energy-related carbon dioxide emissions as per IEO 2019 [23].

The REs can be the sole electricity generation system from sunrise to sunrise only when we have efficient energy storage systems that stocks them as and when available, and releases them in continuous, cost-effective, ecological and fluid manner without causing injunctions. The socio-economic aspects for renewable energy storage is being studied at large [29]. Various energy storage systems are being identified and investigated to obtain a good balance among all the factors and the global requirements at hand. An overview of the energy storage technologies and their characteristics are listed in **Table 1.1**.

Technologies	Power Rating (MW)	Storage Duration (h)	Cycling or Lifetime	Self-Discharge (%)	Energy Density (Wh/l)	Power Density (W/l)	Efficiency (%)	Response Time
Super-Capacitors	0.01-1	ms-min	10,000-100,000	20-40	10-20	40,000-120,000	80-98	10-20ms
SMES	0.1-1	ms-min	100,000	10-15	~6	1000-4000	80-95	<100ms
PHS	100-1,000	4-12h	30-60 years	~0	0.2-2	0.1-0.2	70-85	sec-min
CAES	10-1,000	2-30h	20-40 years	~0	2-6	0.2-0.6	40-75	sec-min
Flywheels	0.001-1	sec-hours	20,000-100,000	1.3-100	20-80	5,000	70-95	10-20ms
NaS battery	10-100	1min-8h	2,500-4,400	0.05-20	150-300	120-160	70-90	10-20ms
Li-ion battery	0.1-100	1min-8h	1,000-10,000	0.1-0.3	200-400	1,300-10,000	85-98	10-20ms
Flow battery	1-100	1-0h	12,000-14,000	0.2	20-70	0.5-2	60-85	10-20ms
Hydrogen	0.01-1000	min-weeks	5-30 years	0-4	600 (200 bar)	0.2-20	25-45	sec-min
SNG	50-1.000	hours-weeks	30 years	Negli-gible	1800 (200 bar)	0.2-2	25-50	sec-min

Table 1.1 Summary of different energy storage technologies and their characteristics (SMES-Superconducting Magnetic Energy Storage, PHS-Pump Hydro Storage, CAES- Compressed Air Energy Storage, SNG- Synthetic Natural Gas).

Electrochemical energy storage systems have emerged as pioneers in solving this issue by utilisation of more efficient batteries and supercapacitors. These in turn have also helped in the abatement of CO$_2$ emissions. Better materials and supported engineering magnificence can turn the ball for a zero-emission society with less volatile climatic adversities. Before taking a closer look at the solutions, it is compelling to have an outlook of the state of the art at practice and the ideas behind it. This would enable us to better understand the needs and possible modifications we need to project to get one step closer to success.

1.1 Electrochemical Energy Storage

The prime issue of energy storage for the renewable energies has been dealt at large in the last decade giving rise to electrical energy storage systems [30]. Electrical storage systems provide a two-fold aid to the current systems. First, it forms an intermediate unit between the generation source and supply end thereby allowing regularisation of the supply as and when needed. Secondly, it facilitates formation of distributed storage units, thereby augmenting the grid security. Out of these energy storage systems, electrochemical energy storage (EES) is one the flag bearers of the future energy systems that will revolutionize the way we think about REs. A proper EES system is the backbone to drive a market shift for an end-to-end RE mobilization. This is indeed the right time to recall the Nobel Prize winners of 2019 which was awarded for the outstanding contribution by J.B. Goodenough, M. N. Wittingham and A. Yosino in the field of Li-ion battery development [31]. Li-ion batteries have been explored largely to cope-up with the energy storage requirements [32, 33]. There has been a growth in metal-air battery scenario also which are considered as a perfect candidate for electronic vehicles (EVs) because of their high energy density [34-36] and usage of non-aqueous electrolyte. Right from the day of Ferdinand Porsche’s race win by the, “Egger-Lohner electric C.2 Phaeton”, electric car carrying a lead-acid battery to today’s tech-savvy dream car, Tesla Model 3, we have come across a long way in EESs in search for greener and more sustainable batteries [37]. But, there are still a lot of stones to be turned, to reach the goal of combined high energy density and high power-density in a single system. Here comes the supercapacitors to the rescue. Supercapacitors (SCs) are energy storage devices that aim to blur the gap between batteries and capacitors. They are the beginning of the end of batteries [38, 39]. A technical investment into perfecting the supercapacitor can ensure the future to be sustainable and greener.

1.1.1 Why Supercapacitors ?

Supercapacitors(SCs), also known as ultracapacitors are electrical double-layer capacitors, and are considered to be the next-generation solution for energy storage issues because of their high power density (> 10 kW kg-1), better charging-discharging rate, superior lifetime, low maintenance, non-toxicity and higher temperature stability [40-43]. The term “Supercapacitor” was coined by the Japanese company Nippon Electric Company (NEC) in 1957 to sell their first ever viable electrochemical capacitor based on the design by Robert A. Rightmire, a chemist at the Standard Oil Company of Ohio (SOHIO). Since then, SCs have gone over a lot of changes to become what we see them now. In 1992, the first electrical double layer capacitance based supercapacitor was developed at Pinnacle Research Institute for military purposes. A decade later, Maxwell Laboratories came out with a series of supercapacitors with a nominal capacitance of 1kF. SCs normally tend to have several orders of magnitude higher energy density compared to conventional capacitors. Besides, their unique charge storage mechanism allows them to deliver the stored energy in a shorter time frame making them better than the existing batteries. They are theoretically designed to utilize the high power density of conventional capacitors and simultaneously provide energy density equivalent to modern day batteries as illustrated by the Ragone plot in **Figure 1.4 (a)**. The goal is to attain both high power and energy density so that energy can be stored like a capacitor and be released like a battery as and when required for a longer duration. SCs are not just a proof of concept anymore or trial case. It has entered the market in various sectors as indicated in **Figure 1.4(b)**. Toyota has been using SCs for their hybrid race car TS2040 [44] whereas Maxwell kickstarts its hybrid buses by SCs [45]. Airbus 380 relies on SCs for their emergency exits which need sudden jolts of energy under pressure conditions [41]. Besides automotive sectors, it is also used in energy harvesting sector for wind turbines requiring sparks of energy to maintain their motions irrespective of wind movement [46]. It has also been used by Zap&Go to make EV and Grid storage system setups [47].

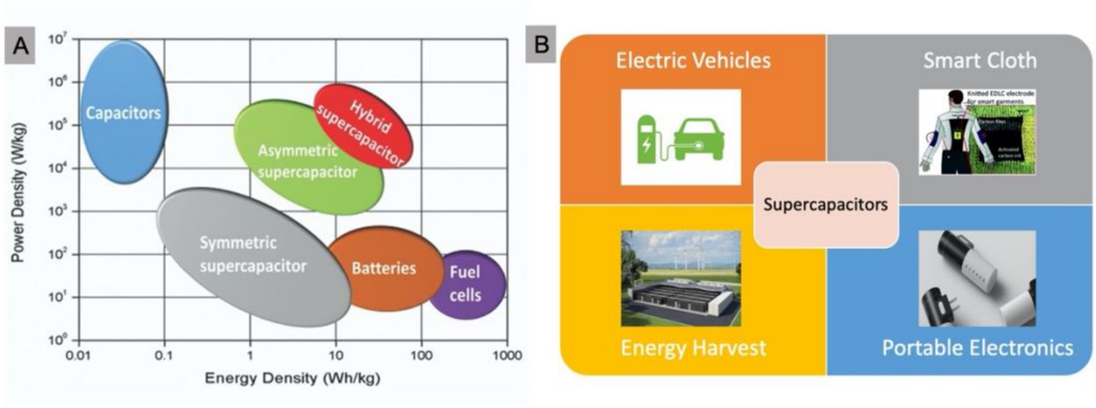

Figure 1.4 (a) Ragone plot comparing the power and energy densities of various supercapacitors [43], (b) Applications of supercapacitors.

1.1.2 Mechanism Guiding Supercapacitors

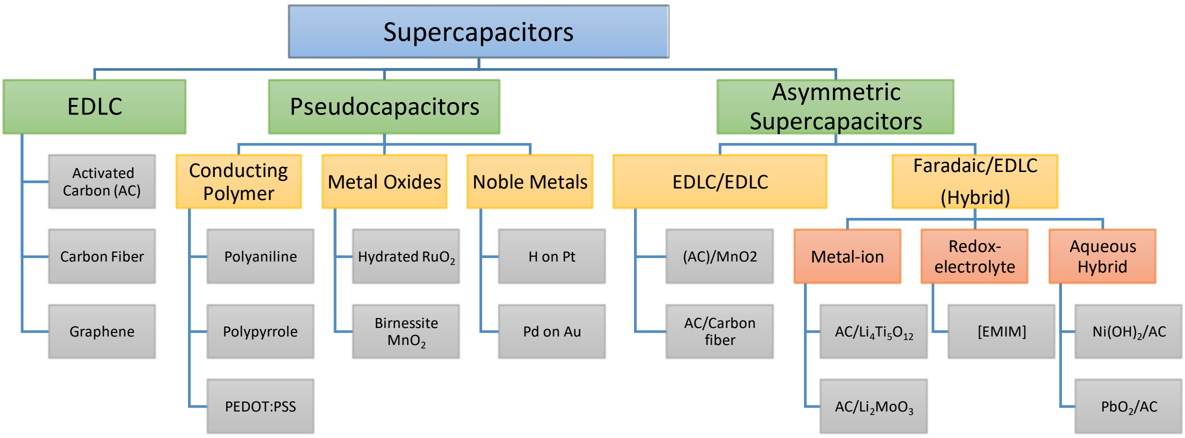

Figure 1.5 Classification and examples of different types of supercapacitors[49].

A typical supercapacitor is made up of two electrodes (anode and cathode) with a separator in between which normally contains the electrolyte and forms a semipermeable membrane system that allows for passage of ions while keeping the electrodes insulated. The SCs can be broadly divided into two categories based on their charge storage mechanism, electrical double layer capacitors (EDLCs) and pseudocapacitors (PCs). EDLCs store charge by virtue of surface adsorption of ions from the electrolyte caused by electrostatic attraction [48, 49], whereas PCs store energy via reversible Faradaic reactions (oxidation/reduction) taking place at the electrode electrolyte interfaces [50]. The possibility of using multiple materials pertaining to various energy storage mechanisms can further add to the basic two categories of supercapacitors as shown in **Figure 1.5**.

Modern day EDLCs are based on the simple principle of charge separation similar to that of the “Leyden Jar”, the first capacitor. But, they can store lot more energy than a regular capacitor by abstaining the free mobility of the ions in the bulk electrolyte [49]. A typical supercapacitor can be made by inserting two conductive electrode rods made up of (or coated with) carbon based materials in an electrolyte like salt solution. Carbon materials have been largely used for electrode material for supercapacitors because of their high surface area, around few thousands of square meters per gram which helps to realise a capacitance of few thousand Farads on a hand held storage device dimension [50]. This high capacitance is limited by the potential in which the electrolyte is stable and their ageing mechanism [50, 51]. Asymmetric supercapacitors are particularly advantageous because they can utilise the potential window of both the electrode materials in relation to the electrolyte to further the operational voltage [49]. The capacity being the main measure of such systems depend on the storage mechanism of batteries and supercapacitors. The rechargeable batteries depend on the redox reactions during intercalation/de-intercalation of cations within the crystal framework for their charging and dis-charging process shown in **Figure 1.6 (a)**. It should be noted that all rechargeable batteries also undergo “phase transformation” and/or alloying reactions. The supercapacitors, on the other hand, derive their capacitance as a result of both double layer capacitance and pseudocapacitance as seen in **Figure 1.6(b)**. The charging/ discharging of the EDLCs takes place electrostatically by formation of electrical double layer at the liquid solid interface between the electrodes and the electrolyte. During the charging process, the cations move towards the negatively charged electrode and the anions towards the positively charged electrode, and vice versa during discharging as depicted in **Figure 1.6(b)**. Carbon based materials are widely used for such electrode materials for EDLCs [52-54]. Thus the electrons during charging move via an external load from the negative electrode to the positive. The accumulation of charges near the electrode gives rise to formation of double layer thereby indicating that the concentration of the electrolyte remains constant during the entire charging/discharging process [55].

Typical electrochemical cell reactions for EDLC can be represented as follows [55, 56]:

One electrode (Cathode),

$$CE_S + A^- \xrightarrow{Charging} CE_S^+ // A^- + e^- \quad \text{(Eq. 1.1)}$$

$$CE_S^+ // A^- + e^- \xrightarrow{Discharging} CE_S + A^- \quad \text{(Eq. 1.2)}$$

Other electrode (Anode),

$$AE_S + C^+ + e^- \xrightarrow{Charging} AE_S^- // C^+ \quad \text{(Eq. 1.3)}$$

$$AE_S^- // C^+ \xrightarrow{Discharging} AE_S + C^+ + e^- \quad \text{(Eq. 1.4)}$$

Overall reaction,

$$CE_S + AE_S + C^+ + A^- \xrightarrow{Charging} CE_S^+ // A^- + AE_S^- // C^+ \quad \text{(Eq. 1.5)}$$

$$CE_S^+ // A^- + AE_S^- // C^+ \xrightarrow{DisCharging} CE_S + AE_S + C^+ + A^- \quad \text{(Eq. 1.6)}$$

where CE_s refers to cathode (positive) electrode, AE_s refers to anode (negative) electrode, A refers to anion, C refers to cation and '//' refers to formation of double layer.

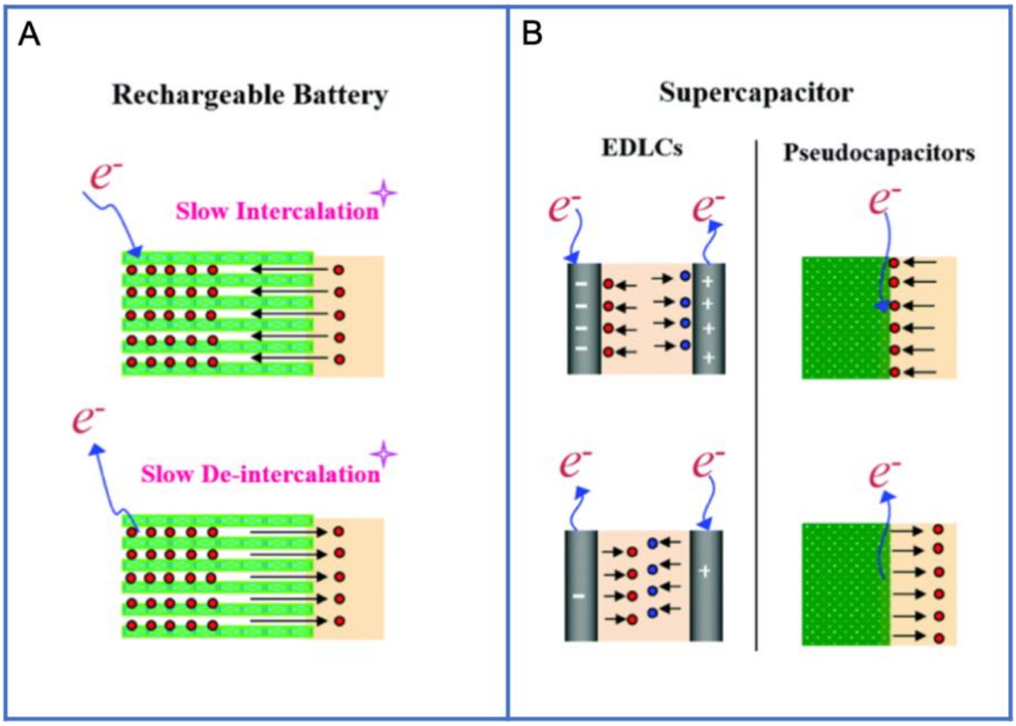

Figure 1.6 Schematic of different charge storage mechanisms. (a) Charge storage mechanism of rechargeable battery. (b) Charge storage mechanism of supercapacitor [48].

PCs charge similar to the batteries with the difference that they are not restricted by the solid state diffusion limit [48] or phase-transformation of electrode materials. Fast reversible redox reactions take place at the surface or near surface of active electrodes at a distance $I \ll \sqrt{2Dt}$ (where *I* is the diffusion thickness, *D* is the diffusion co-efficient of ions, and *t* is time), causing ions to pass through the double layer and generate a Faradaic current. One of the first definitions of pseudocapacitance was given by Conway in his book published in 1999 which states that such capacitance arises as a result of charge gradient (*dQ/dV*) created due to the potential difference (*dV*) over an amount of charge(*dQ*) accepted during the charging process as the ions reach or go away from the electrode [40]. Metal oxides such as RuO_2 [57, 58], MnO_2 [59, 60], and Co_3O_4 [61] have been largely investigated in the last decades as materials which undergo Faradaic charging but also exhibit capacitor characteristics. The model representations of the three basic mechanisms which are believed to guide the pseudocapacitance in such materials, a) underpotential deposition, b) rapid redox reactions, and c) fast intercalation as portrayed in **Figure 1.7**. Underpotential deposition refers to formation of adsorbed monolayer by metal ions over another metal's surface, lead(Pb) on gold(Au) electrode being one common example [62]. Rapid redox pseudocapacitance in RuO_2 [63] type materials involve faradaic charge transfer arising from electrochemical adsorptions of ions onto electrode surfaces whereas fast intercalation pseudocapacitance observed in Nb_2O_5 [64] occurs when faradaic charge transfer occurs due to intercalation of metal ions between the layers or networks of the redox-active electrode material without changing its crystalline phase.

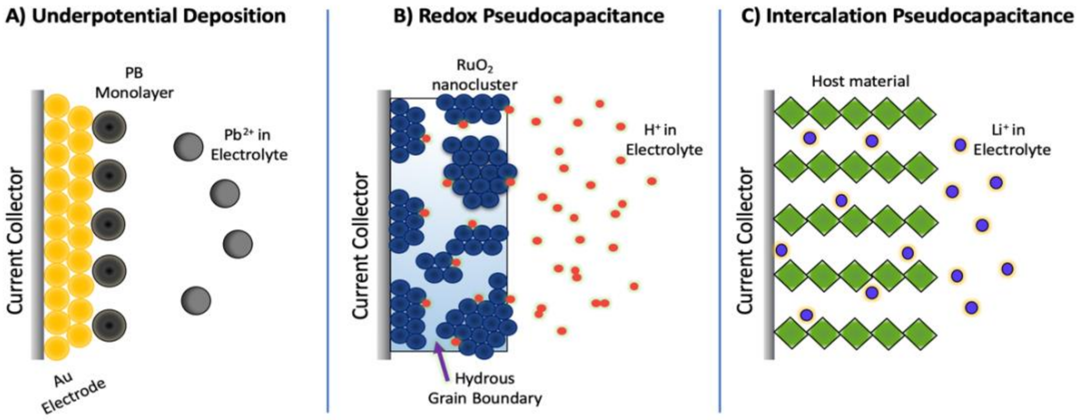

Figure 1.7 Redox mechanisms that guide pseudocapacitance.

The thermodynamics governing the existence of such pseudocapacitance can be mathematically put by help of Langmuir statistics giving as electrosorption isotherm [65] as,

$$\frac{\theta}{1-\theta} = Kc\exp\left(\frac{VF}{RT}\right) \qquad \text{(Eq. 1.7)}$$

where θ refers to partial charge coverage, K being the adsorption constant, c is the concentration of adsorbable ions in the electrolyte, V is the potential, F is Faraday's constant , R is the ideal gas constant and T is the temperature. Capacitance(C) can be defined from the above relation in region where the plot is linear for V vs θ as:

$$C = \left(\frac{nF}{m}\right)\frac{\theta}{V} \qquad \text{(Eq. 1.8)}$$

where n refers to the number of electrons, and m is the molecular weight of the active material.

A theoretical insight to understand the differences these storage mechanisms implicate on the storage devices clarifies their potential applications. A battery stores 1~2 valence electrons per atom or molecule via redox reactions whereas an EDLC stores about ~0.18 electrons per atom at 1V in an aqueous electrolyte [66]. PCs can store about 10~20% of the energy compared to a battery but by virtue of their high reversibility and fast reactions, they can provide very high power density. The kinetic efficacy of these are best understood by cyclic voltammograms (CVs) as shown in **Figure 1.8**. The CVs are based on the relation [67-69]:

$$i\ = av^{b} \qquad \text{(Eq. 1.9)}$$

which indicates that current (i) follows power law relationship with the potential sweep rate (v) at a fixed potential with values of a and b depending on the charge response. For a capacitive response $b=1.0$ (ideal case), as the current is linearly proportional to sweep rate, the equation can be represented as:

$$i = C_{d}Av \qquad \text{(Eq. 1.10)}$$

where C_d is the capacitance and A refers to effective surface area of the electrode active material. For ideal batteries cases, at peak current conditions, $b=0.5$. The electrode potential for pseudocapacitive materials is a continuous logarithmic function of the extent of electrosorption [41] whereas the same for batteries is designated at particular Gibb's energy of pure, well-defined phases of the electrode materials with corresponding electrolyte concentrations [38]. This confirms the b value dependencies used above. Materials giving a capacitor like response tend to show rectangular shaped CV curves (**Figure 1.8 (a,b)**) with triangular shaped continuous charging/discharging curves (**Figure 1.8 (c)**). EDLCs normally show potential-independent capacitance and current [70]. The discrete nature of measurement of battery based electrode at a particular potential explains the plateaus formed in the charge/discharge curves shown in the row labelled Type C set in **Figure 1.8**. An overlap of these two extremes in responses is what indicates the presence of pseudocapacitance. ***Proper optimization of pseudocapacitance can enhance charge storage capacity of supercapacitors. Materials at nano-dimensions need to be studied specifically as the diffusion path length of ions are reduced with simultaneous increase in non-insertion charge storage surface area.***

Summarily, EDLCs store energy electrostatically at surface/near-surface of the electrode material giving rise to very fast charging and discharging cycles contrary to batteries that suffer from low power density but high energy density. Pseudocapactiors are placed in-between these extremes because they exhibit characteristics of both and are not limited by the factors to them. With search for better materials, scientists are looking at the nanoscale and its special attention as Yury Gogotsi has aptly said, "The first question a researcher should ask when doing electrochemical data analyses on a new nanomaterial is whether the material is battery like or capacitor-like" [70].

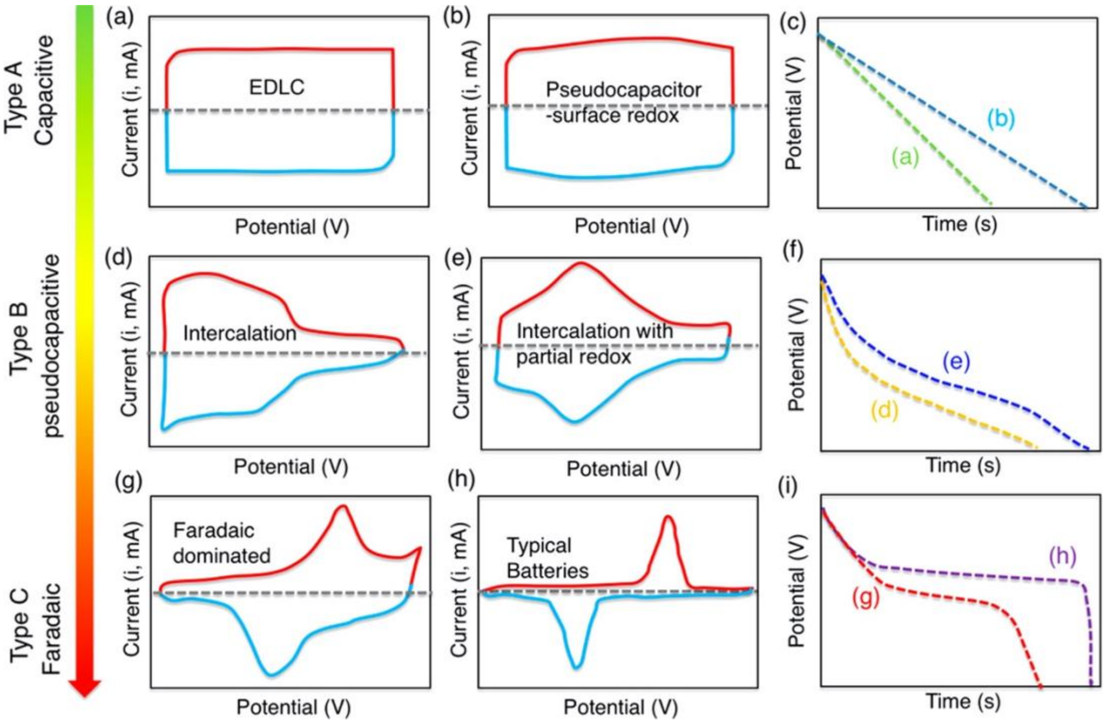

Figure 1.8 (a, b, d, e, g, h) Schematic cyclic voltammograms and (c, f, i) corresponding galvanostatic discharge curves for various kinds of energy-storage materials [70].

1.1.2.1 Models and Scientific Analysis Methods for Supercapacitors

With the idea of the possible types of materials and their nature of response in an electrochemical system we can classify them as EDL capacitor, pseudocapacitor or battery [48, 71, 72]. The main focus lies in developing better EDLC materials that can solve the issues pertaining to energy-storage. The design and identification of such materials can be done only if we better understand the basis of such materials which may provide a high power density as well as energy density to replace the good old batteries. The last few decades have seen evolution of several models and theories explaining the formation of electrical double layer [52, 72, 73].

Helmoltz in 1853 was the first to come up with the theory governing the formation of EDL [75, 76]. According to him, whenever an electrode was charged, counterions start to accumulate in the vicinity of the electrode to maintain charge neutrality as shown in **Figure 1.9 (a)**. This accumulation takes places till a few nanometres close to the surface generally and gradually decreases indicating the decrease in electrode potential similar to a flat-plate di-electric capacitors. Mathematically, the capacitance (C_H) can be represented as [77-79],

$$C_H = \frac{\partial \sigma}{\partial E} = \frac{\varepsilon_0 \varepsilon_r A}{d} \qquad \text{(Eq. 1.11)}$$

where σ is the charge density, E is the applied potential, A is the active surface area of the electrode, d is the distance of Helmholtz layer, and $\varepsilon_0, \varepsilon_r$ are the free space permittivity and the electrolyte relative permittivity, respectively. But the model did not hold good with the experimental results as it neglected the diffusion of ions in the solution and the interaction of the dipole moment of the solvent and the electrode [80].

Early 1900s saw two researchers, Gouy and Chapman, develop a diffused layer model for EDL considering the thermal fluctuations [81, 82]. They introduced the idea that ions are not well-separated in the electrolyte as hypothesized by Helmholtz. They rather form an continuum of charge with decreasing charge concentration as one moves far from the charged electrodes because of inter-ionic electrostatic interaction coupled with thermally originated movements [83] as illustrated in **Figure 1.9 (b)**.

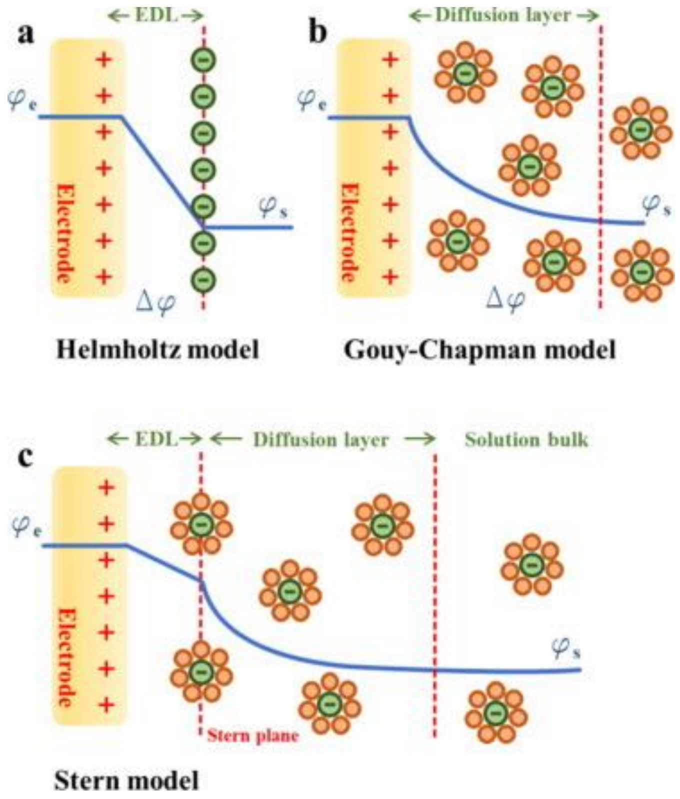

Figure 1.9 Schematics of different kinds of EDL model for charge storage at electrode-electrolyte interface, a) Helmholtz Model, b) Guoy-Chapman model, c) Stern Model

The local ion concentration is detailed according to the Boltzmann distribution function. Chapman utilised the steady-state Poisson-Boltzmann equation to predict the diffused layer and thus the capacitance obtained for a symmetrical z:z electrolyte can be written as [77, 84],

$$C_{GC} = \frac{d\sigma_M}{d\psi_e} = \left(\frac{2z^2e^2n_i^s\varepsilon_0\varepsilon_r}{kT}\right)^{1/2} \cosh\left(\frac{ze\psi_e}{2kT}\right) = \frac{\varepsilon_0\varepsilon_r}{\lambda_D}\cosh\left(\frac{ze\psi_e}{2kT}\right) \qquad \text{(Eq. 1.12)}$$

where σ_M is the charge density, ψ_e is the potential at electrode surface, z is the charge of the ion, *e* is the elementary charge, n_i^s is the concentration of ion *i* in the bulk, , ε_0, ε_r are the free space permittivity and the electrolyte relative permittivity, k is the Boltzmann constant (k = 1.381×10^{-23} m^2 kg $K^{-1}s^{-2}$), *T* is the absolute temperature, and λ_D is known as the Debye Length, respectively. The Debye-length is in fact a measure of the thickness of the diffused layer which can be defined as,

$$\lambda_D = \left(\frac{\varepsilon_0 \varepsilon_r kT}{2z^2 e^2 n_i^s}\right)^{1/2} \qquad \text{(Eq. 1.13)}$$

However, the Gouy-Chapman model was not sufficient as it overestimates the ion concentrations close to charged surfaces largely by considering ions as point charges while they had definitive sizes [85]. This in turn restricts calculation of EDLC characteristics for cases nearing surface potential of 1V along with bulk electrolyte concentration of 1mol l^{-1}.

Later, Stern in 1924 came up with another model that overcomes the previous issues by taking into account both the compact layer of Helmholtz and the diffused layer of Gouy-Chapman [86] as shown in **Figure 1.9 (c)**. Therefore, the combined capacitance of these two layers can be added as capacitors in series to obtain total capacitance as,

$$\frac{1}{C_S} = \frac{1}{C_H} + \frac{1}{C_{GC}} \qquad \text{(Eq. 1.14)}$$

This took care of the overestimated charge by accepting definitive ion size. This model was further modified by Graham to understand the type of ions based on their locations as the Inner Helmholtz Plane (IHP), the diffused layer and the Outer Helmholtz Plane (OHP) [87]. This theory simplifies the electrostatic interactions occurring at the EDL and also indicates the possibility of no electroneutrality in the EDL [83].

The diffusion term in Eq. 1.14 can be neglected because electrolyte concentration in commercial supercapacitors are generally high [88, 89]. A supercapacitor made up of two electrodes has a net capacitance equivalent to the series capacitance circuit including both cathode and anode electrodes, given by,

$$\frac{1}{C_{Total}} = \frac{1}{C_C} + \frac{1}{C_A} \qquad \text{(Eq. 1.15)}$$

For symmetric capacitors with same anode and cathode material of same quantities, $C_C = C_A$, the total capacitance C_{Total} will be half of single electrode capacitance. For asymmetric capacitors, $C_C \neq C_A$, the total capacitance, $C_{Total,}$ depends on the electrode with the smaller capacitance [88]. For the purpose of comparison between various materials total specific (gravimetric) capacitance is commonly used which refers to capacitance per unit mass, *i.e.* C_{SP} (F g^{-1}). The other parameters which indicates the efficiency of supercapacitors are volumetric capacitance (F cm^{-3}), the energy density (or specific energy, in Wh kg^{-1}), power density (or specific power, in W kg^{-1}) of the electrode materials, cyclability, rate of charge/discharge, self-discharge limit, safe operation ability and cost.

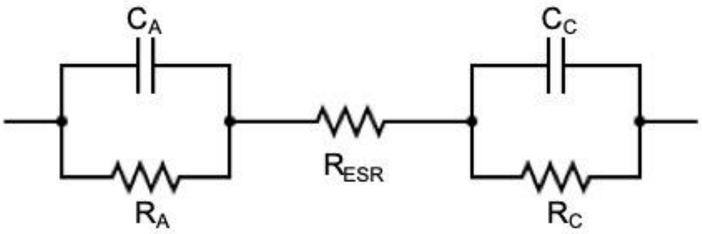

Figure 1.10 Circuit representation of supercapacitor.

The electric circuit equivalent of single cell supercapacitor having two electrodes has been represented in **Figure 1.10** [52]. Besides the usual capacitance for cathode and anode, resistances have been depicted for the same as R_C and R_A respectively. R_{ESR} refers to the equivalent series resistance which takes into account various kinds of resistance present in such electrochemical systems such as, ion mobility resistance in the electrolyte, contact resistance between the electrode and the current collector, intrinsic resistance of bulk electrode material and resistance of electrolyte ions trapped in the separator [90]. The theoretical energy density can be calculated as follows,

$$E = \frac{1}{2} C_{SP} V^2 = \frac{1}{2} Q\ V \qquad \text{(Eq. 1.16)}$$

whereas, theoretical power density can be calculated as,

$$P = \frac{V^2}{4R_{ESR}} \qquad \text{(Eq. 1.17)}$$

The above discussion clarifies that C_{SP}, V, *and* R_{ESR} are the key parameters for optimizing a supercapacitor. Therefore, the materials should be designed so as to have higher C_{SP} and V , but at the same time less R_{ESR} for supercapacitors to replace batteries as a whole. Thus, there is an ongoing search for better materials which have higher stability with the electrolyte and has high cyclability. Carbon based materials, polymers and transition metal di-chalcogenides have emerged as feasible candidates for supercapacitor electrodes.

1.1.3 Carbon Based Materials for Supercapacitors

As electrode materials are one of the most important factors deciding the fate of supercapacitors, the last couple of decades has seen a large amount of research in design of the same [91]. Carbon based materials have become the largely used in various electrolytes as supercapacitor electrodes [92, 93]. The key features that is pondered upon while making an ideal carbonaceous electrode for supercapacitors keeping in mind the interdependence of the electrode microstructure and their electrochemical activity are as follows [94]:

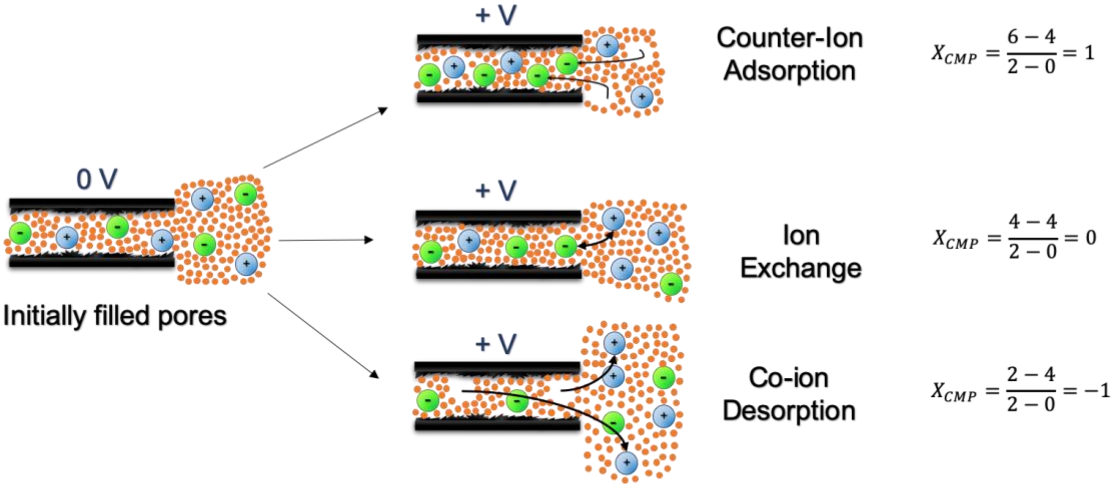

Figure 1.11 Charging mechanisms for carbon pores initially filled with electrolyte.

- **Highly accessible surface area**: The formation of EDL as seen from the above discussions can be considered to depend on the surface area of electrode which makes an interface with the electrolyte solution. Larger surface area normally allows for larger charge accumulation although up to an extent. Very large surface area materials mostly suffer from issues related to low tap density which refers to trapping of electrolyte in voids and channels thereby causing decrease in overall capacitance [95]. Therefore, it is imperative to maintain a balance between porosity and morphology to arrive at conditions suitable for maximum efficiency. The charge storage mechanism changes based on the type and amount of pores. Three specific charge storage mechanisms have been proposed specifically for carbonaceous electrodes for supercapacitors as shown in **Figure 1.11** [96].The mechanisms are characterized by a charging paramenter X_{CMP} which gives a measure of the dependence of counter-ion adsorption, ion exchange and co-ion desorption [96]. It can be defined as,

$$X_{CMP} = \frac{N(V_f)-N(V_i)}{\left(N_{CTR}(V_f)-N_{CO}(V_f)\right)-\left(N_{CTR}(V_i)-N_{CO}(V_i)\right)} = \frac{N(V_f)-N(V_i)}{[(|Q_{ionic}(V_f)|-|Q_{ionic}(V_i)|)/e)}$$

(Eq. 1.18)

where $N(V_f)$, $N_{CTR}(V_f)$, $N_{CO}(V_f)$ refers to the total number of in-pore ions, counter-ions and co-ions at final voltage V_f and $N(V_i)$, $N_{CTR}(V_i)$, $N_{CO}(V_i)$ refers to the number of in-pore ions at an initial voltage V_i(normally 0V) respectively. $Q_{ionic}(V_f)$ and $Q_{ionic}(V_i)$ refers to the net in-pore charges at voltages $V_f$and V_i. This parameter is mostly concerned for the charging process though. The initial mechanism of counter-ion adsorption refers to the traditional idea of Helmholtz. The second idea of ion-exchange actually refers to simultaneous counterion adsorption and co-ion desorption. The third and last possibility is designated to charging of supercapacitors only via desorption of co-ions. In all the three possibilities, the electronic charge in carbon is exactly balanced out by excess ionic charge in the pores. For realistic purposes, it is suggested that a combination of more than one mechanism might take place in the pores for charging.

- **Tailored pore size distribution**: A well-defined porosity is essential for wettability and accessibility of the large surface area to the incoming ions. Micropores (pore size <2nm) enhance the specific surface area of the electrodes whereas mesopores (2nm<pore size<50nm) facilitates ion transportation via channel pathways in the material [97]. Macropores (pore size> 50nm) supplement by acting as an ion reservoir to stabilize any sudden change in electrolyte concentration during high energy density requirements [98]. Therefore, an optimized proportion of pores needs to be obtained to utilize a material to its maximum strengths.
- **High electrical conductivity**: A high electrical conductivity in-between the particles and intra-particles aids electron transportation across the electrode material which is essential for faster charging and discharging. Carbon materials are often annealed at high temperatures to remove oxygen groups which increases the percentage of sp^2-hybridization thereby facilitating electron delocalization [99]. Hetero-atom doping for modulating electrical conductivity does so by increasing the electron density of carbon based materials [100].
- **Electrochemical stability**: Carbon materials are normally stable owing to their EDL nature of charge storage which does not inflict an irreversible reaction or phase change. The presence of functional groups and other trace elements on the other hand are susceptible to interactions when exposed to organic or ionic liquid electrolyte. Therefore, the materials need to be have certain degree of phase purity in order to be stable for large number of cycles [101].
- **Economical and ecological production**: Supercapacitor materials need to be produced easily keeping in mind its ecological impacts in order to have a sustainable growth and future of such materials. A cost-effective green synthesis route which avoids usage of harmful and toxic chemicals at any stage of synthesis or product development would be invaluable to the industry.

Keeping these features in perspective, carbon materials are being developed for supercapacitor applications, although it is yet to satisfy all parameters with appropriate weightage so as to be rolled out in the industry as a replacement to traditional batteries. It is therefore important to have an overview of the possible options based on carbon as shown in **Table 1.2**. Starting from 0-D to 3-D, various carbon materials provide unique features which are beneficial as electrode materials for supercapacitors. Carbon-onions prepared via high-temperature treatments have a surface area of approximately 500-600 $m^2 g^{-1}$ which has made it useful for supercapacitors [102]. The 1-D carbon nanotubes (CNTs) have also garnered a fair share of limelight by virtue of its high surface area surpassing the thousand mark. It has been doped, modified, and used as weaves for supercapacitor applications [53, 92]. The have been used as supports for metal sulphides and also along with polymers to achieve specific capacitance of more than 600F g^{-1} [103, 104].

Material	*Carbon Onions*	*Carbon Nanotubes*	*Graphene*	*Activated Carbon*	*Carbide derived Carbon*	*Templated Carbon*
Dimensionality	0-D	1-D	2-D	3-D	3-D	3-D
Conductivity	High	High	High	Low	Moderate	Low
Volumetric Capacitance	Low	Low	Moderate	High	High	Low
Cost	High	High	Moderate	Low	Moderate	High
Structure		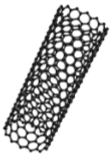	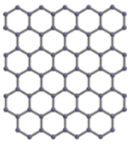	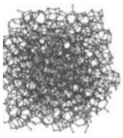		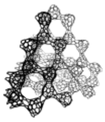

Table 1.2 Different types of Carbon available for supercapacitor applications [101].

Graphene, the 2-D form of carbon, has been also sought upon largely for electrochemical applications, one of which is the supercapacitors. Owing to their unique properties, they have been used in various forms to form supercapacitors [54, 105, 106]. For the case of 3-D carbon materials, there are multiple candidates like activated carbon(AC), carbide derived carbon(CDC), templated carbon, which have been identified for energy storage [107, 108]. The most common of them being AC which is in fact one of the major market shareholders for energy storage at large scale. Of all the carbon based materials discussed above, this study indulges further in structural development of graphene based materials to better utilise its properties for applications for supercapacitors.

1.1.3.1 Why Graphene?

Graphene, a one-atom thick 2-D form of carbon having a honeycomb lattice, since its discovery by K. S. Novoselov in 2003 has caught the eye of numerous researchers in various fields of research [109, 110]. Although there were theoretical ideas as early as 1940s regarding such monolayers of graphite [111, 112], it took 60 more years to finally get hold of this unique material. It, being the basic building block for all kinds of carbon materials, can be wrapped, rolled or stacked to form fullerenes, nano-tubes or 3D foam and graphite respectively [113] as seen in **Figure 1.12**. Graphite is basically huge layered number of graphene sheets stacked onto a hexagonal or rhombohedral crystal which have anisotropic properties (in bulk). It also acts as a primary precursor for graphene synthesis via top-down approaches [114].

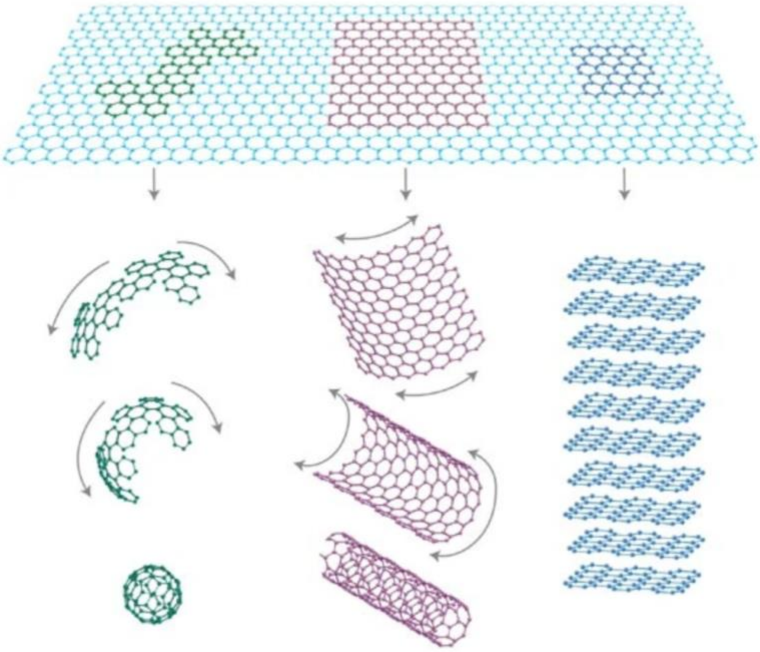

Figure 1.12 Various carbon materials derived from graphene [113].

Graphene can be thought upon as a mesh made up of six membered carbon rings where the carbons are attached by strong C-C σ bonds which help provide high mechanical strength (~1 TPa Young's module and ~130 GPa intrinsic strength), electrical and thermal conductivity (0.5-100 S m^{-1} and 3080-5150 W m^{-1} K^{-1}, respectively) [115, 116]. As simultaneous electrical and thermal conductivity is not suitable for certain applications like thermoelectric devices, some efforts have been made to control the thermal conductivity as per need [117]. The unique Dirac fermion system of each carbon contributing to the delocalized π-electron cloud formed over the sheet of graphene facilitates faster carrier mobility across the plane (~20 $m^2V^{-1}s^{-1}$) [118] and is also the basis for formation of linear dispersions of massless Dirac fermions. The electronic properties of graphene are largely affected by the behaviour of these fermions and the number of layers of graphene sheets stacked together as illustrated in **Figure 1.13** [119, 120]. The electronic structure of graphene is such that the first Brillouin zone has two in-equivalent Dirac points (K and K', as it has two atoms per unit cell) causing a band crossing leading to a zero gap semiconductor in case of monolayer graphene as shown in **Figure 1.13(a)**. Bilayer AB (Bernal stacked) graphene are known to show parabolic π-π^* crossing (shown in **Figure 1.13 (b)**) without noticeable presence of Dirac fermions which can be further controlled by an external electric field [121]. However, for trilayer graphene, the Dirac fermions are back. The band structure of trilayer seems to be an overlap between monolayer and bilayer depicted in **Figure 1.13 (c)**. For higher layers of graphene, the band structure becomes more and more complicated with a constant presence of fermions having odd number of layers stacked together. These unique characteristics of Graphene electronic band structure also gives rise to ambipolar electric field effect and quantum hall effect [109, 113].

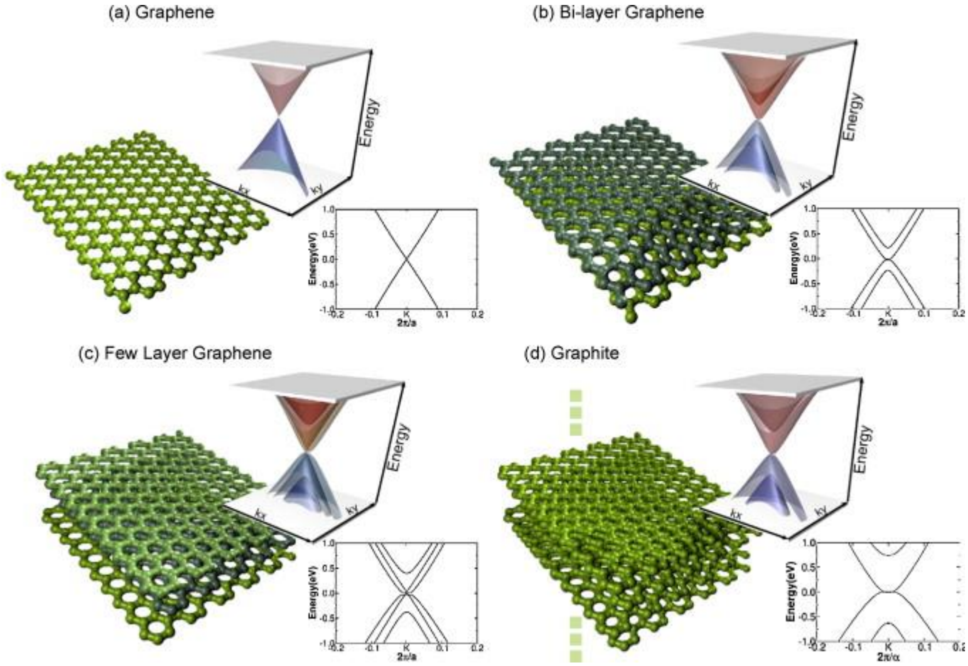

Figure 1.13 DFT based 3D band structures and corresponding projections for, a) graphene, b) bi-layer graphene, c) few-layer graphene, d) graphite. The AB stacking is considered and fermi levels has been set to zero [119].

Besides these, graphene has been largely considered for energy storage applications because of it large theoretical surface area of up to 2675 $m^2 g^{-1}$ [122] which implies the high theoretical capacitance of graphene 550 F g^{-1} (~21 μF cm^{-2}). But, it is to be noticed that according to recent findings, this value has been rectified considering the fact that the contribution for supercapacitance doesn't arise solely from the basal plane. It was found that the edge have a larger contribution. For example, areal capacitance from edges in graphite is found to 4 orders of magnitude higher than that contributed by the basal plane [123]. Regardless of these unique properties, graphene based materials face the following challenges in order to be utilized as energy-storage materials [54]:

- **π-π stacking**: Graphene based materials constantly suffer from π-π stacking due to the weak interplanar van der Waal's force interaction [124] occuring during the synthesis or sample preparation process thereby making them unable to utilise the real specific surface area. This in turn obstructs the ion exchange and movement causing decrease in the overall performance of the electrode.
- **Low Packing density**: Compared to bulk graphite's 2.2 g cm^{-3} graphene has a very low packing density of 0.015g cm^{-3} which leads to low volumetric capacitance and energy density of graphene.

- **Maintaining conductivity**: High electrical conductivity is conducive for higher electrochemical activity. Synthesis of high surface area graphene along with high conductivity is difficult to realize. The methods as etching for instance with KOH are used to enhanced the specific surface area, decreasing often conductivity.
- **Intrinsic structure**: Controlled introduction of defects and impurities in graphene sheet structure along with addition of metals and metal oxides enhances the charge storage capabilities, but needs special attention during synthesis process.

Thus, it is interesting to understand the different derivatives of graphene and the structural modifications that can be made to curtail graphene based materials.

1.1.3.2 Choice of Graphene Derivatives

As mention above the research on energy storage systems with graphene focus largely of utilizing its high surface area and charge mobility properties [105]. The utilization of these properties of graphene has led to development of various graphene derivatives. These derivatives have been used singularly and as composites for supercapacitor applications [125-127].

1.1.3.2.1 Graphene Dots

The very basic and 0D form of graphene are graphene dots (shown in **Figure 1.14(a)**) which are synthesized via graphene oxidation-reduction method and have been known to provide capacitance of ~200 F g^{-1} but suffer from low energy density issues [128]. The synthesis processes make the graphene dots hydrophobic which makes it difficult to be used in aqueous environments, contrary to its precursor graphene oxide(GO) which is amphiphile in nature. Therefore, they are being used in combination with metal oxides and polymers to avoid agglomeration. Transition metal oxides like MnO_2, RuO_2, NiO, CO_3O_4 and conducting polymers like polyaniline, polypyrroles, polythiophenes are used along with these graphene dots in order to integrate pseudocapacitance with EDLC and overall efficiency of the hybrid electrode materials [129].

1.1.3.2.2 Graphene Fibers

Graphene fibers are 1D electrode materials (shown in **Figure 1.14 (b, c)**) which are most sought upon for portable and wearable electronics because of their tiny volume, high flexibility and ease of being woven [127, 131]. Notably, graphene fibers coated on Au wires have been reported to exhibit specific capacitance of 1.9 µF cm^{-1} (6.49 mF cm^{-2}) [132]. Graphene fibers like 1D carbon nano-tubes (CNTs) grown on 2D graphene sheets have shown enhanced mechanical flexibility, stability and conductivity, resulting in an overall areal capacitance of 1.2-1.3 mF cm^{-2} [132]. Various all-graphene yarn based supercapacitors are also being developed, moulded into spring-shapes with high compressibility and stretch resistance with capacitance of 1.2 - 1.7 mF cm^{-2} [133]. The graphene yarn supercapacitors are however prone to short-circuiting even with a coating of polyvinyl alcohol(PVA) solid electrolyte. This issue has been recently addressed by formation of core-sheath fibers where the sheath layer of polyelectrolyte protects the graphene-CNT core [133]. Although it solves the issues of stretching and flexibility, the bottleneck issues stay with achieving high energy density and power density at the same time along with proper modulation of pores in the fibers and yarns.

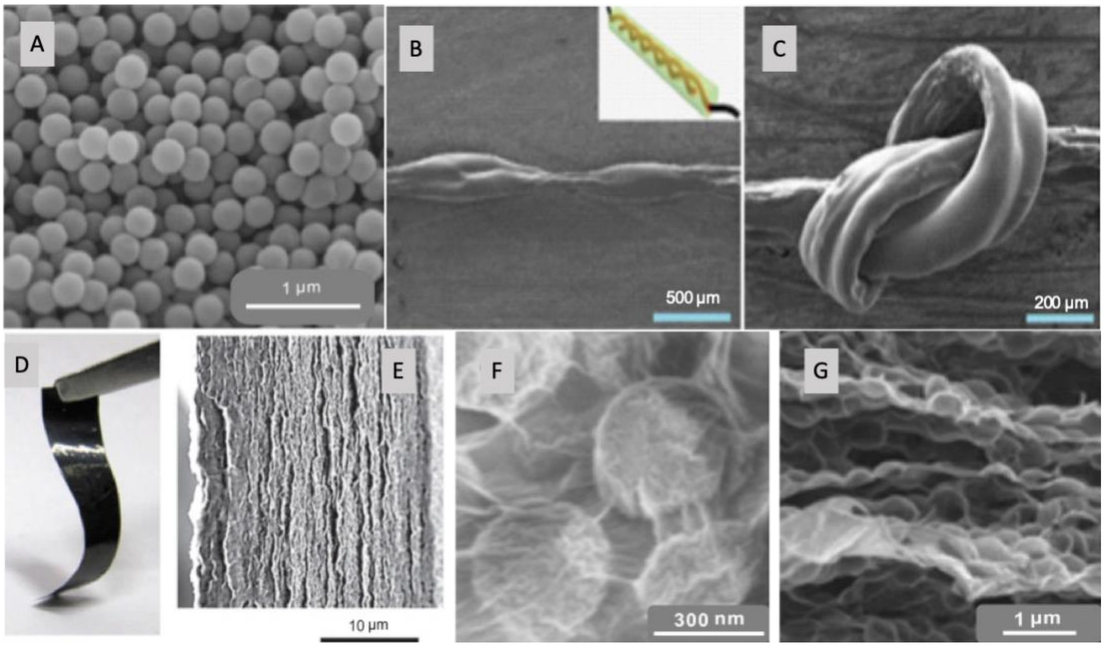

Figure 1.14 SEM and optical images of different kinds of Graphene based materials.

1.1.3.2.3 Graphene Films

Graphene films (as shown in **Figure 1.14 (d, e)**) are 2D graphene forms which also finds usage in flexible supercapacitors by virtue of their light weight, adjustable thickness, low diffusion resistance and superior mechanical property to sustain as a free-standing electrode[134]. Recent efforts towards utilization of graphene films have brought forward many synthesis and processing methods like self-assembly, layer-by-layer deposition, spin-coating, Langmuir-Blodgett, and vacuum filtration [135-137]. Obtaining thin films or specific sheets of graphene is fundamentally difficult as it needs more precision to avoid the π-π stacking. Introduction of carbon spacers and template assisted growth are most used to overcome this difficulty along with above mentioned processes [138, 139]. Using CNT as a carbon spacer for graphene film electrode, a capacitance of 140 F g^{-1} has been obtained 0.1 A g^{-1} in 1M H_2SO_4 solution [140]. After reasonable amount of de-stacking, metal oxides/hydroxides have also been used in order to add pseudocapacitance and thereby increase the overall energy density. In a specific case, $Ni(OH)_2$ nanoplatelets have been intercalated between graphene sheets giving rise to a capacitance of 537 F g^{-1} and a high volumetric capacitance of 655 F cm^{-3} [141]. Pt nanoparticles have also been used as spacers and have been successful to provide a multi-fold increase in the specific capacitance. The specific capacitance has been reported to increase from 14 F g^{-1} for un-spaced graphene sheets to 269 F g^{-1} by use of Pt spacers [142]. The same problem of arriving at a capacitance close to theoretical capacitance of graphene and cost of spacer still exists which provides room for further efforts in this.

1.1.3.2.4 Graphene Foams

Owing to their versatile usability and consistency in pore formation and interconnectivity, 3D graphene foams (as shown in **Figure 1.14 (f, g)**) have varied applications for energy storage and conversion [143]. The 3D structures not only solve the issue of restacking but also facilitate electrolyte diffusion and provide platform for decoration of pseudo-capacitive materials. They are generally prepared via hydrothermal self-assembly, template assisted growth and chemical vapour deposition techniques [144-146]. One of the best composites reported is that of Co_3O_4 nanoparticles decorated on 3D graphene foam grown via CVD on a Ni foam template providing a capacitance as high as 1100F g^{-1} [51]. There is also another group of light-weight and porous carbon material known as the graphene aerogels which are best known for high surface area-to-volume and strength-to-weight ratios [143]. They can be fabricated via 3D printing method besides the usual reduction-oxidation and CVD technique [147]. 3D printed graphene aerogel made up of graphene oxide(GO) and graphene nanoplatelets are known to provide high power density of 4079.9 W kg^{-1} at 0.26 Wh kg^{-1} [148].

1.1.3.2.5 Few-Layer-Graphene

Few-layer-graphene (FLG), also known as quasi-graphene [149], is one such 2D form of graphene which has garnered much attention in the recent times because it behaves as macronized graphene. It is considered. to benefit from the attributes of monolayer graphene and preserve it for its entirety. Normally, flakes of graphene having 3-8 sheets and exhibiting similar characteristics are termed as few-layer-graphene [150]. This class of graphene is specifically interesting as it replaces the monolayer graphene as the fundamental building block to form various graphene derivatives that can be used at industrial scale. Recent stir in automotive sectors turning electric have seen various forms of FLG already in use, though it lacks scaling and theoretical efficiency. Therefore, it is essential to have a proper de-stacking in such FLG systems so that graphene properties can be used at large scale. Various synthesis methods including arc discharge, mechanical exfoliation, self-assembly, electrochemical exfoliation and 3D printing have been used for FLG synthesis [54, 151-155]. Graphene and FLG based composites tends to show a higher amount of capacitance in comparison to their oxide derivatives because they don't have additional pseudocapacitance arising from the residual C-O and C=O bonds [156]. Structuration is achieved in such graphene materials by optimising the synthesis and treatment conditions which enables it to provide better capacitance. This research work focuses on devising such a synthesis route that can avoid restacking and provide access for facile electrolyte diffusion making also sure to get the benefits of the FLG edges which are known to be a larger contributor to overall capacitance. The following two sections are dedicated to synthesis methods and ideas for better structure tailoring of FLG for supercapacitor applications.

1.1.3.3 Synthesis methods for FLG

As discussed above, synthesis processes for FLG play a key part in making them feasible for access to monolayer-graphene like attributes. Several methods for synthesis of FLG involving both top-down and bottom-up approaches have been studied. Although bottom-up processes favours high quality defect free graphene, they are relatively more time consuming and taxing in terms of precision for a comparable yield. Most industrial applications thus demand for top-down synthesis processes. Bottom-up methods principally involve a total organic synthesis where controlled graphene sheets are produced and whose number of carbon atoms depend on the initial precursor material [157].

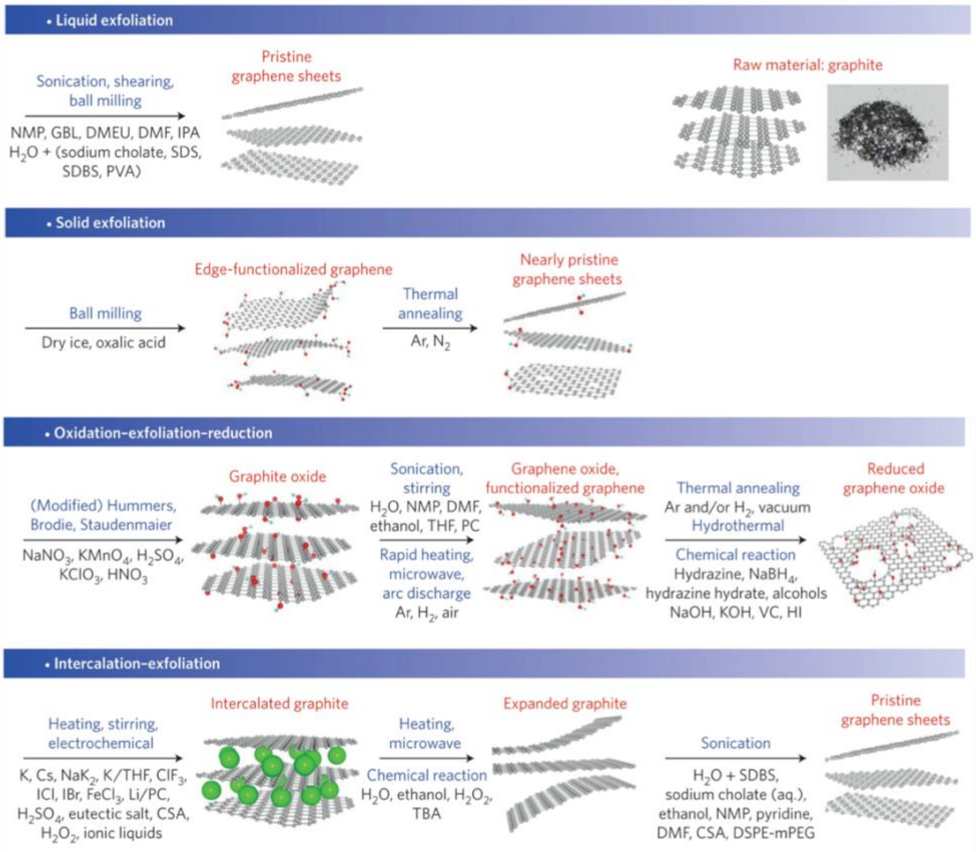

Figure 1.15 Four typical methods of exfoliation for mass production of graphene[160].

Some CVD synthesis process on Ni and Cu catalysts have also been reported at high temperatures (~1000ºC) [158]. Excepting the thermal decomposition on SiC, most other process are relatively costlier in this approach. Even the very first recovery of graphene from graphite was a top down process of mechanical exfoliation by scotch tape [109]. Mechanical and liquid phase exfoliation are one of the most used methods for FLG synthesis. Based on the theory of distance dependent interlayer potentials, the exfoliation energy needed to separate a sheet of graphene from AB stacked graphite is approximately 55.16 meV atom^{-1} which is equivalent to half of the interlayer binding energy [159].

As Van der Waals forces are directly proportional to inverse of interatomic separation distance, systematic exfoliation processes are being researched for large scale graphene synthesis [160]. Some of the basic methods of exfoliations is shown in **Figure 1.15**. Besides exfoliation, there are various other processes being utilized for FLG synthesis and structural modification. A deeper insight into the synthesis methods of FLG based materials is discussed below.

1.1.3.3.1 Liquid Phase Exfoliation

Liquid phase exfoliation is one of the most common methods for synthesis of FLG [161, 162]. Thus, exfoliation of FLG is normally carried out in the presence of spacers and solutions which have adequate interactions with graphene sheets so as to avoid restacking after exfoliation. Water was initially utilised for exfoliation of graphite oxide to graphene oxide, but the disruption of π orbital structure decreased its overall electrical conductivity [163]. Considering the similarities in surface energy of CNTs and graphene, it has been suggested that *N*-methyl-2-pyrrolidone (NMP) can also be used for exfoliation [161]. Solvents like *N,N*-Dimethylformamide(DMF) and *ortho*-dichlorobenzene (*o*-DCB) can also be used as they have surface tension close to 40mN m-1 but they are highly toxic and have high boiling temperatures. Graphite has been known to exhibit dual electronic charge nature on interaction with solvents. It behaves as acceptor for pyridine based solvents whereas it shows donor characteristics in perfluorinated aromatics [164]. Exfoliation of graphite by positively charged poly(p-phenylenevinylene) (PPV-pre) has been known to generate defect-free FLG which can be used with PANI/poly(ethylene terephthalate) electrode to have a volumetric capacitance of 216 F cm^{-3} [165]. A combination of kitchen blender shear force and edible proteins like Bovine serum albumin (BSA), β-lactoglobulin, ovalbumin, lysozyme, and hemoglobine has been proved to produce good quality graphene in concentrations exceeding 4 mg mL^{-1} h^{-1} [166]. Further colloidal approaches have also been made which use stirring combined with sonication to obtain denser graphene solution with larger flakes from graphite precursor [166] which can then be used. Such indigenous methods ascertain the future of cheaper large scale graphene production. More examples have been discussed in Chapter 2.

Electrochemical exfoliation has recently been emphasized as it is useful to obtain FLG of high lateral size extending to tens of micrometres [167]. This method involves an intercalation of ions in-between layers of graphene by an external applied voltage which then turns into gaseous form, expands and exfoliates the layers. It has been suggested as a solution for continuous production of FLG with negligible loss of yield and quality [168]. This method has been used for synthesis of nitrogen doped graphene frameworks which show capacitance of 117.4 F g^{-1} at 0.5A g^{-1} [169]. Electrochemical exfoliation is in use for synthesis of pristine defect free graphene as well as highly oxidised GO sheets with high dispersibility by varying the precursor electrodes, electrolytes, equipment setups and additives [170].

1.1.3.3.2 Mechanical Exfoliation

Mechanical exfoliation is a simple, basic method that can be employed for synthesis of FLG. There are two major pathways for mechanical exfoliation, namely, ball milling and high pressure homogenization methods. NMP is known to be a better solvent for wet ball milling of graphene compared to cyclohexanone [171]. High energy ball milling facilitates through-plane fracture thereby giving room for enhanced edge defects. This has a good scale-up potential but longer reaction time limits it. On the other hand, high pressure homogenization uses both cavitation and shear forces to obtain high-quality graphene [172, 173], but has lesser scope for scaling up. A recent study using a hydrodynamic tube shearing process claims synthesis rate of 500 g h^{-1} [174]. Biomass derived large FLG has been synthesized by this method which has been able to generate a capacitance of 186 F g^{-1} in 1M H_2SO_4 electrolyte [175]. Mechanical thinning of pencil lead to obtain FLG has been developed also which tackles the issues of cost effectiveness and avoids usage of additional chemicals [176]. Besides the two above, another method of mechanical exfoliation is being used which roots on the concept of anionic bonding wherein graphite and borosilicate glass is bonded together at a certain temperature and voltage, and then peeled away leaving behind FLG on the substrate [177].

1.1.3.3.3 Chemical Vapour Deposition (CVD)

CVD is one of the well-known methods to synthesize monolayer or multilayer graphene. This method combines gaseous reactants onto a metallic surface at a particular temperature to produce materials of high purity and performance. Although the underlying mechanism is not pretty clear, the grains and grain boundaries of the metals seem to dictate the solubility and segregation behaviour thereby causing difference in graphene nuclei morphology and carbon diffusion at these sites [178]. The initial reports of growing FLG on hot Ir surface was not suitable as product separation from metal surface was very difficult [179]. Later, FLG has been grown on Ni and Cu surfaces at ambient pressure and paved way for easier metal substrate separation after the growth [180, 181]. The CVD grown on Ni foam had categorically shown the influence of cooling rate on the number of layers of graphene and their consequence on the supercapacitor efficiency [182]. Ni particles have also been used as a template to synthesize curved graphene via CVD process that can provide capacitance of 203.4 F g^{-1} in a KOH electrolyte [183]. This method can be used for FLG synthesis also with other metals like Rh, Pt, Co, Pd and metallic alloys like Co-Ni, Au-Ni, Ni-Mo [184].

1.1.3.3.4 Microwave Assisted Synthesis

Microwave assisted liquid exfoliation helps obtain high quality graphene based on the reaction solvent and temperature conditions [185, 186]. The graphene flakes of average 5 sheets and high lateral size have been obtained with toluene [185]. In case of LPE, the solvent chosen is such that it wets the graphene layers to a large extent which when irradiated by microwaves either vaporises or decomposes to gas molecules thereby causing expansion. The graphene flakes thus produced tend to have high electrical conductivity [186]. This is also used for catalytic unzipping of CNTs into graphene sheets with high oxygen content, supposedly due to the oxidative mechanism of CO_2 [187]. This method has been used for simultaneous exfoliation and reduction of graphene oxide and graphene nanoplatelets to tackle the issues of low electrical conductivity. Such material has been known to be mixed with polypyrrole and used for solid-state supercapacitor application which provide capacitance of 137.2 F g^{-1} [188]. It has be influential for one pot synthesis of electrode materials for supercapacitors as well as for improving the distance between the layers via successive microwave treatments with intermediate intercalation step [189, 190]. Further efforts are being made to perform the yield exfoliation of graphene sheets to be more along in solvent free systems and in air atmosphere [191, 192].

1.1.3.4 Pathways to FLG structuration for energy storage

Taking into account the synthesis methods explained above, it is essential now to understand how to indulge them so as to reap the benefits of the large specific surface area (SSA) of FLG. For each application, the materials design is different and uniquely curtailed. This needs embarkment on the journey to understand the possible pathways for proper structuration of FLG for supercapacitor as discussed below.

1.1.3.4.1 Improving FLG SSA and conductivity

The charge storage capacitance of graphene based materials is found to be largely dependent on interfacial double layer capacitance and specific surface area [54]. Studies indicate the presence of a quantum capacitance component in the interfacial double layer capacitance as the capacitance obtained for dual active side of graphene (5 μF cm^{-2}), found to be less than that of single side of monolayer graphene (8 μF cm^{-2}) by the method of area normalization [193, 194]. Thus the modification of electronic properties of graphene sheets is also essential. It was later found that the capacitance was decreased at the point of zero charge for specific thickness of graphene sheets which could verify the presence of quantum capacitance in graphene sheets [195]. On charging the electrode, the area normalized capacitance seems to increase which is suggested to be result of electrostatic interactions between electrode and electrolyte. This indicates that the overall capacitance can be improved by modulating the charge on graphene sheets. Therefore, FLG materials preparation should not only focus on high SSA but also on the electronic properties and correct charged state. However, these solely cannot confirm a high capacitance. A high power density needs a faster electron transfer between the electrode materials which in turn depends on the electrical conductivity. High SSA and electrical conductivity are often found to be two sides of a coin where increasing one means decreasing the other. Therefore, a right balance of these properties is highly essential. Graphene films have been obtained via direct laser reduction of GO which exhibit high SSA of 1520 m^2 g^{-1} and high conductivity of 1738 S m^{-1} [196]. Such films have been able to demonstrate a high energy density of 1.36 mW h cm^{-3}, which is about 2 times higher than that shown by activated carbon based supercapacitors, and simultaneously show a good power density of 20W cm^{-3}, which is about 20 times higher than its activated carbon counterparts. Another set of graphene thin films has been developed by activation of reduced-GO which when used with $TEABF_4$/AN electrolyte gives a high energy density of 26 Wh kg^{-1} and power density of 200 W kg^{-1} [197]. Thus a good graphene electrode material needs to have well-engineered pores and continuous nanosheet network for high surface area and electrical conductivity respectively.

1.1.3.4.2 Increasing Packing Density

Porous graphene materials help resolve the issues of SSA but at the same time cause low packing density which makes it costlier logistically compared to activated carbon, the current market majority shareholder for electrode materials. The large empty spaces introduced by making graphene materials porous is not utilised for ion storage, rather adds up more weight by requiring more electrolyte [198]. If graphene having packing density 1.1g cm^{-3} is derived from graphite of density 2.2 g cm^{-3}, it generates an interplanar spacing of 6.7Å which allows smooth passage for electrolyte ions like Li+ (0.68 Å), K+(1.37Å) and Na+(0.98Å) [199, 200].

Highly porous graphene with a density of 1.58 g cm^{-3} can be derived from a hydrogel which after evaporation induced drying and shrinkage, and can be used for a high volumetric capacitance of 376 F cm^{-3} [201]. A new form of graphene, Holey Graphene, has been obtained with significantly larger nanopores formed as a result of hierarchical stacking of porous graphene making sure a well-connected transport network for electrolyte ions [202]. This highly packed holey graphene provides gravimetric and volumetric energy densities of 35 Wh kg^{-1} and 49 Wh l^{-1}, which is comparable to lead acid batteries in organic electrolytes.

1.1.3.4.3 Defect Control

Carbon lattice is known to suffer various kinds of defects. The most common structural defects have been illustrated in **Figure 1.16** that include the point defects, dislocation defects and vacancy defects [203]. These defects mostly arise due to the synthesis process and conditions. These defects can introduce local doping of heteroatoms thereby manoeuvre the reactivity and also influence the electrical conductivity of the end product [204]. It is therefore essential to pay attention to the exfoliation process so as to maintain graphene sheets chemically pure and uniformly structured. Although various attempts are being made for proper exfoliation using organic solvents and surfactants, the methods suffer from low yield, decrease in flake size due to longer process, and utilization of hazardous, costlier chemicals [205]. There have been new solutions partially successful in obtaining low defect graphene by method modification [206, 207]. A pre-intercalated process with oleum and co-grinding with sodium has enabled to obtain graphene based materials with low defects, such as 96.3% C and 3.12% O compared to 97.43% C and 2.37% O in natural graphite [208]. The problem of loss of electronic conductivity due to over-oxidation during exfoliation of graphite can be overcome by using Bronsted acids like phosphoric, sulfuric, dichloroacetic and alkylsulfonic acids [209]

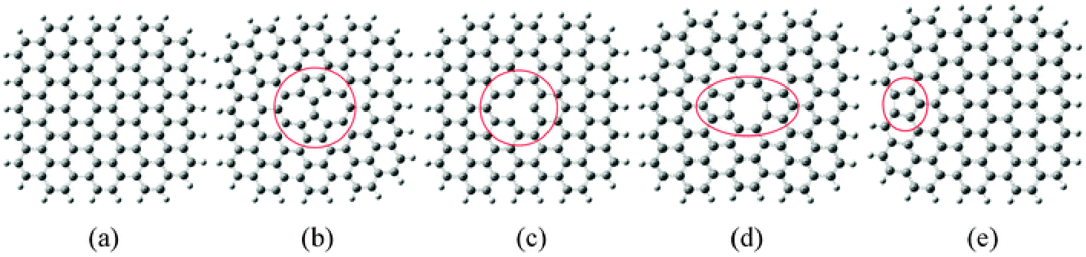

Figure 1.16 Perfect and defective graphene clusters. (a) Perfect graphene cluster, (b) Stone–Wales defect, (c) single vacancy, (d) double vacancy, (e) edge defect with pentagon ring at zigzag edge, octagon and fused pentagon carbon rings line [203].

Some common examples of using such methods for structuration of FLG include aerogels and hydrogels [210, 211]. Graphene aerogels are known to have surface area in the range of 1000 m^{2} g^{-1} which provide capacitance of 220 F g^{-1} at 1 A g^{-1} [210]. Another significant new technique for fabrication highly accessible FLG based materials for supercapacitor applications is 3D [212, 213]. This is similar to 2D printing wherein a suspension of active materials is deposited onto a surface or substrate in a particular fashion and allowed to dry. 3D printing for supercapacitor usage requires additionally µm-level level precision with good adhesion between electrode materials and current collector so as to avoid any short circuiting between positive and negative electrodes [212]. The key factors governing 3D printing for supercapacitor electrodes are: *a*) proper dispersion of printable inks, *b*) consistent and on-demand release of ink, *c*) regulation of the ink wettability so as to avoid electrode short-circuiting and maintaining the feature resolution at the same time, d) suitable solidification conditions for the ink so as to obtain the desired structure. This method has been already shown early signs of success in synthesis of 3D graphene based materials that can be used as supercapacitors with capacitance of ~63F g^{-1} at 10 A g^{-1} and high capacitive retention of about 90% from 0.5 to 10 A g^{-1} [148]. 3D printed graphene electrodes have been known to be cheaper alternative compared to selective laser melting method and can be improved with minimal activation [213]. This method has been used to make GO patterns on A4 paper onto which electrode materials were deposited to obtain volumetric capacitance of 39.65 F cm^{-3} and specific capacitance of 1023 F g^{-1} in a PVA-LiCl electrolyte at a current density of 4 mA cm^{-2} [214].

These are some of the methods and structuration pathways that are widely in use today to synthesize FLG based materials that are being used for supercapacitors. But none of the them has mastered the art yet. Some provide graphene with high energy but low power density whereas other vice versa. Some provide materials easy to handle but low in net quality. Some methods are easy to operate but the process is not completely green and has hazardous by-products. A important aspect of discussed exfoliation methods demands improvement in terms of the bio-surfactant combinations that are used initially, which influence the lateral size of the FLG flakes and their simultaneous concentrations as aqua-colloids. Therefore, focus on proper exfoliation based synthesis methods for utilizing the true potential of graphene is still under the microscope. This combined with right ideas for structuration of FLG can result in the next-gen solution the world needs.

1.2 Chemical Energy Conversion & Storage

It is a well-known fact among the scientific industrial and political communities around the globe that the change in concentrations of gases in the atmosphere, especially CO_2, which has started along with industrialisation, has drastic effects. The anthropogenic emissions of Greenhouse gases have accelerated the rise in terrestrial temperature and needs immediate attention [3]. Additionally, with the possibilities of renewable energy storages that has evolved in the recent years, it will be wise to convert the surplus energy to other forms that can be readily utilized in the society. The surplus from these REs can be used to convert electrical power to gases various products like synthetic gas, liquid, ammonia etc. as shown in **Figure 1.17**. Power-to-gas technology is one of the power-to-*X* methods that helps formulate ideas for utilization of energy from such RE sources and use them for conversion to gaseous fuels thereby relaxing the pressure exerted on fossil fuels and decreasing the consequent pollution in the atmosphere [215, 216]. Using this, CO_2 can be converted to methane and injected to the existing pipeline system for easy access to people. This form of energy storage also aids to the global carbon capture, storage and utilization process where the additional energy helps reduce the global CO_2 percentage by converting it into methane like products which can be easily stored in existing infrastructure and used and when required [24, 25].

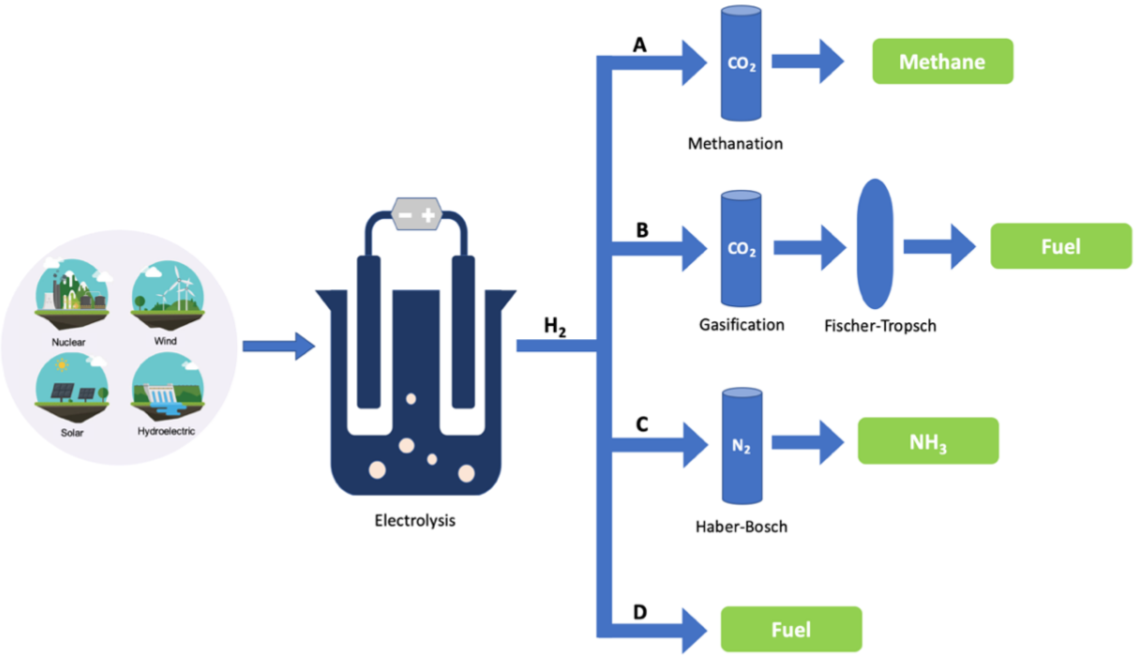

Figure 1.17 Schematic illustration of the described "power-to-X" technologies: (A) Power-to-Gas; (B) Power-to-Liquid; (C) Power-to-Ammonia; (D) All-electrochemical synthesis

1.2.1 Power-to-Gas

The power-to-gas (also known as PtG) concept makes use of excess renewable energy for production of Hydrogen via water electrolysis which can then be used directly or for conversion into to methane or other synthetic natural gasses [215, 216]. It is one of the promising methodology for future where larger amount of energy is sourced from REs. The PtG technology solves the problem of intermittency and round the year availability of the REs as it can convert feedstock gases like CO_2 and store the generated energy for a lot longer timeframe by this method [217]. Most processes involved in PtG setup are mostly mature and require proper integration for the desired output. The converted H_2 and CH_4 can be used directly or stored in the existing pipeline infrastructure for later use. It can also be converted back to useable electricity if need be so (although with some loss in overall efficiency).

Although the PtG technology has not been scaled up to industrial level, European countries have already started developing a roadmap for its swift deployment with proper efficiency standards maintained throughout all the involved processes [218, 219].

As shown in the **Figure 1.18,** the PtG technology can be seen to utilize the multiple processes to convert power to valuable gas. The energy harvested from green sources like hydel, solar and wind which is in excess can generally be first fed to a water electrolyser for production of H_2. The electrolysis of water for H_2 generation is known to be made feasible via catalysts, photoelectrodes, proton exchange membrane and solid oxide electrolysis methods [217, 220, 221]. The generated hydrogen can be used as fuel cells, for automotive transport, stored in tanks and for synthesis of natural gas. Hydrogen economy has seen an upliftment in the recent decade in the fields of transportation and domestic purposes [222].

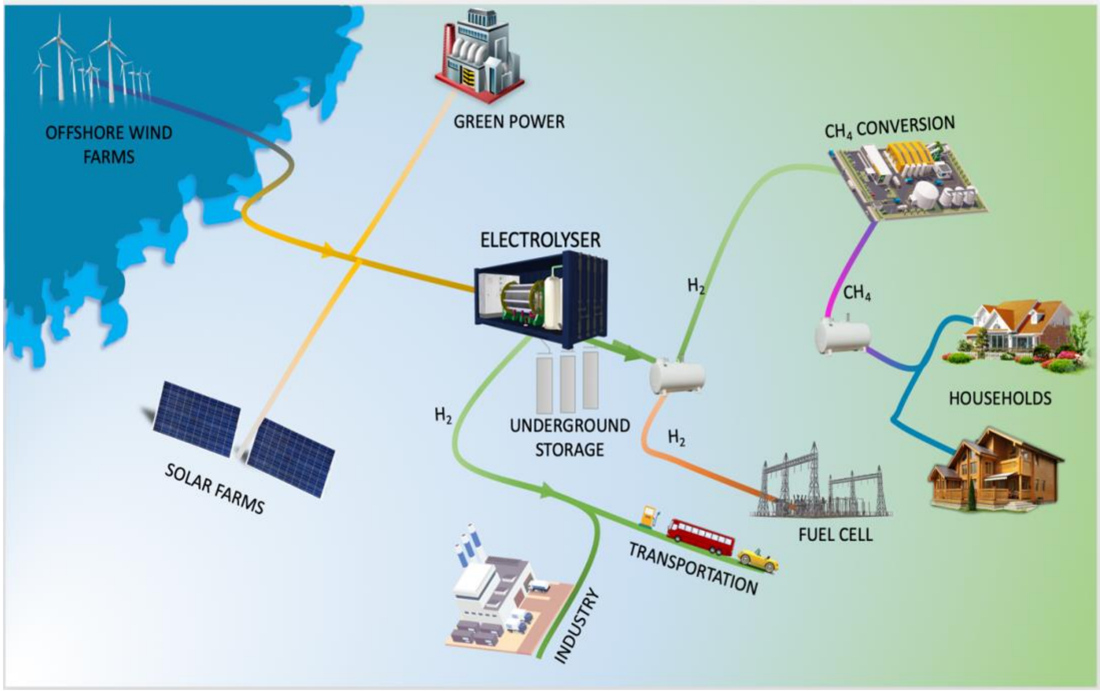

Figure 1.18 Energy Distribution System Based on PtG Technology wherein energy from green sources are utilized to synthesize H_2 which can be directly used or for synthesis of CH_4.

CO_2 can be used as feedstock along with produced H_2 to convert itself to methane which can then be introduced to the existing gas distribution infrastructure as synthetic natural gas. This will aid in global Carbon Capture Utilisation and Storage chains and also increase the volumetric energy density of the stored gas (35-40 MJ m^{-3} for CH_4 vs. 12.75 MJ m^{-3} for H_2) without raising safety issues [223]. CO_2 can also be used as a cushion gas for sequestration of methane underground which provides possibility for zero to negative CO_2 emission in the entire process. To top it all, this technology also helps reduce the effects of the CO_2 emissions which is a big global concern. Therefore, this nascent technology needs to be further explored with proper optimization for storage and transport for a better tomorrow.

1.2.2 Mechanism of CO_2 Methanation

According to the PtG technology discussed above, CO_2 methanation can be carried out via two different ways, viz. biological methanation and catalytic methanation as shown in **Figure 1.19**. The most important parameters guiding the choice of methanation process are the achievable product gas quality, sophistication of reaction setup and reactor volume required for supporting such standards [217]. Biological methanation which is still in its infancy is mostly implemented in small power plants. Although its tolerance for impurities of feed gas is higher compared to the other one, large reactors dedicated to this method is far from reality [224]. Biological methanation is mostly carried out via symbiotic fermentation stages of methanogenesis (Eq. 1.19) and acetogenosis (Eq. 1.20) which require anaerobic reaction conditions with hydrogen partial pressure to be less than 10 Pa [225].

$$4H_2 + CO_2 \leftrightarrow CH_4 + 2H_2O \;; \qquad \Delta G^o = -165\ kJ\ mol^{-1} \qquad \text{(Eq. 1.19)}$$

$$CH_3CH_2CH_2COOH + 2H_2O \leftrightarrow 2CH_3COOH + 2H_2;\ \Delta G^o = +48.3\ kJ\ mol^{-1} \qquad \text{(Eq. 1.20)}$$

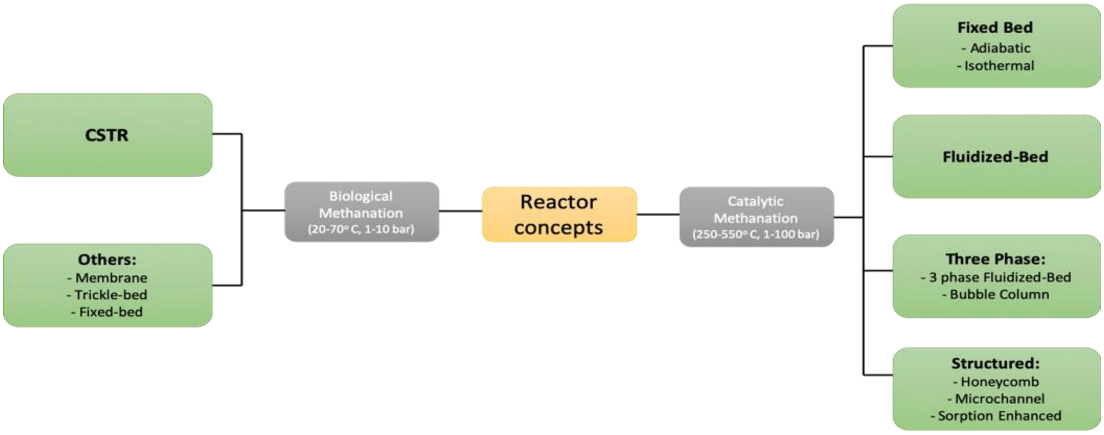

Figure 1.19 Processes for methanation

Catalytic methanation on the other hand is a matured process known since 1902 [226]. But it was not until the oil crisis in 1970s that researchers took larger interest in this. NASA is using this reaction for Mars colonization [227]. It is thermodynamically faster compared to other reactions for formation of hydrocarbons or alcohols [228]. In the methanation process, as shown below in **Table 1.3**, there are possibilities of various side-reactions that affect the main reaction (Eq. 1.19):

REACTION	ΔH_{298} $(kJ\ mol^{-1})$	ΔG_{298} $(kJ\ mol^{-1})$	TYPE	EQN.
$CO + 3H_2 \leftrightarrow CH_4 + H_2O$	-206.1	-141.8	CO methanation	Eq. 1.21
$2CO + 2H_2 \leftrightarrow CH_4 + CO_2$	-247.3	-170.4	Inversed methane CO_2 reforming	Eq. 1.22
$2CO \leftrightarrow C + CO_2$	-172.4	-119.7	Boudouard reaction	Eq. 1.23
$CO + H_2O \leftrightarrow CO_2 + H_2$	-41.2	-28.6	Water-gas shift reaction	Eq. 1.24
$2H_2 + C \leftrightarrow CH_4$	-74.8	-50.7	Inverse methane cracking	Eq. 1.25
$CO + H_2 \leftrightarrow C + H_2O$	-131.3	-91.1	Carbon Monoxide Reduction	Eq. 1.26
$CO_2 + 2H_2 \leftrightarrow C + 2H_2O$	-90.1	-62.5	Carbon Dioxide Reduction	Eq. 1.27

Table 1.3 Possible side-reactions during methanation of Carbon Oxides

Other by-products like methanol, methanoic acid and higher hydrocarbons have not been considered here as they are present in trace amounts in the gas mixture at equilibrium conditions. The methanation of CO_2 is normally considered to follow one of the two mechanisms (associative or dissociative) as shown in **Figure 1.20** [229]. The associative mechanism suggests that CO_2 first forms oxygenated intermediates by adsorption with H_{ad} adatom followed by subsequent hydrogenation to CH_4. Contrarily, the dissociative mechanism suggests that CO_2 is first dissociated to (CO_{ad}) and (O_{ad}) adatoms followed by hydrogenation of carbonyl to CH_4.

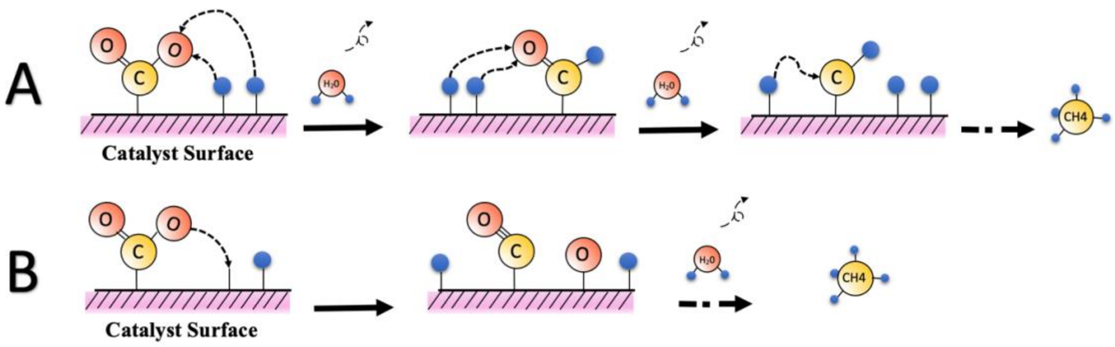

Figure 1.20 CO_2 conversion mechanism, a) associative, b) dissociative

1.2.3 Catalysts for Methanation

Methanation is a thermodynamically facile process ($\Delta G_{298} = -130.8\ kJ\ mol^{-1}$) but faces limitations as it has a linear structure with two oxygen atoms attached to a single carbon atom by double bonds arranged 180° apart from each other. The carbon-oxygen linkage is strong which has an average bond dissociation energy of 782.4 kJ mol^{-1} (or 391.2 for each shared pair of electrons) [230]. This strength is also backed by the fact that the Lewis structure of CO_2 represents both carbon and oxygen with complete octets. The complete hydrogenation of C^{4+} (in CO_2) to C^{4-} (in CH_4) is a eight electron process having various kinetic limitations and therefore require efficient catalysts for suitable methanation outcome [231]. The typical catalysts that are active for methanation are known to be metals from group 8-10 as shown in **Figure 1.21** [232].

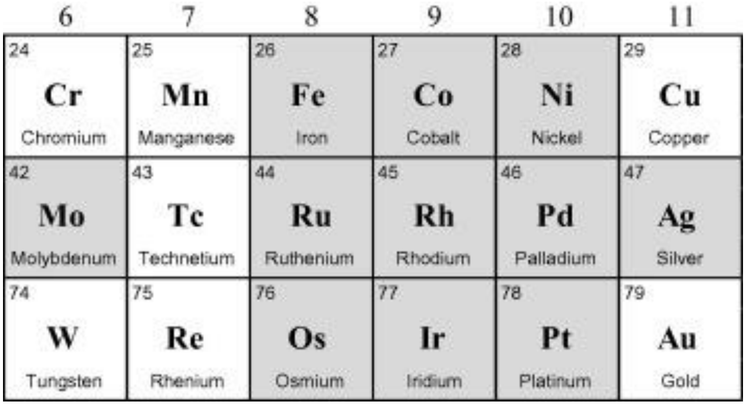

6	7	8	9	10	11
24 **Cr** Chromium	25 **Mn** Manganese	26 **Fe** Iron	27 **Co** Cobalt	28 **Ni** Nickel	29 **Cu** Copper
42 **Mo** Molybdenum	43 **Tc** Technetium	44 **Ru** Ruthenium	45 **Rh** Rhodium	46 **Pd** Palladium	47 **Ag** Silver
74 **W** Tungsten	75 **Re** Rhenium	76 **Os** Osmium	77 **Ir** Iridium	78 **Pt** Platinum	79 **Au** Gold

Figure 1.21 Snippet of Periodic Table with methanation active materials highlighted in grey.[232]

The unsupported catalysts were initially studied for which the order of activity was found out to be [233]:

Activity: Ru > Ir > Rh > Ni > Co > Os > Pt > Fe > Mo > Pd > Ag

But, the above comparison did not consider the metallic surface area which gave rose to a new order of ‘specific’ activity and selectivity as [234]:

Specific Activity: Ru > Fe > Ni > Co > Rh > Pd > Pt > Ir

Selectivity: Pd > Pt > Ir > Ni > Rh > Co > Fe > Ru

It has been further reorganized to identify the most important methanation catalysts as [235]:

Specific Activity: Ru > Fe > Ni > Co > Mo

Selectivity: Ni > Co > Fe > Ru

The active phases of this metals are generally supported on various oxides like, Al_2O_3, CeO_2, ZrO_2, and carbon based materials like, SiC, CNT, FLG [231, 236-239]. Herein, the most active and most selective metal (*i.e.*, Ru and Ni respectively) for methanation will be discussed along with suitable supports.

1.2.3.1 Ruthenium-based Metal Catalysts

Ru based catalysts are well-known for being the most active metal for CO_2 methanation even at low temperatures [227, 228, 237, 240, 241]. Ru has been known to be used at less than 1 wt% dosage with TiO_2 for achieving 100% conversion of CO_2 at 160°C but it is expensive for industrial use [242]. This highly stable (170h test) catalyst had highly dispersed 2.5 nm Ru nanoparticles which were supposed to be the guiding factor for complete conversion of CO_2. This high dispersibility of Ru on TiO_2 has been an interesting property to decrease the temperature requirements for methanation, even to room temperature and atmospheric pressure in certain cases [243]. The introduction of RuO_2 nanoparticles on TiO_2 behaves differently based on the crystal phase of the later [244]. P25 TiO_2 having 20% of anatase and 80% rutile showed the highest CO_2 conversion and selectivity. Further investigations proved that RuO_2 nanoparticles have a tendency to move towards the rutile phase of TiO_2 whenever there is a rutile and anatase co-existence. This biased migration of RuO_2 particles towards rutile phase give rise to its high dispersion in the reduced form [244]. Ruthenium tops Nickel in CO_x methanation, especially in low temperatures, where Ni is considered to undergo deactivation because of sintering, carbon formation, interaction of Ni particles with CO, and formation of Ni subcarbonyls [245, 246]. A DFT study suggests that carbon monoxide is easily activated for chemisorption and dissociation on a high-coordination of Ru atoms (111) in terrace environments [247]. Bimetallic Ru/Ni catalyst has recently been used for ultra-low temperature syngas to methane conversion at around -7°C [248]. It has been predicted that the segregation of Ru on the Ru-Ni/γ-Al_2O_3 composite can provide more active Ru sites with higher sulphur tolerance [249]. Thus it can be used as an additive also for Ni based systems for methanation reactions [250]. Ru has also been used with Co to form bimetallic Ru-Co catalyst [251]. Such catalyst showed that the yield of CH_4 was enhanced by the formation of Ru-Co bimetallic film. It was compared to pure Co and Ru/SiO_2 catalysts in temperature range of 200-340°C indicating that the active phase was indeed the bimetallic film and not the pure metallic phases separately [251]. The addition of yttrium to Ru-based catalysts have a two-fold benefit. It increases the active surface area and dispersion of Ru particles for CO_2 methanation along with increasing its tolerance level for catalyst poisoning [252].

Ruthenium is known to be stable under a wide range of temperatures. Ceria is one of the best supports for ruthenium based catalysts for a higher methane selectivity. It has been found that $Ce_{0.95}Ru_{0.05}O_2$ is able to provide a 55% conversion of CO_2 with a 99% selectivity for methane wherein the Ru particles are the prime reason for providing reducing sites at a lower temperature compared to pure Ceria [253]. The metal oxide support reducibility for Ru- based catalysts has revealed that, CeO_2 being a reducible support is more suitable to hold up Ru for CO_2 methanation in comparison to the irreducible Al_2O_3 which exhibits pseudo-saturated CO adsorption thereby limiting the co-adsorption of H_2 and reducible ZnO leading to reverse water-gas shift reaction [240, 254]. The selectivity during methanation is largely dependent on the cluster sizes of Ru and the support used. Atomically dispersed Ru on Al_2O_3 support gives pathway for higher selectivity towards carbon monoxide whereas larger particle size of Ru on same support facilitates higher methane selectivity [255]. A Steady-State Isotope Transient Kinetic Analysis (SSITKA) experiment has been done of RuO-Al_2O_3 catalyst to better understand the reaction mechanism for CO_2 methanation [256]. An isotope exchange of $^{12}CO_2$ to $^{13}CO_2$ resulted in increased intensity of $^{13}CO_{ad}$ atom and a corresponding reduced intensity of $^{12}CO_{ad}$ indicating the formation of carbonyl intermediate. A simultaneous observation of slow formation of formate bands during isotope exchange stipulates lesser chance of formation of formate intermediates. The detailed mechanism is shown in **Figure 1.22**.

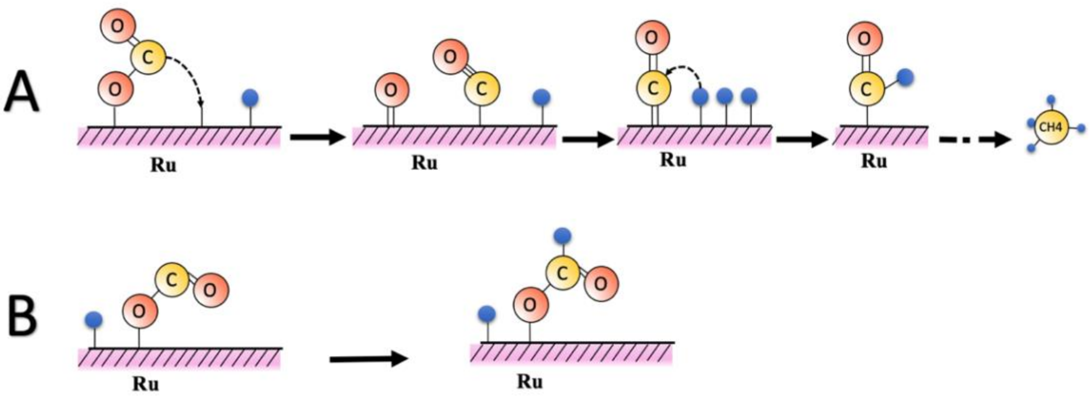

Figure 1.22 Ru based methanation mechanism, (a)CO_2 dissociated to CO_{ad} and O_{ad} on Ru sites. CO_{ad} then evolved to methane in an associative way, (b): Surface formate species accumulated rather than hydrogenated to CH_4. [229]

1.2.3.2 Nickel-based Metal Catalysts

Nickel is one of the most common element that is being used for CO_2 methanation because of low cost (compared to noble metals), easy availability, good activity and high selectivity for methane. It is largely used with other metals, oxide supports and promoters for enhancement of activity and selectivity [236, 257]. Co is one of the most utilised metal for synthesis of bimetallic catalysts with Nickel [258-262]. Usage of Co-Ni bimetallic catalyst over Al_2O_3 substrate can help generate metal-support interactions to avoid the thermal sintering of the metal active centres along with maintaining the pore volumes even after 700°C calcination [258]. Kinetic study of the synergistic effects in the bimetallic Co-Ni catalyst approves that the activation energy for methanation can be decreased with optimized metal ratio (around 20% of Co compared to Ni). During methanation, the Al_2O_3 support matrix has been found to stabilize the nanoparticles by the confinement effect. The advantageous properties of Co are known to be useful on catalysts with low loading of Ni (~ less than 10% by weight) [262]. The addition of Co helps decrease the reaction temperature and improve the Ni surface reducibility. Another such element which shows efficient bimetallic activity with Nickel is Iron [263-265]. According to the order suggested earlier, Fe is more active than Ni, but less selective. Therefore, their combination works pretty good. It has been a subject of interest since 1990s when ultrafine nickel ferrite(UNF) was studied for CO_2 methanation [263] wherein oxygen deficient ferrites (ODF) were obtained from magnetite and M(II)-bearing ferrites. The predicted reaction mechanism proceeds with CO_2 decomposition to carbon and oxygen on contact with ODF followed by penetration of oxygen to the ODF lattice. Carbon on the other hand gets deposited on the ferrite surface and then reacts with H_2 to form CH_4 with 86% yield at around 200-300^{o}C. The UNFs are about 1.5-6 times (depending on GHSV) more competent that the Nickel ferrites for methanation. A combined study of various metals, 'M', with Ni for forming a Ni-M/Al_2O_3 one-pot sol-gel synthesized catalyst for methanation has proved that Fe is better than Zr, La, Cu for enhancing the activity towards methanation [264]. The inclusion of Fe indicated shift in the reduction temperature of NiO species and also helps in making it more resistant to sintering. Ferrites and bimetallic Ni-Fe catalysts have garnered recent attention for their usability in magnetic induction based CO_2 methanation also [266, 267]. Bimetallic Fe-Ni nano-objects have been used both as good heating agents (requiring low magnetic field amplitudes) and high conversion catalyst. An additional Nickel surface layer giving rise to $Fe_{30}Ni_{70}$@Ni nanoparticles have been able to achieve 100% conversion and 100% selectivity [266]. A complete shift from Ni to Fe has been thought upon but lacks feasibility as most studies indicate the need of high dispersion with additional pressured atmosphere for methanation driven reaction product. If not, the Fischer-Tropsch mediated C-C coupling reactions become predominant [265]. La_2O_3 is another candidate for decreasing the methanation starting temperature for Ni/SiC systems from 200^{o}C to 150^{o}C [268]. The Ni-La/SiC has higher stability than Ni/SiC and has restrained growth of NiO NPs. La changes the electronic environment around Ni atoms thereby facilitating easier activation of sites for CO_2 methanation.

One of the most important factors that drive CO_2 methanation via Nickel is the kind of support on which the NPs are placed and how they behave with the heating environment. The dispersion of metal NPs and their stability depends largely on the surface and textural properties whereas the activity and selectivity depends on the surface reducibility and metal-support interactions [230, 236]. The study of such active phase carriers or supports are highly essential as they also avoid sintering of metal NPs by confinement effect [258]. A recent study has provided an order of activity based on CH_4 yield for Ni over various metal oxides support as Ni/Y_2O_3 > Ni/Sm_2O_3 > Ni/ZrO_2 > Ni/CeO_2 > Ni/Al_2O_3 > Ni/La_2O_3 [269]. In this study, the

CO_2 conversion increased rapidly from 225-250ºC reaching a maximum at around 300ºC. The study emphasized on the fact that moderate basic sites are advantageous for CO_2 methanation. The in-situ studies revealed that Al_2O_3 based catalyst tends to for CO intermediate whereas La_2O_3 only formed carbonates. Contrarily, in the case of Ni/Y_2O_3 the carbonates were converted to formate species which were later decomposed because of the H_2 atmosphere during methanation. This swift decomposition of formate species is predicted to be the precedent for such high activity of Y_2O_3 support. Similar results for Ni/CeO_2 has also been confirmed when compared to another set of oxides as: Ni/CeO_2 > Ni/α-Al_2O_3 > Ni/TiO_2 > Ni/MgO [270]. The study indicated CeO_2 supports larger surface absorption of CO_2 which improves its performance. CeO_2 is also a good catalyst for low temperature methanation at 150-200ºC but the investigation utilises larger molar ratio of Hydrogen which doesn't seem cost effective for industrial level scale up [271]. Besides, larger H_2 content in the reaction atmosphere also changes the dynamics of the reaction such as generation of local hotspots and easier reduction of intermediate species than under normal conditions prescribed. The mechanism for methanation on Ni based catalyst has been studied via in-situ FTIR on a Ceria-Zirconia support as shown in **Figure 1.23** [272]. It showed that carbonate (CO_3) was formed on the support which with increase in temperature gets converted to bicarbonate (HCO_3) which subsequently dehydrates to formate (HCOO) giving rise to CH_4 as the final product (**Figure 1.23, A**).

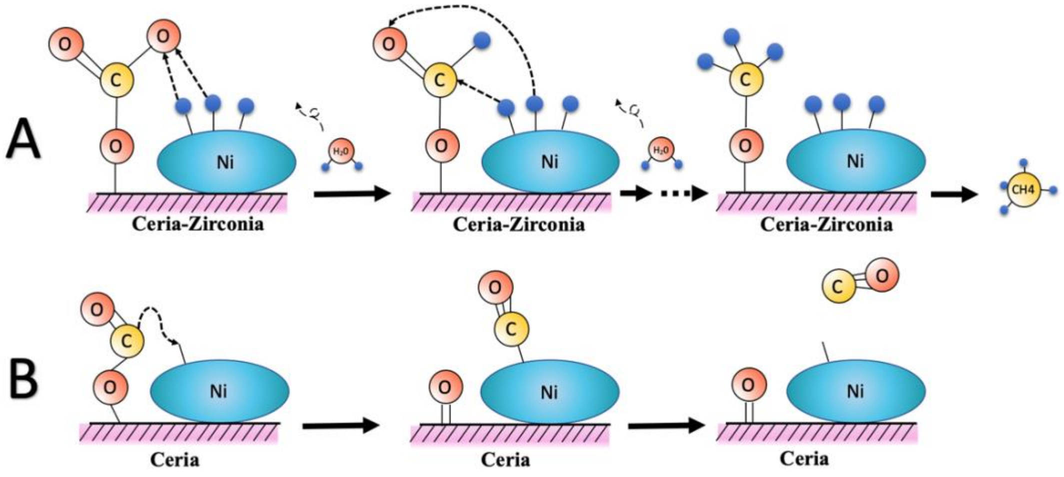

Figure 1.23 Methanation mechanism of Ni NPs supported on Ceria-Zircona

On the other hand, the carbonyl (CO) formed on the Ni by initial docking on Ce^{3+} sites remains stable and is removed as product (**Figure 1.23, B**). Interestingly, the Ni/ZrO_2 interactions beg to differ from the earlier concepts. The vibrational bands obtained for Ni/ZrO_2 showed negligible presence of carbonyl species [273]. Rather, both Ni and ZrO_2 showed the carbonate and bicarbonate formation indicating bi-functionality of metal and support towards CO_2 methanation. The metal sites were considered to be the H_2 reservoir whereas the support stabilized CO_2. Another important support which have shown promising results for nickel based catalysts are mesostructured silica nanoparticles (MSN). MSN has been reported to be more active and better candidate than MCM-41(Mobile Crystalline Material), HY (protonated Y zeolite) and SiO_2 [274]. The Ni/MSN has been able to hydrogenate CO_2 with 64% conversion and 99.9% selectivity at 300ºC. The abundance of basic sites, which favoured augmentation of the concentration of adsorbed CO_2 molecules on the catalyst surface, has been attributed to the intra and inter-particle high porosity of Ni/MSN catalyst. This catalyst, though provides moderate conversion, has very high stability and no coke deactivation for 200 h. Metal supported M/MSN (M= Rh, Ru, Ni, Ir, Fe, Cu) catalysts were further studied to identify the best metal and the plausible mechanism of methanation over such MSN catalysts [275]. Ni, Rh and Ru had almost similar rate of methane formation but Nickel was better in terms of specific area. The mechanism as shown in **Figure 1.24** indicates that initially the CO_2 and H_2 get dissociated on the metal surface to produce CO, O, and H atom which then get transferred to the MSN surface. The O atom reacts with H atoms to form water molecule. It is the oxygen vacancies in the MSN catalyst which anchors the carbon species leading to CH_4 with help of the dissociated hydrogen species one the metal surface active sites. This mechanism gives room for formation of bridged carbonyl, linear carbonyl, and bidentate formate based intermediates.

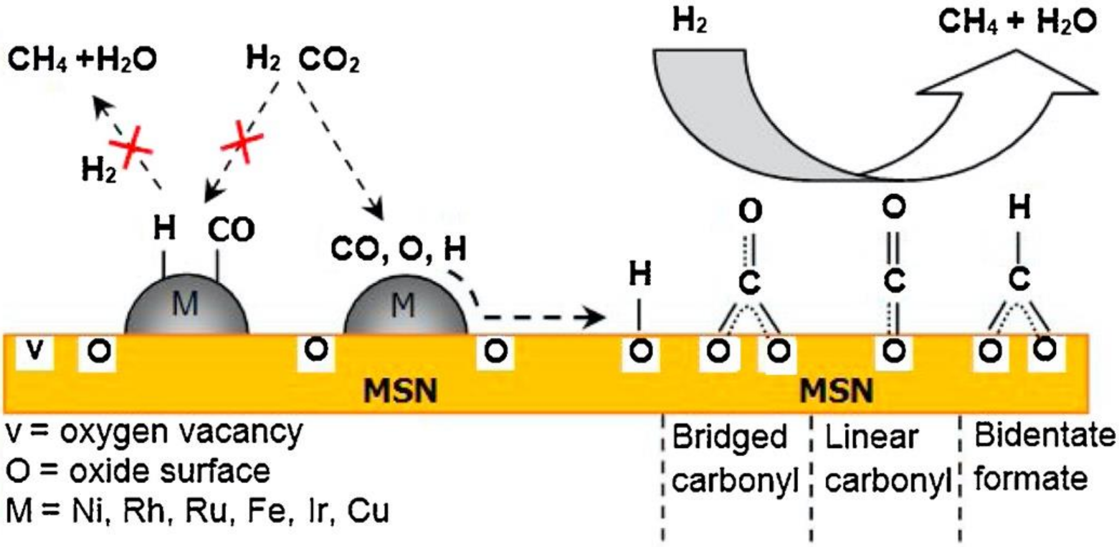

Figure 1.24 Methanation mechanism on MSN substrate having metal NPs [275].

Besides the support, the loading amount of Nickel plays a crucial role for hydrogenation of CO_2 [276-278]. A study on Ni/Al_2O_3 explains that the Ni metal active sites for CO_2 hydrogenation can be formed in-situ if the loading is high whereas it needs to be pre-reduced in case of lower dosage [279]. The effect of increase in loading was already reflected at small dosages. The reaction activity for loading in the range of 1-10% Ni on MSN followed the trend: 10Ni/MSN ≈ 5Ni/MSN > 3Ni/MSN > 1Ni/MSN [276]. It also confirmed that presence of very small Ni particles facilitates high selectivity towards methane compared to CO. The increase in metal loading normally gives rise to increase in basic sites [278]. XRD results indicate formation of new nickel phases after high temperature treatment on high Ni loading. This also welcomes low dispersion with increase in size of metal sites. Ru was also used for the same test at similar conditions. Ru was completely reduced at 300°C whereas heavy Ni loading made sure that all Ni was not reduced even with a temperature of 500°C. Similarly, a study with a large loading of Ni (ca. 70%) on Al showed some theoretically challenging results [280]. Contrary to the idea of lower Ni loading providing a better methanation selectivity, the Ni-Al catalyst showed high conversion and near 100% selectivity arising out of nanoscale Ni crystallites formed over NiO-alumina by partial reduction. This sums up the idea that the change in reactivity is not based on just Ni loading but also depends on the corresponding interaction with the support.

Last but not the least is the influence of the preparation method of the Ni NPs that affect the reactivity towards methanation. Varied SSA attributed CeO_2 have been studied with fixed loading of Ni but different dispersions prepared via wetness impregnation [271]. CeO_2 sample with highest SSA showed the best dispersion and performance. Near 75% metal loading on another set of catalyst $Ni_aCe_{1-a}O_x$ ($0.3 \leq a \leq 0.9$) prepared via co-precipitation had same crystallite size of Ni as that 10% Ni/CeO_2 prepared via impregnation. These results back the idea that part high reduction temperature was required as part of the nickel was involved in synthesis of the complex composite support for Ni NPs. NiO/SBA-15 of low metal loading has been also reported to show difference in dispersion when prepared via solvent impregnation (SI) versus simple heat treatment (HT) [281]. There were no specific changes in dispersion with a high Ni loading though. The method of preparation also influenced the temperature for attaining maximum conversion. All loadings of Ni on SBA-15 prepared via HT had high thermal stability whereas those prepared via SI had the same for only high loadings of Ni. The overall performance of Ni/SiO_2 samples have been known to be greatly enhanced by synthesis process involving impregnation followed by glow plasma treatment [282]. The conversion and space-time yield of CH_4 over catalysts prepared via plasma were significantly higher than those attained by conventional impregnation.

1.2.3.3 Carbon Supports for methanation

Besides the various oxide supports described earlier, there is another family of supports derived from carbon based materials that is being studied for CO_2 methanation. Carbon nanotubes and graphene based materials have been proved to be most efficient supports for methanation [283-286]. CNTs loaded with 10-15% Ni with Ce promoter, prepared via co-impregnation method has been able to achieve reactivity of about 83.5% with a 100% selectivity [283]. CNTs by virtue of their structural derivation from graphene sheets are able to have a better metal-support interaction giving rise to high dispersion and very small size

NPs. The same loading of metal and promoter was also done onto an γ-Al_2O_3 support which yielded with lower reactivity of about 64.5% conversion and 97.4% selectivity for the same test conditions. The tubular nature of the CNTs were particularly helpful in implementation of confinement effect as the metal NPs inside the tubes retained the size after an 100h stability test whereas the NPs outside showed minor growth. The majority of the metal-CNT interactions arises from the defects and the dangling bonds associated with them. Some of the types of defects associated generally with the CNTs are shown in **Figure 1.25** [287]. The isolate pentagon give rise to cone structure whereas the heptagon whereas a heptagon leads to a horn.

A 5|7 hole in the CNT changes the chirality to (9,0) whereas similar hole with different orientation as shown in the figure leads to (9,1) chirality. Such vacancy defects facilitate introduction of heteroatoms of nitrogen and oxygen which aid to the metal interaction with CNT. Ni loaded on nitrogen doped CNTs have shown promising CO_2 methanation activity of about 75% conversion with 95% selectivity [288]. Such N-CNTs are known to provide preferential Ni binding sites along with stabilization against coke formation. Ni supported on oxygen functionalized CNTs shows anomalous metal-support interaction mode wherein higher temperature leads the weaker interaction [284]. It has been reported that such behaviour arises due to the presence of the surface oxygen groups (SOGs) on the CNTs.

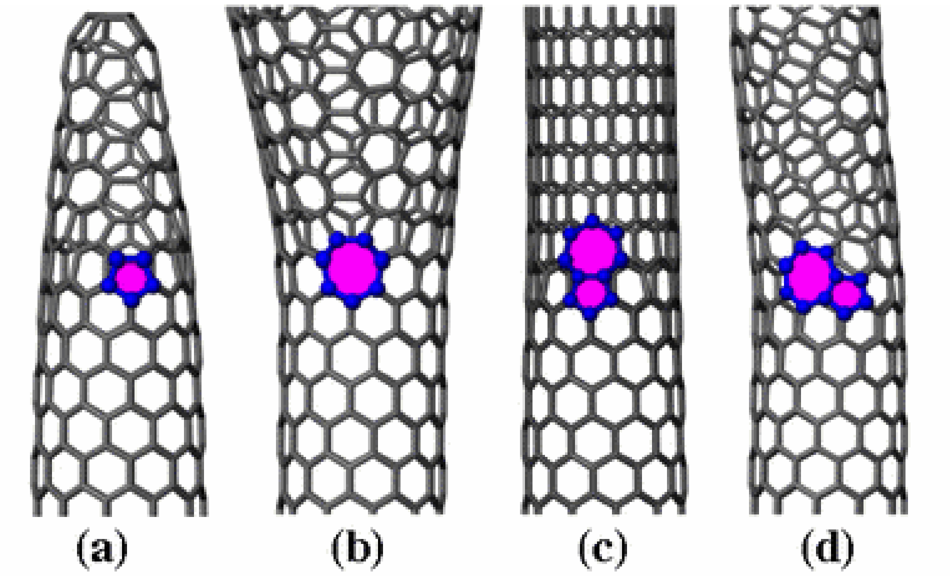

Figure 1.25 Different types of defects observed in CNTs: a)isolated pentagon, b) isolated heptagon, c) a 5|7 hole along the tube, d)) a 5|7 hole of different orientation [287].

Higher calcination temperatures causes removal of such SOGs which then further lead to detachments of flat Ni particles from CNTs leading to formation of larger spheres via geometric effect. The flat Ni NPs were not accessible from both sides as that would have a large amount of active surface. Therefore, spheres provided better reactivity. Ni-ZrO_2

supported on CNT have also been investigated where the influence by difference in preparation method has been highlighted [289]. It has proved that sequential impregnation of Ni and ZrO_2 is advantageous compared to co-impregnation which leads to core-shell type of structures. Separate phase formation of Ni and ZrO_2 via sequential impregnation confirm higher reactivity.

Few-layer-graphene and other graphene structures have also recently gained exposure as a possible alternative for metal support towards CO_2 methanation. Most of the studied metal-carbon interactions for catalytic applications are based on 1D nanofibers which normally tend to have reciprocal arrangement of graphene sheets with different edges-to-plane ratio as shown in **Figure 1.26** [290]. They are differentiated based on the angle formed between the layer of graphene and the longitudinal fiber axis.

Herring bone carbon fibers have either a hollow core or solid connected layers wherein the layers are inclined with respect to the central fibril axis. The edges of such structures are stabilized by hydrogen. Ribbons as CNFs are found when unrolled graphene layers tend to align themselves parallel along the central fibril axis whereas stacked-cup architecture refers to continuous layering of rolled graphene one on top of the other. The stacked-cup fibers have a wide internal hollow space. Platelet structure refers to layering of graphene sheets of about 100 nm about the central axis which are stabilized by a large number of hydrogen and other hetero atoms.

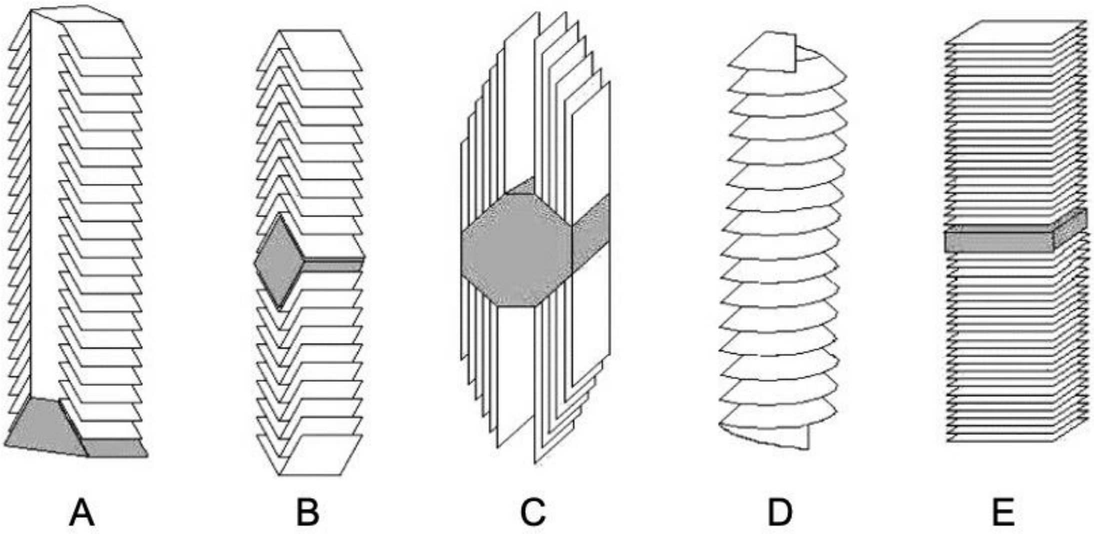

Figure 1.26 Schematic diagram of various types of CNFs, a) hollow-center herring bone, b) solid core herring bone, c) ribbons, d) stacked-cup, e) platelets

Graphene has been intercalated onto Ni foam via combined CVD and plasma treatment process to form a support that can be loaded with Ni active sites having high dispersion and stability. This catalyst has been able to obtain CH_4 conversion of 83% at a higher temperature of 470ºC [291]. The utilization of graphene in the catalyst brings around a large amount of stability to the system as it avoids the process of physical adsorption of Ni from Ni-SiO_2 onto Ni foam by forming an intermediate layer. Further, the intercalation of graphene gave rise to strong metal-support interaction (SMSI) evidenced by the increased adsorption energy compared to only Ni-SiO_2. The lack of nitrogen heteroatoms on graphene structures precludes its usability as a standalone catalyst. A heavily pyridinic nitrogen doped metal-free graphene quantum dot (NGQD) has been able to carry out methanation with reasonable activity and selectivity [285]. A shift in selectivity from CO to CH_4 was observed at around 300°C. The catalytic activity rose mostly from the anchored N hetero atoms. Ni supported reduced graphene oxide(RGO) promoted by Ceria has been reported to provide 83% conversion at 350°C [286]. Simple metal loading without promoter has also been effective in enhanced reactivity as RGO behaves as a better support material. When compared with same loading, promoter and test conditions a relative order has emerged as Ni-Ce/RGO > Ni-Ce/γ-Al_2O_3 > Ni-Ce/Activated Carbon. The positive support effect of RGO is derived from its large surface area and oxygen containing functional groups on the surface. A recent study indicates that using graphene as support drives the selectivity of MoS_2 platelets from CO to CH_4 [292]. This study also confirmed that using graphene as a support decrease the temperature of CO_2 conversion to a large extent along with an increase in the rate of conversion. It indicated negligible activity of graphene alone towards CO_2 methanation but only at temperature more than 400°C which indicated that it behaves as a support and facilitates the activity of MoS_2 below this temperature. This also opens the possibility of synthesizing graphene materials which can be used as self-promoting supports for CO_2 methanation and a suitable heating system that utilize the inherent properties of graphene. The metal free NGQDs and the possible activity of support in case of MoS_2 based methanation can bring a consensus that more investigations are needed for utilizing graphene as a support towards CO_2 methanation [285, 292].

1.2.4 Reactors for CO_2 Methanation

Efficient reactor design is one of the most important components for scaling up of methanation process. Methanation being an exothermic reaction needs special attentions so as to support controled continuous heat fluxes, which, if not done properly would render the system inefficient by formation of hot spots and giving rise to various undesirable by-products and deactivation of catalyst by coke formation [240, 293]. The goal is normally to maintain thermodynamically favourable conditions and to preserve the catalyst from deactivation. A typical reaction setup having GHSV of 5000 h^{-1} and obtaining complete CO_2 conversion requires removal of heat in the rate of approximately 2MW per m^3 of catalyst bed [217]. The loss in efficiency from the beginning of the PtG process of acquiring energy till utilizing it for conversion of CO_2 that can be injected in grid goes via various energy losses as shown in **Figure 1.27** [294]. The conversion of electrical energy to Hydrogen faces loss arising from the internal resistance. The next step sees further reduction of efficiency up to 64%. It is estimated that by the end of the entire chain, there should about 63.6% that can be introduced to the grids. Thus it is imperative to design reactors with well-established temperature control. For this purpose, different reactor setups using different strategies are being developed, such as using fixed bed, fluidized bed, three-phase and structured reactors.

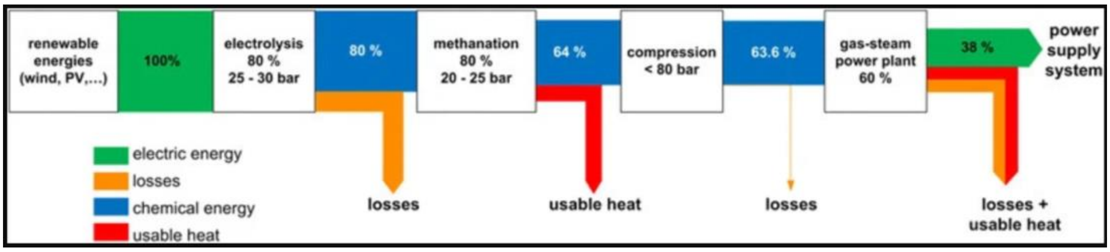

Figure 1.27 Schematics of energy loss from renewable sources till it reaches power supply system

Adiabatic fixed bed reactors are one the oldest and most utilized reactor designs that has been employed for CO_2 methanation. The usual setup includes a series of reactors with intermediate cooling or gas circulation for controlling the temperature of the exit gas [295]. The fixed bed reactor has different heat zones which further require multiple thermocouples. The adiabatic mode of operation requires stable catalyst that remain operable in a wide range of temperature, generally 250-700ºC. Cooled fixed bed reactors made with cooling tube bundles can be used as an alternative, but are comparatively expensive for a scale-up.

Fluidized bed reactors maintain isothermal conditions by usage of fluidized solid reactants thereby providing larger control over all operations. This approach uses a lot simpler design having a single reactor which is advantageous for easier heat removal [296]. The process suffers from fear of catalyst deactivation caused by attrition in relation to the catalyst and the wall of the reactor [293]. They are also disadvantageous as there is possibility of incomplete CO_2 conversion caused due to bubbling of the fluidized reactants. Further, these reactors are restricted by the superficial gas velocity which can sometimes be very low to provide the fluidizing conditions and can sometimes be too high in order to avoid catalyst oxygenation.

The three-phase reactors generally consist of a slurry reactor filled with liquid phase and suspended catalyst particles by the help of a continuous gas flow [297]. The reactor model has easier heat removal technique and thus can operate almost isothermally. The high heat capacity of the liquids facilitates temperature control. The limiting factor for this technology are the resistances at the gas liquid mass-transfer interface and the decomposition and evaporation of the suspension liquid.

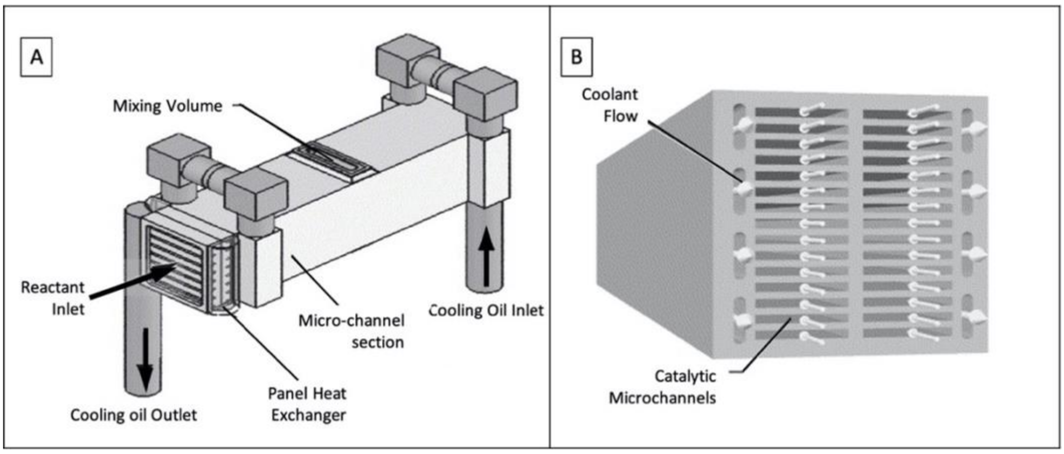

Figure 1.28 Structured micro-reactor setup [217].

Structured reactors are a developing alternative that overcomes the issue concerning development of hotspots and pressure drops found in adiabatic fixed-bed reactors. Monolith reactors based on this are designed with internal metallic structure that improves the radial heat transport by two to three orders of magnitude compared to other systems [217]. Micro-structured reactor as shown in **Figure 1.28** are one of the best examples of this concept which are very compact in nature with a high surface-to-volume ratio [298]. The only drawback of the micro-reactors is the complicacy involved in catalyst loading and unloading (after deactivation).

The above discussion verifies that a proper heating system is essential along with the suitable catalyst for better CO_2 methanation. Macroscopic catalysts are well-suited as they would cause a lesser pressure drop in the reactor bed. The main challenge still lies to make both work in the kinetic window of the catalyst and also optimize it so as to obtain desired products efficiently. The energy and raw material supply for such PtG systems being intermittent in nature requires reactors that can sustain such dynamic on/off operations. The reactors also need to be equipped enough so as to carry out rapid increase and decrease of temperature making sure to not damage the catalyst in the process. This also brings in another important parameter of pressure which needs special emphasis. The operational pressure conditions for such reactors should be normally atmospheric pressure in order to avoid heat increase in the reaction chamber caused by apparent increase in pressure. Thus, the project envisages on utilizing a new heating method based of induction technology to overcome the aforementioned issues.

1.2.5 Inductive Heating (IH) Technology

Current day heterogenous catalysis involves usage of multiphase reactant and gases which demands better heat management systems at place. Electromagnetic inductive heating (IH) or radio frequency (RF) heating of magnetic or electrically conductive catalysts has recently been a new avenue of interest among researchers globally [299-301]. Compared to conventional heating, IH provides unique features based on heat convection and conduction which renders it effective in various situations requiring better heat management. IH works on the concept that an electrically conductive material is heated when exposed to an electromagnetic field by virtue of eddy currents, the field being created by passage of high-frequency alternating current through an electromagnet. The IH approach to directly heat only the active materials in the reactor is particularly helpful to tackle the heating limits faced in a conventional setup. Direct heating of the catalyst core without heating the entire setup from the outer walls helps save energy. This also helps in reducing the amount of heat loss and heat waste generated as a consequence of overall heating used in the previous technologies, thereby improving the catalyst lifecycle [302, 303]. The preliminary proof-of-concept of such an interesting IH technology for facing catalytic challenges were summarized in the view of using magnetic iron nanoparticles for Fischer-Tropsch synthesis process known as “cold catalysis” [304]. The concept leads to development of methods that optimize the entire process so as to converge on the idea of heating only the catalyst as and when needed, and designing it such that it can respond to sudden magnetic field variations. The non-contact nature of the heating process makes it cleaner, safer and long-lasting. Therefore, a proper design of inductive coil adaptive to catalyst structure needs to developed along with compatible support or susceptor that can heat the active material in the reactors.

1.2.5.1 Mechanism of IH Technology

In 1831, it was Michael Faraday who is accredited for discovering the basic mechanism and ideas governing formation of currents in a magnet. Later, Maxwell developed the theory of electromagnetism and James Joule postulated the basis of heating generated in a conductor due to current, thereby giving rise to the fundamentals of inductive heating. The underlying concept of IH is based on Faraday’s law which states that whenever an electrically conductive material is placed in an varying magnetic field, the RF energy generates heat energy. As far as early applications are considered, this method was proposed in 1887 by Sebastian Ferranti to melt metals. The application and scale-up went largely in the following years. But, World War II saw a boom in utilisation of IH technology in order to build huge quantities of materials and equipment with lesser manual labour and costs. The heat generated in magnetic induction system based reactors arises from three different sources: a) hysteresis losses in case of ferromagnetic materials (FM) [305], b) eddy current losses from electrically conductive materials [306], c) Neel and Brownian relaxations loss in superparamagnetic nanoparticles (SPM) [307].

1.2.5.1.1 Hysteresis Loss

The anisotropic nature of the magnetic domains in ferromagnetic materials give rise to hysteresis loss. A hysteresis loop is a term used to represent the non-linear magnetisation behaviour of such materials when exposed to an alternating magnetic field. The magnetic domains whose moments are along the external field axis tend to grow whereas the domains having opposite moments tend to shrink. This 'domain wall displacement' continues till the entire volume becomes a single domain. As seen from the **Figure 1.29**, these materials are characterized by remnant magnetization, M_r, which is the magnetization that remains after the removal of magnetic field (H=0) once the material reaches its magnetic saturation M_s, and the coercive field H_c which is the magnetic field required to demagnetise the material [308] . A magnetic field with amplitude twice that of the coercivity of the particles flips the magnetisation of the particles leading to heat dissipation. The heat generated is equal to the area under the hysteresis loop.

Thus, for a typical case of hysteresis loop generated heat, it is seen that when FM particles are subjected to an magnetic field of frequency f and amplitude $\mu_o H_{max}$, the amount of heat released can be defined by,

$$A = \int_{-H_{max}}^{+H_{max}} \mu_o M(H) dH \qquad \text{(Eq. 1.28)}$$

where, M is the magnetization and, μ_o is the relative permeability in air and, H is the applied magnetic field.

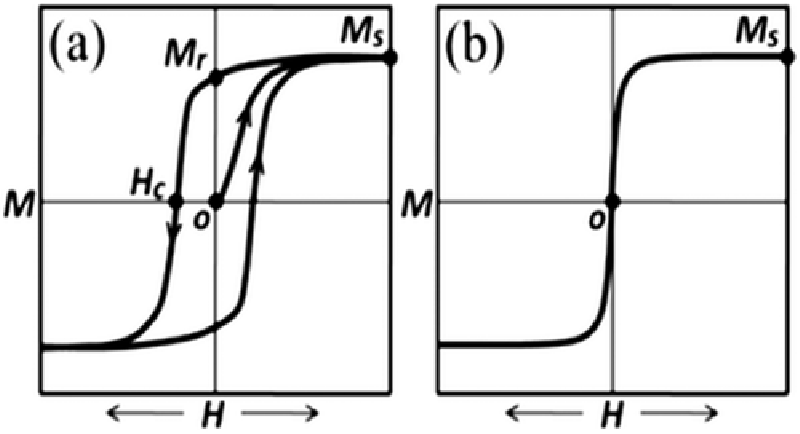

Figure 1.29 Schematic illustration of (a) exemplary hysteresis loop of an array of single domain FM NPs and (b) exemplary curve for a SPM sample. [308]

1.2.5.1.2 Eddy Current Loss

Eddy currents are basically swirling eddies which circulate on the conductor as a result of resonance. They are generated by the electromagnetic field induction leading to Joule heating of the material which is generally negligible because of nano-dimensions of the particles [309]. These are essentially loops of electric currents moving perpendicular to the applied magnetic field. These electrical loops generate magnetic field opposite to the initial magnetic field caused by the induction coil. It depends on the field frequency, permeability and electrical conductivity of the material. The heat generated by eddy current can be represented as,

$$ED = \frac{(\mu\pi d f H)^2}{20\,\rho} \qquad \text{(Eq. 1.29)}$$

where, μ is the permeability of a material, d is the diameter of the particle, and ρ is the resistivity of the material.

1.2.5.1.3 Relaxation Loss

When particles are restricted in volume to a certain size known as the critical domain size, $D_{critical}$, the magnetic domains of the particle tend away from anisotropy. The domains tend to coalesce and form one single giant magnetic domain that drives all the magnetic moments giving rise to a superparamagnet. This single large magnetic domain when subjected to an external alternating magnetic field rotates the magnetic moments with an energy E which is equivalent to the cross of anisotropy constant (K), and volume of the magnetic core (V_c), i.e. E~ KV_c. Such paramagnetic particles generate heat via two distinct relaxation mechanism, Néel relaxation and Brownian relaxation as shown in **Figure 1.30**.

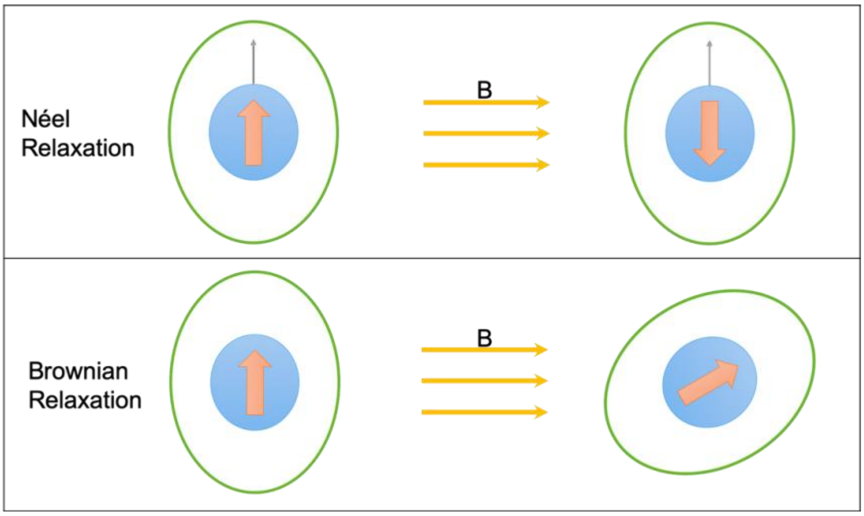

Figure 1.30 Different Types of relaxation losses

Néel relaxation refers to the change in the direction of magnetic spin moment as a result of applied magnetic field as shown in **Figure 1.30** [310]. It requires to overcome the magnetic anisotropy energy barrier which depends on the intrinsic properties of the material and the volume of the material behaving as single domain. The time constant for Néel relaxation is defined by,

$$\tau_N = \tau_0 e^{\frac{K V_m}{k_B T}} \qquad \text{(Eq. 1.30)}$$

where, τ_O is the relaxation factor (10-9 – 10-10 s), K is the magnetic anisotropy energy density, V_m is the mean particle volume, k_B is the Boltzmann constant, and T is the absolute temperature.

Brownian relaxation, on the other hand, is a form of rotational relaxation with reference to the magnetic field. The magnetic moment remains aligned with the magnetic field and rotates with changing magnetic field as **Figure 1.30** [311]. The rotation occurs as a result of the torque exerted of the magnetic moment by the applied field. During this process of rotation, it collides with neighbouring materials thereby generating heat. The Brownian relaxation time constant is defined by,

$$\tau_B = \frac{3\eta V_H}{k_B T} \qquad \text{(Eq. 1.31)}$$

where, η is the viscosity of the solvent, V_m is the hydrodynamic volume of the magnetic nanoparticles, k_B is the Boltzmann constant, and T is the absolute temperature.

The effective relaxation as a result of these two separate mechanisms if given by,

$$\tau_{eff} = \frac{\tau_N\ \tau_B}{(\tau_N + \tau_B)} \qquad \text{(Eq. 1.32)}$$

The heat dissipated is thus expressed as [312],

$$P = \pi\mu_0\chi_0 H_0 f \frac{2\pi f\tau_{eff}}{1+(2\pi f\tau_{eff})^2} \qquad \text{(Eq. 1.33)}$$

where, μ_0 is the permeability of free space, χ_0 is the magnetic susceptibility, $H_0$is the magnetic field intensity, f is the cyclic frequency.

1.2.5.2 IH for Gas-Phase Synthesis

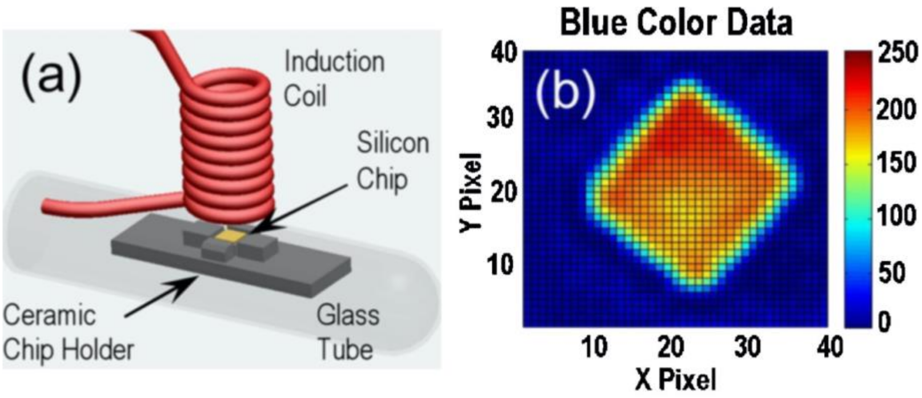

Figure 1.31 a) Schematic of Induction Heating based CNT synthesis, b) Temperature estimation along the reactor indicating heating of active material [315]

IH having the unique advantage of selective heating only the electroactive material in the active material is useful in synthesis of various materials, viz. large scale synthesis of SiC nanowires, Mo_2C thin films, carbon nanotubes and high-quality graphene [313-317]. This method is inherently cost-effective as the heat removal is easier and faster as heating is local to the catalyst inside and not the entire reactor used in conventional methods. IH helps control the growth mechanism and morphology of such materials as shown in **Figure 1.31**. It has enabled to obtain vertically obtained carbon nanotubes of high growth rate of about 200 µm min^{-1} [315].

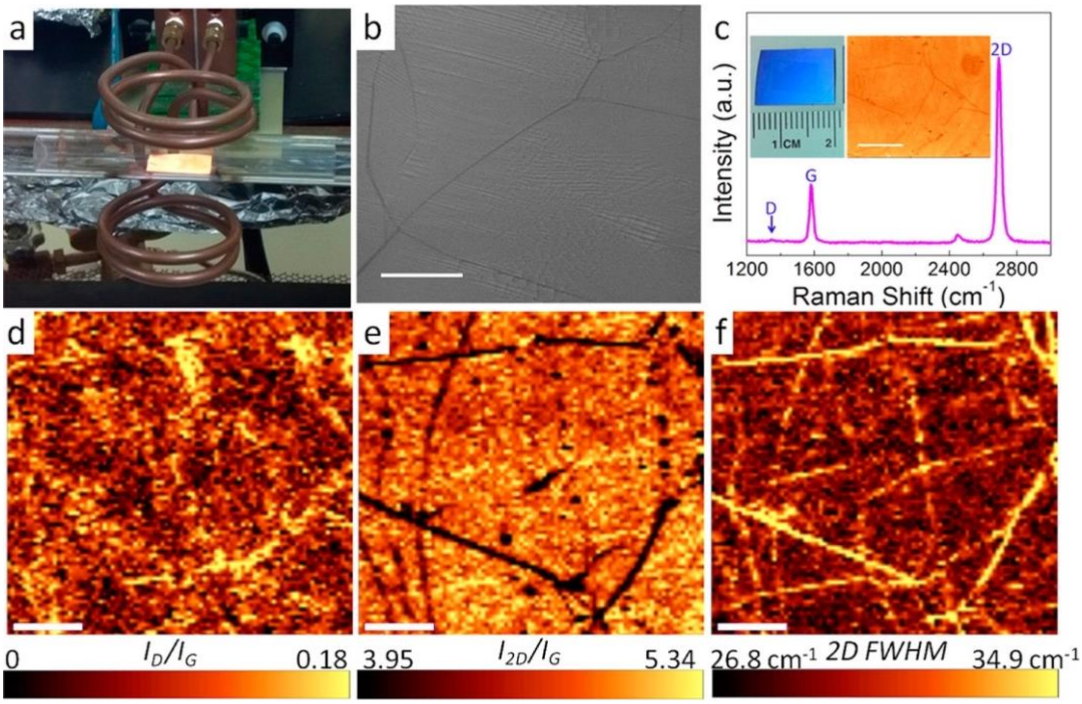

Figure 1.32 a) IH setup. (b) SEM image of as-grown monolayer graphene on copper foil substrate (Scale bar is 3 µm). (c) Raman spectrum of Graphene sheets. Insets are photograph and optical microscopic image (scale bar is 20 µm) of transferred graphene on a SiO_2/Si substrate.(d–f) Raman mapping of transferred graphene film with different intensity band ratios(Scale bars are 6 µm) [323]

It has been proved that IH provides a more uniform heating giving rise to better quality of CNTs opposed to conventional heating methods used earlier [318, 319]. IH helps achieve CNTs with controlled diameter, homogenous diameter dispersion and high graphitization. The CNTs, thus have been grown with definite diameters by usage of size-classified Ni NPs [318]. Similarly, a RF induction based CVD using Fe:Co:$CaCO_3$ catalyst has been able to synthesize CNTs with external to internal diameter ratio in the range of 2-2.5 [319]. This study also confirmed that the CNTs grown via IH have smaller external diameters, lesser walls and very high aspect ratio in the range of hundreds. It also reduces the overall energy consumption and time required for overall reaction thereby helping decrease the price. Highly pure CNTs (95%) with internal diameter ranging from 0.8-1 nm have also been produced at low temperature via

IH [320]. This revealed that shorter time frame for reaching the reaction temperature avoids dimensional growths of metal active sites. It also emphasized on the fact that the atomic hydrogen and OH radicals formed out of the reactant stream have an etching effect on the weakly bonded amorphous carbon giving path to formation of hydrocarbons at high temp. IH has been instrumental also in production of high-quality monolayer and few-layer graphene on various metal substrates as it requires fast ramp to achieve a small time frame for heating thereby making sure unplanned growth of multiple layers is avoided. However, the decomposition of reactants during the cooling process can still affect the quality of graphene produced [321]. Helmholtz like geometry setup is generally utilized in IH to obtain a uniform perpendicular magnetic field as shown in **Figure 1.32(a)** for a copper substrate [322].Such a setup ensures passage of maximum amount of magnetic field lines across the reacting surface of the Cu substrate thereby requiring lower frequency and power for operation and graphene deposition. **Figure 1.32 (b,c)** shows the graphene film formed by IH with Cu metal steps and the typical Raman spectra for monolayer graphene. The Raman mapping in **Figure 1.32 (d-f)** shows low I_D/I_G ratio and high I_{2D}/I_G ratio which is indicative of high quality monolayer graphene film.

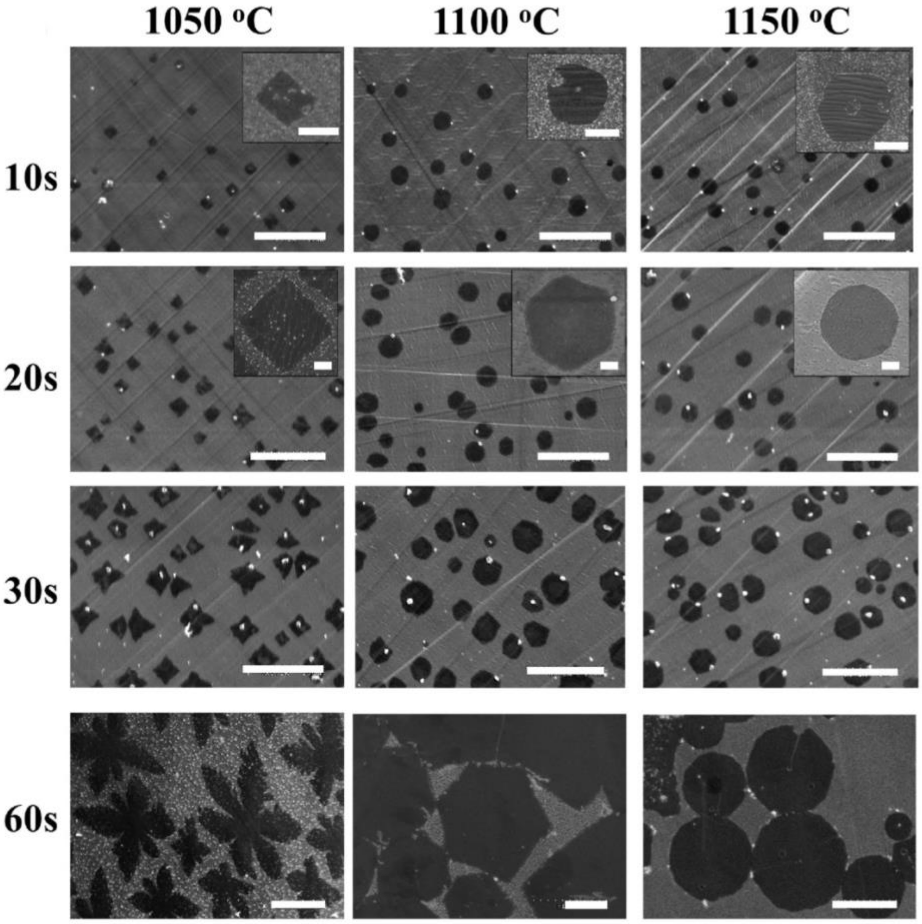

Figure 1.33 SEM images of graphene domains grown on Cu at different growth temperatures and times. Scale bar: 10 μm; inset scale bar: 500 nm [323]

The graphene films with enhanced field effect mobility (FET) (~ 14000 $cm^2V^{-1}s^{-1}$ under ambient conditions on conventional SiO_2/Si substrate) have also been obtained on similar Cu foils with 240 kHz frequency IH input. Such properties of the graphene produced by IH were definitely a step-up from the hot-wall furnace setups (using similar substrate and reaction conditions) of the ambient pressure based CVD (APCVD) and low-pressure CVD (LPCVD). IH has been effective for single crystalline graphene synthesis with controlled grain size and morphology as seen in **Figure 1.33** [323]. IH has made it feasible to have a real-time understanding of the reaction parameters on the growth of the graphene. This enabled researcher to confirm that the graphene nucleation occurs only in the initial time frame and is dependent on the surface state of the Cu substrate. Subsequently, the domain density is independent of the growth temperature as proposed earlier [324]. Rather, it undergoes the surface-limiting effect to have the defined structures.

1.2.5.3 IH for Methanation Reaction

Methanation via IH is still at a very nascent stage as very few research works have been focused on this since the idea of "cold catalysis" was floated [266, 267, 325-327]. Methanation being an exothermic reaction, IH is particularly helpful in avoiding large temperature gradients in the reactor. Soon after the proof-of-concept suggested in 2015, Iron-Carbide nanoparticles (ICNPs) have been used for CO_2 hydrogenation with exceptionally high heating power [325]. These NPs have high heat capacities which could be easily realised via Inductive heating. They have been coated with Ni for methanation with a conversion of 50% but low CH_4 yield. The induced heat on these ICNPs activated the Ru NPs at relatively low amplitude (< 30 mT). This ICNP support has been used later along with Ni, Co to obtain 90% conversion and high selectivity [326]. Optimizations have been done so as to reduce the magnetic field and amount of catalyst to be used. An increase in temperature causes reduction in the heating power of magnetic materials leading to zero as it reaches to Curie temperature. The curie temperature for FeC_x materials is close to 450ºC, is dependent on the exact stoichiometry. Co, on the other hand, is a hard material having a high curie temperature (T_c > 1000ºC) which makes it inefficient for heating magnetic materials. But a mixture of ICNPs and Co nanorods gives rise to reduction in the anisotropy of the system thereby making it viable for IH at lower temperature.

Engineering of bimetallic $Fe_{30}Ni_{70}$ NPs have been able to achieve 100% conversion and selectivity, although the catalyst loses stability over time [266]. Proper engineering of these bimetallic NPs enabled them for good heating properties at lower magnetic field strengths, which thereby improves the energy efficiency of the entire system. Cobalt ferrite and core-shell based $CoFe_2O_4–Fe_3O_4$ have also proved to have good heating abilities [267].

They were further mixed with Ni/Ni/SiRAlOx to obtain CFO/Ni/S and CFO@FO2/Ni/S catalytic systems which provide about 95% conversion without any signs of sintering at temperatures ranging 400-440ºC as shown in **Figure 1.34**. The thickness of the shell has been found to influence the heating power of the material at various magnetic field intensities. A recent report indicates that a highly Ni loaded γ-alumina can be used in the IH setup for a low temperature methanation at about 210ºC with a conversion of 95% at a GHSV of 20,000 mL g^{-1} h^{-1} [327] Ni has been used on oxidised carbon-felt disks (OCF) to obtain 74% conversion and 97% selectivity at 320ºC [327]. OCF is found to be a good susceptor material for inductive heating setup. The carbon supports for methanation reactions have been scarcely studied although they possess high heat conductivity and are well suited for induction. Thus it indicates that further investigations for carbon based materials is needed for finding more cost effective and high heat capacity supports which require lower metal loading to achieve higher catalytic activity and selectivity.

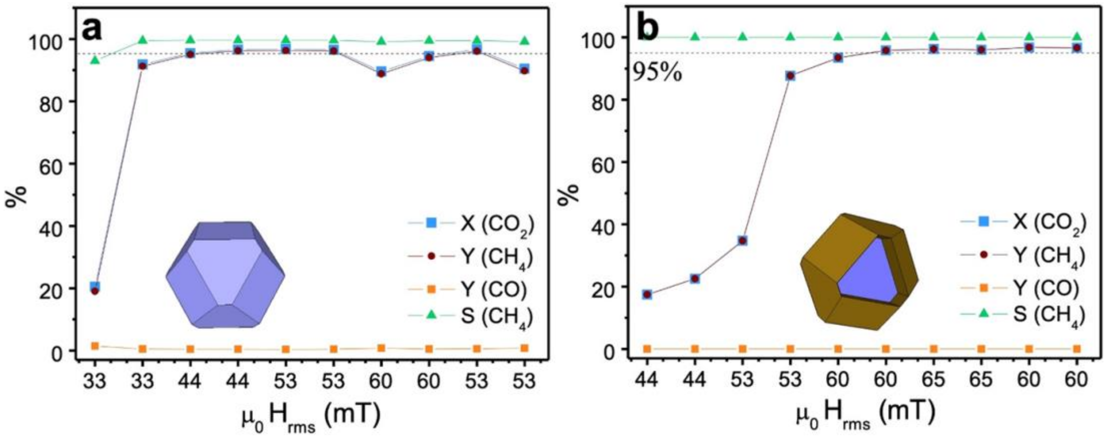

Figure 1.34 Percentage of CO_2 conversion, CH_4 and CO yields, and CH_4 selectivity as a function of $\mu_0 H_{rms}$ for, a) CFO/Ni/S and, b) CFO@FO2/Ni/S systems. Sketches in blue and in blue-brown represent the single $Co_{0.6}Fe_{2.4}O_4$ phase and the core–shell $Co_{0.6}Fe_{2.4}O_4$@ Fe_3O_4 cuboctahedron employed for the heating, respectively. Dashed lines indicate the 95 % level [267].

1.3 Scope and Outline of the Thesis

Structuration of graphene based materials is the cornerstone to deal with the energy storage and conversion issues. A proper utilization of REs requires better supercapacitors which demand for maximum utilization of graphene based materials which have theoretically very high charge storage properties. Besides, they can be an essential component in the PtG schematic which can decrease the energy loss and provide methane in a much cheaper manner which can be directly injected or stored for further utilisation. This thesis deals with the structure tailoring of graphene based materials so that it can utilize the maximum potential for supercapacitor applications as well as for a good support for methanation via inductive heating process with high capacity and low heat wastage.

Chapter 2 summarizes the synthesis of aligned few-layer-graphene based materials which can be used for supercapacitor applications. The goal has been to improve the intrinsic capacitance by modification of the synthesis parameters so as to reach the maximum capacitance of graphene envisaged earlier. Further, the textural and electrochemical properties have been fully investigated and discussed. The contribution of pseudocapacitance and electrical double layer capacitance has been found out theoretically to better understand the synthesized materials.

Chapter 3 emphasizes on utilisation of few-layer-graphene for synthesis of flat Fe NPs which can be used for catalytic applications. It discusses two main approaches for the formation of flat Fe-NPs (with increased aspect ratio) over FLG..

Chapter 4 deals with the effect of growth parameters of CNFs grown on few-layer-graphene to be used as a prospective support for methanation based on inductive heating technology. It discusses the efficiency of these composites in Inductive Heating and Joule Heating setup. Further, it identifies how the dispersion and metal NP-carbon morphology changes with increase in metal loading thereby affecting the heating limitations.

Chapter 5 draws a conclusion to all the research work carried out during the thesis. It gives an idea about the methods and process for structuration of FLG materials depending on its specific applications. It further provides a perspective into future strategies that can be implemented to improve the efficiency and curtail it for industrial usage.

References

[1] U.S. Energy Information Administration (EIA), International Energy Outlook 2019 (IEO2019), https://www.eia.gov/todayinenergy/detail.php?id=41433, (accessed: July, 2020)

[2] IEA, Total primary energy supply by fuel, 1971 and 2017, IEA, Paris https://www.iea.org/data-and-statistics/charts/total-primary-energy-supply-by-fuel-1971-and-2017, (accessed: July, 2020)

[3] T. R. Karl, K. E. Trenberth, *Science*, 2013, Vol. 302, 5651, 1719-1723

[4] N. Abas, A. Kalair, N. Khan, *Futures*, 2015, Vol. 69, 31-49

[5] An Analysis of Amazonian Forest Fires, Matthew Stewart, Nov 2019, https://towardsdatascience.com/an-analysis-of-amazonian-forest-fires-8facca63ba69 (accessed: July, 2020)

[6] IEA (2020), Global Energy Review 2020, IEA, Paris https://www.iea.org/reports/global-energy-review-2020, (accessed: July, 2020)

[7] IEA (2019), Renewables 2019, IEA, Paris https://www.iea.org/reports/renewables-2019, (accessed: July, 2020)

[8] European Commission, A European Green Deal, https://ec.europa.eu/info/strategy/priorities-2019-2024/european-green-deal_en, (accessed: July, 2020)

[9] McKinsey & Company, Recharging economies: The EV-battery manufacturing outlook for Europe, https://www.mckinsey.com/industries/oil-and-gas/our-insights/recharging-economies-the-ev-battery-manufacturing-outlook-for-europe, (accessed: July, 2020)

[10] H. Chen, T. N. Cong, W. Yang, C. Tan, Y. Li, Y. Ding, *Prog. Nat. Sci.*, 2009, Vol. 19, 3, 291-312

[11] J. Vimpari, S. Junnila, *Energy*, 2019, Vol. 172, 1087-1097

[12] T. H. J. Inderberg, H. Rognstad, I.-L. Saglie, L. H. Gulbrandsen, *Energy Res. Soc. Sci.*, 2019, Vol. 52, 181-191

[13] B. Sivaneasan, M. L. Lim, K. P. Goh, *Energy Procedia*, 2017, Vol. 143, 2017, 210-215

[14] S Hong, T. Yang, H. J. Chang, S. Hong, *Energy Policy*, 2020, Vol. 138, 111233

[15] N. Phuangpornpitak, S. Tia, *Energy Procedia*, 2013, Vol. 34, 282-290

[16] T. Fiedler, *Renew. Energy*, 2019, Vol. 130, 319-328

[17] N. Pearre, L. Swan, *Energy*, 2020, Vol. 203, 117917

[18] M. Shahbaz, C. Raghutla, K. R. Chittedi, Z. Jiao, X.V. Vo, *Energy*, 2020, Vol. 207, 118162

[19] D. Timmons, K. Elahee, M. Lin, *Solar Energy*, 2020, Vol. 206, 171-180

[20] K. Saidi, A. Omri, *Prog. Nucl. Energy*, 2020, Vol. 126, 103425

[21] R. Rehan, M. Nehdi, *Environ. Sci. Policy*, 2005, Vol. 8, 2, 105-114

[22] A. R. Holdway, A. R. Williams, O. R. Inderwildi, D. A. King, *Energy Environ. Sci.*, 2010, Vol. 3, 1825-1832

[23] U.S. Energy Information Administration, International Energy Outlook 2019, https://www.eia.gov/outlooks/ieo/pdf/ieo2019.pdf, (accessed: July, 2020)

[24] M. Bui, C. S. Adjiman, A. Bardow, E. J. Anthony, A. Boston, S. Brown, P. S. Fennell, S. Fuss, A. Galindo, L. A. Hackett, J. P. Hallett, H. J. Herzog, G. Jackson, J. Kemper, S. Krevor, G. C. Maitland, M. Matuszewski, I. S. Metcalfe, C. Petit, G. Puxty, J. Reimer, D. M. Reiner, E. S. Rubin, S. A. Scott, N. Shah, B. Smit, J. P. M. Trusler, P. Webley, J. Wilcoxx, N. M. Dowell, *Energy Environ. Sci.*, 2018, Vol. 11, 1062-1176

[25] N. Assen, J. Junga, A. Bardow, *Energy Environ. Sci.*, 2013, Vol. 6, 2721-2734

[26] P. Markewitz, W. Kuckshinrichs, W. Leitner, J. Linssen, P. Zapp, R. Bongartz, A. Schreibera, T. E. Müller, *Energy Environ. Sci.*, 2012, Vol. 5, 7281-7305

[27] M. F.-Granobles, M. Saeys, *Energy Environ. Sci.*, 2020, Vol. 13, 1923-1932

[28] R. Snoeckx, A. Bogaerts, *Chem. Soc. Rev.*, 2017, Vol. 46, 5805-5863

[29] Y. Liu, J.-l. Du, *J. Clean. Prod.*, 2020, Vol. 277, 122183

[30] T. M. Gur, *Energy Environ. Sci.*, 2018, Vol. 11, 2696-2767

[31] The Nobel Prize 2019, https://www.nobelprize.org/prizes/chemistry/2019/press-release/, (accessed: July, 2020)

[32] John B. Goodenough, *Acc. Chem. Res.*, 2013, Vol. 46, 5, 1053-1061

[33] K. Amine, R. Kanno, Y. Tzeng, *MRS Bulletin*, 2014, Vol. 39, 5, 395-401

[34] P. Tan, H. R. Jiang, X. B. Zhu, L. An, C. Y. Jung, M. C. Wu, L. Shi, W. Shyy, T. S. Zhao, *Appl. Energy*, 2017, Vol. 204, 780-806

[35] L. Ye, Y. Hong, M. Liao, B. Wang, D. Wei, H. Peng, L. Ye, Y. Hong, M. Liao, B. Wang, D. Wei, H. Peng, *Energy Storage Mater.*, 2020, Vol. 28, 364-374

[36] J. Zhou, J. Cheng, B. Wang, H. Peng, J. Lu , *Energy Environ. Sci.*, 2020,Vol. 13, 1933-1970

[37] D. Larcher, J-M. Tarascon, *Nat. Chem.*, 2015, Vol. 7, 19-29

[38] P. Simon, Y. Gogotsi, B. Dunn, *Science*, 2014, Vol. 343, 6176, 1210-1211

[39] Z. Lin, E. Goikolea, A. Balducci, K. Naoi, P. L. Taberna, M. Salanne, G. Yushin, P. Simon, *Mater. Today*, 2018, Vol. 21, 4, 419-436

[40] B. E. Conway. Springer US, 1999. ISBN: 978-0-306-45736-4, DOI:10.1007/978-1-4757-3058-6

[41] P. Simon, Y. Gogotsi, *Nat. Mat.*, 2008, Vol. 7, 845–854

[42] Z. L. Wang, *Nano Today*, 2010, Vol. 5, 540

[43] N. Choudhary, C. Li, J. Moore, N. Nagaiah, L. Zhai, Y. Jung, J. Thomas, *Adv. Mater.*, 2017, Vol. 29, 1605336

[44] J. German, Hybrid Vehicles: Technology Development and Cost Reduction, ICCT technical Brief No. 1, July 2015

[45] Maxwell Technologies, Inc., http://www.maxwell.com/solutions/transportation/auto/start-stop-micro-hybrid (accessed: July, 2020).

[46] E. Naswali, C. Alexander, H. Y. Han, D. Naviaux, A. Bistrika, A. V. Jouanne, A. Yokochi, T. K. A. Brekken, *IEEE Energy Conversion Congress*, 2011, 298

[47] Zapgo, https://zapgo.com/technology/ (accessed: July, 2020).

[48] Y. Wang, Y. Song, Y. Xia, *Chem. Soc. Rev.*, 2016, Vol. 45, 21, 5925-5950

[49] Y. Shao, M. F. El-Kady, J. Sun, Y. Li, Q. Zhang, M. Zhu, H. Wang, B. Dunn, R. B. Kaner, *Chem. Rev.*, 2018,Vol. 118, 9233-9280

[50] J. R. Miller, P. Simon, *Science*, 2008, Vol. 321, 5889, 651-652

[51] B. E. Conway, V. Birss, J. Wojtowicz, *J. Power Sources*, 1997, Vol. 66, 1-14

[52] L. L. Zhang, X. S. Zhao, *Chem. Soc. Rev.*, 2009, Vol. 38, 2520-2531

[53] H. Jiang, P. S. Lee, C. Li, *Energy Environ. Sci.*, 2013,Vol. 6, 41-53

[54] K. Chen, S. Song, F. Liu, D. Xue, *Chem. Soc. Rev.*, 2015, Vol. 44, 6230

[55] G. Wang, L. Zhang, J. Zhang, *Chem. Soc. Rev.*, 2012, Vol. 41, 797-828

[56] J. P. Zheng, J. Huang, T. R. Jow, *J. Electrochem. Soc.*, 1997, Vol. 144, 2026-2031

[57] W. Sugimoto, H. Iwata, Y. Murakami, Y. Takasu, *J. Electrochem. Soc*., 2004, Vol. 151, 8

[58] Z. J. Han, S. Pineda, A. T. Murdock, D. H. Seo, K. Ostrikovba, A. Bendavida, *J. of Mat. Chem. A*, 2017, Vol. 5, 17293-17301

[59] M.-S. Wu, P.-C. J. Chiang, *Electrochem. Solid State Lett.*, 2004, Vol. 7, 6, A123-A126

[60] Q.-Z. Zhang, D. Zhang, Z.-C. Miao, X.-L. Zhang, S.-L. Chou, *Small*, 2018, Vol. 14, 24, 1702883

[61] X. Hu, L. Wei, R. Chen, Q. Wu, J. Li, *Chem. Select*, 2020, Vol. 5, 17, 5268-5288

[62] E. Herrero , L. J. Buller, H. D. Abruña, *Chem. Rev.*, 2001, Vol. 101 , 1897-1930

[63] C. Choi, D. S. Ashby, D. M. Butts, R. H. DeBlock, Q. Wei, J. Lau, B. Dunn, *Nat. Rev. Mater*, 2020, Vol. 5, 5-19

[64] J. W. Kim, V. Augustyn, B. Dunn, *Adv. Energy Mat.*, 2012, Vol. 2, 141-148

[65] B. E. Conway, *Electrochim. Acta*, 1993, Vol. 38, 9, 1249-1258

[66] B. E. Conway, *J. Electrochem. Soc.*,1991, Vol. 138, 1539-1548

[67] H. Lindstrom, S. Sodergren, A. Solbrand, H. Rensmo, J. Hjelm, A. Hagfeldt, S. E. Lindquist, *J. Phys. Chem. B*, 1997, Vol. 101 , 7717-7722

[68] T. Brezesinski, J. Wang, S. H. Tolbert, B. Dunn, *Nat. Mater.*, 2010, Vol. 9, 146-151

[69] J. Wang, J. Polleux, J. Lim, B. Dunn, *J. Phys. Chem. C*, 2007, Vol. 111, 40, 14925-14931

[70] Y. Gogotsi, R. M. Penner, *ACS Nano*, 2018,Vol. 12, 3, 2081-2083

[71] M. Winter, R.J. Brodd, *Chem. Rev.*, 2004, Vol. 104, 4245-4269

[72] J. Xie, P. Yang, Y. Wang, T. Qi, Y. Lei,C. M. Li, *J. Power Sources*, 2018, Vol. 401, 213-223

[73] A. J. Bard, L. R. Faulkner, John Wiley & Sons: New York, 2001, ISBN: 978-0-471-04372-0.

[74] L. Xie, F. Su, L. Xie, X. Guo, Q. Kong, G. Sun, A. Ahmad, X. Li, Z. Yi, Z. Wang, C. Chen, *Mater. Chem. Front.*, 2020, DOI: 10.1039/D0QM00180E

[75] H. V. Helmholtz, *Ann. Phys.*, 1853, Vol. 165, 7, 353-377

[76] H. V. Helmholtz, *Ann. Phys.*, 1879, Vol. 243, 7, 337-382.\

[77] H. Wang, H., L. Pilon, *J. Phys. Chem. C*, 2011, Vol. 115, 33, 16711-16719

[78] J. Kang, J. Wen, S. H. Jayaram, A. Yu, X. Wang, *Electrochim. Acta*, 2014, Vol. 115, 587-598

[79] G. Dai, L. Zhang, Y. Liao, Y. Shi, J. Xie, F. Lei, L. Fan, *J. Phys. Chem. C*, 2020, Vol. 124, 7, 3952-3961

[80] F. Béguin, V. Presser, A. Balducci, E. Frackowiak, *Adv. Mat.*, 2014, Vol. 26, 2219-2251

[81] M. Gouy, *J. Phys. Theor. Appl.*, 1910, Vol. 9, 1, 457-468

[82] D. L. Chapman, *The London, Edinburgh, Dublin Philos. Mag. J. Sci.*, 1913, Vol. 25, 148, 475-481

[83] J. H. Masliyah, S. Bhattacharjee, *Electrokinetic and Colloid Transport Phenomena*, 2006

[84] E. Gongadze, S. Petersen, U. Beck, U. van Rienen, *Excerpt from the Proceedings of the COMSOL Conference*, Milan, 2009

[85] J. Varghese, H. Wang, L. Pilon, *J. Electrochem. Soc.*, 2011, Vol. 158, A1106

[86] O. Stern, *Z. Elektrochem. Angew. Phys. Chem.*,1924, Vol. 30, 508-516

[87] D. C. Grahame, *Chem. Rev.*, 1947, Vol. 41, 441-501

[88] C. Zhong, Y. Deng, W. Hu, J. Qiao, L. Zhang, J. Zhang, *Chem. Soc. Rev.*, 2015, Vol. 44, 7484-7539

[89] E. Frackowiak, F. Beguin, *Carbon*, 2001, Vol. 39, 937-950

[90] P.L. Taberna, P. Simon, J. F. Fauvarque, *J. Electrochem. Soc.*, 2003, Vol. 150, A292

[91] Z. Yu, L. Tetard, L. Zhaia, J. Thomas, *Energy Environ. Sci.*, 2015, Vol. 8, 702-730

[92] S. Kumar, G. Saeed, L. Zhu, K. N. Hui, N. H. Kim, J. H. Lee, *Chem. Eng. J.*, 2021, Vol. 403, 126352

[93] Y. Liu, B. Réty, C.M. Ghimbeu, B. S.-Guillous, P.L. Taberna, P. Simon, *J. Power Sources*, 2019, Vol. 434, 226734

[94] C. Li, X. Zhang, K. Wang, F. Su, C.-M. Chen, F. Liu, Z.-S. Wu, Y. Ma,, *J. Energy Chem.*, 2021, Vol. 54, 352-367

[95] M. F. El-Kady, Y.L. Shao, R.B. Kaner, *Nat. Rev. Mater.*, 2016, Vol. 1, 16033

[96] A. C. Forse, C. Merlet, J. M. Griffin, C. P. Grey, *J. Am. Chem. Soc.*, 2016, Vol. 138, 18, 5731-5744

[97] B. Xu, S. Hou, H. Duan, G. Cao, M. Chu, Y. Yang, *J. Power Sources*, 2013, Vol. 228, 193-197

[98] T. Kim, G. Jung, S. Yoo, K. S. Suh, R. S. Ruoff, *ACS Nano*, 2013, Vol. 7, 6899-6905

[99] M. Inagaki, H. Konno, O. Tanaike, *J. Power Sources*, 2010, Vol. 195, 7880-7903

[100] B. Guo, Q. Liu, E. Chen, H. Zhu, L. Fang, J. R. Gong, *Nano Lett.*, 2010, Vol. 10, 4975-4980

[101] P. Simon, Y. Gogotsi, *Acc. Chem. Res.*, 2013, Vol. 46, 5, 1094-1103

[102] X. Li, B. Wei, *Nano Energy*, 2013, Vol. 2, 159-173

[103] X. Yang, L. Zhao, J. Lian, *J. Power Sources*, 2017, Vol. 343, 373-382

[104] H. Zhang , G. Cao , Z. Wang , Y. Yang , Z. Shi and Z. Gu , *Electrochem. Commun.*, 2008, Vol. 10, 1056-1059

[105] C. Hu, L. Song, Z. Zhang, N. Chen, Z. Feng, L. Qu, *Energy Environ. Sci.*, 2015, Vol. 8, 31-54

[106] P. Xiong, J. Zhu, L. Zhang, X. Wang, *Nanoscale Horiz.*, 2016, Vol. 1, 340

[107] M. Sevilla, R. Mokaya, *Energy Environ. Sci.*, 2014, Vol. 7, 1250-1280

[108] M. R. Benzigar, S. N. Talapaneni, S. Joseph, K. Ramadass, G. Singh, J. Scaranto, U. Ravon, K. A.-Bahily, A. Vinu, *Chem. Soc. Rev.*, 2018, Vol. 47, 2680-2721

[109] K. S. Novoselov, A. K. Geim, S. V. Morozov, D. Jiang, Y. Zhang, S. V. Dubonos, I. V. Grigorieva, A. A. Firsov, *Science*, 2004, Vol. 306, 5696, 666-669

[110] K. S. Novoselov, D. Jiang, F. Schedin, T. J. Booth, V. V. Khotkevich, S. V. Morozov, A. K. Geim, *Proc. Natl Acad. Sci. USA*, 2005, Vol. 102, 30, 10451-10453

[111] P. R. Wallace, *Phys. Rev.*, 1947, Vol. 71, 622-634

[112] J. C. Slonczewski, P. R. Weiss, *Phys. Rev.*, 1958, Vol. 109, 272-279

[113] A. K. Geim, K. S. Novoselov, *Nat. Mater.*, 2007, Vol. 6, 183

[114] M. I. Kairi, S. Dayou, N. I. Kairi, S. A. Bakar, B. Vigolo, A. R. Mohamed, *J. Mater. Chem. A*, 2018, Vol. 6, 15010-15026

[115] C. Lee, X. Wei, J. W. Kysar, J. Hone, *Science*, 2008, Vol. 321, 385-388

[116] A. A. Balandin, S. Ghosh, W. Bao, I. Calizo, D. Teweldebrhan, F. Miao, C. N. Lau, *Nano Lett.*, 2008, Vol. 8, 3, 902-907

[117] J. Haskins, A. Kınacı, C. Sevik, H. Sevinçli, G. Cuniberti, T. Cağın, *ACS Nano*, 2011, Vol. 5, 3779-3787

[118] J. C. Meyer, A. K. Geim, M. I. Katsnelson, K. S. Novoselov, T. J. Booth, S. Roth, *Nature*, 2007, Vol. 446 , 60-63

[119] *Energy Environ. Sci.*, 2013,6, 1388-1414

[120] S. Latil, V. Meunier, L. Henrard, *Phys. Rev. B*, 2007, Vol. 76, 20

[121] T. Ohta , A. Bostwick , T. Seyller , K. Horn, E. Rotenberg , *Science*, 2006, Vol. 313 , 951-954

[122] M. J. McAllister, J.-L. Li, D. H. Adamson, H. C. Schniepp, A. A. Abdala, J. Liu, M. H.-Alonso, D. L. Milius, R. Car, R. K. Prud'homme, I. A. Aksay, *Chem. Mater.*, 2007, Vol. 19, 18, 4396-4404

[123] W. Yuan, Y. Zhou, Y. Li, C. Li, H. Peng, J. Zhang, Z. Liu, L. Dai, G. Shi, *Sci. Rep.*, 2013, Vol. 3, 2248

[124] C Liu, Z Yu, D Neff, A Zhamu, BZ Jang, *Nano Lett.*, 2010, Vol.10, 4863-4868

[125] A. S. Lemine, M. M. Zagho, T. M. Altahtamouni, N. Bensalah, *Int J Energy Res.*, 2018, Vol. 42, 4284-4300.

[126] H. B. Huang, H. D. Shi, P. Das, J. Q. Qin, Y. G. Li, X. Wang, F. Su, P. C. Wen, S. Y. Li, P. F. Lu, F. Y. Liu, Y. J. Li, Y. Zhang, Y. Wang, Z. S.Wu, H. -M. Cheng, *Adv. Funct. Mater.*, 2020, Vol. 30, 1909035

[127] Q. Ke, J. Wang, *J. Materiomics*, 2016, Vol. 2, 1, 37-54

[128] X. Cao, Y. Shi, W. Shi, G. Lu, X. Huang, Q. Yan, Q. Zhang, H. Zhang, *Small*, 2011, Vol. 7, 22, 3163-3168

[129] C. Wang, V. Strauss, R. B. Kaner, *Trends Chem.*, 2019, Vol. 1, 9, 858-868

[130] Y. Meng, Y. Zhao, C. Hu, H. Cheng, Y. Hu, Z. Zhang, G. Shi, L. Qu, *Adv. Mater.*, 2013, Vol. 25, 2326-2331

[131] B. Fang, D. Chang, Z. Xu, C. Gao, *Adv. Mater.*, 2019, Vol. 32, 5

[132] G. Shi, L. Zhang, *J. Phys. Chem. C*, 2011, Vol. 115, 34,17206-17212

[133] L. Kou, T. Huang, B. Zheng, Y. Han, X. Zhao, K. Gopalsamy, *Nat. Commun.*, 2014, Vol. 5, 3754

[134] R. Karthick, F. Chen, *Carbon*, 2019, Vol. 150, 292-310

[135] F. Gӧnes, H. J. Shin, C. Biswas, G. H. Han, E. S. Kim, S. J. Chae, J.-Y. Choi, Y. H. Lee, *ACS Nano*, 2010, Vol. 4, 4595-4600

[136] S. Gan, L. Zhong, T. Wu, D. Han, J. Zhang, J. Ulstrup, Q. Chi, L. Niu, *Adv. Mater.*, 2012, 24, 3958-3964

[137] D. Li, M. B. Muller, S. Gilje, R. B. Kaner, G. G. Wallace, *Nat. Nanotechnol.*, 2008, Vol. 3, 101-105

[138] Z. Lei, N. Christov, X.S. Zhao, *Energy Environ. Sci.*, 2011, Vol. 4, 1866-1873

[139] C. Liu, Z. Yu, D. Neff, A. Zhamu, B.Z. Jang, *Nano Lett.*, 2010, Vol. 10, 4863-4868

[140] L. Qiu, X. Yang, X. Gou, W. Yang, Z.F. Ma, G.G. Wallace, D. Li, *Chem. Eur. J.*, 2010, Vol. 16, 10653-10658

[141] M. Li, Z. Tang, M. Leng, J. Xue, *Adv. Funct. Mater.*, 2014, Vol. 24, 7495-7502

[142] C. Emmenegger, P. Mauron, P. Sudan, P. Wenger, V. Hermann, R. Gallay, A. Züttel, *J. Power Sources*, 2003, Vol. 124, 1, 321-329

[143] J. Mao, J. Iocozzia, J. Huang, K. Meng, Y. Lai, Z. Lin, *Energy Environ. Sci.*, 2018, Vol. 11, 772-799

[144] G. Moussa, S. H.-Garreau, P.-L. Taberna, P. Simon, C. M. Ghimbeu, *C*, 2018, Vol. 4, 20

[145] M. Tynan, D. Johnson, B. Dobson, K. Coleman, *Nanoscale*, 2016, Vol 8, 13303-13310

[146] Z. Chen, W. Ren, L. Gao, B. Liu, S. Pei, H.-M. Cheng, *Nat. Mater.*, 2011, Vol. 10, 424-428

[147] Q. Zhang, F. Zhang, S. P. Medarametla, H. Li, C. Zhou, D. Lin, *Small*, 2016, Vol. 12, 1702-1708

[148] C. Zhu, T. Liu, F. Qian, T. Y. Han, E. B. Duoss, J. D. Kuntz, C. M. Spadaccini, M. A. Worsley, Y. Li, *Nano Lett.*, 2016, Vol. 16 , 3448-3456

[149] D. A. C. Brownson , S. A. Varey , F. Hussain , S. J. Haigh, C. E. Banks , *Nanoscale*, 2014, Vol. 6 , 1607-1621

[150] L. Zhou, L. Fox, M. Włodek, L. Islas, A. Slastanova, E. Robles, O. Bikondoa, R. Harniman, N. Fox, M. Cattelan, W. H. Briscoe, *Carbon*, 2018, Vol. 136, 255-261

[151] M. Terrones, A. R. B.-Mendez, J. C.-Delgado, F. L.-Urias, Y. I. V.-Cantu, F. J. R.-Macias, A. L. Elias, E. M.-Sandoval, A. G. C.-Marquez, J. C. Charlier, H. Terrones, *Nano Today*, 2010, Vol. 5, 351-372

[152] J. Azadmanjiri, V. K. Srivastava, P. Kumar, M. Nikzad, J. Wang, A. Yu, *J. Mater. Chem. A*, 2018, Vol. 6, 702-734

[153] H. J. Park, J. Meyer, S. Roth, V. Skákalová, *Carbon*, 2010, Volume 48, 4, 1088-1094

[154] W. Wang, S. Guo, M. Penchev, I. Ruiz, K. N. Bozhilov, D. Yan, M. Ozkan, C. S. Ozkan, *Nano Energy*, 2013, Vol. 2, 2, 294-303

[155] Z. Yan, W. Yao, L. Hu, D. Liu, C. Wang, C.-S. Lee, *Nanoscale*, 2015,7, 5563-5577

[156] L. Zheng , G. Zhang , M. Zhang , S. Guo, Z. H. Liu , *J. Power Sources*, 2012, Vol. 201, 376-381

[157] X. Yang, X. Dou, A. Rouhanipour, L. Zhi, H. J.Räder, K. Müllen, *J. Am. Chem. Soc.*, 2008, Vol. 130, 13, 4216-4217

[158] P. Y. Huang, C. S. Ruiz-Vargas, A. M. van der Zande, W. S. Whitney, M. P. Levendorf, J. W. Kevek, S. Garg, J. S. Alden, C. J. Hustedt, Ye Zhu, J. Park, P.L. McEuen, D. A. Muller, *Nature*, 2011, Vol. 469, 389-392

[159] X. Chen, F. Tian, C. Persson, W. Duan, N.-x. Chen, *Sci. Rep.*, 2013, Vol. 3, 3046

[160] W. Ren, H. Cheng , *Nat. Nanotechnol.*, 2014, Vol. 9, 726-730

[161] J. N. Coleman, *Acc. Chem. Res.*, 2013, Vol. 46, 1, 14-22

[162] C. G.-Navarro , R. T. Weitz , A. M. Bittner , M. Scolari , A. Mews , M. Burghard, K. Kern , *Nano Lett.*, 2007, Vol. 7, 3499

[163] A. B. Bourlinos, V. Georgakilas, R. Zboril, T. A. Steriotis, A. K. Stubos, *Small*, 2009, Vol. 5, 1841-1845.

[164] B.-H. Wee, T.-F. Wu, J.-D. Hong, *ACS Appl. Mater. Interfaces*, 2017, Vol. 9, 5, 4548-4557

[165] A. Pattammattel, C. V. Kumar, *Adv. Funct. Mater.*, 2015, Vol. 25, 7088-7098.

[166] H. Ba, L. T.-Phuoc, C. P.-Huu, W. Luo, W. Baaziz, T. Romero, I. Janowska, *ACS Omega*, 2017, Vol. 2, 12, 8610-8617

[167] M. Z. Cai, D. Thorpe, D.H. Adamson, H.C. Schniepp, *J. Mater. Chem*, 2012, Vol. 22, 24992

[168] S. Tian, P. He, L. Chen, H. Wang, G. Ding, X. Xie, *Chem Mater*, 2017, Vol. 29, 6214

[169] X. Xiao, Y. Zeng, H. Feng, K. Xu, G. Zhong, S. Wu, C. Wang, W. Zhao, W. Su, Z. Wei, X. Lu, *ChemNanoMat*, 2019 , Vol. 5, 152

[170] F. Liu, C. Wang, X. Sui, M. A. Riaz, M. Xu, L. Wei, Y. Chen, *Carbon Energy*, 2019, Vol. 1, 173-199

[171] C. Damm, T. J. Nacken, W. Peukert, *Carbon*, 2015, Vol. 81, 284-294

[172] M. Yi , Z. Shen , W. Zhang , J. Zhu , L. Liu , S. Liang , X. Zhang, S. Ma , *Nanoscale*, 2013, Vol. 5, 10660-10667

[173] Y. Arao , Y. Mizuno , K. Araki and M. Kubouchi , *Carbon*, 2016, Vol. 102 , 330-338

[174] N. Blomquist, A. C. Engstrom, M. Hummelgard, B. Andres, S. Forsberg, H. Olin, *PLoS One*, 2016, Vol. 11, 67-75

[175] T. Purkait, G. Singh, M. Singh, D. Kumar, R. S. Dey, *Sci. Rep.*, 2017, Vol. 7, 15239

[176] I. Janowska, F. Vigneron, D. Bégin, O. Ersen, P. Bernhardt, T. Romero, M. J. Ledoux, C. P.-Huu, *Carbon*, 2012, Vol. 50, 8, 3106-3110

[177] A. Shukla, R. Kumar, J. Mazher, A. Balan, *Solid State Commun.*, 2009, Vol. 149, 718-721

[178] J. Hou, Y. Shao, M. W. Ellis, R. B. Moored, B. Yi, *Phys. Chem. Chem. Phys.*, 2011, Vol. 13, 15384-15402

[179] J. Coraux, A. T. N‘Diaye, C. Busse, T. Michely, *Nano Lett.*, 2008, Vol. 8 , 565-570

[180] A. Reina, X. Jia, J. Ho, D. Nezich, H. Son, V. Bulovic, M. S. Dresselhaus, J. Kong, *Nano Lett*., 2009, Vol. 9, 30-35

[181] X. Li, W. Cai, J. An, S. Kim, J. Nah, D. Yang, R. Piner, A. Velamakanni, I. Jung, E. Tutuc, S. K. Banerjee, L. Colombo, R. S. Ruoff, *Science*, 2009, 324,1312-1314

[182] W. Chen, Z. Fan, G. Zeng, Z. Lai, *J. Power Sources*,2013, Vol. 225, 251-256

[183] S. Zhou, J. Xu, Y. Xiao, Ni Zhao, C.-P. Wong, *Nano Energy*, 2015, Vol. 13, 458-466

[184] R. S. Edwards, K. S. Coleman , *Nanoscale*, 2013, Vol. 5, 38-51

[185] I. Janowska, K. Chizari, O. Ersen, S. Zafeiratos, D. Soubane, V. D. Costa, V. Speisser, C. Boeglin, M.Houllé, D. Bégin, D. Plee, M.-J. Ledoux, C. P.-Huu, *Nano Res*., 2010, Vol. 3, 126-137

[186] A. A. Pirzado, G. Dalmas, L. N.-Dinh, I. Komissarov, F. L. Normand, I. Janowska, *Current Microwave Chemistry*, 2016, Vol. 3, 139-144

[187] I. Janowska, O. Ersen, T. Jacob, P. Vennégues, D. Bégin, M.-J. Ledoux, C. Pham-Huu, *Appl. Catal. A Gen.*, 2009, Vol. 371, 1-2, 22-30

[188] A. A. B. Hamra, H. N. Lima, N. M. Huang, N. S. K. Gowthaman, H. Nakajima, M. M. Rahman, *J. Mol. Struct.*, 2020, Vol. 1220, 128710

[189] Domga, M. Karnan, F. Oladoyinbo, G. B. Noumi, J. B. Tchatchueng, M. J. Sieliechi, M. Sathish, D. K. Pattanayak, *Electrochim. Acta*, 2020, Vol. 341, 135999

[190] X. Liu, D. Zhan, D. Chao, B. Cao, J. Yin, J. Zhao, Y. Li, J. Lin, Z. Shen, *J. Mater. Chem. A*, 2014, Vol. 2, 12166-12170

[191] M. V. Sulleiro, S. Quiroga, D. Peña, D. Pérez, E. Guitián, A. Criado, M. Prato, *Chem. Commun.*, 2018, Vol. 54, 2086-2089

[192] W.-S. Jiang, C. Yang, G.-X. Chen, X.-Q. Yan, S.-N. Chen, B.-W. Su, Z.-B. Liu, J.-G. Tiana, *J. Mater. Chem. C*, 2018, Vol. 6, 1829-1835

[193] J. Xia , F. Chen , J. Li and N. Tao , *Nat. Nanotechnol.*, 2009, Vol. 4, 505-509

[194] M. D. Stoller , C. W. Magnuson , Y. Zhu , S. Murali , J. W. Suk , R. Piner and R. S. Ruoff , *Energy Environ. Sci*., 2011, Vol. 4, 4685-4689

[195] H. Ji, X. Zhao, Z. Qiao, J. Jung, Y. Zhu, Y. Lu, L. Zhang, A. H. MacDonald, R. S. Ruoff , *Nat. Commun.*, 2014, Vol. 5, 3317

[196] M. F. E.-Kady, V. Strong, S. Dubin, R. B. Kaner, *Science*, 2012, Vol. 335, 1326-1330

[197] L. Zhang, X. Zhao, M. D. Stoller, Y. Zhu, H. Ji, S. Murali, Y. Wu, S. Perales, B. Clevenger, R. S. Ruoff, *Nano Lett.*, 2012, Vol. 12, 1806-1812

[198] Y. Gogotsi, P. Simon , *Science*, 2011, Vol. 334, 917-918

[199] X. Yang, C. Cheng, Y. Wang, L. Qiu, D. Li, *Science*, 2013, Vol. 341, 534-537

[200] O. Ghodbane, J. Pascal, F. Favier, *ACS Appl. Mater. Interfaces*, 2009, Vol. 1, 1130-1139

[201] Y. Tao, X. Xie, W. Lv, D. Tang, D. Kong, Z. Huang, H. Nishihara, T. Ishii, B. Li, D. Golberg, F. Kang, T. Kyotani, Q. Yang , *Sci. Rep.*, 2013, Vol. 3, 2975

[202] Y. Xu, Z. Lin, X. Zhong, X. Huang, N.O. Weiss, Y. Huang, X. Duan, *Nat. Commun.*, 2014, Vol. 5, 4554

[203] L. Zhang, Q. Xu, J. Niua, Z. Xia, *Phys. Chem. Chem. Phys*., 2015, Vol. 17, 16733-16743

[204] L. Y. Jiao, L. Zhang, X. R. Wang, G. Diankov, H. J. Dai, *Nature*, 2009, Vol. 458, 877

[205] Q. H. Wang, Z. Jin, K. K. Kim, A. J. Hilmer, G. L. Paulus, C. J. Shih, M. H. Ham, J. D. S.-Yamagishi, K. Watanabe, T. Taniguchi, J. Kong, P. J.-Herrero, M. S. Strano, *Nat. Chem.*, 2012, Vol. 4, 724-732

[206] C. Valles, C. Drummond, H. Saadaoui, C. A. Furtado, M. He, O. Roubeau, L. Ortolani, M. Monthioux, A. Penicaud, *J. Am. Chem. Soc.*, 2008, Vol. 130, 15802-15804

[207] Y. Hernandez, V. Nicolosi, M. Lotya, F. M. Blighe, Z. Y. Sun, S. De, I. T. McGovern, B. Holland, M. Byrne, Y. K. Gun'ko, J. J. Boland, P. Niraj, G. Duesberg, S. Krishnamurthy, R. Goodhue, J. Hutchison, V. Scardaci, A. C. Ferrari, J. N. Coleman, *Nat. Nanotechnol.*, 2008, Vol. 3 , 563-568

[208] H. Feng, Y. Wu, J. Li , *Small*, 2014, Vol. 11, 2233-2238

[209] N. I. Kovtyukhova, Y. Wang, A. Berkdemir, R. Cruz-Silva, M. Terrones, V. H. Crespi, T. E. Mallouk, *Nat. Chem.*, 2014, Vol. 6, 957-963

[210] Y.-Z. Zhang, Y. Wang, T. Cheng, L.-Q. Yao, X. Li, W.-Y. Lai, W. Huang, *Chem. Soc. Rev.*, 2019, Vol. 48, 3229-3264

[211] J. P. Mensing, T. Lomas, A. Tuantranont, *Sustain. Mater. Techno.*, 2020, Vol. 25, e00190

[212] T. M. Dinh, K. Armstrong, D. Guay, D. Pech, *J. Mater. Chem. A*, 2014, Vol. 2, 7170-7174

[213] M. P. Browne, F. Novotný, Z. Sofer, M. Pumera, ACS Appl. Mater. Interfaces 2018, Vol. 10, 46, 40294–40301

[214] P. Sundriyal, S. Bhattacharya, *ACS Appl. Mater. Interfaces*, 2017, Vol. 9, 38507-38521

[215] R. G. Grim, Z. Huang, M. T. Guarnieri, J. R. Ferrell, L. Tao, J. A. Schaidle, *Energy Environ. Sci.*, 2020, Vol. 13, 472-494

[216] M. Thema, F. Bauer, M. Sterner, *Renew. Sust. Energ. Rev.*, 2019, Vol. 112, 775-787

[217] M. Götz, J. Lefebvre, F. Mörs, A. M. Koch, F. Graf, S. Bajohr, R. Reimert, T. Kolb, *Renew. Energy*, 2016, Vol. 85, 1371-1390

[218] C. Wulf, J. Linßen, P. Zapp, *Energy Procedia*, 2018, Vol. 155, 367-378

[219] A. Belderbos, T. Valkaert, K. Bruninx, E. Delarue, W. D'haeseleer, *Appl. Energy* 2020, Vol. 275, 115082

[220] N. A. Kelly, *Advances in Hydrogen Production, Storage and Distribution*, Woodhead Publishing, 2014, 159-185

[221] A. Buttler, H. Spliethoff, *Renew. Sust. Energ. Rev.*, 2018, Vol. 82, 3, 2440-2454

[222] J. O. Abe, A. P. I. Popoola, E. Ajenifuja, O. M. Popoola, *Int. J. Hydrog. Energy*, 2019, Vol. 44, 29, 15072-15086

[223] H. Blanco, A. Faaij, *Renew. Sust. Energ. Rev.*, 2018, Vol. 81, 1, 1049-1086

[224] J. Ma, Q. Li, M. Kühn, N. Nakaten, *Renew. Sust. Energ. Rev.*, 2018, Vol. 97, 478-496

[225] S. Fukuzaki, N. Nishio, M. Shobayashi, S. Nagai, *Appl. Environ. Microbiol*, 1990, Vol. 56, 719-723

[226] P. Sabatier, J. B. Senderens, *Comptes Rendus de l'Académie des Sciences*, 1902, Vol. 134, 514-5166.

[227] P. J. Lunde, F. L. Kester , *Ind. Eng. Chem. Process Des. Dev.*, 1974, Vol. 13, 27-33

[228] J. Gao, Q. Liu, F. Gu, B. Liu, Z. Zhong, F. Su, *RSC Adv.*, 2015, Vol. 5, 22759-22776

[229] B. Miao, S. S. K. Ma, X. Wang, H. Su, S. H. Chan, *Catal. Sci. Technol.*, 2016, Vol. 6, 4048-4058

[230] M. Younas, L. L. Kong, M. J. K. Bashir, H. Nadeem, A. Shehzad, S. Sethupathi, *Energy Fuels*, 2016, Vol. 30, 11, 8815–8831

[231] W. Wang, S. Wang, X. Maa, J.Gong, *Chem. Soc. Rev.*, 2011, Vol. 40, 3703-3727

[232] S. Rönsch, J. Schneider, S. Matthischke, M. Schlüter, M. Götz, J. Lefebvre, P. Prabhakaran, S. Bajohr, *Fuel*, 2016, Vol. 166, 276-296

[233] F. Fischer, H. Tropsch, P. Dilthey, *Brennst-Chem*, 1925, 6, 265-271

[234] M.A. Vannice, *Catal. Rev.*, 1976, 14, 153-191

[235] G.A. Mills, F.W. Steffgen, *Catal. Rev.*, 1974, Vol. 8, 159-210

[236] M. A. A. Aziz, A. A. Jalil, S. Triwahyono, A. Ahmad, *Green Chem.*, 2015, Vol. 17, 5, 2647-2663

[237] P. Frontera, A. Macario, M. Ferraro, P. Antonucci, *Catalysts*, 2017, Vol. 7, 2, 59-86

[238] I. Sreedhar, Y. Varun, S. A. Singh, A. Venugopal, B. M. Reddy, *Catal. Sci. Technol.*, 2019, Vol. 9, 4478-4504

[239] W. J. Lee, C. Li, H. Prajitno, J. Yoo, J. Patel, Y. Yang, S. Lim, *Catal.Today*, 2020, DOI: 10.1016/j.cattod.2020.02.017

[240] W. Li, H. Wang, X. Jiang, J. Zhu, Z. Liu, X. Guo, C. Song, *RSC Adv.*, 2018, Vol. 8, 7651-7669

[241] P. J. Lunde, Frank L. Kester, *J. Catal.*, 1973, Vol. 30, 3, 423-429

[242] T. Abe , M. Tanizawa , K. Watanabe, A. Taguchi, *Energy Environ. Sci.*, 2009, Vol. 2, 315-321

[243] K. R. Thampi, J. Kiwi, M. Grätzel, *Nature*, 1987, Vol. 327, 506–508

[244] A. Kim, C. Sanchez, G. Patriarche, O. Ersen, S. Moldovan, A. Wisnet, C. Sassoye, D. P. Debecker , *Catal. Sci. Technol.*, 2016, Vol. 6, 8117-8128

[245] M. Agnelli, M. Kolb, C. Mirodatos, *J. Catal.*, 1994, Vol. 148 , 9

[246] M. Agnelli, H. M. Swaan, C. M.-Alvarez, G. A. Martin, C. Mirodatos, *J. Catal.*, 1998, Vol. 175, 117

[247] B. T. Loveless, C. Buda, M. Neurock, E. Iglesia, *J. Am. Chem. Soc.*, 2013, Vol. 135, 6107-6121

[248] T. Siudyga, M. Kapkowski, P. Bartczak, M. Zubko, J. Szade, K. Balin, S. Antoniotti, J. Polanski, *Green Chem.*, 2020, Vol. 22, 5143-5150

[249] W. Zhen, B. Li, G. Lu, J. Ma, *RSC Adv.*, 2014, Vol. 4, 16472-16479

[250] C. F. J. König, T. J. Schildhauer, M. Nachtegaal, *J. Catal.*, 2013, Vol. 305, 92-100

[251] Y. Zhu, S. Zhang, Y. Ye, X. Zhang, L. Wang, W. Zhu, F. Cheng, F. Tao, *ACS Catal.*, 2012, Vol. 2, 2403

[252] L. T. Luo, S. J. Li, Y. Zhu, *J. Serb. Chem. Soc.*, 2005, Vol. 70, 1419-1425

[253] S. Sharma, Z. Hu, P. Zhang, E. W. McFarland, H. Metiu, *J. Catal.*, 2011, Vol. 278, 297

[254] J. A. H. Dreyer , P. Li , L. Zhang , G. K. Beh , R. Zhang , P. H. L. Sit, W. Y. Teoh, *Appl. Catal. B*, 2017, Vol. 219, 715-726

[255] J. H. Kwak , L. Kovarik, J. Szanyi, *ACS Catal.*, 2013, Vol. 3, 2449-2455

[256] S. Eckle , H. G. Anfang, R. J. Behm , *J. Phys. Chem. C*, 2011, Vol. 115, 1361-1367

[257] C. Lv, L. Xu, M. Chen, Y. Cui, X. Wen, Y. Li, C. Wu, B. Yang, Z. Miao, X. Hu, Q. Shou, *Front. Chem.*, 2020, Vol. 8, 269

[258] L. Xu, X. Lian, M. Chen, Y. Cui, F. Wang, W. Li, B. Huang, *Int. J. Hydrog. Energy*,2018, Vol. 43, 36, 17172-17184

[259] P. Frontera, A. Malara, V. Modafferi, V. Antonucci, P. Antonucci, A. Macario, *Canadian J. Chem. Eng.*, 2020, 1-11

[260] P. Liu, B. Zhao, S. Li, H. Shi, M. Ma, J. Lu, F. Yang, X. Deng, X. Jia, X. Ma, X. Yan, *Ind. Eng. Chem. Res.*, 2020, Vol. 59, 5, 1845-1854

[261] J. Harmel, L. Peres, M. Estrader, A. Berliet, S. Maury, A. Fécant, B. Chaudret, P. Serp, K. Soulantica, *Angew. Chem. Int. Ed.*, 2018, Vol. 57, 10579

[262] B. Alrafei, I. Polaert, A. Ledoux, F. A.-Jury, *Cat. Today*, 2020, Vol. 346, 23-33

[263] M. Tsuji, T. Kodama, T. Yoshida, Y. Kitayama, Y. Tamaura, *J. Catal.*, 1996, Vol. 164, 2, 315-321

[264] S. V. Moghaddam, M. Rezaei, F. Meshkani, R. Daroughegi, *Int. J. Hydrog. Energy*, 2018, Vol. 43, 34, 16522-16533

[265] T. Franken, A. Heel, *J. CO_2 Util.*, 2020, Vol. 39, 101175

[266] D. De Masi, J. M. Asensio, P.-F. Fazzini, L.-M. Lacroix, B. Chaudret, *Angew. Chem. Int. Ed.*, 2020, Vol. 59, 6187.

[267] B. R.-Murias, J. M. Asensio, N. Mille, B. R.-González, P.-F. Fazzini, J. Carrey, B. Chaudret, V. Salgueiriño, *Angew. Chem. Int. Ed.*, 2020, Vol. 59, 15537

[268] G. Zhi , X. Guo , Y. Wang , G. Jin and X. Guo , *Catal. Comm.*, 2011, Vol. 16, 56

[269] H. Muroyama, Y. Tsuda, T. Asakoshi, H. Masitah, , T. Okanishi, T. Matsui, K. Eguchi, *J. Catal.*, 2016, Vol. 343,178-184

[270] S. Tada, T. Shimizu, H. Kameyama, T. Haneda, R. Kikuchi. *Int. J. Hydrog. Energy*, 2012, Vol. 37, 7, 5527-5531

[271] T. A. Le, M. S. Kim, S. H. Lee, T. W. Kim, E. D. Park, *Catal. Today*, 2017, Vol. 293, 89-96

[272] P. A. U. Aldana , F. Ocampo , K. Kobl , B. Louis , F. Thibault-Starzyk , M. Daturi , P. Bazin , S. Thomas, A. C. Roger , *Catal. Today*, 2013, Vol. 215 , 201-207

[273] A. S.-Garcia, J. F. L.-Hernandez, A. A.-Camarillo, J. C. F.-Gonzalez, *Appl. Catal. B*, 2017, Vol. 218, 611-620

[274] M. A. A. Aziz, A. A. Jalil, S. Triwahyono, R. R. Mukti, Y. H. T.-Yap, M. R. Sazegar, *Appl. Catal. B.*, 2014, Vol. 147, 359-368

[275] M. A. A. Aziz, A. A. Jalil, S. Triwahyono, S. M. Sidik. *Appl. Catal. A: Gen.*, 2014, Vol. 486, 115-122.

[276] M. A. A. Aziz, A. A. Jalil, S. Triwahyono, M. W. A. Saad, *Chem. Eng. J.*, 2015, Vol. 260, 757-764

[277] Z. Zhang, Y. Tian, L. Zhang, S. Hu, J. Xiang, Y. Wang, L. Xu, Q. Liu, S. Zhang, X. Hu, *Int. J. of Hydrog. Energy*, 2019, Vol. 44, 18, 9291-9306

[278] A. Quindimil, U. De-La-Torre, B. P.-Ayo, A. D.-Quiñonero, E. B.-García, D. L.-Castelló, J. A. G.-Marcos, A. B.-López, J. R. G.-Velasco, *Catal. Today*, 2019, Vol. 356, 419-432

[279] G. Garbarino, P. Riani, L. Magistri, G. Busca, *Int. J. Hydrogen Energy*, 2014, Vol. 39, 11557

[280] S. Abelló, C. Berrueco, D. Montané, *Fuel*, 2013, Vol. 113, 598

[281] B. Lu, K. Kawamoto, *Fuel*, 2013, Vol. 103, 699

[282] X. Zhang , W.-J. Sun and W. Chu , *J. Fuel Chem. Technol.*, 2013, Vol. 41, 96

[283] W. Wang, W. Chu, N. Wang, W. Yang, C. Jiang, *Int. J. Hydrog. Energy*, 2016, Vol. 41, 2, 967-975

[284] J. Li, Y. Zhou, X. Xiao, W. Wang, N. Wang, W. Qian, W. Chu, *ACS Appl. Mater. Interfaces*, 2018, Vol. 10, 48, 41224-41236

[285] J. Wu, C. Wen, X. Zou, J. Jimenez, J. Sun, Y. Xia, M.-T. F. Rodrigues, S. Vinod, J. Zhong, N. Chopra, I. N. Odeh, G. Ding, J. Lauterbach, P.M. Ajayan, *ACS Catal.*, 2017, Vol. 7, 4497-4503

[286] I. C. Gerber, P. Serp, *Chem. Rev*., 2020, Vol. 120, 2, 1250-1349

[287] Q. Yuan, Z. Xu, B. I. Yakobson, F. Ding, *Phys. Rev. Lett.*, 2012, Vol. 108, 24, 245505

[288] W. Wang, C. D.-Viet, H. Ba, W. Baaziz, G. Tuci, S. Caporali, L. N.-Dinh, O. Ersen, G. Giambastiani, C. P.-Huu, *ACS Appl. Energy Mater.*, 2019, Vol. 2, 2, 1111-1120

[289] M. R.-Sáez, A. B. Dongil, N. Benito, R. E.-González, N. Escalona, F. Graciaa, *Appl. Catal. B*, 2018, Vol. 237, 817-825

[290] I. M.-Gullon, J. Vera, J. A. Conesa, J. L. González, C. Merino, *Carbon*, 2006, Vol. 44, 8, 1572-1580

[291] HaibinMa, KuiMa, JunyiJi, SiyangTang, ChangjunLiu, WeiJiang, HairongYue, BinLiang, *Chem. Eng. Sci.*, 2019, Vol. 194, 2 10-21

[292] A. Primo, J. He, B. Jurca, B. Cojocaru, C. Bucur, V. I. Parvulescu, H. Garcia, *Appl. Catal. B*, 2019, Vol. 245, 351-359

[293] C. H. Bartholomew, *Appl. Catal. A: Gen.*, 2001, Vol. 212, 1-2, 17-60.

[294] T. Schaaf, J. Grünig, M. R. Schuster, T. Rothenfluh, A. Orth, *Energy, Sustainability and Society*, 2014, Vol. 4, 2

[295] T. Schaaf, J. Grünig, M. Schuster, A. Orth, *Chem. Ing. Tech.*, 2014, Vol. 86, 476-485

[296] J. Kopyscinski, T. J. Schildhauer, S. M. A. Biollaz, *Chem. Eng. Sci.*, 2011, Vol. 66, 924-934

[297] J. Lefebvre, M. Götz, S. Bajohr, R. Reimert, T. Kolb, *Fuel Process. Technol.*, 2015, Vol. 132, 83-90

[298] K. P. Brooks, J. Hu, H. Zhu, R. J. Kee, *Chem. Eng. Sci.*, 2007, Vol. 62, 1161-1170

[299] S. Ceylan, L. Coutable, J. Wegner, A. Kirschning, *Chem. Eur. J.*, 2011, Vol. 17, 1884-1893

[300] Z. Hedayatnasab, F. Abnisa, W. M. A. W. Daud. *Mater. Des.*, 2017, Vol. 123, 174

[301] W. Wang, G. Tuci, C. Duong-Viet, Y. Liu, A. Rossin, L. Luconi, J. M. Nhut, L. Nguyen-Dinh, C. Pham-Huu, G. Giambastiani. *ACS Catal*., 2019, Vol. 9, 7921-7935

[302] A. Ovenston, J. R. Walls, *J. Chem. Soc., Faraday Trans. 1*, 1983, 79: 1073-1084

[303] J. Bursavich, M. A.-Laban, P. D. Muley, D. Boldor, D. J. Hayes, *Energy Convers. Manage.*, 2019, Vol. 183, 689-697

[304] A. Meffre, B. Mehdaoui, V. Connord, J. Carrey, P. F. Fazzini, S. Lachaize, M. Respaud, B. Chaudret. *Nano Lett.*, 2015, Vol. 15, 5, 3241-3248

[305] S. Ruta, R. Chantrell, O. Hovorka, *Sci. Rep.*, 2015, Vol. 5, 9090

[306] C. Appino, O. De La Barrière, F. Fiorillo, M. Lobue, F. Mazaleyrat, C. Ragusa. *J. Appl. Phys.*, 2013, Vol. 113, 17, 17A322

[307] J. Pearce, A. Giustini, R. Stigliano, P. J. Hoopes, *J. Nanotechnol. Eng. Med.*, 2013, Vol. 4, 1, 011005

[308] N. A. Frey, S. Peng, K. Cheng, S. Sun, *Chem. Soc. Rev.*, 2009, Vol. 38, 9, 2532-2542.

[309] R. Hergt, S. Dutz, *J. Magn. Magn. Mater*., 2007, 311, 187

[310] L. Néel, *Ann. Geophys.*, 1949, Vol. 5 , 99-136

[311] W. F. Brown, *Phy. Rev.*, 1963, Vol. 130, 5, 1677-1686.

[312] R. E. Rosensweig, *J. Magn. Magn. Mater*., 2002, Vol. 252, 370-374

[313] W. M. Zhou, Z. X. Yang, F. Zhu, Y. F. Zhang. *Physica E*, 2006, Vol. 31, 1, 9-12

[314] H. Y. Chen, L. Chen, Y. Lu, Q. Hong, H. C. Chua, S. B. Tang, J. Lin, *Catal. Today*, 2004, Vol. 96, 3, 161-164.

[315] B. D. Sosnowchik, L. Lin. *Appl. Phys. Lett.*, 2006, Vol. 89, 19, 193112

[316] A. Okamoto, H. Shinohara. *Carbon*, 2005, Vol. 43, 2, 431-436.

[317] L. Tao, J. Lee, H. Li, R. D. Piner, R. S. Ruoff, D. Akinwande. *Appl. Phys. Lett.*, 2013, Vol. 103, 18, 183115

[318] S. Sato, A. Kawabata, M. Nihei, Y. Awano, *Chem. Phys. Lett.*, 2003, Vol. 382, 3-4, 361-366

[319] A. R. Biris, A. S. Biris, D. Lupu, S. Trigwell, E. Dervishi, Z. Rahman, P. Marginean. *Chem. Phys. Lett.*, 2006, Vol. 429, 1-3, 204-208

[320] Z. Li, B. Zhao, P. Liu, B. Zhao, D. Chen, Y. Zhang, *Physica E*, 2008, Vol. 40, 3, 452

[321] R. Muñoz, C. G.-Aleixandre, *Chem. Vap. Deposition*, 2013, Vol. 19, 297-322

[322] P. Piner, H. Li, X. Kong, L. Tao, I. N. Kholmanov, H. Ji, W. H. Lee, J. W. Suk, J. Ye, Y. Hao, S. Chen, C. W. Magnuson, A. F. Ismach, D. Akinwande, R. S. Ruoff, *ACS Nano*, 2013, Vol. 7, 9, 7495-7499

[323] C. Wu, F. Li, W. Chen, C. P. Veeramalai, P. C. Ooi, T. Guo, *Sci. Rep.*, 2015, Vol. 5, 9034

[324] H. Kim, C. Mattevi, M. R. Calvo, J. C. Oberg, L. Artiglia, S. Agnoli, C. F. Hirjibehedin, M. Chhowalla, E. Saiz. *ACS Nano*, 2012, Vol. 6, 4, 3614-3623

[325] A. Bordet, L.-M. Lacroix, P.-F. Fazzini, J. Carrey, K. Soulantica, B. Chaudret, *Angew. Chem. Int. Ed.*, 2016, Vol. 55, 15894

[326] S. S. Kale, J. M. Asensio, M. Estrader, M. Werner, A. Bordet, D. Yi, J. Marbaix, P.-F. Fazzini, K. Soulantica, B. Chaudret, *Catal. Sci. Technol.*, 2019, Vol. 9, 2601-2607

[327] W. Wang, C. D.-Viet, G. Tuci, Y. Liu, A. Rossin, L. Luconi, L., J.-M. Nhut., L. N.-Dinh, G. Giambastiani, C. Pham-Huu, *ChemSusChem*, 2020, doi:10.1002/cssc.202001885

[328] W. Wang, C. Duong-Viet, Z. Xu, H. Ba, G. Tuci, G. Giambastiani, Y. Liu, T. Truong-Huu, J.-M. Nhut, C. P.-Huu, *Catal. Today*, 2019, DOI : 10.1016/j.cattod.2019.02

Chapter 2

Tailoring FLG composites for Electro-chemical energy storage

The use of FLG in the field of electrochemistry charge storage depends largely on utilizing its intrinsic properties. As discussed earlier, although the theoretical surface area of graphene is large, it does not provide good capacitance from the basal plane. The theoretical values of 21 µF cm^{-2} have been later rectified based on the edge contributions [1]. Instead, multiple times larger capacitance arises from the edges of graphene [2]. Therefore, the goal lies in making the maximum amount of edges accessible to the electrolyte for formation of electrical double layer. In order to achieve this, a simultaneous approach towards avoiding restacking of graphene layers is essential. A green synthesis approach to make FLG composites with edges accessible has been developed and their electrochemical properties has been studied for supercapacitors. For this, cheaply available expanded graphite is exfoliated along with high-Hydrophilic-Lyophilic Balance (hHLB) systems. The hHLB systems refers to the easily water soluble hydrophilic non-ionic surfactants. A colloidal approach for top-down synthesis has already revealed that high-HLB systems like agar-agar, hemoglobine, maltodextrine and, bovine serum albumin(BSA) are good candidates for obtaining high-quality laminar 2D materials like FLG [3]. The kitchen based "emulsion homogenisation" concept is used along with simultaneous vortex formation by stirring and sonication giving rise to FLG solutions of concentrations 45 g L^{-1} with FLG flake size in the range of several microns. The earlier studies made use of hHLB systems for exfoliation of graphite to obtain graphene but it has not yet been explored to be utilised in a much larger ratio compared to FLG to form an all-carbon composite. Thus the existing exfoliation method is modified further as shown in **Figure 2.1** in order to obtain FLG based nanocomposites for supercapacitors.

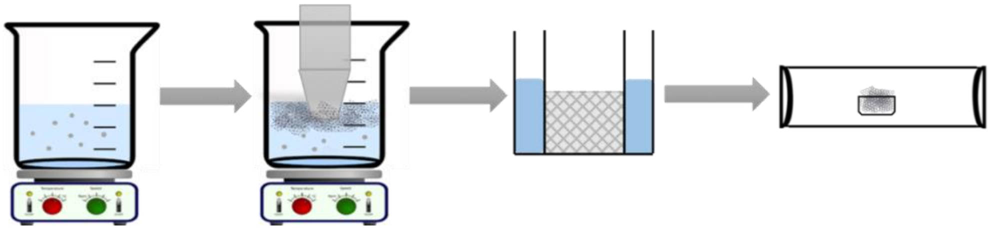

Figure 2.1 Synthesis schematic: HLB stirring → EG addition with sonication & stirring → Drying → Carbonization

A typical active material synthesis process involves initial dissolution of h-HLB surfactant in water followed by addition of Expanded Graphite (EG) with simultaneous top sonication and stirring. The method makes use of a large amount of hHLB precursor and their mixture compared to the amount required for simple exfoliation. This approach allows then not only exfoliate EG to FLG but also access to micronized structures of FLG with carbon spacers, and as we see later with optimized porosity and FLG alignment. The obtained suspension is the dried followed by carbonization of HLB precursors. Thus the key parameters which dictate the material properties lie on the type of HLB precursor along with the time of sonication-cum-stirring and power to be used based on their ability to obtain thin FLG flakes. Further, the method of drying modulates the morphology and arrangement of the FLG flakes which in turn conditions the access to functional groups. Lastly, the gas treatment was carried out to carbonize the precursors and provide stability to the composite. In some cases, this carbonization process also acted as a doping process wherein oxygen and nitrogen atoms were introduced into the composite by treatment under O_2 and NH_3 respectively. The concentration and type of hHLB precursor influences the strength and ability to withstand the alignment obtained during the drying and the type of amorphous carbon network formed between the FLG flakes after carbonisation. Besides, it also steers the porosity of the materials which plays an important role in tuning the capacitance. This helps produce graphene of high density which ultimately gives rise to high volumetric capacitance which is uncommon for supercapacitance from all-carbon based materials.

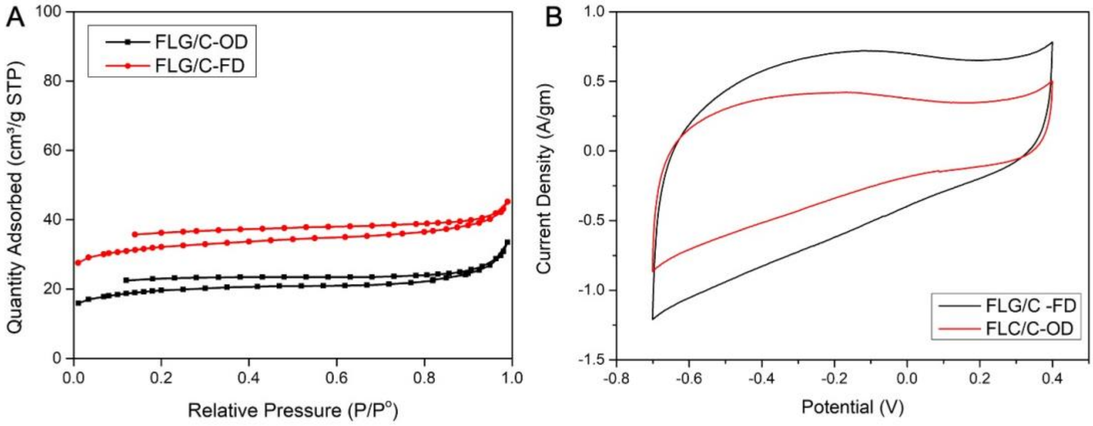

Figure 2.2 BET Isotherm plots and I-V characteristics of FLG-C samples under the freeze drying(FD) and oven drying(OD).

Before considering the choice of precursors and optimizing their ratios, it was imperative to first fix up the post-synthesis parameters. Therefore, initially FLG based samples were synthesized with BSA which was converted to mostly amorphous carbon structures, indicated as FLG/C composites. FLG/C-FD refers to freeze-dried sample whereas FLG/C-OD refers to the oven-dried sample. Both samples used for this optimization were treated under 600°C NH_3 for 2 hours in a quartz furnace. The use of freeze-drying over conventional oven drying was found to be noticeably advantageous in terms of preserving the network and edge-access. The use of freeze-drying improved the surface area of the materials, typically from 64 m^2 g^{-1} to 105 m^2 g^{-1} for the studied FLG/C sample as shown in **Figure 2.2 (a)**. Freeze-drying helps maintain the porosity. The relatively low surface area of the FLG samples is attributed to the π-π stacking during the degassing process and the non-rigidity of the samples. The disjointed nature of the BET isotherms can be attributed to the slit pores developed in the materials. A detailed discussion about the same and the ultramicroporosity of these materials have been presented for the best samples in the later sections. Further, the effect of these increased surface area on electrochemical performances was studied. All the electrochemical measurements were performed measured in three electrode set-up having 0.5M H_2SO_4 aqueous electrolyte and in a potential window of 1.1V. This improved surface area and micro-porosity led to enhanced capacitance reflected in the CV curves shown in **Figure 2.2(b)**.

Having the process of drying optimized, the next step was to identify the suitable parameters for gas treatment so as to retain the porosity as well as to make it more efficient for electrochemical charge storage. The FLG-C samples have been denoted with the type of gas used and their temperature of treatment alongside in the electrochemical measurements presented in **Figure 2.3**. NH_3 and Ar were initially used at different temperatures to identify the suitable temperature as shown in **Figure 2.3 (a)**. The study revealed that gas treatment at 600°C was most beneficial for improved capacitance. Tests were also done at 800°C which resulted in a capacitance similar to 400°C-NH_3 possibly because of loss of carbon by burning and destruction of the porous network. But low temperature inactivity arises mostly due to the lack on conversion of the hHLB precursor materials giving rise to interactions with electrolyte as well as deformity of pores. A constant 2h treatment at 600°C makes sure the conversion of non-FLG precursors to amorphous carbon with sustained intra-carbon interaction preserves the edge access of the FLG sheets and improves the porosity of the composite.

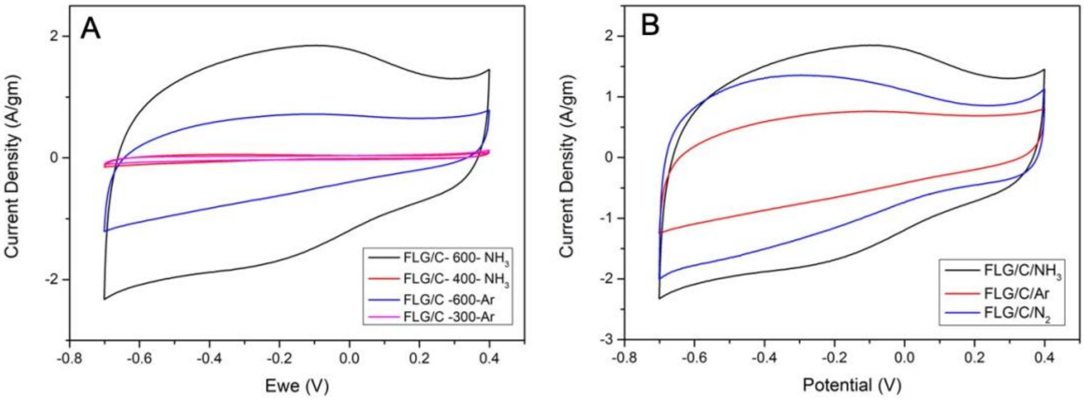

Figure 2.3 I-V characteristics of FLG/C samples under different gas and temperature conditions.

The gas treatment was also carried out under N_2 to understand the change in atomic nitrogen percentage which is helpful for electrochemical charge storage. **Figure 2.3 (b)** shows that NH_3 improves the capacitance the most compared to Ar and N_2 treated samples which can be attributed to the increase in the percentage of pyrollic and pyridinic N-groups which are known to enhance the pseudocapacitance [4]. Such N-groups aid the charge density on graphene surface and facilitate proton exchange under acidic conditions.

With confirmed drying and gas treatment, the next step was to identify the best initial hHLB precursor(s) which resulted in various new material composites structuration although the base was FLG as shown in **Figure 2.4**. Tannic acid was also studied for exfoliation and composite formation. The composites presented were all treated with NH_3 at 600°C. The SEM images of FLG exfoliated in a mixture of hemoglobine and tannic acid gives rise to fibril like structures unlike others which form particle type structure in-between and on the surface of the graphene flakes (**Figure 2.4 (a,d)**). The fibrillar morphology are generally produced by conversion of some soluble proteins to insoluble forms upon external heat treatment [5]. Such fibril morphology also gives rise to larger diameter channels which increases the amount of wet weight in the active composite volume without formation of double-layer capacitance.

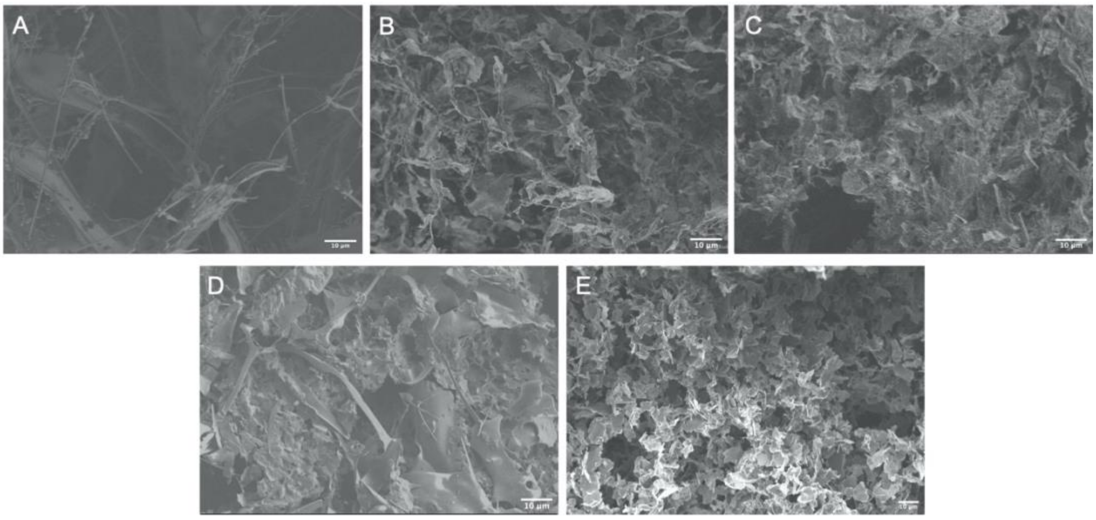

Figure 2.4 SEM images reflecting the structuration obtained from various HLB systems with initial EG:HLB ration of 0.5:4; A) FLG-Haemoglobin, B) FLG- Agar-Agar, C) FLG-Bovine Serum Albumin, D) FLG-Tannic Acid, E) FLG-Maltodextrin (Scale: 10 µm).

FLG prepared via agar-agar on the other hand has a rather dense structure with very less amount of channels. FLG-BSA and FLG-maltodextrine on the other hand has a good balance between network formation and channels which provides a lot better access to the FLG edges. The capacitance observed for such FLG-hHLB having same ratios follow the order: FLG-BSA> FLG- Maltodextrine> FLG- Agar Agar > FLG-Tannic Acid ~ FLG- Hemoglobine.

The detailed study of the best system obtained for supercapacitor applications using these HLB precursors is discussed below as an adaptation form of the publication; *Electrochimica Acta*, 2019, Vol. 308, 206-216.

2.1 Tuning the structure of in-situ synthesized few layer graphene/carbon composites into nanoporous vertically aligned graphene electrodes with high volumetric capacitance.

Anurag Mohanty,[a] Izabela Janowska[a]*

[a] Institut de Chimie et Procédés pour l’Énergie, l'Environnement et la Santé (ICPEES), CNRS UMR 7515-University of Strasbourg, 25 rue Becquerel 67087 Strasbourg, France

2.1.1 Abstract

Few layer graphene/carbon (FLG/C) composites are prepared directly via the rapid and simple exfoliation of expanded graphite in the presence of carbon based natural precursors (i.e. protein, polysaccharide) in water, followed by carbonization process. Several parameters such as nature of C-precursor, FLG/C ratio and carbonization conditions (gas, temperature) are modified in order to optimize the morphology, composition and porosity of FLG/C and thereby investigate their impact on gravimetric and volumetric capacitance, their stability and contribution of pseudocapacitance (Ps) vs. double-layer capacitance (DL). Few composites exhibit extremely high capacitance considering their low BET- surface area ranging in 130-260 m^2/g. The highest gravimetric and volumetric capacitance of 322 F/g and 467 F/cm^3 respectively (0.5 A/g); and energy/power performance is reached for FLG/C:1/2, synthesized from graphite-bovine serum albumin(BSA). Despite relatively high theoretical pseudocapacitance contribution of 69% (1.1V), this sample shows also high capacity retention at high current density and elevated energy -to- power densities. The overall great capacity performance is attributed to the high electrochemical surface area from combined structural features: nanoporosity, FLG alignment with high accessibility of FLG edges and elevated packing density.

Keywords: nanoporosity, graphene edges, vertically aligned graphene, volumetric capacitance, graphene composites, pseudocapacitance

2.1.2 Introduction

The need in global usage of advanced technological devices aiding to human life in various fields has initiated in search for alternative renewable energy production, such as electricity, which in turn has created a surge in research of energy storage systems. The latter ones are traditionally based on batteries or capacitors, while the most recent development concerns the supercapacitors, the systems that hopefully can bridge the gap between relatively expensive and short-life time batteries and capacitors. Supercapacitors are known to work on two-different mechanisms, i) electrical double layer capacitance (EDLC, DL) relating to ion adsorption on high surface area, porous surfaces and, ii) pseudocapacitance (Ps) via slower chemical reversible faradic reactions. The major stepping stones in supercapacitor electrodes developments are carbon based materials including weakly graphitized activated carbon and graphitic carbons (graphene, carbon nanotubes/nanofibers), in which the Ps contribution from redox reactions is usually not negligible especially in activated and/or functionalized carbons and worthy to be considered [6]. Only recently, few works on Ps contribution investigations, in N-doped RGO [4] or graphitized carbons derived from aromatic cross-linked polymers [7], have been reported. The two ways to store energy entail in general trade-off in power and energy performance, i.e. good power and limited energy densities are measured for fast and reversible DL, while higher energy and lower power densities come from slower kinetically redox reactions [8, 9]; and for example the high capacitance and significant energy of highly heteroatom-doped graphene could be obtained (629 F/g at 0.2A/g) but at power density of only 140 W/kg [10].

The initially reported theoretical capacitance of graphene with theoretical surface area of 2675 m^2/g [1], 21 $\mu F/cm^2$ (550 F/g), has been rectified due to the graphene edges contribution. It was found that the theoretical specific capacitance of graphene edges is 4 orders of magnitude higher than the one of graphene planes [2], and for instance, the minimum areal capacitance for edges-oriented graphite reaches 50-70 $\mu F/cm^2$ [11]. The « common » graphene based electrodes including graphene films and reduced graphene oxide (rGO) exhibits usually quite high power density resulted due to relatively high surface area and electronic properties (high conductivity, rapid charge transfer) but they attain moderate capacitance of c.a. 200 F/g [12-14]. Higher values, 349 F/g (2 mV/s), 604F/g (3mA) and 253 F/g (1A/g) were obtained for corrugated/prostruted/perforated graphene/rGO nanorribons/nanomeshs respectively [15-17]. One of the main reason of lowered experimental capacities, far from the theoretical one, is an excessive inter-layer π-π stacking of graphene sheets [18]. To overcome this drawback a formation of graphene aerogels/hydrogels, often by cross-coupling reactions are applied. High surface area, usually between 1000-3000 m^2/g and abundant macropores in aerogels result in high specific gravimetric capacitance (222F/g (1A/g) and 325 F/g (1A/g) [19, 20] but in turn entails poor specific volumetric capacitance, C_{vol}, due to a low packing density [20, 21]. To increase a density of the active materials some efforts have been undertaken, e.g. converting of graphene hydrogel by capillary pressure and passing from 0.13 to 1.3 g/cm^3 yield 255,5 F/cm^3 at 0.1 A/g [22], compressing nanoporous N-doped graphene gives 300 F/cm^3 (0.6 A/ cm^3) that is 15-20 times higher than un-compressed sample [23], evaporation-induced drying of graphene hydrogel resulting in 376 F/cm^3 [24]. The ultrahigh volumetric capacitance has been reported for densely packed fluorine and nitrogen co-doped carbon microspheres, 521 F/cm^3, while for solely N-doped it drops to 262 F/cm^3 [25]. Other approach to avoid graphene aggregation deals with a growth and application of high surface area vertically aligned graphene nanosheet arrays benefiting from accessible graphene edges [26-30]. High gravimetric capacitance of such arrays can be reached but still the arrays have large mesopores (intersheets distance) and consequently low volumetric performance. Also sophisticated and relatively heavy techniques are applied to get aligned graphene/FLG, i.e. plasma-enhanced chemical vapor deposition technique PECVD [28], microwave plasma torch (MPT)-PCVD [30], CVD [27], sputtering [31], antifreezing-template-assisted drying [32] or strong magnetic field in resin composites [33]. The milder conditions were just reported for bi-directional freeze casting assisted drying [34]. Only recently, a direct anodic exfoliation of graphite into aligned rGO were reported but volumetric capacitance for graphite-rGO was of only 3.9 F/cm^3 in 6 KOH [35]. The alignment of graphene or other 2D materials showed to provide as well other important advantages: the use of high voltage cells in organic liquid electrolytes of the MPT-PCVD grown aligned graphene [30] and of the mesoporous carbon with edge-free graphene walls [36]; the benefit from the directional transport on the capacity efficiency (thickness independent) was also demonstrated in aligned MXenes [37].

The activated porous carbons are another large family of commonly used capacitive electrodes. They are in general prepared from the synthetic or natural precursors such as polymers [38], synthetic organic molecules [4], sugars or directly from bio-mass [39] (fruits, fruits shells, etc). In term of specific capacitance, they can reach at low current densities the values such as 374 F/g (0.1 A/g) [4]. The similar capacity performances have been observed in several graphene-carbon composites, i.e. the graphene-carbon composites reached the capacitance of 324 F /g at 0.3 A/g in 1M H_2SO_4 [40]. The composite of polypyrrole and graphene has shown capacitance of 326 F/g at 0.5 A/g (250 F/g at 2A/g) (obtained by electropolymerization) [41]. The composite, sugar-derived carbon/graphene has shown 273 F/g at 0.5 A/g in 6M KOH [42]. Still other examples deal with the use of carbon nanotubes (CNTs) as graphene spacers: 211 F/g at 0.5 A/g [43], or double spacers CNTs and NPs reaching in rGO/CNTs/NiO composite the capacitance of 1180 F/g at 1A/g [44]. High gravimetric and volumetric capacitance were obtained for hybrid film of GO/NaCl/ urea at 1A/g in 1M H_2SO_4 in symmetrical cell (425 F/g and 693 F/cm^3, respectively) [45]. High volumetric capacitance of 364 F/g was obtained also for multilayered rGO/polymer architecture [46].

Apart from some issues described above there are other ones linked to the preparation of electrode materials for high scale applications. Most forms of graphene used is in fact the reduced graphene oxide, the synthesis of which, including reduction, is relatively long and harsh process [47], while the graphene monolayer doesn't solve the issue of expensive scaling and difficulty to be obtained at large scale by exfoliation methods. The activated carbon electrodes originating from the natural sources (fruits) suffer in turn from a weak control of their final structures.

Herein we present the electrodes that are composites of few layer graphene (FLG) and carbon (FLG/C), obtained by *in*-situ exfoliation of graphite in the presence of natural bio-compatible C precursor, followed by carbonization process. The preparation method makes no room for waste in the entire process, while water is used as the exfoliation medium, making the approach attractive from the economic and environmental point of view. The C from the natural precursors (albumin/maltodextrin), as described below plays the role of spacer for FLG, inducing interesting FLG-C compact arrangement, also facilitating vertical alignment, and nanoporosity. The electrochemical measurements are performed in three-electrode system in 0.5M H_2SO_4 electrolyte. The DL and Ps capacities contributions as well as electrochemical performance – structure relation are investigated.

2.1.3 Experimental

2.1.3.1 Synthesis of FLG/C composites

Expanded Graphite (EG) was purchased from Carbon Lorraine company , Bovine Serum Albumin (A) and Maltodextrin(M) were purchased from Sigma-Aldrich and MyProtein company respectively.

General approach: x mg of bovine serum albumin (and y mg of maltodextrin) was first solubilized in 200 ml of deionized water by stirring for about 15 min. Then z mg of EG was added to the solution under constant stirring at 700 rpm for about 15 min, such that all of added EG is visibly wet and mixed with the solution. Then the mixture is subjected to simultaneous stirring and sonication (top ultrasonicator) in a cooling water bath for 2 h. After the completion of the reaction, the obtained suspension is dried using freeze-drying method for 24 h at -80°C. The sample is then carbonized in a quartz reactor at 600°C for 2 h under NH_3 atmosphere. The heating and cooling of the reactor is done under Ar atmosphere. The sample thus obtained is used to fabricate electrodes for electrochemical tests.

Table 2.1 below includes the compositions of the composites before (FLG/A/M) and after (FLG/C) carbonization.

FLG/C(final composition/after carbonization)	FLG/hHLB (FLG/A/M, initial composition/before carbonization)
1/2	0.5/4/0

1.4/1	1/3/1
1/1.2	1/1/3
1/1.6	0.5/3/1
1/2.3	0.5/1/3
1/2.5	0.25/3/1

Table 2.1 Final (after carbonization) and initial (before carbonization) compositions of FLG-C.

2.1.3.2 Preparation of electrodes

For fabrication of electrodes, circular glassy carbon (GC) of 5mm diameter obtained from HTW Hochtemperatur-Werkstoffe GmbH, Germany was used. Each of the GC was initially polished with sand paper on one side to have a mirror-like reflection surface. Further, it was sonicated in ethanol for five minutes and washed three times with ethanol to make sure it is free from surface contaminants. The ink for the GC was made with a suspension of FLG/C samples and ethanol with a conc. of 1mg/ml. To this, 1% by vol. of Nafion (5% by vol. in Ethanol) was added. It was sonicated for 20-30 min. to obtain a homogenous ink. The ink was then drop-casted on the GC using a pipette of 10-100 µl precision. Each cast was generally of 10-20 µl. Considering the visual surface coverage of the GC, each electrode was made of 100-140 µg of the composite. After drop-casting, the electrode was air-dried in oven at 60°C for 15 min. to make sure there was no ethanol left. Then, it was used for electrochemical test.

2.1.3.3 Characterization tools

XPS analyses were performed with a MULTILAB 2000 (THERMO) spectrometer equipped with Al K anode ($h\nu$= 1486.6 eV). For deconvolution of spectra, the CASA XPS program with a Gaussian−Lorentzian mix function and Shirley background subtraction was employed.

Transmission electron microscopy (TEM) was carried out on a Topcon 002B - UHR microscope working with an accelerated voltage of 200 kV and a point-to-point resolution of 0.17 nm. The sample was dispersed in ethanol and a drop of the suspension was deposited onto a holey carbon coated copper for analysis.

Scanning electron microscopy (SEM) analysis was carried out on a Jeol JSM-6700F working at 3 kV accelerated voltage, equipped with a CCD camera.

TGA analyses were carried out on TA instrument SDT Q600, the rate of the heating was fixed at 10^{o} per min under air flow.

BET surface area and porosity analysis were carried out on Micrometrics ASAP 2420 instrument, by the adsorption of N_2 at 77K. Each sample were measured few times at different conditions of time and temperature degassing as well as different interval equilibration time.

For the analysis of microporosity between 0.5 and 0.9 nm a dosage amount of N_2 was decreased to 2-6 cm^3/g STP with an max. equilibration time of 2-3h, and the tubes were calibrated prior to the measurements.

The pores size distribution was obtained by BJH method (comparing the desorption and adsorption branches and excluding eventual artefacts [48].

The microporosity size distribution were estimated in accordance to Horvath-Kawazoe method.

The densities of the prepared FLG/A/M composites were measured using a liquid pycnometer. For each sample, the average of 3 measurements were used.

2.1.3.4 Electrochemical measurements

The electrochemical measurements were carried out in a three-electrode cell setup using a Biologic SP-300 system. The three-electrode setup had GC with sample material as working electrode, platinum wire as counter electrode and Mercury Standard Electrode (MSE) as reference electrode. All the measurements were performed in 0.5M H_2SO_4 electrolyte at potential window of 1.1 V. The electrolyte was first degassed with N_2 for at least 20 min before starting any experiments.

The specific capacitance was obtained from galvanostatic charge/discharge measurements according to the equation:

$$C_{GCD} = \frac{It}{m.V}\ (Fg^{-1})$$

where, $I(A)$, $t(s)$, $m(g)$ and V represent the discharge current, discharge time, mass of active material and discharge voltage (The slopes from the linear fit of linear regions from the discharge curves were used).

The voltametric capacitance, C_{CV} was calculated from the CV curve according to the formula:

$$C_{CV} = \frac{CV\ Area}{2\ m\ s\ \Delta V}\ (Fg^{-1})$$

where, s represents potential scan rate at 5mV/s and ΔV the potential window of 1.1 V .

The specific energy density (SE) and specific power density (SP) was calculated according to the equations:

$$SE = \frac{1}{2} C_{GCD} \Delta V^2\ x\ \frac{1000}{3600}\ (Wh\ kg^{-1})$$

$$SP = \frac{SE}{t}\ x\ 3600\ (W\ kg^{-1})$$

The volumetric capacitance was obtained according to the equation:

$$C_{vol} = C_{GCD}\ x\ d\ (F\ cm^{-3})$$

where d represents the density of active material.

2.1.4 Results and Discussion

2.1.4.1 Morphology/composition of FLG/C

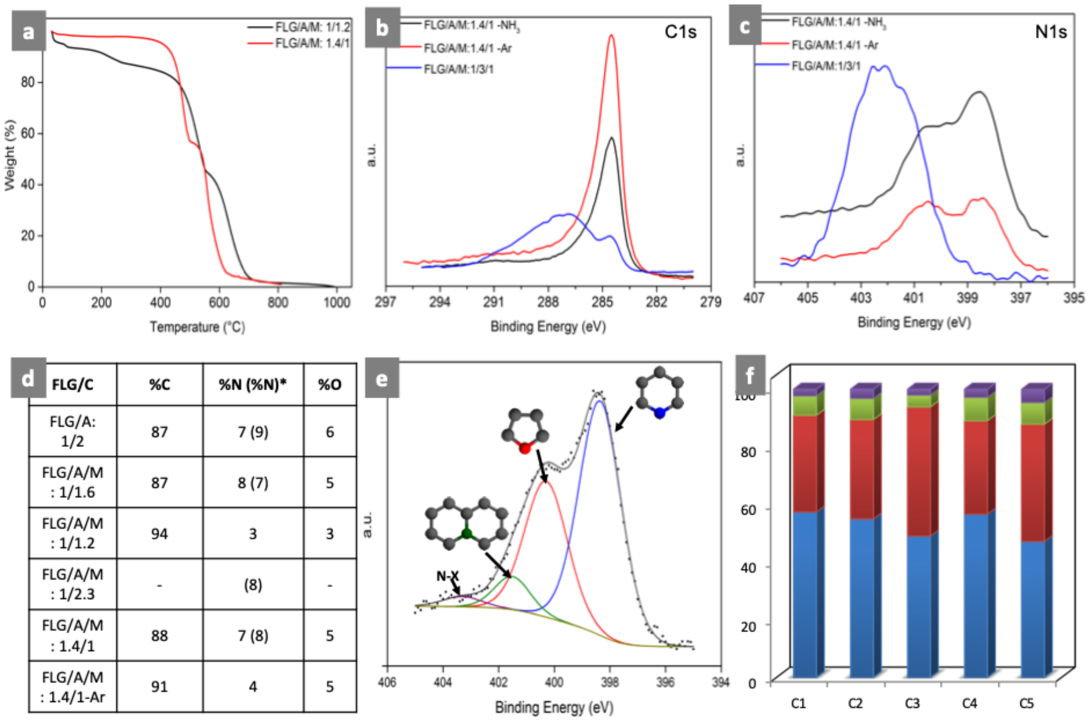

FLG/C	%C	%N (%N)*	%O
FLG/A: 1/2	87	7 (9)	6
FLG/A/M : 1/1.6	87	8 (7)	5
FLG/A/M : 1/1.2	94	3	3
FLG/A/M : 1/2.3	-	(8)	-
FLG/A/M : 1.4/1	88	7 (8)	5
FLG/A/M : 1.4/1-Ar	91	4	5

Figure 2.5 Exemplary TGA curves of two FLG/A/M composites after carbonization, b,c) the exemplary XPS C1s and N1s spectra of FLG/A/M: 1.4/1 before and after carbonization under NH3 and Ar, d) Table 2 containing the % of C, N, O elements according to XPS and/or elementary analysis, e) deconvoluted N1s spectrum of FLG/A: 1/2 , f) % contribution of N-containing groups (blue-pyridinic; red-pyrolic; green-quaternary; purple-N-X) in different composites (C1-FLG/A:1/2; C2-FLG/A/M:1/1.6; C3-FLG/A/M:1/1.2; C4-FLG/A/M:1.4/1; C5-FLG/A/M:1.4/1-Ar).*

The first step of FLG/C composites' preparation in water relates to the *in*-situ occurring exfoliation of EG that is possible due to the presence of large natural bio-surfactants with high hydrophilic-lipophilic balance (hHLB) and ultrasonication/mixing action [49, 50], FLG/hHLB. In the present study two hHLB systems, bovine serum albumin (A) and maltodextrine (M), are used for exfoliation process and as precursors of the carbon that is next formed via carbonization treatment yielding the composites (FLG/C). The composites are denoted as FLG/A and FLG/A/M, since all composites were formed from the mixture of FLG and A or FLG, A and M, with different ratio (**Table 2.1**). On the contrary to a simple exfoliation, the amount of used hHLB vs. FLG (also mixed A/M) is much higher in order to get sufficient final C content (300-1600% compared to 10% in a simple exfoliation). This amount decreases of course in significant way after carbonization while the final ratio of FLG/C is found by TGA analysis and e.g. resulting from FLG/A/M of initial ratio of 1/3/1 the final composite is defined as FLG/A/M:1.4/1, other one, the sample FLG/A/M:1/1.2 results from FLG/A/M of initial ratio of 1/1/3 (**Figure 2.5 (a)**). According to the TGA analysis higher amount of C is found after carbonization in the composites containing an excess of M vs. A. Most of the thermal decomposition of hHLB into C in the composites are performed under NH_3 at 600°C and are called simply carbonization, however it entails N-doping as well and the formation of new N-type groups can be observed by XPS spectroscopy. For the reason of comparison few selected composites are subjected to carbonization under Ar or temperatures lower then 600°C.

The exemplary C1s and N1s XPS spectra of FLG/A/M: 1/3/1 before and after carbonization in Ar and NH_3 are presented in **Figure 2.5 b** and **c** respectively. Table in **Figure 2.5** illustrates the relative % of C, N and O obtained from XPS and elemental analysis for selected samples. As one can see the C1s spectra (**Figure 2.5 (b)**) change totally after carbonization from the sp^3C and sp^3C- heteroatoms rich-signature at higher binding energy (BE) values related to the presence of hHLB(A/M) into sp^2C rich-signature at ~ 284.5 eV from FLG. The significant modification of N1s spectra after carbonization (**Figure 2.5 (c)**) includes a disappearance of the N-peaks from albumin (essentially amide groups) at higher BE and appearance of new peaks at lower BE from newly formed groups. A deconvolution of N1s spectra, exemplary from FLG/A: 1/2, **Figure 2.5 (e)**, indicates the presence of four type of peaks attributed to the pyridinic-N at 398.4 eV, pyrrolic/pyridone-N at 400.3 eV, quaternary-N at 401.5 eV and N-oxide (N-X) at 403.3 eV [51]. The **Figure 2.5 (f)** illustrates the % contribution of the N-containing groups in the most important samples and the one carbonized under Ar. In all composites the pyridinic and pyrrolic/pyridone N groups are in high excess compared to the rest and according to the literature these are the groups providing a pseudocapacitance from proton exchange [4]. In the composite subjected to NH_3 assisted doping a total % of N reaches c.a. 7-8%. The much lower % of N observed for Ar-treated sample is because of a doping effect from the decomposition of albumin. Consequently, the amount of N is poorer in the sample with initially high M content (FLG/C:1/1.2). We do not investigate in details the oxygen effect since its % is relatively low compared to N, while commonly only quinone-type groups can undergo redox reaction efficiently at low pH [4]. Likewise, the amount of sulfur that could remain in the composites from the albumin (e.g. cysteine) is hardly detected and consequently not considered for the investigations.

The morphological investigation by TEM micrography of carbonized FLG/C composites reveals that obtained FLG flakes have few microns' lateral size and 5-10 number of sheets, in average (**Figure 2.6 a, b**). In the carbon layer adsorbed over FLG surface the mesopores of c.a. 10-15 nm can be locally observed (**Figure 2.6 c**). This carbon derived from hHLB covers the surface of FLG flakes and at some extend links FLG flakes (**Figure 2.6 d**).

Some hHLB spheres are observed before the carbonization, that constitute an excess and is not adsorbed over FLG surface (**Figure 2.6 e**).

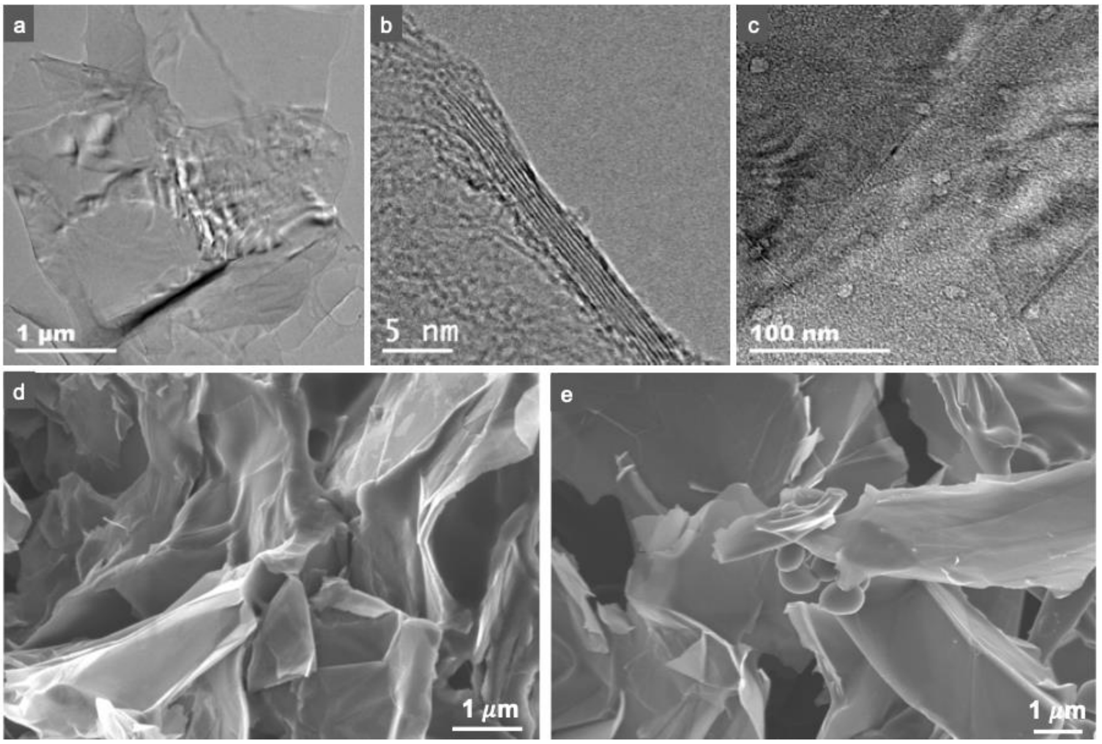

Figure 2.6 Representative TEM and SEM micrographs of FLG/C composites: a) few microns size FLG flakes, b) edge of FLG flakes containing 8 sheets, c) FLG surface covered by C with some mesopores, d) FLG-C composite after carbonization, e) FLG/A/M composite (before carbonization) with visible hHLB spheres.

An interesting difference was observed within the structures of the composites with variable A/M content at micro/macro-scale. The FLG/hHBL containing solely an albumin or its excess (vs. M) exhibits a strong tendency to form vertically aligned patterns. **Figure 2.7 (a,b)** are SEM micrographs of FLG/A: 0.5/4 after freeze-drying. The degree of alignment increases with A content and is almost absent in FLG/A/M: 1/1.2 (in. 1/1/3). On the contrary, the samples containing higher excess of maltodextrin demonstrates optically more typical porous, foam like structure. (This difference can already be observed in separately carbonized A and M alone, optical photos, **(Figure SI 2.1 a-c**). The vertically aligned FLG flakes in FLG/A (0.5/4) (**Figure 2.7 a,b**) form locally the hexagonal network in the horizontal plane (**Figure 2.7 b**). We assume that the observed tendency of alignment in A-rich FLG/hHLB composites are caused first of all by hydrogen bonding enhanced at some points by van der Waals interactions. The part of albumin adsorbed on FLG surface is denaturized and exist in secondary linear structure. The hydrogen bonding responsible for natural tridimensional conformation of albumin is destroyed during the ultrasonication, while new hydrogen bonds are formed between adsorbed linear chains of A on FLG and water, that next freezes and sublimes during the freeze-drying process. The linear A chains are uniformly adsorbed on FLG surface giving an access to homogenous and densely localized hydrogen bonding groups. One can find in the literature only recently reported freeze dried GO that alignment symmetry could be modified by addition of different additives such as ethanol, chitosan or ethanol [34]. In spite of the fact that the structures are somehow affected by carbonization process, less dense but still aligned patterns are observed (**Figure 2.7 (c)**) (It is worthy to note that it was possible to handle and manipulate the carbonized A-rich composites with some limitation but no difference was observed in specific gravimetric capacitance if compared to dispersed and dried composites' electrodes). Even though the composites are dispersed for the preparation of electrodes, a dense compact arrangement is again observed in dried electrode material **Figure 2.7 (d, e)**: side view and **Figure 2.7 (f)**: top view (locally, small extra part of less dense FLG/C splits out of the aligned patterns of **Figure SI 2.1**(d)). In the in-set of **Figure 2.7 (f)** in top-view, we can see some edges of the protruding FLG flakes. Such arrangement can be substantiated by a diffusion limited aggregation (DLA), the process occurring during the solvent evaporation. Such evaporation-induced aggregation are either unwanted in colloidal science or it brings interesting structures and e.g. in the case of FLG, the flat conductive fractal-like networks assemblies were obtained through DLA [51]. Several factors play a role in how DLA process runs and what kind of arrangement comes out and deeper studies are necessary to describe with certitude herein assembling process (are undergoing).

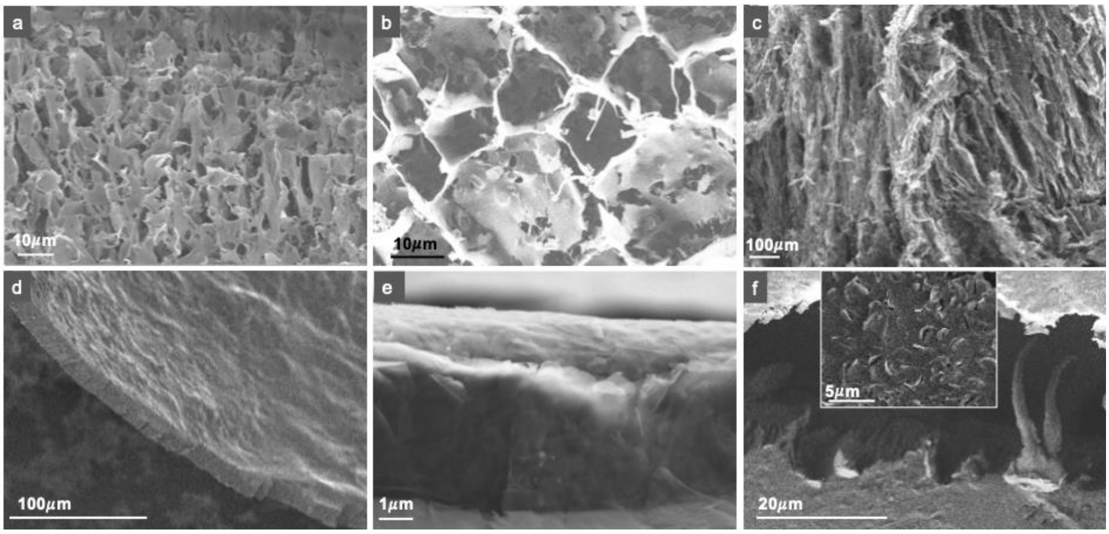

Figure 2.7 The representative SEM micrographs of FLG/A composite: a and b) before carbonization (side and top view), c) side view of FLG/C (FLG/A after carbonization, a.c.)), d and e) side-view of FLG/C (FLG/A a.c.) electrode, f) top-view of FLG/C (FLG/A a.c.) electrode.

Table 3 in **Figure 2.8** groups the values of specific surface area S_{BET} and $S_{micr.}$ contribution from micropores obtained by T-plot extrapolation, for the most important selected composites. All composites show low surface area, first, due to the relatively important thickness of FLG, and second and more significantly, due to the probable partial π-π interlayer re-stacking of the FLG during degassing process prior to the BET measurements. Relatively low S_{BET} of the composites is not surprising since we expect that the produced FLG flakes include minimum 5,6 graphene sheets in average, according to previously reported method for the exfoliation of graphite (EG) [3]. The exfoliation efficiency depends indeed on the nature of hHLB and hHLB: EG ratio that vary strongly within the present composites family. In addition, no separation step that can remove the thicker FLG flakes (sedimentation) after the exfoliation is applied here. Consequently, considering a theoretical value of surface area of graphene of 2675 m^2/g the obtained here surface values indicate the presence of 6-20 sheets in average within the FLG flakes depending on the composite.

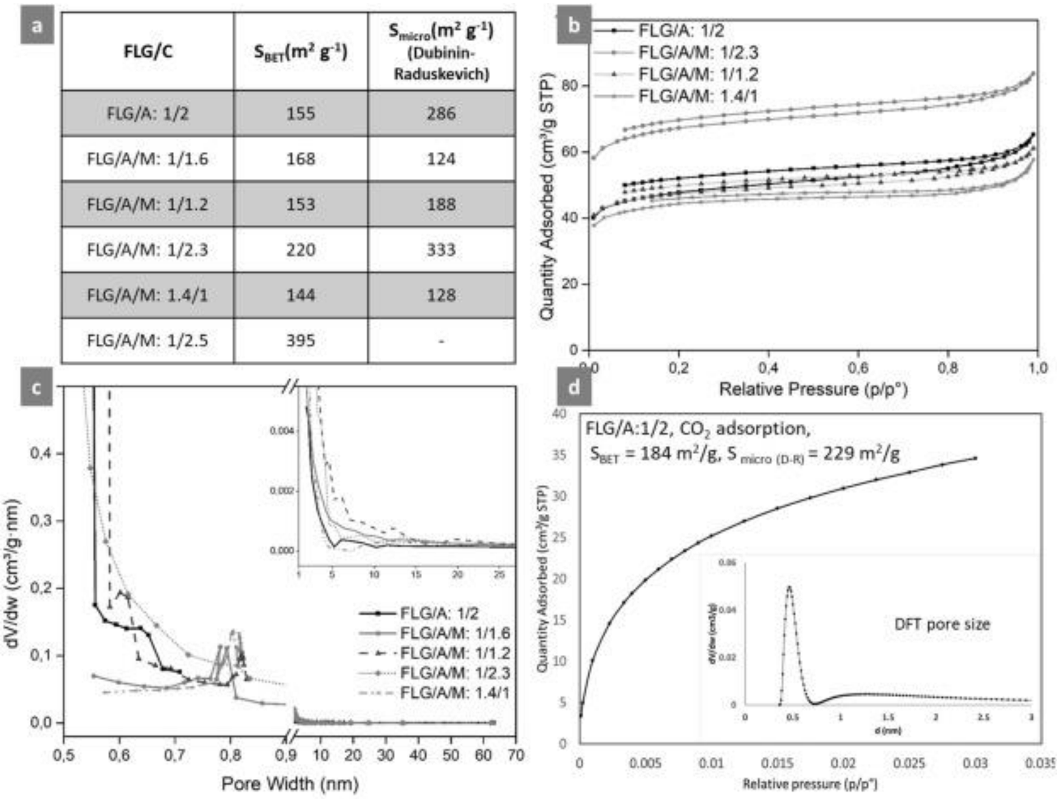

FLG/C	S_{BET}(m^2 g^{-1})	S_{micro}(m^2 g^{-1}) (Dubinin-Raduskevich)
FLG/A: 1/2	155	286
FLG/A/M: 1/1.6	168	124
FLG/A/M: 1/1.2	153	188
FLG/A/M: 1/2.3	220	333
FLG/A/M: 1.4/1	144	128
FLG/A/M: 1/2.5	395	-

Figure 2.8. a) Table 3 containing the total S_{BET} and contribution of micropores S_{BET}, b). exemplary isotherms, c) pore size distribution curves, inset: mesoporous region, d) isotherm from CO2 uptake with obtained SBET and S_{micro}, as well as DFT pore size distribution, for FLG/A:/1/2.

All composites show Type I isotherms and are predominantly microporous **Figure 2.8 (b)**. Some mesopores are detected through the pore size analysis that could correspond to the pores ~ 10 nm observed by TEM. The highly microporous (ultramicroporous) character can be observed also by the behavior of the N_2 adsorption and desorption isotherms, where necessary efforts need to be undertaken to choose the appropriate conditions for N_2 adsorption (equilibration time, degassing time and temperatures) [48, 52, 53]. The desorption isotherms do not completely overlap at lower pressure range. This suggests the presence of slit type pores, in which the lateral interaction between the adsorbed molecules is larger than the interactions between the C-covered FLG flakes during the adsorption and the width of slit pores (space between the flakes) increase. The materials are not rigid, what additionally can impact sorption process. The second adsorption analysis at lower N_2 speed supply, **Figure 2.8 (c)**, allowed to detect the very small micropores between 0.5 and 0.9 nm, nanopores, with relatively large distribution but for some samples a significant excess of pores with diameter around 0.5 nm (and/or below) were detected. These ultramicropores can be attributed to the slit pores created between aligned C-covered FLG flakes. For the reason of comparison, the adsorption was also performed by CO_2 uptake for one sample, FLG/A:1/2 (the method being more appropriate for the micropores < 1 nm). The analysis resulted in relatively comparable SBET and Smicro with N_2 adsorption values, while distribution of micropores size via DFT method confirmed the excess of pores of around 0.47 nm, **Figure 2.8 (d)**.

2.1.4.2 Supercapacitance of FLG/C composites

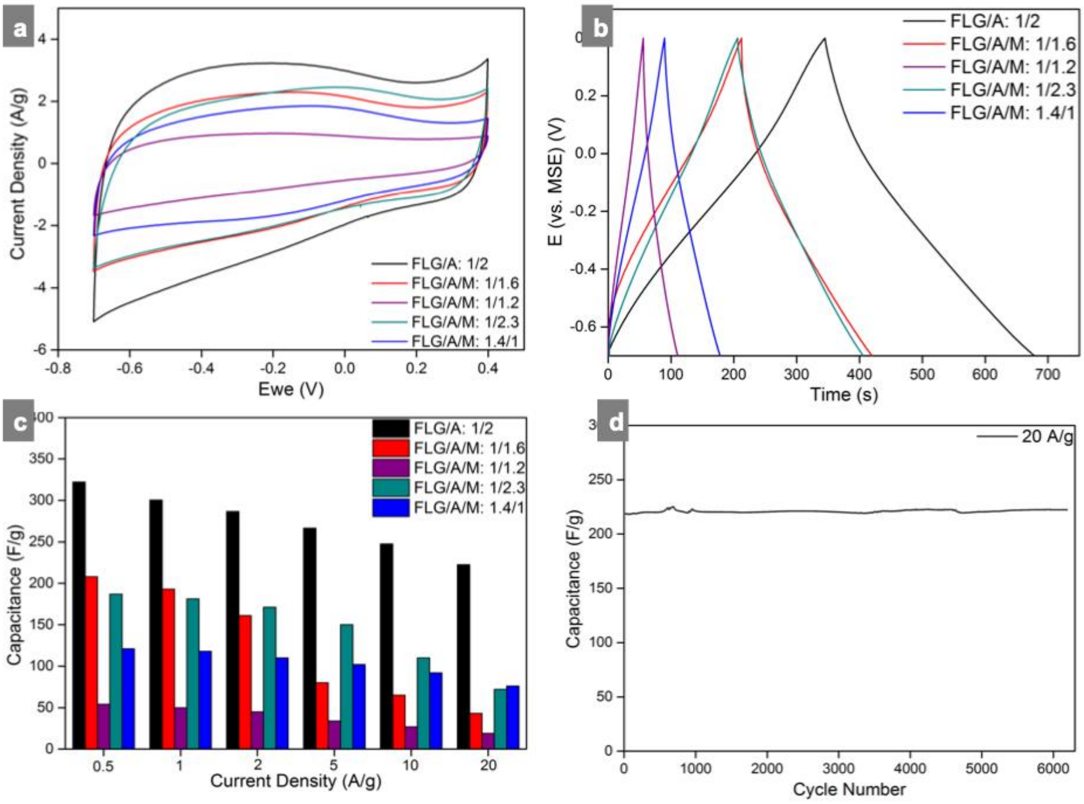

Figure 2.9 a) CV curves of FLG/A/(M) composites at 20 mV/s, b) GCD curves of FLG/A/(M) composites at 1 A/g, c) a graph combining obtained specific gravimetric capacitance values, CGCD at different current densities, d) stability test for FLG/A composite at 20 A/g.

The electrochemical performance of FLG/C composites were measured in 0.5M H_2SO_4 aqueous electrolyte in three electrode set-up and at a potential window of 1.1 V. **Figure**

2.9 illustrates the cyclic voltammograms at 20 mV/s **(a)**, galvanostatic charge-discharge curves (GCD) at current density of 1A/g **(b)**, a graph with specific gravimetric capacitance values and their retention at higher current densities (0.5 A/g to 20A/g) **(c)** and cyclic stability test of 6000 cycles (capacitance retention) at 20 A/g for the best sample **(d)**.

Five composites were investigated (the composites treated under Ar and/or under lower temperature (400°C) exhibited lower electrochemical performance compared to the ones carbonized/N-doped under NH_3 at 600°C and consequently they will be not discussed here). In all composites the symmetrical CV curves and triangular shapes of the GCD for all composites reveal good reversibility behavior, also, the CV curves of few samples show quasi-rectangular shape.

The CV current density first increases, next stabilized and finally decreases systematically along the potential shift towards positive values. The potential window of the stable current density corresponding to double layer capacity contribution varies however with the samples being low in sample poor in FLG e.g. FLG/A/M:1/1.6 and relatively large in FLG/A/M/:1.4/1. The highest capacity, 322 F/g at 0.5 A/g, is measured for FLG/A:1/2 (in. 0.5/4), the composite initially consisting of albumin hHLB solely. Two other best capacitances at 0.5 A/g belong to the composites with similar initial ratio to the best sample of FLG/C, i.e. 208 F/g for FLG/A/M: 1/1.6 (in. 0.5/3/1) and 187 F/g for FLG/A/M:1/2. (in. 0.5/1/3). Likewise, the FLG/A/M:1/1.14 originating from FLG/A/M:1/3/1 demonstrates higher capacity than FLG/A/M:1/1.2 originating from FLG/A/M:1/1/3. The composites with high amount of M show lower capacities compared to their A-rich counterparts. There is no correlation between capacitance of the composites and S_{BET}. The three composites exhibiting the highest but different capacitances at 0.5 A/g have similar S_{BET}. The composite with highest S_{BET} (FLG/A/M:1/2.5) show very low capacitance (F ≈ 22 F/g, 0.5 A/g). Simply, also all the S_{BET} values obtained for FLG/C composites are extremely low considering very good capacities demonstrated by the composites. This inconsistency comes from the fact that the S_{BET} does not necessarily reflect the effective surface area accessible by electrolyte ions (E-SSA) [54], especially if ultramicropores are present in excess. The “traditional” and “basic” figures of merit for design of high capacitance, i.e. high specific surface area and sufficiently large pores diameter, were shown to collapse in the case of “nanoporous” materials. In carbide derived carbon, the capacitance decreased with lowering the pore size to the size lower than twice the solvated electrolyte ions, then it increases again for the pores below the size of solvated ions, below 1 nm [55]. It seems that the optimal initial ratio of hHBL vs. FLG is like 8 to 1 (FLG/A:0.5/4, FLG/A/M: 0.5/3/1). The increase or decrease of hHBL content results in lower capacity values. The capacitance values obtained from A and M alone prepared at the same conditions as the FLG/C shows very low capacitance of c.a. 7 F/g. Such small value suggests that most of the measured capacitance in the composites comes from FLG, maintaining in mind, that the presence of minimum amount of C that is necessary to make the spacer for FLG flakes. From the other hand the FLG flakes permit first for A/M adsorption and consequently better dispersion of C. The additional capacitance investigations were performed for FLG/A/M: 1.4/1 (in. 1/3/1 carbonized under Ar or under NH_3 but at lower or higher temperature (200, 400 and 800°C). All these samples showed much lower electrochemical performance compared to the ones carbonized under NH_3 at 600°C.

The highest capacitance retention at higher current density (up to 20 A/g) is observed for the composites rich in FLG, **Figure 2.9 (c)**, confirming a great ability of graphene/FLG to sustain high current density. (The additional measurements of stability was performed for doubled mass of FLG/A samples, i.e. 1 mg/cm^2, **Figure SI 2.2**). Still, the stability is very good, while the capacitance is more than twice lower probably due to the increase of the samples thickness with related slowed transport through the sample film and /or modification of the FLG alignment/density).

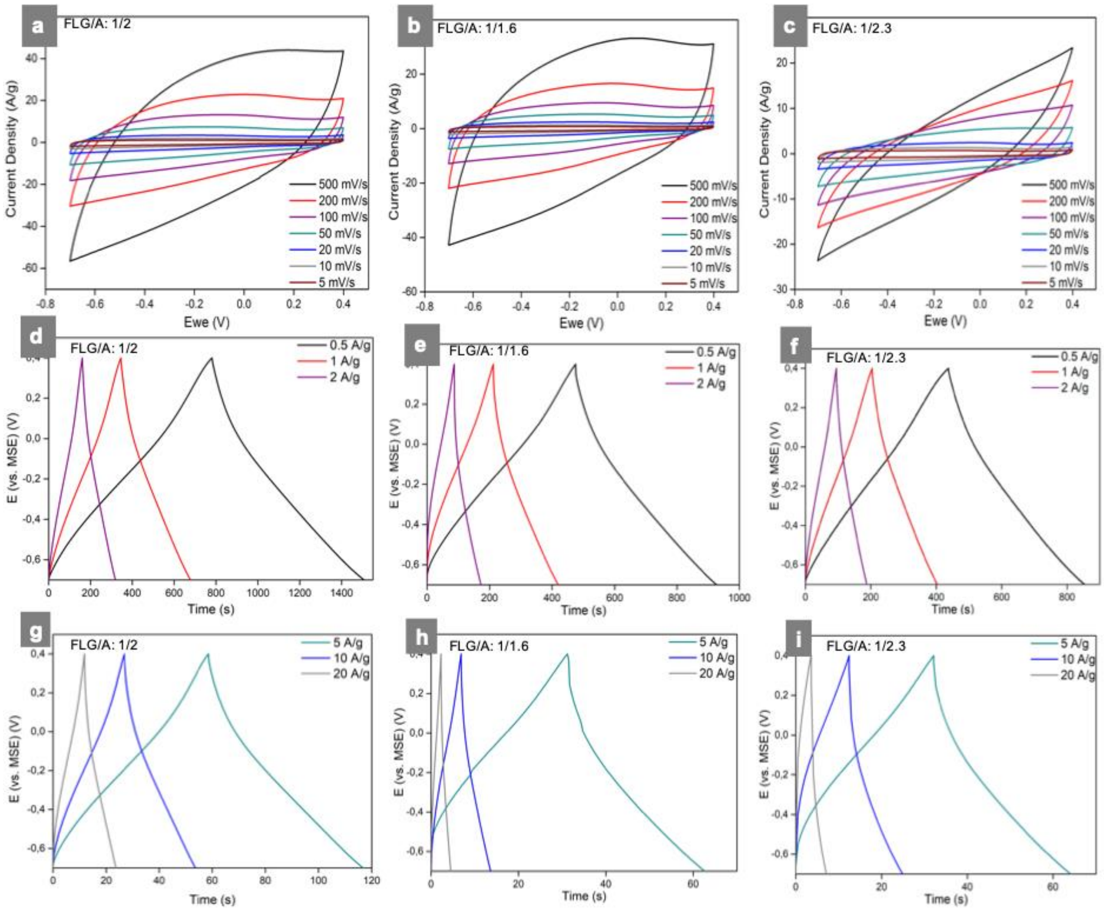

Figure 2.10 a–c) CV and d-i) GCD curves of FLG/A:1/2, FLG/A/M:1/1.6, FLG/A/M:1/2.3 at different potential sweeps.

The excellent retention is measured for the FLG/A:1/2, its capacitance drops from 322 F/g at 0.5 A/g to 222 F/g at 20 A/g, i.e. ~ 30% of drop. Slightly higher drop of capacitance of 37%

is measured for FLG/A/M: 1.4/1 (in. 1/3/1), from 121 F/g to 76 F/g, respectively, while a significant capacitance reduction is successively observed for the samples containing higher amount of C, i.e. ~ 88% for FLG/A/M : 1/1.6 (206 F/g at 0.5A/g to 25 F/g at 20 A/g) and ~ 61 % for FLG/A/M : 1/2.3. In the initially M-rich sample (in. FLG/A/M : 1/1/3), despite relatively high amount of FLG, a drop of capacitance is relatively high (~ 65%), and the capacitance is very low, 54 F /g at 0.5A/g. **Figure 2.10** illustrates also CV curves at different potential scan rate up to 500 mV/s (**a-c**) and GCD curves for current densities between 0.5 to 20 A/g for three composites (**d-i**) , FLG/A: 1/2, FLG/A/M:1/1.6 (excess of A) and for the one containing initially an excess of M, FLG/A/M:1/2.3 (excess of M). As one can see with the increase of potential sweep, the CV curves exhibit increasing features of pseudocapacitance in FLG/A/M:1/2 and especially in FLG/A/M:1/2.3. This behavior at high scan rate, far from "ideal" supercapacitor, can be probably associated with electrical transport limitation as well as the electrolyte transport limitation, i.e. resistance in the ultramicroporous that limit effective, accessible surface area [56, 57].The impact of ultramicropores structures seems to be significant, the highest S_{micro} was measured in FLG/G/A:1/2.3; consequently the interfacial DL capacitance does not have enough time to form at high fast scan rate.

In order to investigate the contribution of C_{Ps} originating from redox reactions vs. C_{DL} we applied the method recently adapted for carbon based materials [4, 7] from metal oxides [58]. Accordingly, the total voltammetric charge Q_T is obtained by plotting 1/q vs. $\nu^{1/2}$ and extrapolation of the tendency curve to $\nu = 0$, while q_{DL} by plotting q vs. $\nu^{-1/2}$ and extrapolation of charge (tendency curve) to ∞, **Figure 2.11 (a, b)**. The corresponding C_T and C_{Ps} values are next obtained by dividing q_T and q_{DL} by the potential window (1.1V), while q_{Ps} and/or C_{Ps} can be consequently achieved by differencing corresponding T and DL values.

The obtained voltammetric capacitance values: maximum total C_T, C_{Ps}, C_{DL} and C_{Ps}% are presented in Table 4, **Figure 2.11** (**c**), as well as calculated from the CV curves the CV capacitance (C_{CV}). The increasing tendency of calculated C_T is consistent with the obtained $C_{GCD,}$ except one sample which further shows very high pseudocapacitive contribution. This latter, pseudocapacitive contribution, is probably a main reason of the observed discrepancies between C_T and C_{GCD} in all composites. The discrepancies increase with increase of C_{Ps}%. Due to the relatively slow sweep in CV the C_{CV} were calculated at 5 mV/s. Likewise, the omitted initial part of discharge curves (GCD) related to IR drop form the internal resistance could be also the reason for the difference between obtained C_{GCD} and C_{CV} for few samples.

The estimated C_{Ps} varies from 68 to 87%. They are quite high even if taking into account the fact that most of the composites has significant amount of C. If we look however the CV curves as a function of potential sweep, **Figure 2.11** (**a-c**), we clearly find evolution of C_{Ps} contribution with increasing of V sweep, especially for FLG/A/M:1/2.3, the sample with the initial excess of M. Considering a C_{DL} contribution, the estimated values do not follow obtained SBET or S_{micro} area. We assign this behavior to different edges exposure of FLG sheets, which differs more due to the composites' architecture and not to the edges content. Consequently, despite relatively low S_{BET}, the best samples show high CDL contribution, since it origins from the easily accessible aligned flakes with exposed edges but also inter-flakes slit ultramicropores.

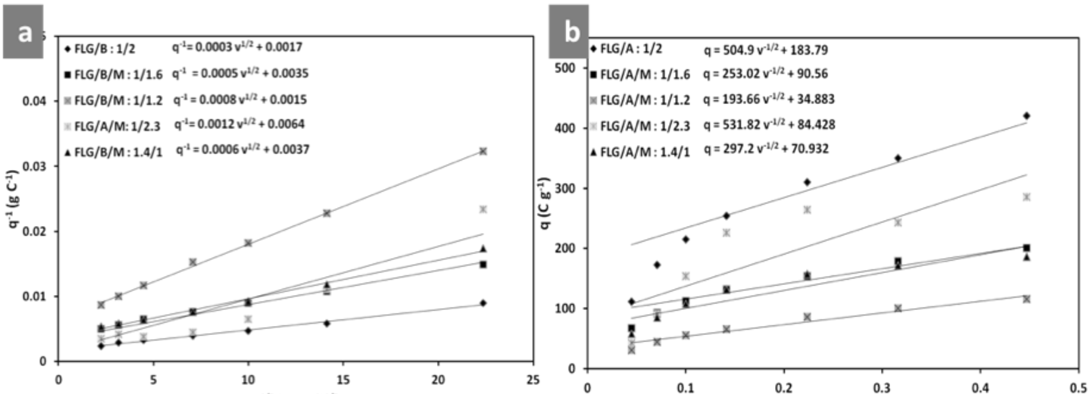

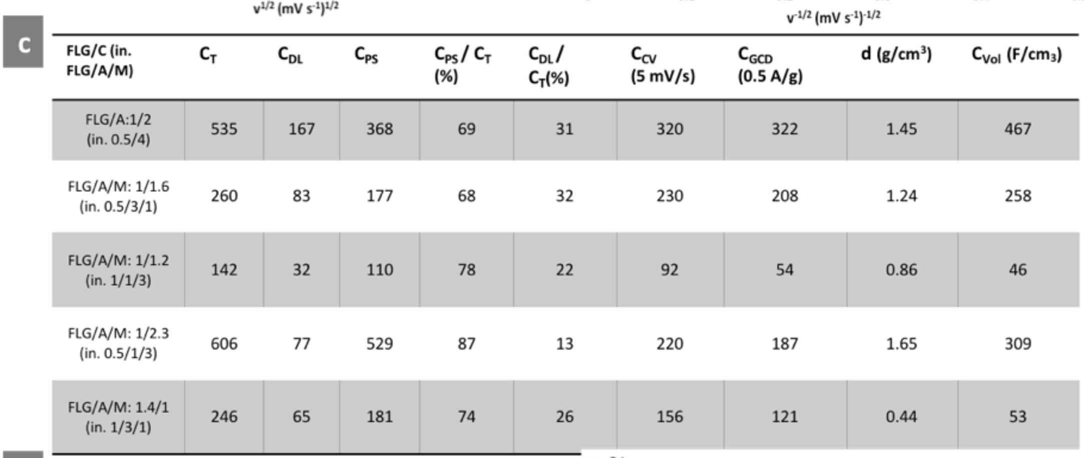

FLG/C (in. FLG/A/M)	C_T	C_{DL}	C_{PS}	C_{PS} / C_T (%)	C_{DL} / C_T(%)	C_{CV} (5 mV/s)	C_{GCD} (0.5 A/g)	d (g/cm³)	C_{Vol} (F/cm₃)
FLG/A:1/2 (in. 0.5/4)	535	167	368	69	31	320	322	1.45	467
FLG/A/M: 1/1.6 (in. 0.5/3/1)	260	83	177	68	32	230	208	1.24	258
FLG/A/M: 1/1.2 (in. 1/1/3)	142	32	110	78	22	92	54	0.86	46
FLG/A/M: 1/2.3 (in. 0.5/1/3)	606	77	529	87	13	220	187	1.65	309
FLG/A/M: 1.4/1 (in. 1/3/1)	246	65	181	74	26	156	121	0.44	53

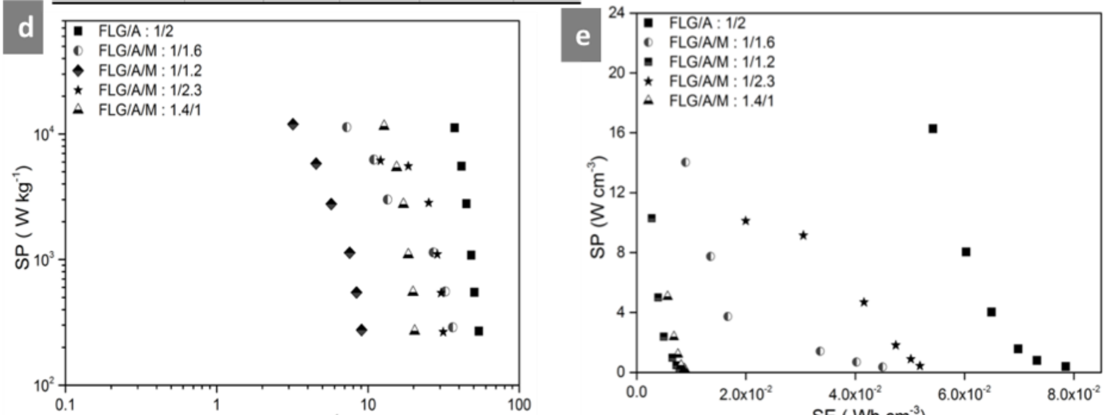

Figure 2.11 Estimations of DL/Ps capacitance contribution: a) dependence of q^{-1} vs. $\nu^{1/2}$, b) dependence of q vs. $\nu^{-1/2}$; c) table 4 regrouping the maximum total C from CV and DL, Ps contributions (C_T, C_{DL}, C_{Ps}, C_{Ps}/C_T, C_{DL}/C_T), capacitance from GCD (C_{GCD}), voltametric C (C_{CV}), packing density (d) and volumetric capacitance (Cvol); d and e) mass and volume normalized Ragone plots.

Let's recall that FLG/A (FLG:1/2) is the one where the alignment of the FLG and consequently the exposition of the edges is maximal. Good accessibility of the FLGs' edges in the composites, exhibiting FLG's alignment tendency (initially A-rich), induce higher electrochemically active surface area. As mentioned in the introduction, the input of the graphene edges into total capacitance was confirmed recently several times [10, 11, 15-17, 59-61]. In the theoretical studies using edges-passivated graphene nanoribbons the effect of edges on quantum and DL capacitances were clearly demonstrated [61]. The graphite containing the KOH-etched pits with very small micropores and exposed edges showed optimal capacitance [62]. It was found that the capacitance decreased with increase of SSA. The exposure of the edges and significant nanoporous feature entails also high volumetric capacitance [55, 62], the microporosity maximize a density of ion storage and the exposed edges with superior ability for charge accumulation compared to the basal plane. This is also true for the present FLG/C composites. The observed nanoporosity comes indeed from the space between vertically aligned FLG-C flakes of those the edges which are "necked" towards the electrolyte ions.

Due to the alignment and quite compact structure, most of the composites exhibit very high densities, between 0.44 and 1.65 g/ cm^3, and consequently high volumetric capacities (Table 4, **Figure 2.11**), with the best sample showing the volumetric capacity as high as 467 F/cm^3. Such high densities for densely aligned FLG-C flakes are expected; they are placed between the low density of graphene (in 3D foam structures) and that of graphite (~ 2.2 g/cm^3). Relatively low densities were measured for two composites with higher FLG content (0.88 and 0.44 g/cm^3) which can be due to the insufficient C-to-FLG ratio and more hydrophobic character from FLG counterpart; these two composites are the ones with lower M content.

The Ragone plots, based on mass and volume normalized capacitance values show similar tendency within the composites except FLG/A/M: 1.4/1, of which C_{vol} significantly decreases due to the relatively low density, **Figure 2.11 (d, e)**. The three composites with optimal initial ratio of FLG/A/M: 0.5/4, i.e. FLG/A/M: 0.5/1/3, FLG/A/M: 0.5/3/1 and FLG/A: 0.5/4 revealed higher volumetric energy and power densities compare to the gravimetric merits. The most significant change is established for FLG/A/M: 0.5/1/3, for which additionally relatively fast discharging results in very high power density of 0.437 W/cm^3 and energy of 0.052 Wh/cm^3. The best sample, i.e FLG/A shows 54 Wh/kg at 269 W/kg of gravimetric and 0.078 Wh/ cm^3 at 0.39 W/cm^3 of volumetric energy and power densities respectively. The obtained performance is quite high compared it for instance with the results obtained also for one electrode in N-graphene [8].

2.1.5 Conclusion

FLG/C composites with different FLG/C ratio were prepared by direct exfoliation of graphite in water, followed by carbonization-N-doping treatment, where C were initially albumin or albumin/maltodextrin. The DL and Ps capacitance contribution are estimated for the composites. Despite very low specific surface area S_{BET}, high capacities are obtained for FLG/A/(M) with general ratio of 0.5/4, i.e. FLG/A/M: 0.5/3/1, FLG/A/M: 0.5/1/3 and the best one for FLG/A: 0.5/4. The later one exhibits the gravimetric and volumetric capacity of 322 F/g and 467 F/ cm^3 at 0.5 A/g respectively and shows superior stability at high current density. The great performances obtained for few composites are the result of their unique architecture; first, a presence of nanopores; second, a vertical alignment of FLG-C flakes was obtained in the composites with albumin or albumin excess composites. The vertically aligned FLG/C brings great edges exposure increasing efficient electrochemical surface. Most of the composites have also high to very high packing density, what entails non-negligible volumetric capacitances. The charge and ionic transport limitations are present at scan rates above 100 mV/s especially for the samples with high C content and S_{micro} area.

References

[1] M. Pumera, *Chem. Rec.*, 2009, Vol. 9, 211-223

[2] W. Yuan, Y. Zhou, Y. Li, C. Li, H. Peng, J. Zhang, Z. Liu, L. Dai, G. Shi, *Sci. Rep.*, 2013, Vol. 3, 2248

[3] H. Ba, L. T.-Phuoc, C. P.-Huu, W. Luo, W. Baaziz, T. Romero, I. Janowska, *ACS Omega*, 2017, Vol. 2, 12, 8610-8617

[4] Y.-H. Lee, K.-H. Chang, C.-C. Hu, *J. Power Sources*, 2013, 227, 300-308

[5] R. N. Rambaran, L. C. Serpell, *Prion*, 2008, Vol. 2, 3, 112–117

[6] Frąckowiak, P. Ratajczak, F. Béguin, Electrochemical Capacitors Based on Carbon Electrodes in Aqueous Electrolytes, in: Electrochemistry of Carbon Electrodes, Wiley-VCH Verlag GmbH & Co. KGaA (2015)

[7] J.-S. M. Lee, M. E. Briggs, C. C. Hu, A. I. Cooper, *Nano Energy*, 2018, Vol. 46, 277-289

[8] P. Simon, Y. Gogotsi, *Nat. Mater.*, 2008, Vol. 7, 845

[9] B. You, L. Wang, L. Yao, J. Yang, *Chem. Comm.*, 2013, Vol. 49 , 5016-5018.

[10] Y. Zhou, X. Xu, B. Shan, Y. Wen, T. Jiang, J. Lu, S. Zhang, D. P. Wilkinson, J. Zhang, Y. Huang, *Energy Storage Mater.*, 2015, Vol. 1, 103-111

[11] J.P. Randin, E. Yeager, *J. Electrochem.*, 1971, Vol. 118, 711-714

[12] X. Yang, J. Zhu, L. Qiu, D. Li, *Adv. Mater.*, 2011, Vol. 23, 2833-2838

[13] M. D. Stoller, S. Park, Y. Zhu, J. An, R. S. Ruoff, *Nano Lett.*, 2008, Vol. 8, 3498-3502

[14] L. L. Zhang, R. Zhou, X. S. Zhao, *J. Mater. Chem.*, 2010, Vol. 20, 5983-5992

[15] V. Sahu, S. Shekhar, R.K. Sharma, G. Singh, *ACS Appl. Mater. Interfaces*, 2015, Vol. 7, 3110-3116

[16] J. Yan, J. Liu, Z. Fan, T. Wei, L. Zhang, *Carbon*, 2012, 50, 2179-2188

[17] H.-K. Kim, S.-M. Bak, S. W. Lee, M.-S. Kim, B. Park, S. C. Lee, Y. J. Choi, S. C. Jun, J.T. Han, K.-W. Nam, K. Y. Chung, J. Wang, J. Zhou, X.-Q. Yang, K. C. Roh, K.-B. Kim *Energy Environ. Sci.*, 2016, Vol. 9, 1270-1281

[18] C. Liu, Z. Yu, D. Neff, A. Zhamu, B.Z. Jang, *Nano Lett.*, 2010, Vol. 10, 4863-4868

[19] L. Zhang, G. Shi, *J. Phys. Chem. C*, 2011, Vol. 115, 17206-17212

[20] S. M. Jung, D.L. Mafra, C.-T. Lin, H.Y. Jung, J. Kong, *Nanoscale*, 2015, Vol. 7, 4386-4393

[21] C. Li, G. Shi, *Nanoscale*, 2012, Vol. 4, 5549-5563

[22] X. Yang, C. Cheng, Y. Wang, L. Qiu, D. Li, *Science*, 2013, Vol. 341, 534-537

[23] H. J. Qiu, L. Y. Chen, Y. Ito, J. L. Kang, X. W. Guo, P. Liu, H. Kashani, A. Hirata, T. Fujita, M. W. Chen, *Nanoscale*, 2016, Vol. 8, 18551-18557

[24] Y. Tao, X. Xie, W. Lv, D.-M. Tang, D. Kong, Z. Huang, H. Nishihara, T. Ishii, B. Li, D. Golberg, F. Kang, T. Kyotani, Q.-H. Yang, *Sci. Rep.*, 2013, Vol. 3, 2975

[25] J. Zhou, J. Lian, L. Hou, J. Zhang, H. Gou, M. Xia, Y. Zhao, T.A. Strobel, L. Tao, F. Gao, *Nat. Commun.*, 2015, Vol. 6, 8503

[26] Y. Yoon, K. Lee, S. Kwon, S. Seo, H. Yoo, S. Kim, Y. Shin, Y. Park, D. Kim, J.-Y. Choi, H. Lee, *ACS Nano*, 2014, Vol. 8, 4580-4590

[27] J. R. Miller, R.A. Outlaw, B.C. Holloway, *Science*, 2010, Vol. 329, 1637-1639

[28] Z. Zhang, C.-S. Lee, W. Zhang, *Adv. Energy Mater.*, 2017, Vol. 7, 1700678

[29] J. J. Yoo, K. Balakrishnan, J. Huang, V. Meunier, B. G. Sumpter, A. Srivastava, M. Conway, A. L. Mohana Reddy, J. Yu, R. Vajtai, P. M. Ajayan, *Nano Lett.*, 2011, Vol. 11, 1423-1427

[30] Y.-W. Chi, C.-C. Hu, H.-H. Shen, K.-P. Huang *Nano Lett.*, 2016, Vol. 16, 5719-5727

[31] J.-H. Deng, S.-L. Wu, Y.-M. Yang, R.-T. Zheng, G.-A. Cheng, *Nucl. Instrum. Methods Phys. Res. Sect. B Beam Interact. Mater. Atoms*, 2013, Vol. 307, 177-180

[32] P. Zhang, J. Li, L. Lv, Y. Zhao, L. Qu, *ACS Nano*, 2017, Vol. 11, 5087-5093

[33] D. Li, Y. Liu, H. Ma, Y. Wang, L. Wang, Z. Xie, *RSC Adv*., 2015, Vol. 5, 31670-31676

[34] C. Wang, X. Chen, B. Wang, M. Huang, B. Wang, Y. Jiang, R.S. Ruoff, *ACS Nano*, 2018, Vol. 12, 5816-5825

[35] L. Hu, X. Peng, Y. Li, L. Wang, K. Huo, L. Y. S. Lee, K. Y. Wong, P. K. Chu, *Nano Energy*, 2017, Vol. 34, 515-523

[36] K. Nomura, H. Nishihara, T. Asada, N. Kobayashi, T. Kyotani, *Energy Environ. Sci*., 2019, Vol. 12, 1542-1549

[37] Y. Xia, T. S. Mathis, M.-Q. Zhao, B. Anasori, A. Dang, Z. Zhou, H. Cho, Y. Gogotsi, S. Yang, *Nature*, 2018, Vol. 557, 409-412

[38] L. Li, E. Liu, J. Li, Y. Yang, H. Shen, Z. Huang, X. Xiang, W. Li, *J. Power Sources*, 2010, Vol. 195, 1516-1521

[39] H. Ba, W. Wang, S. Pronkin, T. Romero, W. Baaziz, L. Nguyen-Dinh, W. Chu, O. Ersen, C. P.-Huu, *Adv. Sustain. Syst.*, 2018, Vol. 2, 1700123

[40] M. X. Wang, Q. Liu, H.-f. Sun, E.A. Stach, H. Zhang, L. Stanciu, J. Xie, *Carbon*, 2012, Vol. 50, 3845-3853

[41] Y. Li, G. Louarn, P.-H. Aubert, V. Alain-Rizzo, L. Galmiche, P. Audebert, F. Miomandre, *Carbon*, 2016, Vol. 105, 510-520

[42] J. Ma, T. Xue, X. Qin, *Electrochim. Acta*, 2014, Vol. 115, 566-572

[43] D. T. Pham, T. H. Lee, D. H. Luong, F. Yao, A. Ghosh, V. T. Le, T. H. Kim, B. Li, J. Chang, Y. H. Lee, *ACS Nano*, 2015, Vol. 9, 2018-2027

[44] Y. Bai, M. Du, J. Chang, J. Sun, L. Gao, *J. Mater. Chem. A*, 2014, Vol. 2, 3834-3840

[45] Y. Zhao, J. Liu, B. Wang, J. Sha, Y. Li, D. Zheng, M. Amjadipour, J. MacLeod, N. Motta, *ACS Appl. Mater. Interfaces*, 2017, Vol. 9, 22588-22596

[46] Z. Lei, T. Mitsui, H. Nakafuji, M. Itagaki, W. Sugimoto, *J. Phys. Chem. C*, 2014, Vol. 118, 6624-6630

[47] D. R. Dreyer, A.D. Todd, C.W. Bielawski, *Chem. Soc. Rev.*, 2014, Vol. 43, 5288-5301

[48] M. F. De Lange, T. J. H. Vlugt, J. Gascon, F. Kapteijn, *Micropor. Mesopor. Mat.*, 2014, Vol. 200, 199-215

[49] I. Janowska, L. T.-Phuoc, H. Ba, C. P.-Huu, Colloidal Nanomaterials/ polymolecular System Nanocomposites, and Preparation Methods, 2018

[50] D. H.-Jurcakova, M. Seredych, G. Q. Lu, T. J. Bandosz, *Adv. Funct. Mater.*, 2009, Vol. 19, 438-447

[51] I. Janowska, *Phys. Chem. Chem. Phys.*, 2015, Vol. 17, 7634-7638

[52] A. M. S.-Albero, J. M. J.-Galán, J. Silvestre-Albero, F. R.-Reinoso, *J. Phys. Chem. C*, 2012, Vol. 116, 16652-16655

[53] P. Bertier, On the use and abuse of N2 physisorption for the characterisation of the pore structure of Shales The Clay Minerals Society Workshop Lectures Series, 2016, 151-161

[54] L. Zhang, X. Yang, F. Zhang, G. Long, T. Zhang, K. Leng, Y. Zhang, Y. Huang, Y. Ma, M. Zhang, Y. Chen, *J. Am. Chem. Soc.*, 2013, Vol. 135, 5921-5929

[55] J. Chmiola, G. Yushin, Y. Gogotsi, C. Portet, P. Simon, P. L. Taberna, *Science*, 2006, Vol. 313, 1760-1763

[56] J. Niu, W.G. Pell, B.E. Conway, *J. Power Sources*, 2006, Vol. 156, 725-740

[57] W.-C. Chen, T.-C. Wen, *J. Power Sources*, 2003, Vol. 117, 273-282

[58] D. Baronetto, N. Krstajić, S. Trasatti, *Electrochim. Acta*, 1994, Vol. 39, 2359-2362

[59] Y. A. Kim, T. Hayashi, J. H. Kim, M. Endo, *J. Energy Chem.*, 2013, Vol. 22, 183-194

[60] I. Janowska, M. Lafjah, V. Papaefthymiou, S. Pronkin, C. Ulhaq-Bouillet, *Carbon*, 2017, Vol. 123, 395-401

[61] A. J. Pak, E. Paek, G. S. Hwang, *J. Phys. Chem. C*, 2014, Vol. 118, 21770-21777

[62] Y. J. Kim, C.-M. Yang, K. C. Park, K. Kaneko, Y. A. Kim, M. Noguchi, T. Fujino, S. Oyama, M. Endo, *ChemSusChem*, 2012, Vol. 5, 535-541

Supporting Information

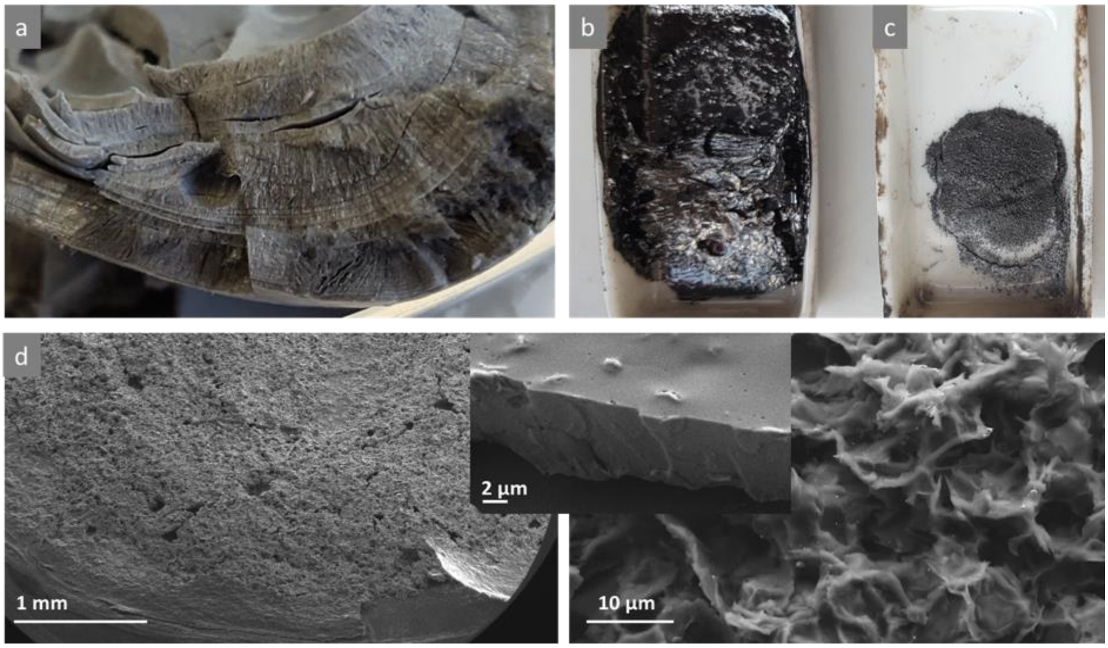

Figure SI 2.1Optical photos of a) FLG-A after freeze drying, b) carbonized albumin, c) carbonized maltodextrin, d) SEM micrographs of FLG/C electrode: top-view (left), basic main layer of aligned composite (in-set, center), top view of the zone with "extra" protruded FLG-C flake (right).

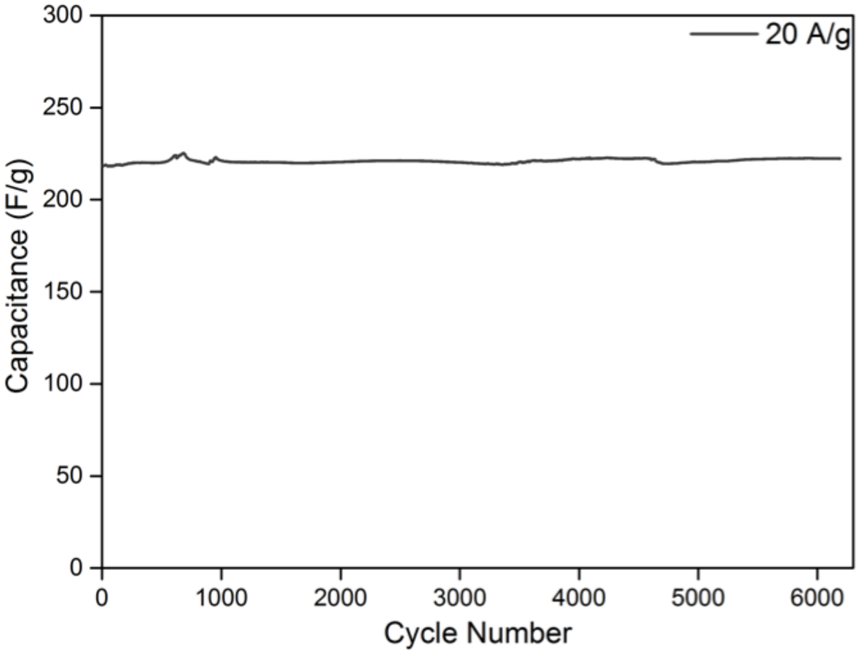

Figure SI 2.2 Stability test for the FLG/C:1/2 with mass of 1 mg cm^{-2}

Chapter 3

Using FLG as template for flat metal based nanoplatelets

FLG structuration is not only restricted to providing access to its edges and layers for electrochemical applications. Such materials are also helpful in acting as a support for obtaining more efficient metal nanoparticles. The progress of reaction is mostly driven by the nature of the catalyst used which in turn depends on the amount of active sites. As Richard Feynman said in his talk, "*There is plenty of room in the bottom*", which inspired the idea of moving to the nanoscale aspects of particles which in fact helps generate a larger number of active sites for any reaction. However, not only size but also a shape of metal-based particles influences their performance, and efficiently tailored, became a way to help "low active" metals to improve their activity. A constant need for making the non-noble metals competitively efficient for scale up demands push us to synthesise a thermally stable 2D NPs with enhanced surface-to-volume ratio and high dispersibility. The support centric catalyst design ideas identifies such issues. In this chapter, we discuss how the FLG materials can be used to obtain non noble metal nanoparticles (Fe-based) with enhanced 2D aspects.

The detailed study of two approaches to form flat Fe nanoparticles over FLG , including their synthesis/treatment is discussed below as an adaptation form of the publication; *Flatchem,* 2018, Vol. 9, 15-20

3.1 Few layer graphene as a template for Fe-based 2D nanoparticles

A. Mohanty,[a] W. Baaziz,[a,b] M. Lafjah,[a,c] V. da Costa,[b] I. Janowska[a*]
[a] Institut de Chimie et Procédés pour l'Énergie, l'Environnement et la Santé (ICPEES), CNRS UMR 7515-University of Strasbourg, 25 rue Becquerel 67087 Strasbourg, France
[b]Institut de Physique et Chimie des Matériaux de Strasbourg (IPCMS), CNRS UMR 7504-University of Strasbourg, France
[c] Laboratoire de Chimie des Matériaux (LCM), Faculté des Sciences Exactes et Appliquées, Université d'Oran1 Ahmed Ben Bella, BP 1524 EL Menouer, 31000 Oran, Algeria

3.1.1 Abstract

FLG supported structurally flat polygonal and hexagonal iron platelet NPs are prepared by two different high temperature annealing approaches, i.e., under "conventional" and µ-wave assisted heating. Both methods confirm that FLG acts as a template for 2D NPs tailoring and flat Fe-based NPs with high surface-to-volume ratio are still well dispersed and stable at the temperatures as high as several hundreds of C° despite weakened interfacial interactions between FLG and NPs. The high surface-to-volume ratio benefit of 2D NPs geometry is highlighted by mathematical estimation. The additional morphology of grown CNFs confirms the flat faceted structures of NPs catalysts.

Keywords: 2D nanoparticles, Graphene, Surface-to-volume ratio, Structurization

3.1.2 Introduction

The continuous accelerating development and societal needs calls for the sustainability of the processes respecting the economic and environmental issues. Apart from the green technologies, synthesis and proceedings, the choice of crucial materials which are cost-benign, abundant but still highly active are being investigated at large. One of the examples reflecting such research are the efforts aiming to replace noble metal nanoparticles (NPs) catalysts such as Pt in fuel cells by non-noble metals or metal-free catalysts that are often based on graphitic carbons [1-3]. Generally, the activity and properties of NPs, and materials does not depend exclusively on their chemical nature but also on their geometrical morphology entailing the related electronic structure modifications and exposition of chemically active sites. It has been shown several times that the geometry of metal nanoparticles influences their charge transport, optical features and reactivity [4-7] and so its tailoring is interesting from the fundamental knowledge and applications point of view. The most common methodology to achieve variable well shaped metal-based NPs is the solution route synthesis processes such as solvothermal method, in which apart from the metal precursors, organic stabilizers and capping agents are used [5]. Some applications however, such as high temperature catalytic processes, require well dispersed, thermally stable, high surface-to-volume ratio metal-based NPs with pure, ready to react active surfaces (or defects). The appropriate choice and modification of the support should help to address the problem of dispersion and stability; while the morphology of the NPs are driven by the strength of metal-support interactions, which in turn depends on the surface-free energy of the separated systems. The oxide supports commonly used in heterogenous catalysis provide 3D NPs, although several reports indicating well-structured facet and 2D NPs obtained through the SMSI effect (strong metal/support interactions), can be cited, viz. Pt/TiO_2, Ag/Al_2O_3, Pt/Fe_3O_4 [7]. In principle, the supports are rarely used for tailoring of metals' geometry. The recent years have seen carbon nanomaterials as metal supports because of their nanoscopic dimension, weak porosity and unique electrical/thermal conductivities with 2D graphene at the forefront. The presence of defects (point, edges) or functionalized groups (often oxygen rich) in graphitic carbons similarly as in oxides are highly important to help attach the metal NPs and increase their thermal stability [8-11]. For this reason the edges-to plane rich carbon structures such as CNFs or oxygen rich graphene oxide (GO) are often used to support metal-based NPs [12, 13].

Herein, we forsake the granular structure and propose few layer graphene (FLG) as a template for tailoring of Fe-based NPs into 2D geometry platelets at reductive and annealing conditions. We use two different hybrids and heating modes for this purpose. The first mode is used for synthesis of spherical FLG-Fe_xO_y-1 (**Figure SI 3.1 (a)**), wherein $Fe_{3-x}O_4$ NPs synthesized by solvothermal method are supported on FLG obtained by surfactant assisted liquid exfoliation method from expanded graphite [14]. The NPs quite rapidly evolve with time into iron (II) oxide. This system is subjected to the hydrogen flow under "standard" heating mode. The second mode involves deposition of iron oxide NPs by wetness impregnation method over FLG obtained by mechanical ablation of graphite [15] (**Figure SI 3.1 (b)**). They are further subjected to microwaves heating in liquid ammonia.

3.1.3 Material and Methods

3.1.3.1 FLG-Fe_xO_y-1

FLG has been prepared by liquid ultrasonication of expanded graphite in toluene in the presence of Triton X-100 using probe sonicator. The spherical $Fe_{3-x}O_4$ NPs over (FL)G were prepared according to the procedure described earlier by solvothermal synthesis method [14]. In brief, 150 mg of (FL)G were dispersed in 20ml of octyl by ultrasonication for 40 min. then

200 mg of iron stearate and 250 ml of oleic acid were added. All was heated up first to 120°C and next to 287°C with the heating rate of 5°C/min. in Air and remain in this temperature for 2h. The product was precipitated after cooling and addition of acetone to the mixture, and washed next by acetone/hexane mixture and centrifugation.

$Fe_{3-x}O_4$ NPs over (FL)G were submitted to annealing under Ar for 1h at 400°C. The second annealing was performed by heating up to 800°C and remaining in this temperature for 2h under H_2/Ar (1:1 vol.).

3.1.3.2 FLG-Fe_xO_y-2

FLG were prepared according to the procedure described earlier based on the mechanical ablation of graphite [15].

500 mg of (FL)G were dispersed by probe sonicator and under stirring for 30 min. 110 mg of iron nitrite dissolved in 20 ml of water was added dropwise to the (FL)G suspension under stirring. The mixture was stirred at 80°C till evaporation of water was complete. The powder was next calcinated at 250°C for 2 h and then pre-reduced under H_2/Ar (1:1 vol.) for next 2 h at 350°C. The resulted product was then shortly redispersed in liquid ammonia with concentration 1 mg/mL and subjected to the μ-wave heating at 800 W for 1h (Mars, CEM Corp). The final product was washed by water until neutral pH and dried at r.t. for 24 h and at 100 °C for 2h.

3.1.3.3 CNFs growth

FLG-Fe_xO_y-1 has been placed in the quartz reactor localized in the oven within typical CVD set-up conditions. After 0.5h of degassing with Ar, a temperature was raised to 800°C and at this temperature the gas flow containing ethane: H_2: Ar (100: 50:100 ml) was subjected for 40 min. All was next cooled to r.t. under Ar flow.

XPS analyses were performed with a MULTILAB 2000 (THERMO) spectrometer equipped with Al K anode (hν= 1486.6 eV). For deconvolution of spectra the CASA XPS program with a Gaussian−Lorentzian mix function and Shirley background subtraction was employed.

Transmission electron microscopy (TEM) was carried out on a Topcon 002B - UHR microscope working with an accelerated voltage of 200 kV and a point - to -point resolution of 0.17 nm. The sample was dispersed in ethanol and a drop of the suspension was deposited onto a holey carbon coated copper for analysis. Scanning electron microscopy (SEM) analysis was carried out on a Jeol JSM-6700F working at 3 kV accelerated voltage, equipped with a CCD camera.

TGA analyses were carried out on TA instrument SDT Q600, the rate of the heating was fixed at 5^o per min.

Raman spectroscopy was performed using Horiba Scientific Labram Aramis Raman Spectrometer (Jobin Yvon technology) with the following conditions: laser wavelength of 532.15 nm, D2 filter (1% power) and spectrum in regions from 1250 to 1650 and from 2600 to 2800 cm^{-1}, with integration time of 100 s for each phase.

AFM microscopy Atomic force microscopy (AFM) measurements were carried out with Dimension 3100 model from Veeco. The images were recorded using the tapping operating mode. We used standard cantilever with integrated Si tip; the resonant frequencies were in the range of 200-400 kHz (PPP-NCHR POINT PROBE-PLUS from Nanosensors).

3.1.4 Results and Discussion

The TEM micrograph of initial iron oxide /FLG system of FLG-FexOy-1, **Figure SI 3.1(a)**, shows uniformly spherical NPs with good homogenous distribution over the FLG surface. It was revealed previously that these NPs are relatively stable under heating in Ar atmosphere up to 400 °C [14]. Herein, the Ar treatment is also applied in order to remove the capping agent (oleate) and eventual surfactant residues (Triton X-100) from the FLG surface. Consequently, the temperature is increased to 800 °C and kept for 2 h under H_2/Ar flow (1:1 vol). Such treatment provides obviously some hydrogenation etching of FLG, as confirmed by TEM micrographs (**Figure 3.1 (c)**) [16], but primarily, it results in faceted flattened Fe-base NPs, **Figure 3.1**.

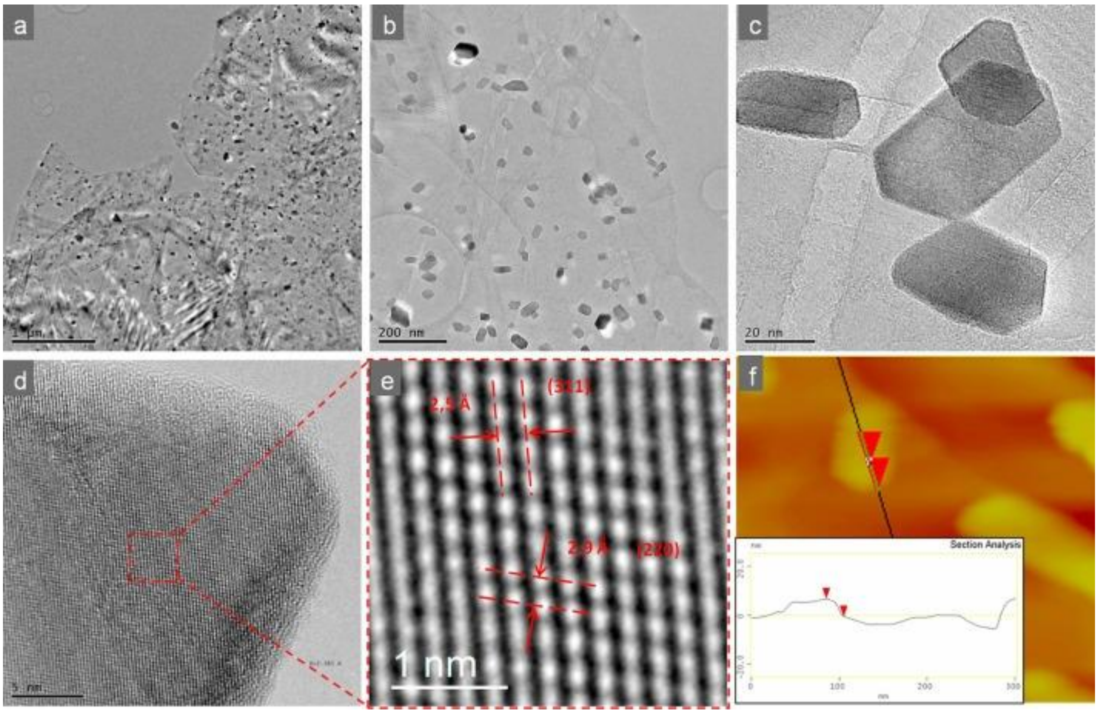

Figure 3.1 a-e) TEM micrographs with different magnifications of flattened iron oxide NPs over FLG (after annealing at 800°C under H_2/Ar (FLG-Fe_xO_y-1), f) AFM image and profile of (FLG-Fe_xO_y-1) system.

Despite some coalescence of NPs the metal is still relatively well distributed over the FLG support (**Figure 3.1 a** and **b**). It forms mostly the flattened rods with an average longitudinal size of 60 nm and other less symmetrical flattened polygons with visible facets. The intentional prolonged reductive/annealing treatment is aimed to "purify" the FLG surface and thus obtain a neat lattice that can further interact with NPs. The most possible scenario occurring during the annealing and in accordance with some previous individual observations, includes the stabilization of NPs along the edges/steps [17], where the number of FLG edges is additionally enhanced due to the etching phenomena [18], while the flattening of NPs is a result of their interaction with the neat FLG terraces' surfaces [2]. The elongation aspect of many polygons (rods like) confirms the stabilization action of the FLG edges, which are the linear defects.

The stabilization action of graphene edges was previously observed for Pt or Pd NPs over FLG [2, 9, 17], along with some degree of flattening for Pd NPs [2]. **Figure 3.1 (f)** shows an AFM image and topography profile of obtained flat Fe – based rods. The analysis of several profiles reveal that the ratio between the length of the rods and their thickness is around 10, e.g. 70 : 7 nm according to the presented AFM analysis. The TGA analysis confirms the removal and higher graphitization degree of FLG after annealing treatment, the shift of the main combustion temperature is significant, **Figure 3.2 (a)**. Likewise, the initial drop in weight of the sample before annealing is linked first to the loss of oleate/triton residue (few percent) and next to the oxidation of defected carbon which is significantly facilitated by the presence of iron oxide-oxidation catalyst. There is no significant change in contribution of oxygen containing groups' in the sample before and after the annealing according to the deconvoluted XPS C1s spectra, **Figure 3.2 (b)**, but the overall atomic percentage of O decreases after the annealing from c.a. 7 to 4 %.

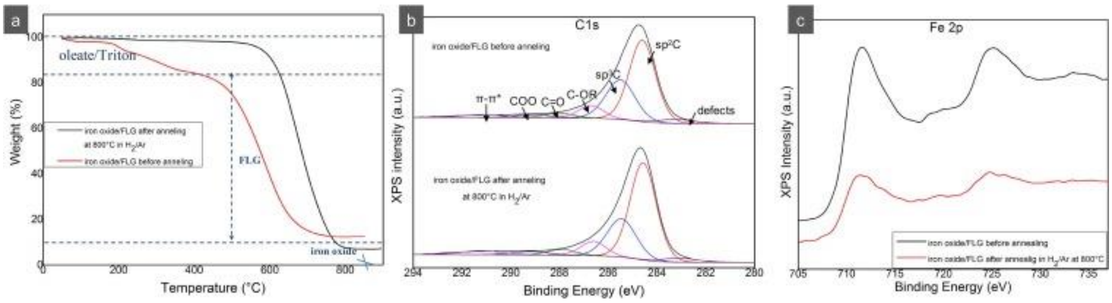

Figure 3.2 a) TGA curves of iron oxide/FLG before and after annealing at 800°C under H_2/Ar, (b, c) corresponding XPS C1s and Fe 2p spectra.

According to the high magnetization measurements performed just after treatment (not shown in this work) the NPs could be initially composed of FeO and/or Fe-Fe_3O_4 nanocomposites [19]. Since the reductive conditions induce the reduction of iron oxide, quite rapidly (several days) the chemical modification towards more oxidized phases occurs due to the well-known superior stability of the latter [19]. The presence of iron oxide is observed consequently by TEM and XPS analysis. The TEM reveals the iron oxide spinel structure and the XPS spectroscopy shows iron oxide (III) phase [20], the same that can be observed for the initial sample after certain time (**Figure 3.2**).

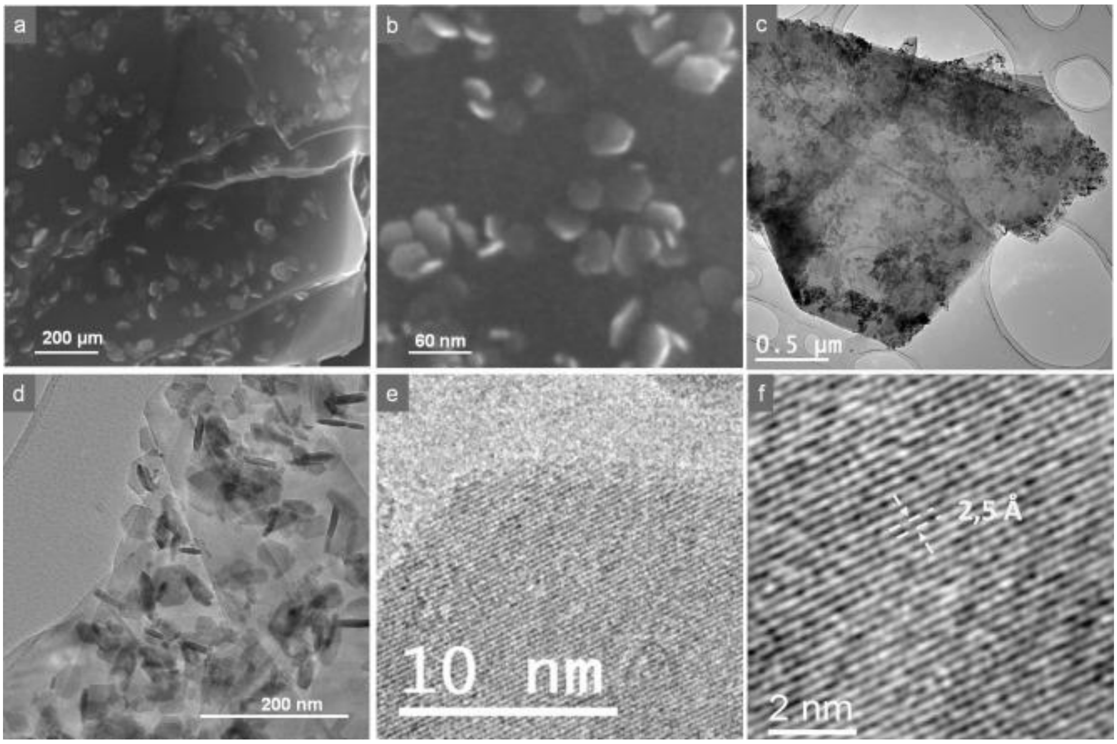

Figure 3.3 a, b) SEM micrographs and, c-f) TEM micrographs of iron oxide hexagonal platelets over FLG (FLG-Fe_xO_y-2).

The second sample, iron oxide over FLG prepared by impregnation method, is stirred in liquid ammonia under microwaves irradiation for 1h, (FL)G-Fe_xO_y-2. Due to the high microwaves absorption properties of the material, the irradiation with power of 800 W results in rapid significant increase of temperature in the reaction medium. While only temperatures of the liquid could be detected (they exceed the boiling point of the ammonia solution, accompanied by the increase of pressure), it is expected that the temperature of the iron oxide/FLG itself is incomparably higher, easily exceeding several hundred degrees. The short local hot spots (microplasmas) can be indeed created on the FLG surface [21]. **Figure SI 3.1 (b, c**) shows TEM and SEM micrographs of the initial materials. Since in the starting material after reductive decomposition of iron precursor at 350°C, a tendency to form metal islands rather than spherical particles is already observed, after microwaves irradiation the thin very well shaped polygon platelets, mostly hexagons are formed, **Figure 3.3**. The flat hexagons have an average size of 60 nm, but smaller, c.a. 35 nm platelets could be also rarely observed by TEM (**Figure SI 3.1**). The analysis of the interplane lattice spacing confirms the iron oxide spinel structure (**Figure 3.3 (f)**) and the iron oxide (III) phase is confirmed by XPS analysis

(**Figure 3.4 (a)**). Similarly to the previous sample, there are no significant changes in the type of oxygenated groups (**Figure 3.4 (b)**), while much higher graphitization degree of FLG can be observed after µ-wave treatment from the clear shift of combustion temperature in TGA curve, **Figure 3.4 (c)**. The latter has also the reflection in Raman spectra: I_D/I_G ratio decreases from 0.21 to 0.18, where D peak (~1347 cm^{-1}) and G peak (~1581 cm^{-1}) are vibration signatures of "defected" and highly graphic carbon, respectively, (**Figure 3.4 (d)**).

Apart from hexagonal platelets the second elongated form of iron oxide NPs, sticks, can be observed, **Figure SI 3.1 (d)**. Their presence could be possibly attributed to the formation at the (FL)G sheets' edges, without significant interactions with graphitic terraces' surface. Such situations could be attributed to the multi-step structure defined by us earlier for the used here (FL)G and the presence of short terraces [9]. It cannot be however excluded that the sticks are not also an issue of the scrolled thin platelets; their length corresponds to the lateral size of the hexagons (**Figure SI 3.1 (e, f)**).

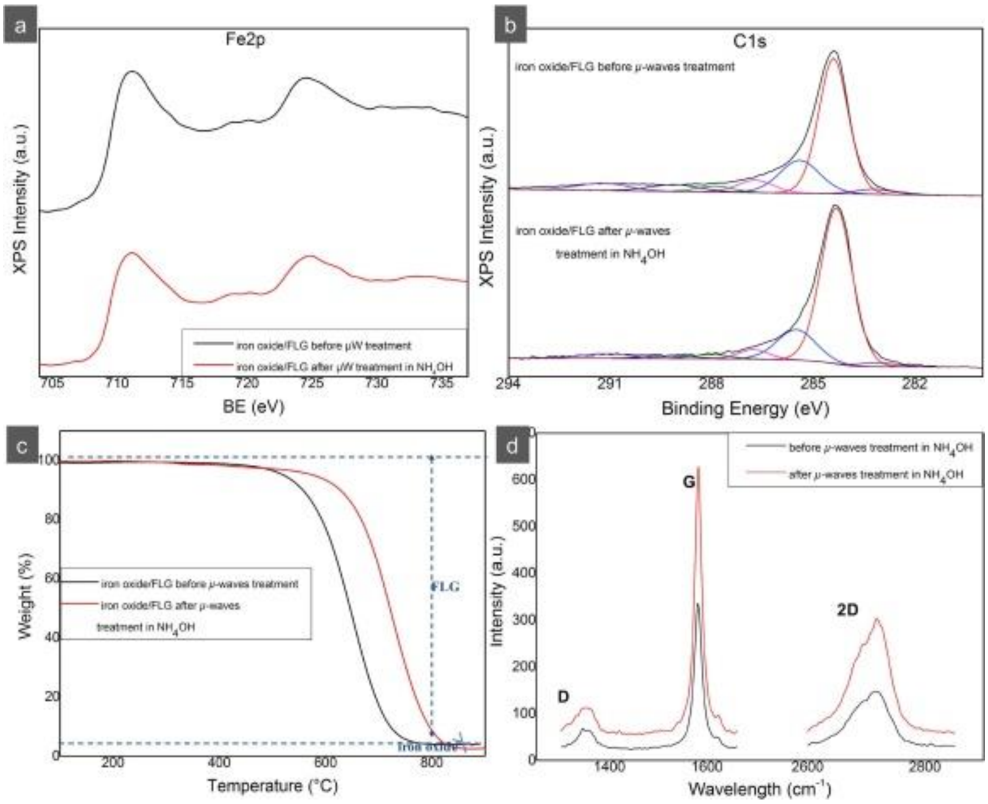

Figure 3.4 a, b) Fe 2p and C1s XPS spectra of iron oxide over FLG before and after µ-waves treatment, c, d) corresponding TGA and Raman spectra.

The presented examples show that not only the flattening of metal occurs but also graphene became a template for the well-defined metal nanoplatelets, especially in the case of µ-waves treated sample. While the interactions between the graphitic support and metal provide the well-structured flattened metal species, once the latter are formed and the support has high graphitization degree, the interfacial interactions become much weaker. The overall dispersion of metal over FLG surface remains significant, which confirms the existence of significant interactions between FLG and metal, before and initially during the annealing treatments. Gradually, most of the 2D NPs don't lie on but tilt from FLG support indicating that the surface- free energy of separated FLG and NPs systems decreased. This phenomenon could be explained by the fact that at standard conditions the graphitic surface is always "defected", including the adsorbed impurity while Fe NPs have higher degree of oxidation. With the increase of annealing temperature, both the graphitic sheets and metal became "impurity-free" loosing again their "pure" state in the post-treatment standard conditions. Passing then through several potential phenomena such as melting or surface melting (in the first example), coalescence, splitting [21-24] (regardless the carbon etching), the NPs crystallize in hexagonal flattened form. This is especially pronounced in the case of µ-waves treated sample, where extremely high temperatures at FLG surface are expected and the melting of Fe NPs, even of relatively large size occur before their crystallization over graphitic template.

The Fe-based hexagonal NPs are no more chemically attached to the graphene surface, but demonstrate significant attractive (or the balance between attractive and repulsive) interactions with the support surface thereby ensuring homogenous distribution of the crystals. The titling of the Fe-based NPs from the (FL)G surface is an important advantage since not only one but two flat surfaces of NPs are accessible for their future potential applications. The weak interactions between Fe-based NPs and FLG are also indirectly confirmed through the results obtained from the CVD synthesis of carbon nanofibers (CNF) on the Fe_xO_y-FLG-1 sample.

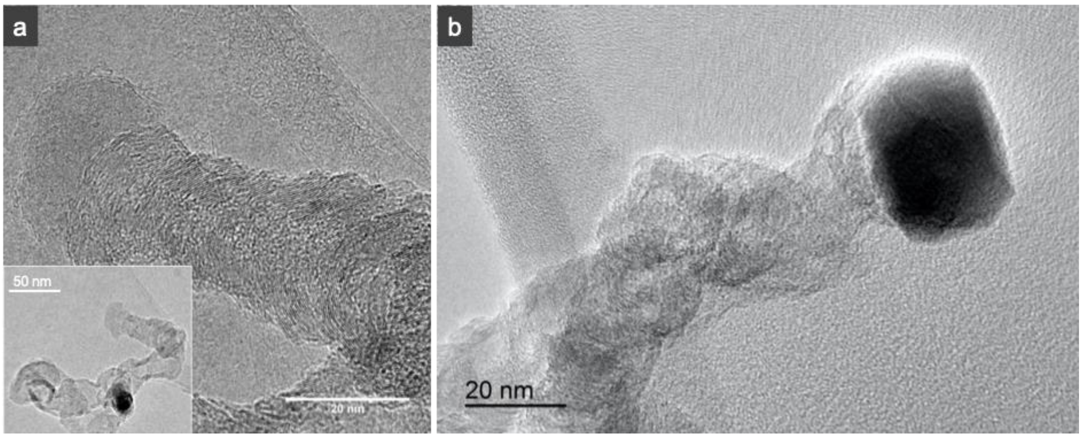

Figure 3.5 TEM micrographs of CNFs growth over iron-oxide/FLG catalysts.

Figure 3.5 shows the TEM micrographs of the synthesized CNFs. As can be seen from **Figure 3.5 (a)**, the tip-growth type of CNFs is observed, i.e. Fe-based catalyst NPs lift with grown fibers. This type of growth is attributed to the weak interactions between catalyst NPs and the support. It seems in addition that both flat surface of the catalyst are active, since the growth of CNF can be observed from both sides of the NPs as well (**Figure 3.5 (b)**).The growth of such morphology CNFs, i.e. in which graphitic planes are perpendicular to the longitudinal axe of fibers confirm flattened morphology of NP catalyst and its sharp edges [16]. The graphitic planes are indeed formed parallel to the catalyst surface [25, 26]. The sharp edged polygonal catalyst NPs are also observed after CNFs grown on the FLGs surface, the potential reconstruction of the catalysts depends as well on the CNFs morphology (in analogical way to the FLG support) [27]. Worthy to underline is also the fact that for the "traditional" catalytic supports such as alumina or silica, the iron NPs catalyzes most often the growth of nanotubes and not nanofibers.

The use of (FL)G permits the preparation of flat particles and even if the notion of surface-to-volume is commonly known and instinctively high for the flat species vs. spherical ones for instance, no concrete comparative examples are reported. In this regard we present below some simple estimation on how the surface changes moving from sphere to hexagonal platelets keeping the same volume, and focusing on the platelets dimensions obtained in this work, i.e. hexagonal platelets of diameter (2a) of 60 nm and high (h) of 6 nm (**Figure 3.6**). The calculations, since they concern the same chemical element, are based purely on the mathematical geometrical factors without considering the crystallographic atomic arrangement.

Surface of regular hexagon with side a is: $S_h = \frac{3a^2\sqrt{3}}{2}$

Total surface of hexagonal plates with side a and high h (TSA) is:

$$TSA = 2 \times S\, x\, 6(a \times h)$$

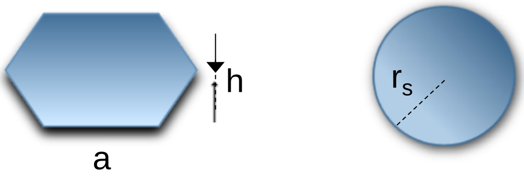

Figure 3.6 Scheme of hexagonal platelet vs. spherical particle.

If we estimate that volume of hexagonal plate is equal to volume of sphere (the same number of volumetric atoms):

$$V_h = V_s$$

$$\frac{3ha^2\sqrt{3}}{2} = \frac{4}{3}\pi r_s^3$$

, so: $$r_s = \sqrt[3]{\frac{3ha^2\sqrt{3}\times 3}{2\times 4\pi}}$$

The $r_s \approx 15$ nm (a=30 nm, h= 6 nm)

We can calculate the surface of sphere corresponding to this V_s:

$$S_s = 4\pi r_s^2$$

The ratio between TSA and S_s for a hexagonal plate with 2a=60 nm and aspect ratio (2a/h) of 10 (h=6 nm), and the sphere with r ≈ 15 nm is around 2.

$$k = {}^{TSA}/_{S_s} \approx 2$$

The gain in surface area is twice, while the sphere with the same volume of atoms than hexagonal plate of 60 nm would have 30 nm of diameter. The k would increase of course in non-linear manner with the increase of aspect ratio of the hexagonal plate: e.g.: the k ≈ 5.7 for 2a/h = 60, k ≈ 7.9 for 2a/h = 100, and k ≈ 91 for 2a/h=476, the h = 0.126 nm equivalent to hypothetical monoatomic Fe layer. The latter one, the monoatomic hexagonal plate would correspond to sphere of 4 nm.

To satiate the curiosity, we have also calculated what size of Fe monoatomic hexagonal plate would correspond to a sphere of 60 nm in diameter; such platelets would be of 1.167 μm size.

3.1.5 Conclusion

We show that due to its 2D nature, FLG can be used as a template for the synthesis of flat metal NPs, i.e. with enhanced surface-to-volume ratio. Despite a high temperature applied for the preparation of flat NPs (annealing conditions) and certain coalescence, the overall dispersion of the metal remains high; while the surface-to-volume ratio of NPs is kept in some extend due to the flat NPs’ structure. The stability of well dispersed Fe NPs at such high temperature provides an important advantage for different applications such as catalysis. The work is undergoing in order to obtain and control optimally thin NPs mainly for catalytic applications.

References

[1] Y. Liang, Y. Li, H. Wang, J. Zhou, J. Wang, T. Regier, H. Dai, *Nat. Mat.*, 2011, Vol. 10, 780

[2] L. Truong-Phuoc, C. P.-Huu, V. D. Costa, I. Janowska, *Chem. Comm.*, 2014, Vol. 50, 14433-14435

[3] C. Zhang, R. Hao, H. Yin, F. Liu, Y. Hou, *Nanoscale*, 2012, Vol. 4, 7326-7329

[4] A. R. Harutyunyan, G. Chen, T. M. Paronyan, E. M. Pigos, O. A. Kuznetsov, K. Hewaparakrama, S. M. Kim, D. Zakharov, E. A. Stach, G. U. Sumanasekera, *Science*, 2009, Vol. 326, 116

[5] Y. Yang, S. Matsubara, L. Xiong, T. Hayakawa, M. Nogami, *J. Phy Chem*., 2007, Vol. 111, 9095-9104

[6] W. Mengting, T. Yanase, F. Uehara, S. Watanabe, T. Miura, T. Nagahama, T. Shimada, *CrystEngComm*, 2017, Vol. 19, 3915-3920

[7] N. Niklas, M. Sterrer, S. Shaikhudinov, D. Menzel, H. J. Freund, *Chemical Energy Storage*, Walter de Gruyter GmbH, Berlin/Boston, 2012, 329-352

[8] A. A. Pirzado, L. T.-Phuoc, V. Papaefthimiou, C. M. Ghimbeu, F. Le Normand, H. Ba, T. T.-Tung, C. P.-Huu, I. Janowska, *J. Colloid Interface Sci.*, 2015, Vol. 451, 221-230

[9] M. S. Moldovan, H. Bulou, Y. J. Dappe, I. Janowska, D. Bégin, C. P.-Huu, O. Ersen, *J. Phys. Chem.*, 2012, Vol. 116, 9274-9282

[10] Q. Yuan, Z. Xu, B. I. Yakobson, F. Ding, *Phys. Rev. Lett.*, 2012, Vol. 108, 245505

[11] F. Banhart, J. Kotakoski, A. V. Krasheninnikov, *ACS Nano*, 2011, Vol. 5, 26-41

[12] B. F. Machado, P. Serp, *Catal. Sci. Technol.*, 2012, Vol. 2, 54-75

[13] J. Zhu, A. Holmen, D. Chen, *ChemCatChem*, 2013, Vol. 5, 378-401

[14] W. Baaziz, L. T.-Phuoc, C. D.-Viet, G. Melinte, I. Janowska, V. Papaefthimiou, O. Ersen, S. Zafeiratos, D. Begin, S. B.-Colin, C. P.-Huu, *J. Mater. Chem. A*, 2014, Vol. 2, 2690-2700

[15] I. Janowska, F. Vigneron, D. Bégin, O. Ersen, P. Bernhardt, T. Romero, M. J. Ledoux, C. P.-Huu, *Carbon*, 2013, Vol. 50, 3106-3110

[16] S. S. Datta, D. R. Strachan, S. M. Khamis, A. T. C. Johnson, *Nano Lett.*, 2008, Vol. 8, 1912-1915

[17] I. Janowska, M.-S. Moldovan, O. Ersen, H. Bulou, K. Chizari, M. J. Ledoux, C. P.-Huu, *Nano Res*., 2011, Vol. 4, 511-521

[18] Y. Hou, Z. Xu, S. Sun, *Angew. Chem. Int. Ed*., 2007, Vol. 46, 6329-6332

[19] M. J.-Baptiste, *J. Phys. D: Appl. Phy*s., 2013, Vol. 46, 143001

[20] J. A. Menéndez, A. Arenillas, B. Fidalgo, Y. Fernández, L. Zubizarreta, E. G. Calvo, J. M. Bermúdez, *Fuel Proc. Technol.*, 2010, Vol. 91, 1-8

[21] W. Baaziz, G. Melinte, O. Ersen, C. P.-Huu, I. Janowska, *Phys. Chem. Chem. Phys.*, 2014, Vol. 16, 15988-15993

[22] F. Schäffel, J. H. Warner, A. Bachmatiuk, B. Rellinghaus, B. Büchner, L. Schultz, M. H. Rümmeli, *Nano Res.*, 2009, Vol. 2, 695-705

[23] C. W. Keep, S. Terry, M. Wells, *J. Catal.*, 1980, Vol. 66, 451-462

[24] K.-H. Kim, A. Gohier, J. E. Bourée, M. Châtelet, C.-S. Cojocaru, *Thin Solid Films*, 2015, Vol. 575, 84-91

[25] I. M.-Gullon, J. Vera, J. A. Conesa, J. L. González, C. Merino, *Carbon*, 2006, Vol. 44, 1572-1580

[26] A. Rinaldi, J.-P. Tessonnier, M. E. Schuster, R. Blume, F. Girgsdies, Q. Zhang, T. Jacob, S. B. Abd Hamid, D. S. Su, R. Schlögl, *Angew. Chem. Int. Ed.*, 2011, Vol. 50, 3313-3317

[27] X. Duan, G. Qian, X. Zhou, Z. Sui, D. Chen, W. Yuan, *App. Catal. B*, 2011, Vol. 101, 189-196

Supporting Information

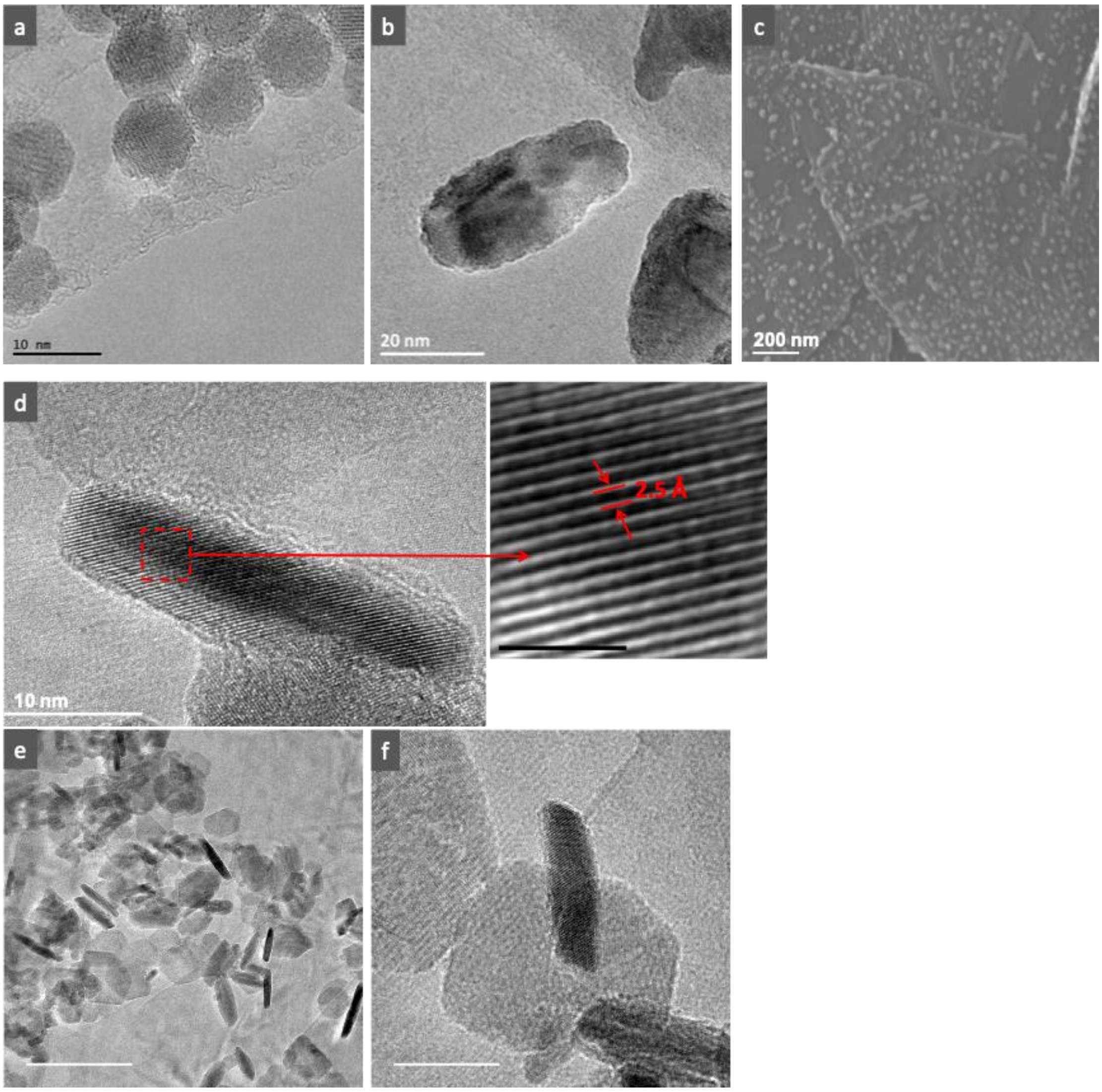

Figure SI 3.1TEM and SEM (c) micrographs of iron oxides over FLG: a) spherical NPs before annealing obtained by solvothermal synthesis, b and c) iron oxide island obtained by impregnation method, d-f) iron oxide sticks obtained together with hexagonal platelets after µ-wave treatment

Chapter 4

Developing FLG based supports for CO_2 methanation

Graphene being a very good conductor of heat (3080-5150 W m^{-1} K^{-1}) has been identified as a promising candidate for catalytic applications as support as discussed in the previous chapter [1]. Keeping the idea of structuration of FLG in mind, this chapter focuses on the synthesis and use of FLG based supports for Carbon capture and utilization process, i.e. hydrogenation of carbon dioxide (CO_2) to methane (CH_4). CO_2 hydrogenation is an exothermic reaction but requires some temperature (typically between 200-600°C) (and historically the pressure) to get good conversion and selectivity. To work in atmospheric pressure and relatively low temperature the catalysts with highly dispersed active and stable sites, easily prepared, are of high industrial applications interest. One way to proceed with low energy demanding process is the use of an alternative heating technique such as Inductive heating (IH) which makes use of local contactless heating of magnetic NPs without heating of the entire reactor. The idea of graphene based material as support for such IH setup is guided by the fact that these materials don't require an additional susceptors like OCF and carbon felt for heating the catalyst.

Two different approaches using FLG as support have been developed. The first one includes the use of FLG-hHLB systems described before in **Chapter 2**. The second one concerns the preparation of the support containing the carbon nanofibers grown over FLG.

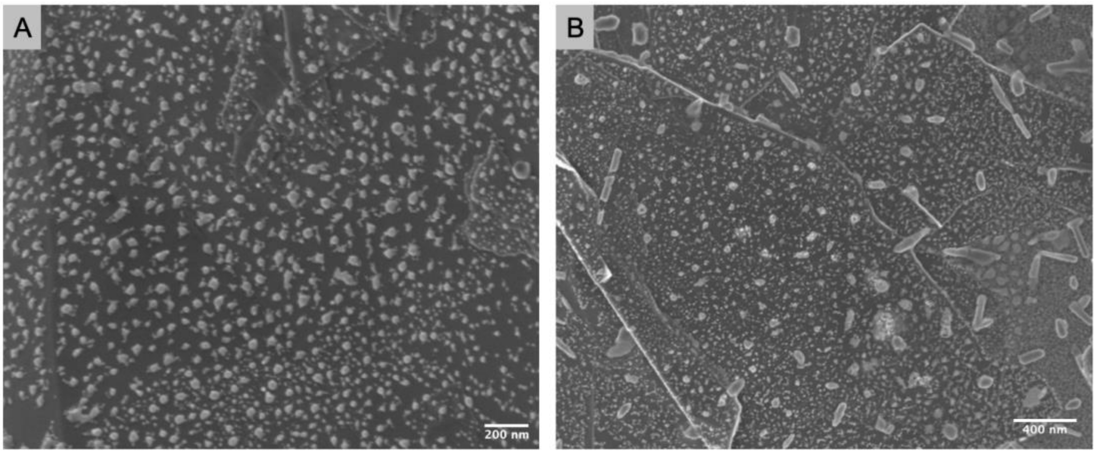

Figure 4.1 Freeze dried FLG-Agar-agar sample loaded with 10% Ni NPs via wetness impregnation, A) before reduction, B) after reduction.

1) Ni/FLG-hHLB

FLG was first synthesized with hHLB precursors like Agar-agar, tannic acid and Bovine Serum Albumin (BSA) by the combined top sonication and stirring process discussed in **Chapter 2**. The Ni NPs were introduced by two methods onto the FLG substrates. First, by adding Ni precursors, $Ni(acac)_2$ or $Ni(NO_3)_2.9H_2O$, at the beginning of the reaction during FLG exfoliation followed by freeze-drying, and second, via wetness impregnation onto the freeze-dried sample before carrying out the calcination and reduction procedures for obtaining the final catalyst. It is essential that the Ni NPs are not only well dispersed on the support but also well exposed for proper reaction to happen. The Ni precursor, $Ni(acac)_2$, was also comparatively studied with the idea of providing a better spacer to the flakes when used in the beginning during the exfoliation of FLG. But the consequent heat treatment processes led to larger stacking giving rise to a lower conversion of CO_2 via $Ni(acac)_2$ based samples. Therefore Ni from $Ni(NO_3)_2.9H_2O$ was used for synthesis of Ni NPs for rest of the samples. The reaction was carried out in a quartz tube with 200mg of the catalyst placed at the centre by help of quartz wool. The details of the reaction conditions and setups are discussed below with the best samples optimized for CO_2 methanation using such FLG substrates.

FLG-HLB System (1:8)	**Method of formation of Ni NPs**	**Amount of Ni in catalyst**	**Max Temp. attained (ºC)**	**CO_2 conversion**
FLG-Agar-Agar	Wetness Impregnation	~15%	230	12%
FLG-Agar-Agar	Wetness Impregnation	~20%	244	14%
FLG-Agar-Agar	Wetness Impregnation	~40%	285	16%
FLG-Agar-Agar	During Exfoliation	~20%	226	7%
FLG-Tannic Acid	Wetness Impregnation	~20%	284	19%
FLG-BSA	Wetness Impregnation	~10%	320	22%
FLG-BSA	Wetness Impregnation	~40%	296	12%
FLG-BSA	During exfoliation	~40%	265	8%

Table 4.1Performance of FLG-HLB based Ni catalysts of different loadings in IH set-up.

Table 4.1 gives an overview of the FLG catalysts prepared via freeze-drying with various impregnation properties and their reactivity in IH setup. First of all, it can be clearly seen that for similar Ni loading, the wetness impregnation process is better than the in-situ addition of Ni precursor during exfoliation. This is possibly due to the fact that in-situ addition leads to covering of Ni NPs in-between FLG flakes thereby not allowing maximum active sites to be available for the reaction. Whereas, wetness impregnation leads to a more surface based attachment of the Ni NPs giving rise to a higher conversion. These initial measurements also gave an idea that FLG-BSA based samples were able to reach a higher temperature compared to other FLG-HLB systems. But, there was a long way ahead in order to obtain a conversion worthy of upscaling. There are two main problems occurring for these systems. The hHLB systems are not completely carbonized after in-situ reduction at 350ºC, reducing the heat conductivity. Also the amount of reduced h-HLB would be insufficient to protect efficiently FLG from stacking making a lot of Ni inaccessible. Likewise, the very well dispersed and small NiNPs observed on FLG-hHLB, (**Figure 4.1 (a)**) coalesce to big NPs along the edges of the FLG flakes once the process of reduction occurs (**Figure 4.1 (b)**)and probably during the methanation it-self. A reverse approach, i.e. the use of FLG/C composites (made from FLG/hHLB precursors) and decorated them next by Ni NPs are still to be studied.

2) Ni/CNFs-FLG

In order to not only benefit from the FLG thermal conductivity but also to be able to access the active sites for Ni NPs attachment with stabilization, the edges-rich CNFs are grown on FLG. The following section discusses in detail the optimizations of the growth of carbon nanofibers via CVD process on FLG which also act as spacers for FLG flakes. Optimized, high and stable dispersion of Ni NPs of size 5-10 nm has been achieved by this manner. The difference in local deposition of NPs over FLG was observed based on their dependence on the Ni NPs loading. The Ni/CNFs-FLG morphologies have been studied in details. CNF-FLG has been found to be a highly stable support system, which can sustain the rapid heating process in IH setup and provide a good constant conversion.

4.1 Structural impact of Carbon Nanofibers/Few-Layer-Graphene decorated with Ni/NiO for CO_2 methanation via Inductive Heating

4.1.1 Introduction

Recent years have seen huge spike in the global emissions of carbon dioxide (CO_2) reaching the values of 36.57 billion metric tons [2]. Rapid increase in the population has paved pathways for unprecedented demands in various sectors causing various global climatic changes. Industrialisation has aided in furthering the emission of CO_2 gases by forming a majority share of 30%. Mitigation of such issues is of prime importance in order to have sustainable development of the society. This brings us to the two-faceted solution at hand to not only immediately help reduce the CO_2 content in the atmosphere but also to convert it into a form which can be utilised as renewable energy. Catalytic hydrogenation of CO_2 to form methane (CH_4) has spurred an interest among researchers worldwide advocating the power-to-gas technology [3-7], as it can used for chemical energy storage as well as directly pumped into the existing gas lines without major modifications. Further, it has recently been viewed as a plausible candidate for space applications [7]. The catalytic hydrogenation is based on the Sabatier reaction, $CO_2 + 4\,H_2 \rightleftharpoons CH_4 + 2H_2O;\ \Delta H^0 = 165\ kJ\ mol^{-1}$, which requires 4 moles of hydrogen which can be obtained from renewable sources, such as converting excess electricity to hydrogen from catalytic water splitting and biomass gasification [8-10].

Metal-metal oxides (M-M_xO_y) based systems have been inherently utilised to tackle the issue of methanation of CO_2 because of their superior mechanical performance and high stability. The most common active metals being Ni [11-18], Fe [19-21], Co [22-25] whereas the most common metal oxides supports are Al_2O_3 [13-15, 22, 25-28], SiO_2 [29-31], ZrO_2 [11, 32-34], CeO_2 [12, 27, 35-37] etc. Some noble metals like Ru [26, 38-41]and Rh [42-44] provide better activity but are costly and susceptible to deactivation. The primary disadvantage of such systems is the ease of sintering of the metal nanoparticles (NPs) across the metal oxide supports because of lack of intrinsic M-M_xO_y interactions. Muroyama et. al. have reported the order of influence M-M_xO_y interactions according to the CH_4 yield at 250ºC as Ni/Y_2O_3 > Ni/Sm_2O_3 > Ni/ZrO_2 > Ni/CeO_2 > Ni/Al_2O_3 > Ni/La_2O_3 [45]. It is regularly reported to be utilised in oxide based supports as they provide structural support necessary for high efficiency and recyclability, but is not ideal due to structural issues such as formation of spinel structures during calcination of Al_2O_3 supports [46]. Recently, Ni has also been used along with promoters like Co[47], La[48] and Mn[49, 50] to obtain CO_2 conversions of 65-82% with selectivity ranging from 84-99 %. The (111) facet of Ni has proved to be beneficial for CO_2

methanation over Metal-Organic framework substrates[51]. But, few studies have been carried out to utilise metal-non-metal oxide(M_x-NM_y) based catalysts for CO_2 hydrogenation, and even lesser reports involve carbon based nanomaterials for such reactions.

Carbon nanomaterials like nanotubes, nanofibers, graphene oxide and few-layer-graphene have been known to have unique properties which have shown promising results in the field of catalysis for energy applications [52]. The most common carbon structures studied for catalytic methanation of CO_2 have been carbon nanotubes [50, 53] which provide the idea that there is still room for further investigations involving graphene and its derivatives. Graphene based derivatives needs to be studied as they can provide unique charge-transfer and heat transfer characteristics which can accelerate the catalytic processes. The π-electron charges clouding the basal plane of graphene makes it viable for anchoring of functional groups that can interact with excess electrons present on the oxygen atom of the CO_2 species which in turn acts as a self-promoting substrate. The extended π-orbital of graphene planes favour its interaction with the d-orbitals of metal-support atoms increasing their stability [54], while the defects and edges are known to be good sites for attachment and stabilisation of metallic species [55, 56]. Graphene has been used as photocatalyst with Ni dopants for CO_2 reduction but lacks high quantum yield [57].It has also been studied for gas-phase methanation reactions. Ana et. al. have reported a directly proportional relationship between conversion rate and temperature using MoS_2 platelets along with FLG [54], but substantial conversion of CO_2 for this system arrives at a temperature of around 600°C which is pretty high in comparison to M-M_xO_y systems. Feiyang et. al. have recently demonstrated that Ni/RGO support alone is not a suitable candidate and needs Ce as promoter to achieve a conversion greater than 80% [58]. In the family of carbon supported Ni NPs, the best performance of methanation without additional promoter has been obtained for Ni/N-CNT showing 81% conversion at 360°C with a selectivity of 98% [53], while the reaction mechanism has been rarely discussed.

The heating conditions required to carry out methanation have recently been of interest as many studies tend towards using cleaner methods where highly disperse temperature ramp could be generated in few minutes contrary to the traditional Joule Heating method. Research driven towards Induction Heating (IH) has been gaining momentum recently pertaining to its favourable characteristics which allows for a precise, cost-effective and repeatable high temperature ramp and cool down within a few minutes [59, 60]. The laser pyrometer guided real-time temperature control of reactor beds for such IH setups makes it a promising candidate for future applications in heterogenous catalysis where isothermal conditions and instant temperature ramps are considered essential. It has been already put into use for methanation of CO_2 [61], but the type of catalyst and substrate used has been restrictive in terms of need for additional promoter and efficiency. Wang et. al. have initially used this technique to achieve 71% conversion at 320°C with a carbon felt support [62]. Recently, they have reported use of a composite having high Ni loading (~ 40%) on an alumina support which has been able to provide a low temperature methanation [63].There are several avenues concerning the design of catalyst and its integration to magnetically induced setup that can be improved. Graphene having its unique heat transfer properties becomes a suitable candidate for using such inductive heating based method [1]. FLG is advantageous considering the fact that it has properties similar to graphene while crediting itself as a good substitute for substrate for magnetic induced heating setups. It can help avoid formation of hotspots thereby increasing the lifecycle of catalyst and its methanation efficiency.

Herein, we demonstrate the use of carbon nanofibers covered few-layer-graphene as a suitable new hybrid support of Ni NPs for CO_2 methanation via inductive-heating process. The grown “herring bone” type CNFs having large number of active edges sites provide enhanced stabilisation of Ni NPs to achieve high NPs’ dispersion, while the presence of FLG enhances thermal conductivity [64]. Additional acid treatment of the support is applied to increase the CNFs edges activity. The impact of the growth parameters of CNFs on their morphology and distribution on FLG followed by their consequent effect on the NPs dispersion and methanation has been investigated. Ni has a double facetted role in the composite by contributing to the heating via induction process as well as acting as active site for methanation.

4.1.2 Experimental Section

4.1.2.1 Synthesis of Carbon Nanofibers on FLG

Expanded Graphite (EG) was purchased from Carbon Lorraine company, Bovine Serum Albumin(A) was purchased from Sigma Aldrich. $Ni(NO_3)_2.9H_2O$ and $Ni(acac)_2$ was obtained from Sigma Aldrich. Gases used for growth of CNFs was obtained from Air Liquide. The FLG was obtained similar to the previously reported work from the lab [64] with some modifications wherein EG is used in huge excess compared to the hHLB precursor. A typical synthesis involves dissolving about 600 mg of BSA (10% w/w of EG) in 500 ml ultra-pure water for 10 minutes followed by step-wise addition of 6gm of EG making sure it is properly wet and not coming out of the reaction beaker. Then the beaker is moved onto the stirring plus top-sonication setup which exfoliates the EG to FLG for about 2 hours at an amplitude of 25% power for the sonicator (BRANSON Sonifier 550) and stirring speed of 500-600 rpm. The solution was then centrifuged to remove major water content and obtain a paste like consistency of the FLG/hHLB mixture.

The product obtained was then mixed with 2% Ni from Ni(acac)$_2$ precursor in an autoclave with 300ml EtOH:H$_2$O mixture of ratio 1:2. The sealed autoclave was subjected to 180^{o}C for 24 hours. The autoclave was cooled down under tap water followed by retrieval of product. The product obtained was washed 3 times in water followed by oven drying. After overnight drying, it was calcined at 400^{o}C for 3 hours.

This 2% Ni-FLG composite was used for growth of carbon nanofibers (CNF) by Chemical Vapour Deposition (CVD) process at 3 different temperatures, viz. 700^{o}C, 800^{o}C, 900^{o}C. Initially, the composite was heated under Argon till 400^{o}C. The hydrogen was introduced and argon was cut-off. The oven remained at 400^{o}C for 2 h to obtain maximum reduced Ni NPs which will be the active sites for CNF growth. After reduction, the temperature was increased up to the 3 different temperatures mentioned earlier by changing back to Ar atmosphere. At the target temperature, CNF was grown for 2 h under 1:1 mixture of ethane and hydrogen flowing at a combined rate of 65 ml min^{-1}. After the growth time, the reaction mixture was replaced with Ar and the reactor was cooled to room temperature.

4.1.1.1 Preparation of Final Catalyst

After the growth of CNFs, the product recovered was treated with nitric acid (35%) at 800^{o}C for 24 h under reflux conditions for complete removal of Ni used for growth. The composite was washed multiple times with ultrapure water till the litmus gave a neutral pH. Then it was dried overnight following which Ni was introduced with different mass loadings of 10%, 20%, 40% compared to FLG-CNF weight. A Ni ethanol solution from (NiNO$_3$)$_2$.9H$_2$0 was added via wetness impregnation followed by overnight oven drying at 110^{o}C. Next, it was calcined at 250^{o}C for 2 h to get rid of all excessive moisture. Lastly, the sample was reduced at 350^{o}C for 2 h under hydrogen before use in reactor. Thus, the catalyst was ready for further analysis and tests.

4.1.1.2 Characterisation

Scanning electron microscopy (SEM), Scanning transmission electron microscopy (STEM) and High-angle annular dark-field (HAADF) was conducted on a ZEISS Gemini SEM 500 microscope with a resolution of 5 nm. For each measurement, samples were dispersed in ethanol for a few minutes and were drop-casted onto copper grids. Transmission Electron Microscopy (TEM) was carried out on a JEOL 2100 F microscope working at 200 kV voltage with a point-to-point resolution of 0.2 nm. For TEM also, samples were previously dispersed in ethanol using ultrasonication (for few minutes) till a homogeneous dispersion is obtained and the resulting solution was drop-casted on a copper grid covered with a holey carbon membrane. Thermal gravimetric analysis (TGA) analysis was carried out in the 30-850 °C temperature range (heating rate of 5 °C min^{-1}) using a TGA Q5000 instrument operating under an air flow (25 mL min^{-1}). The Brunauer-Emmett-Teller (BET) specific surface areas (SSA) and porosity were calculated from N_2 physisorption isotherms recorded at 77 K on an ASAP 2020 Micromeritics® instrument. Pore size distribution was determined by Barrett-Joyner-Halenda (BJH) method. XPS analyses were performed with a MULTILAB 2000 (THERMO) spectrometer equipped with Al K anode (hν = 1486.6 eV). For deconvolution of spectra, the CASA XPS program with a Gaussian-Lorentzian mix function and Shirley background subtraction was employed. Powder X-ray Diffraction (PXRD) measurements were carried out on a Bruker D-8 Advance diffractometer equipped with a Vantec detector (Cu Kα radiation) working at 40 kV and 40 mA. X-ray diffractograms were recorded in the 10-80° 2θ region at room temperature in air.

CO_2-temperature programmed desorption (TPD) experiments were performed on a mass spectrometer (MS). Prior to CO_2-TPD, 50 mg of catalyst was in situ reduced by H_2 flow (30 mL min^{-1}) at 350 °C for 1 h. Then, the sample was cooled to room temperature with Ar and saturated by CO_2. After flushing with Ar for 1 h, the sample was heated to 600 °C by ramping at 5 °C min^{-1} in Ar flow. The detected signals for CO_2 was m/z = 44.

Temperature-programmed surface reaction (TPSR) experiment was carried out on a mass spectrometer using Ar as the carrier gas. The main detected signals for each gas were m/z = 44 (CO_2), 2 (H_2), 28 (CO), 16 (CH_4), and 40 (Ar). The flow rate was corrected to be 40, 4, and 1 mL min^{-1} for Ar, H_2, and CO_2, respectively. Prior to the experiment, the catalyst was reduced by H_2 at 350 °C for 1 h. The temperature was cooled down to 150 °C and maintained for 1 h until the baseline was stable. The reaction mixture was introduced into the reactor and the evolution of gases were monitored until the temperature increased to 450 °C at a rate of 5 °C min^{-1}.

4.1.1.3 Inductive Heating (IH) Setup

The induction heating setup (EasyHeat 8310, 10 kW, Ambrell Ltd) is made up of a spiral 6-turn induction coil (length =1.05 m, pure coil resistance = 2.066×10^{-3} Ω), cooled by means of an external chiller with recirculated water/glycerol (10 %) mixture. The sample was initially placed inside a quartz reactor fabricated specifically considering the internal diameter of the coil. In a typical experiment, the quartz reactor was first placed inside the induction heater coils such that the catalyst held by quartz wool is placed midway of the induction coil. The temperature was controlled in real-time by a PID system (Proportional Integral Derivative controller, Eurotherm model 3504) connected to a laser pyrometer (Optris, Ø laser beam: ≈500 µm, power <1mW, located at ≈30 cm from the catalyst) directed to the catalyst bed and working in the 150-1000 °C range (accuracy ±1 °C). The temperature ramp rate allowed for the system is 50-70 °C min^{-1} in the 250-450 °C temperature range.

CO_2 methanation reaction was carried out at atmospheric pressure in a fixed bed quartz tubular reactor [$Ø_{\text{internal}}$ = 12 mm, length = 400 mm] loaded with 200 mg of FLG-CNF/Ni catalyst over quartz wool. The reactants and products for IH heating setup were analysed online by a CP-3800 gas chromatograph (GC) equipped with a thermal conductivity detector (TCD) and a flame ionization (FID) detector. All reactor exit lines were maintained at 110 °C by external heating tapes so as to avoid condensation of residual water in the gaseous feedstock to the GC.

4.1.2.2 Joule Heating Setup

Carbon dioxide methanation was conducted at atmospheric pressure in a fixed-bed down-flow reactor at 350°C. A thermocouple was inserted in the furnace to measure the pre-treatment and reaction temperatures *in-situ*. The reactor was heated in a tubular furnace monitored by a temperature controller.

The flow of reactants was regulated by calibrated mass flow controllers (Brooks). H_2 and CO_2 were mixed at a stoichiometric H_2:CO_2 ratio of 4:1 and N_2 was added as an internal standard. The total flow rate was set to 55 mL min^{-1} with catalyst charged (for e.g. 30 mg of FLG/C catalyst diluted with 300 mg of SiC) into the quartz tube reactor [$Ø_{\text{internal}}$ = 6.5 mm, length = 300 mm] corresponding to a gas hourly space velocity of around 60 000 h^{-1}/ 180 000 h^{-1}. The feed and products were analysed on-line by a micro gas chromatograph (INFICON-3000 Series Micro GC equipped with MS5A and PPQ columns).

4.1.2.3 Catalytic Test Measures

CO_2 conversion and CH_4 selectivity were calculated according to the following equations:

$$X_{CO_2}(\%) = \frac{F_{CO_2(inlet)} - F_{CO_2\,(outlet)}}{F_{CO_2(inlet)}} \times 100$$

$$S_{CH_4}(\%) = \frac{F_{CH_4\,(outlet)}}{F_{CO_2(inlet)} - F_{CO_2\,(outlet)}} \times 100$$

4.1.3 Results

Seven different main samples containing FLG, CNFs and Ni NPs were synthesised. The CNFs were grown at 700, 800 and 900°C. The Ni loading was designed to be 10, 20 for all and additionally 40% for the carbon hybrid grown at 800°C. The catalysts have been denoted as FC-XXX-YY wherein XXX refers to the temperature of the growth of CNFs on FLG and YY refers to the percentage of Ni loading on the FLG-CNF composite. An additional remark of 'F' and 'S' is added to distinguish between fresh and spent catalyst correspondingly. Further, another set of samples without any loading recovered just after nitric acid treatment and washing are denoted as FC-XXX-NA (essentially the pure carbon supports before any metal loading).

4.1.1.4 Morphological and Physico-chemical Characterisation

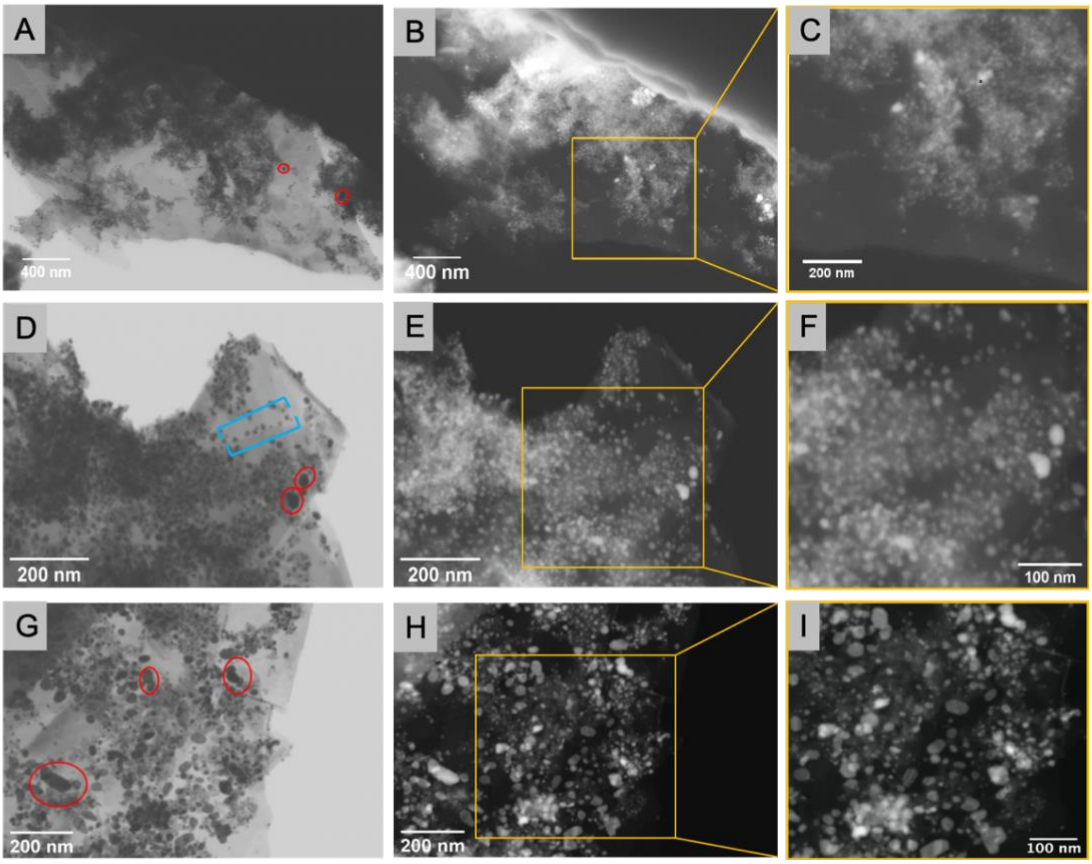

Figure 4.2 STEM (1st column), HAADF (2nd column) and enlarged section(3rd column) of FC-800-10Ni(1st row), FC-800-20Ni (2nd row) and FC-800-40Ni (3rd row) respectively.

In order to understand the suitability of CNFs grown on FLG as a suitable support for Ni based CO_2 methanation in an inductive heating setup, the samples were characterised using SEM, TEM, TGA, XRD, N_2- adsorption desorption. After synthesis, initially the samples were studied under the HR-SEM. **Figure 4.2** shows the SEM images of the FC-800 samples with various Ni loadings in each row. According to the HR-SEM and TEM observations, CNFs with herring-bond attributed morphology has been found to be formed over the FLG flakes (**Figure SI 4.1 (a, b)**) (similar to the structure shown in **1.2.3.3 Carbon Supports for methanation**). Such CNFs have higher number of accessible edges which facilitate attachment and stabilization of active metal species. Multiple layers of graphene sheets forming FLG flakes tend to curl around each other with some wrinkles. The flakes seem to be tossed one above the other in a fashion that exposes their edges and partial surface every time. The Ni nanoparticles are mostly attached to the grown CNFs and edges of the FLG flakes (marked in blue in the images). Lesser amount has been found to be attached to the surface of the FLG sheets (**Figure SI 4.1 (c, d, e**). There is a distinct rise in the size of Ni NPs and a gradual increase in agglomeration (marked in red in the images) of the same with the increase in amount of metal loading as can be seen from the high resolution images. A flattening of nanoparticles to platelet forms along with agglomeration was observed for FC-800-40Ni sample having a high Ni loading of 40% (**Figure SI 4.2**) which is characteristic of high metal loadings on FLG [65].

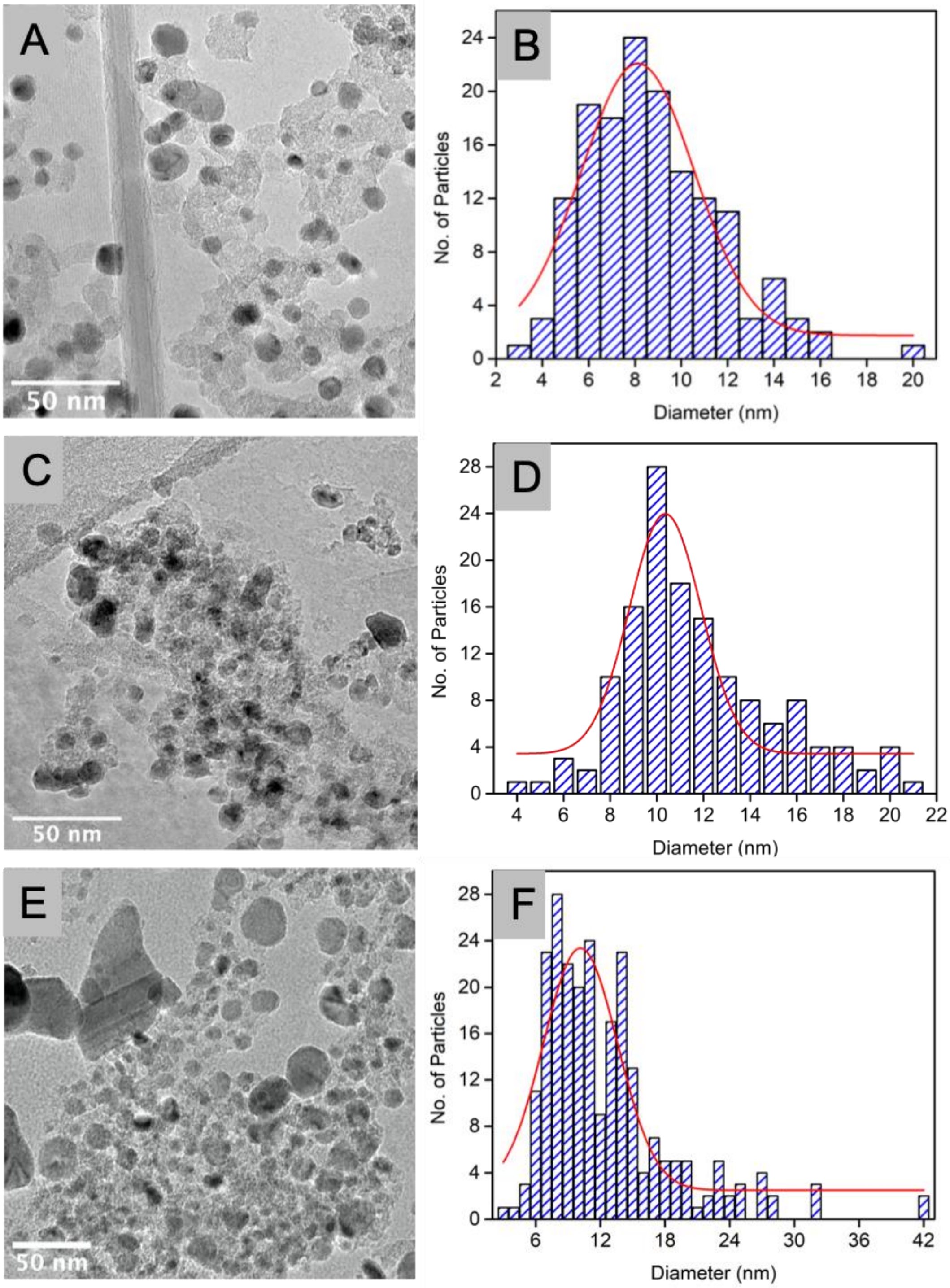

Figure 4.3 TEM images and Particle Size Distribution of FC-800-10Ni (a, b),C-800-20Ni (c, d), and FC-800-40Ni (e,f).

The samples were further studied with TEM microscopy in order to evaluate the particle size distribution as shown in **Figure 4.3**. The average particle size (obtained via Gaussian distribution of >100 NPs as sample set) for FC-800-10Ni was found to be ca. 8 nm, and that for the FC-800-20Ni and FC-800-40Ni was found to be ca. 10 nm. FC-800-10Ni sample has however most of the Ni NPs in the range of 5-10 nm whereas FC-800-20Ni has most of the NPs in the range of 8-13 nm. It is interesting to note that although FC-800-40Ni has an average particle size of Ni NPs of ca. 11nm, a larger amount of the particles are more than 13 nm with some even higher than 30 nm. Further investigations revealed that the Ni NPs on FC-800-40Ni tend to stabilize to a larger extent along the edges of the FLG flakes (**Figure SI 4.3**) forming Ni NPs distinctively bigger than those attached to the CNFs edges. This proves that with increase in the Ni loading on the supports, the particle size also increases. The increased size is typically detrimental for methanation reaction because the conversion depends on the amount of accessible active sites. Further, in **Figure 4.3 (a)**, a small amount of large particles can be seen which are mostly attached to the FLG edges as discussed earlier. It is noteworthy that with the increase in Ni loading, the particle size distribution sees not only a shift towards larger value, but also a more pronounced increase in the edge attachments can be seen as the population of NPs greater than 16 nm increases.

Sample	*Amount of Ni (%)* [a]	*Size of Ni NPs* [b]	*T_{max} –IH (ºC)*	*C/O ratio* [c]
FC-800-10Ni-F	9	5-10 nm	>420	20
FC-800-20Ni-F	22	8-13 nm	>420	17
FC-800-40Ni-F	43	8-15 nm	>420	11
FC-700-10Ni-F	12	6-9 nm	>420	21
FC-700-20Ni-F	23	-	270	19
FC-900-10Ni-F	10	6-10 nm	>420	23
FC-900-20Ni-F	21	-	320	22

*Table 4.2 List of samples with their chemical composition and average particle size. *a- obtained from TGA; *b- Average diameter obtained from TEM analysis; *c- Obtained from XPS (have approximative character)*

Table 4.2 comprehensively identifies the chemical composition of the samples and average particle size of the Ni NPs present on the FLG-CNFs (FC) composite. TGA studies revealed that the actual Ni weight present in the catalyst after all treatments is not exactly equivalent but very close to the theoretical approximation used during the incipient wetness impregnation method. The TGA curves for the set of samples prepared at 800ºC are presented in **Figure SI 4.4**, which reaffirms the fact that deposition of Ni in the FC-800-NA samples reduces their combustion temperature based on the type of carbon Ni is attached to. The two distinctly observed slopes arise from the two different types of carbon present in the composites. It can be considered that the CNFs are burnt faster than the graphene flakes since the amount of edges in CNFs which aid combustion is much higher than the C=C planes contrary to the large flakes of FLG. Further, composite localizations having higher amount of Ni gives rise to higher presence of Ni oxides, thus confirming that CNFs will burn faster than FLG because of higher Ni attachments.

An important aspect of the materials was understood by heating them under Argon in the IH setup. It was found that not all the samples can be heated to the reaction temperature in this set-up contrary to that in the Joule Heating setup. All the FC-800 derived samples were easy to heat to 420^{o}C and beyond whereas the samples from FC-700 and FC-900 had issues with higher Ni loading. Both systems had good heating with a 10% Ni doping but failed to heat after a certain extent when loaded with 20% Ni owing to limitations of power supply. This is supposedly due to their differences in the interactions dominated by the structure of the supports and metal dispersions which is explained in detail later **(4.1.1.10 Role of Support Structure**).

An insight into the elemental composition were obtained by XPS studies of the composites (**Table 4.2** and **Table SI 4.1**). The various types of carbon bonding were approximated based on the deconvolution of XPS C1s spectra. XPS being a local measurement and the samples being readily oxidised render a close resemblance of C1s peaks and percentage of different kind of bondings for all samples. For this reason, the C/O ratios and the sp^2 carbon values presented in the table have an approximative character. A deconvoluted C1s spectra shown in **Figure SI 4.5 (a)** indicates a typical carbon peak for graphene the materials with a large percentage of sp^2 carbon. The two different types of carbon present in the sample makes it difficult for a proper estimation. The Ni 2p spectra for all samples follow the same order as FC-800 samples shown in **Figure SI 4.5 (b)**. The increase in Ni loading increases the intensity but the peak formation remains constant.

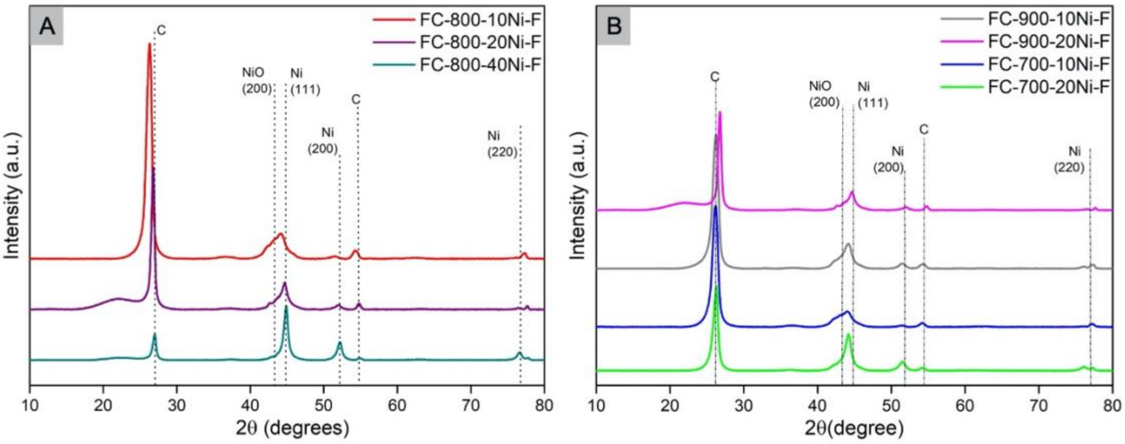

Figure 4.4 XRD spectra of, (a) FC-800-YY, (b) FC-700-YY & FC-900-YY.

The XRD patterns obtained for the composites were in agreement to that studied in literature [66,67]. The diffraction peaks at 2θ = 26.6°, 54.8° corresponded to carbon peaks arising from the FLG/C supports. In particular, characteristic FLG, metallic Ni and NiO peaks can be seen for all samples in **Figure 4.4**. The face centred cubic (fcc) Ni peaks were observed at 44.8° (111), 52.2° (200), and 76.8° (220) (JCPDS card no.: 04-0850), whereas distinct NiO peaks were also visible at 43.2° (200) (JCPDS card no.: 44-1159) because of inherent oxidation reaction taking place when the samples were exposed to atmospheric air. The increase in the Ni content in FC-800-20Ni-F and FC-800-40Ni-F is evident from the relative increase in height of the combined Ni and NiO peaks in comparison to the sharp FLG peaks for these samples. The sharp signal of metallic Ni in the FC-800-40Ni-F is attributed to the fact that larger Ni loading causes an agglomeration of Ni nanoparticles thereby allowing a larger amount of metallic Ni remain unoxidized. This is also in tandem to the particle size obtained via TEM.

Sample	**S_{BET} [m^2 g^{-1}]^a**	**V_p [cm^3 g^{-1}]^b**	**d_p [nm]^c**
FC-800-AAC	37	0.12	13
FC-800-NA	179	0.55	13.4
FC-800-10Ni-F	172	0.42	11
FC-800-20Ni-F	147	0.33	10
FC-800-40Ni-F	107	0.25	10.4
FC-900-10Ni-F	54	0.14	12
FC-900-20Ni-F	48	0.14	10.3
FC-700-10Ni-F	160	0.3	7.5
FC-700-20Ni-F	128	0.25	7.4

*Table 4.3 Table showing surface properties of various FC samples. *a- Specific surface areas calculated from the BET equation, *b- Mesopore volumes obtained from the BJH desorption calculation method, *c- Average pore width from the BJH desorption calculation method.*

BET surface area measurements reveal that the growth of nanofibers improves the surface area of the FLG composites largely. The multi-fold increase in surface area from 37 m^2 g^{-1} of FC-800-AAC (sample after auto clave) to 179 m^2 g^{-1} FC-800-NA (after growth of CNFs followed by nitric acid treatment) indicates that the introduction of CNFs onto the FLG flakes enhances its surface area and porosity. Such low surface area of the FC-800-AAC sample is also be attributed to the interlayer π-π restacking increased during the long degassing process before the chemisorption studies and also due to inherent tendency of FLG flakes of 7-9 layers. All the samples tend to follow Type IV isotherms with a one-step capillary condensation typical of NiO composites with CNFs (**Figure SI 4.6**) [68]. The increase in metal loading leads to a decrease in porosity (especially mesopores of c.a. 30-35nm) which is indicative of the pore blocking effect caused by the Ni NPs. The size and amount of CNFs grown on the FLG seem to have a dominating effect on the S_{BET} as composites with same Ni loading tend to have distinctly different surface areas. S_{BET} clearly decreases with increase in % of Ni loading in the samples. Likewise, the S_{BET} also decreases with increase in diameter of CNFs (see **4.1.1.10**. for CNFs diameter)

4.1.1.5 CO_2-TPD Measurements

The basicity and CO_2 adsorption capacity of FLG-CNFs samples were studied according to their CO_2-TPD profiles as shown in **Figure 4.5**. For all catalysts, no physisorbed and weaker chemisorbed CO_2 basic sites were observed as no desorption occurred below 300°C. Most of them indicated presence of moderate basic sites indicated by the peaks in between 380-470°C. The FC-800 samples desorb at a lesser temperature compared to FC-700 and FC-900 samples which makes it a better candidate for CO_2 methanation. The CO_2 desorption curves for the support sample (FC-900-NA) presented in **Figure SI 4.7** suggests that both support has minor contribution in CO_2 adsorption for formation of reaction intermediate which results in methanation. Thus metal NPs are the most active sites for such catalysts.

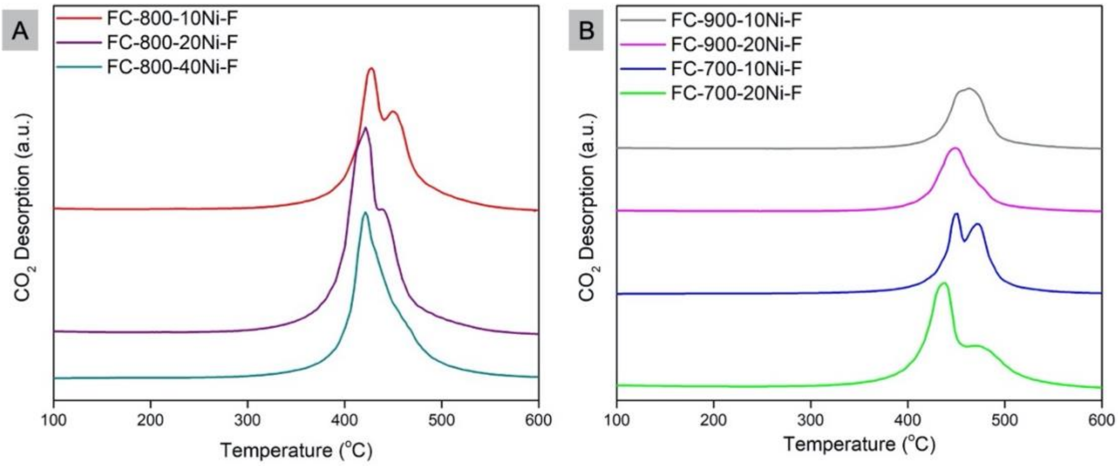

Figure 4.5 CO_2-TPD profiles of FLG-CNFs composites.

4.1.1.6 Catalytic Activity

The performances of the catalysts were measured at 280-420°C temperature range by quantifying the CO_2 conversion (X_{CO_2}) and CH_4 selectivity (S_{CH_4}) as can be seen from **Figure 4.6**. It must be noted that, in all the cases, CO was not detected by the GC-MS at all temperatures. For all the samples, the FLG-CNFs support synthesized at different temperatures were first heated under regular reaction conditions in the induction heating setup without any Ni loading in order to confirm the negligible/null activity of the carbon support in absence of

Ni. This ensured that all of the conversion obtained after loading arises due to the metal NPs. As a general trend, it can be noticed that the rate of X_{CO_2} increased with increasing temperature till 360ºC for most samples indicating that the reaction is under thermodynamic control in this regime optimising for stable product [69,70]. This effect is more pronounced for the FC-800 samples whereas the maximum X_{CO_2} for FC-700-10Ni and FC-900-10Ni samples were observed at 400ºC and 340ºC respectively. As the loading is similar to that of FC-800-10Ni, it is imperative that such shift in conversion arises from the structural incoherencies of the samples.

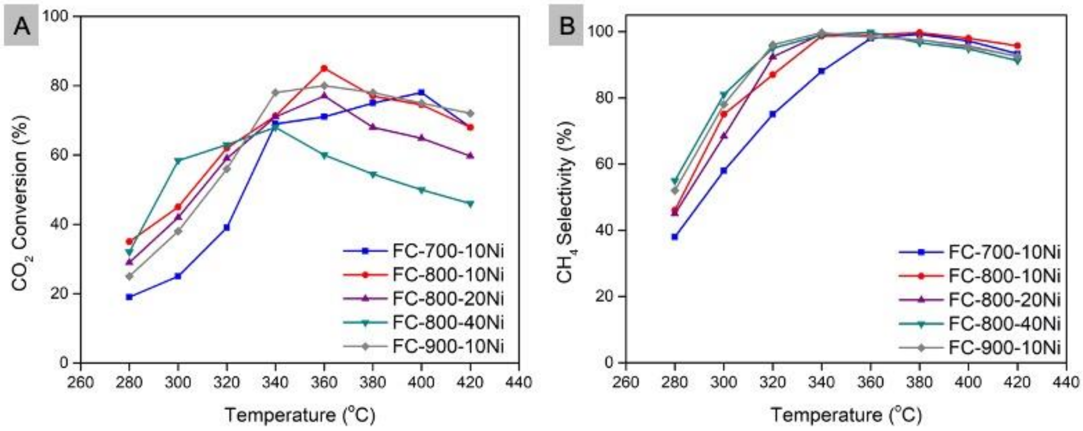

Figure 4.6 Conversion and Selectivity of CO_2 and CH_4 respectively on FC samples.

Comparing the conversion at the lowest feasible temperature under GHSV of 30,000 ml g_{cat}^{-1} h^{-1} constituting of pure reaction gas mixtures only without any adulteration of inert gas, FC-800-10Ni-F seems to be significantly superior with an 85% CO_2 conversion and 99.6% CH_4 selectivity at 360ºC. This proves that FLG as a support having a very good thermal conductivity is able to avoid formation of local heat gradients which is common in methanation reactions even at low GHSV with inert gas mixtures [71]. The decrease in gradient of both X_{CO_2} and S_{CH_4} after these temperatures is common for methanation with such carbon based supports [53, 62] and can be attributed to the occurrence of overpowering parallel reactions like water-gas shift reaction, reverse water-gas shift reaction or steam reforming reaction [72] which are favoured at higher temperatures. Water gas shift reaction causes decrease in X_{CO_2} whereas both reverse water-gas shift reaction and steam reforming reaction cause decrease in S_{CH_4}. It is noteworthy that with such FC support materials, X_{CO_2} decreases with the increase in Ni loading which can be attributed to the increase in the Ni NPs size. The increase in the particle size reduces the effective active surface area of the catalyst for reaction to occur. The FC-700 and FC-900 samples on the other hand showed reasonable amount of X_{CO_2} with 10% Ni loading but faced issues via inductive heating when the loading was increased to 20%. As discussed earlier, we claim that this is because of the agglomeration of Ni NPs on CNF and

FLG and their modified interaction with the FLG-CNF support structure causing anisotropic heat conduction and thereby limiting the temperature the sample can obtain for the same applied power.

4.1.1.7 Effect of Reaction Gas Ratio and GHSV

In order to better understand the X_{CO_2} capabilities of the best sample identified earlier, i.e. FC-800-10Ni, tests were carried out under various conditions mimicking the idea of dynamic nature in upscaled industrial plants. The X_{CO_2} and S_{CH_4} was measured in a reaction mixture having a stochiometric excess of hydrogen which makes it more favourable for methanation. An increase in H_2 indeed resulted an increase in X_{CO_2} up to a maximum of 96.8% with an S_{CH_4} of 99.8% as shown in **Figure 4.7 (a)**. All the tests with various H_2 to CO_2 ratios and different temperatures were carried out on the same sample with changing temperature and gas inflow as and when required. Such rapid change of heat is possible only in case of an inductive heating setup where temperature gradient can be neutralised at an approximate rate of more than 150°C min^{-1}. The adaptability of the FC-800-10Ni catalyst to such dynamic stat/stop cycles with changing gas mixture and temperature, providing similar X_{CO_2} at the end indicates the stability of such composite material to adverse conditions. This also confirms that FLG as a support having a very good thermal conductivity can be used in stress conditions without formation of local heat gradients and can provide a better CH_4 output when hydrogen is provided in stochiometric excess.

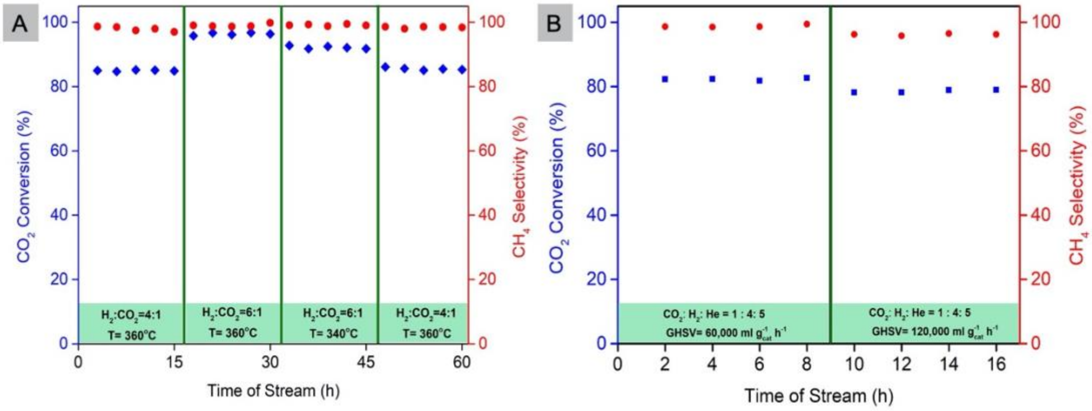

Figure 4.7 FC-800-10Ni sample under, (a) different reaction mixture ratio and temperature, (b) under different GHSV (blue dot- conversion, red dot- selectivity for the same sampling).

The validation of the catalyst stability to adverse conditions were further done by subjecting the FC-800-10Ni sample to gas flows having twice the GHSV or by reducing the mass of catalyst used initially. To make up for the high GHSV, equal amounts of reaction mixture and an inert gas like He was used as shown in **Figure 4.7 (b)**. It was found that X_{CO_2} decreased by 3% and 8% for 60,000 ml g$_{cat}^{-1}$ h^{-1} and 120,000 ml g$_{cat}^{-1}$ h^{-1} GHSV respectively. A lesser loss in S_{CH_4} was observed though for the same experiment with the lowest being ~95% for GHSV of 120,000 ml g_{cat}^{-1} h^{-1}. This further reassured the fact that a four times increase in GHSV does not decrease the efficiency of the catalyst to a larger extent.

4.1.1.8 Comparison with Joule Heating

The benefits of using an Inductive heating (IH) setup was understood by carrying out the same reaction in a conventional Joule heating (JH) setup. **Figure 4.8** shows the results of CO_2 methanation carried out with FC-800-10Ni catalyst under IH and JH setups at 60,000 ml g_{cat}^{-1} h^{-1} (108,000 h^{-1})and 60,000 h^{-1} (33,333 ml g_{cat}^{-1} h^{-1}) GHSV respectively with a gas ratio maintained as CO_2: H_2: Inert gas (He/Ar) = 1: 4: 5. The test under JH was carried out up to 440oC where X_{CO_2} achieved was only 70%. It can be clearly seen from the two curves that the reaction takes off at a higher temperature in a JH setup compared to an IH setup. For example, a X_{CO_2} of 61% and $S_{CH_4}$of 98% can be achieved at 340°C in an IH (**Figure 4.8 (a)**) whereas similar results under a JH setup requires temperature as high as 400°C (**Figure 4.8 (b))**The difference of 60°C for such conversion which prolongates further with increasing conversion proves the fact that IH is indeed a better approach for heating compared to JH for methanation reactions with samples at low loading. This has a great industrial advantage as it has been already proven that a large amount energy for such reaction is used to heat the reaction unit rather than the catalyst itself [73]. Air-cooled reactors are being modelled to tackle with such situations [74]. Thus, IH not only facilitates tuning of the temperature and direct heating of only catalyst but it also prevents loss of heat via convection and conduction from the reactor tube observed in case of JH.

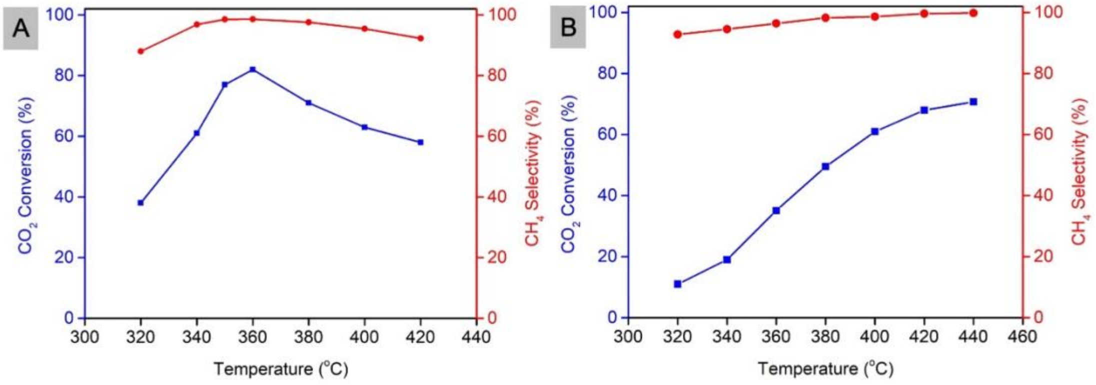

Figure 4.8 FC-800-10Ni CO_2 methanation under, (a) Inductive Heating at 60,000 ml g_{cat}^{-1} h^{-1} GHSV and, (b) Joule Heating at 60,000 h^{-1} GHSV.

Temperature Programmed Surface Reaction (TPSR) studies being carried out in a manner analogous to the JH setup heats the entire sample chamber and sample as a whole and provides qualitative information concerning decomposition and formation of gas species as shown in **Figure 4.9**. TPSR studies revealed an interesting observation concerning the heating of the samples in two different setups. It shows that JH is indeed helpful in case of samples like FC-700-20Ni and FC-900-20Ni which when tried in the IH setup could not be heated beyond a certain temperature owing to the limitations of the heating equipment which in turn depends on the structural properties and Ni NPs dispersion of the given composite. According to the TPSR analysis, the FC-700-20Ni-F catalyst seems to be active and worthy for study in an IH setup.

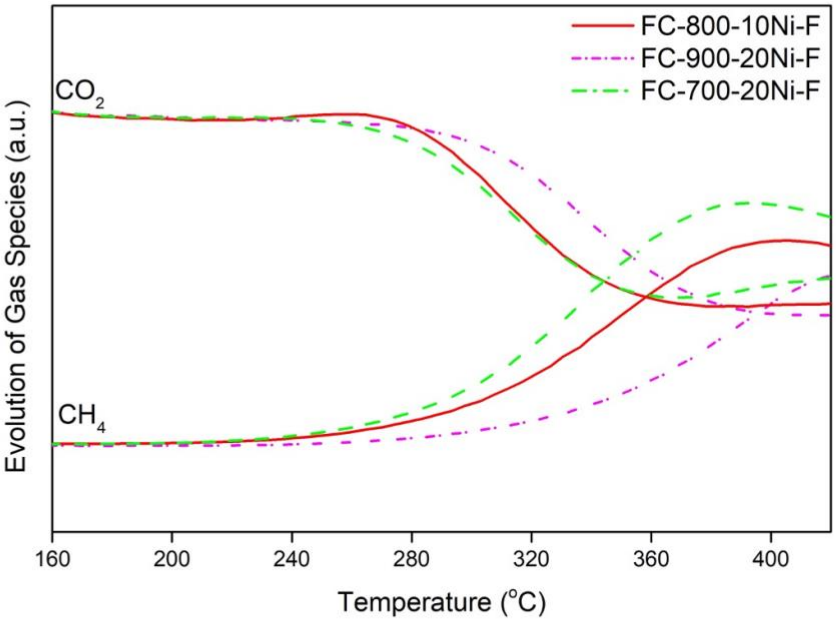

Figure 4.9 TPSR studies of some FLG-CNF samples.

4.1.1.9 Stability Tests

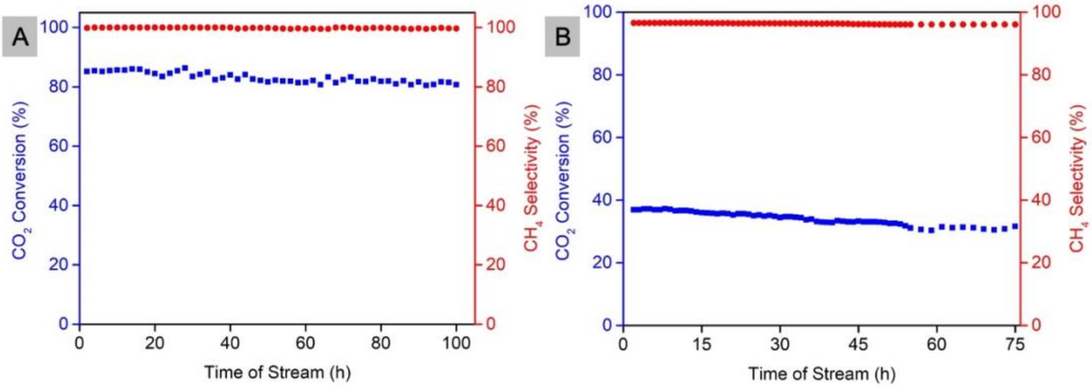

Figure 4.10 (a) Thermodynamic stability under IH and, (b) kinetic stability under JH for methanation with FC-800-10Ni sample.

A catalyst cannot be proposed for upscaling for industrial applications if the conversion is temporary or easily deactivated. In order to verify this, FC-800-10Ni sample was subjected to long term stability tests under different conditions. Initially it was tested under the IH setup at 30,000 ml g_{cat}^{-1} h^{-1} GHSV under only H_2 and CO_2 gas mixture in stochiometric ratios. After a test for 100 h as shown in **Figure 4.10 (a)**, it was found that the conversion has decreased by 4% with the selectivity remaining almost the same. This confirmed that the catalyst is able to perform the conversion in the desired form for a larger timeframe without any significant deactivation by processes like coke formation on active sites, sintering of metal nanoparticle or metal leaching.Sintering of Ni NPs due to formation of local temperature gradients in conventional setups has been confirmed by works of Wang [54] and Olesen [75]. Similarly, Salvatore et. al. have identified the formation of coke during methanation over Ni NPs is partially support dependent where-in the interaction of the Ni NPs with the support material govern their reactivity towards coke formation [76].

A similar test was carried out in the JH setup at 180000 h^{-1} GHSV (**Figure 4.10 (b)**)contrary to the previous measurements at 60,000 h^{-1} GHSV so as to better understand the kinetic product formation under more adverse conditions. A temperature of 360ºC was chosen so as to avoid the thermodynamic equilibrium states where the majority product is methane. This test proved not only that the catalyst is stable in the JH setup for about 75 h with a slight decrease of 5-6% in conversion but also proved that the selectivity stays high. It also confirmed that even at low conversion there was no CO product formation. We can find in literature that the lower selectivity observed in the IH setup can be attributed to the formation of other hydrocarbons at lower temperatures that are more kinetically favorable [77].

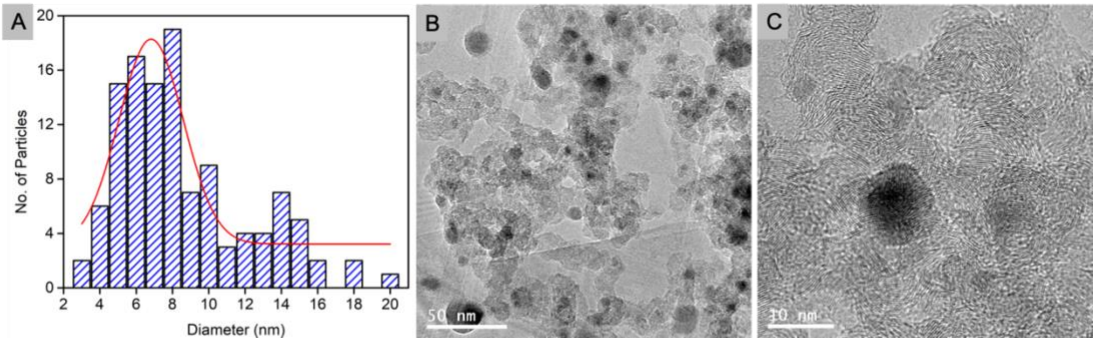

Figure 4.11 Particle size distribution (a),and TEM micrographs (b, c) of FC-800-10Ni catalyst after stability test.

A particle size analysis of the sample (**Figure 4.11 (a)**) retrieved after stability tests by TEM microscopy revealed that the majority of Ni NPs stay in the particle size range of 6-8 nm (**Figure 4.11 (b)**) similar to the ones before the test. Some of the particles in the image are larger than the rest which are mostly connected to the edges of the FLG flakes which has been a pronounced effect in all the samples. A strong interaction between the CNFs and the Ni NPs observed in **Figure 4.11 (c)** accounts for the high dispersity and avoidance of agglomeration after withstanding stability tests for 100 h. XPS surface analysis of the spent catalyst (**Figure**

SI 4.8) further confirms absence of Ni-carbide species. Also, according to the TEM analysis, the formation of coke is null or negligible.

4.1.1.10 Role of Support Structure

The current study deals with three unique batches of materials which were prepared to identify the best balance between FLG and CNF deposits which can be doped with Nickel for efficient CO_2 methanation. The herring bond shaped CNFs forming in a stacked manner parallel to the FLG surface confirms the flat morphology of the Ni NPs during growth. It can be noted that initially FC composites were prepared at three different temperatures to which multiple loading of Ni were done to understand the influence of CNF growth temperature on the dispersion and stability of active sites. The thermal conductivity of the FLG support is very essential for such inductive-heating setups which in-turn depends on the crystal anharmonicity of the FLG lattice and defect scattering between the layers [78]. It has been found that the thermal conductivity of FLG decreases with the increase in the number of layers, thereby traversing towards bulk graphite limit [79].

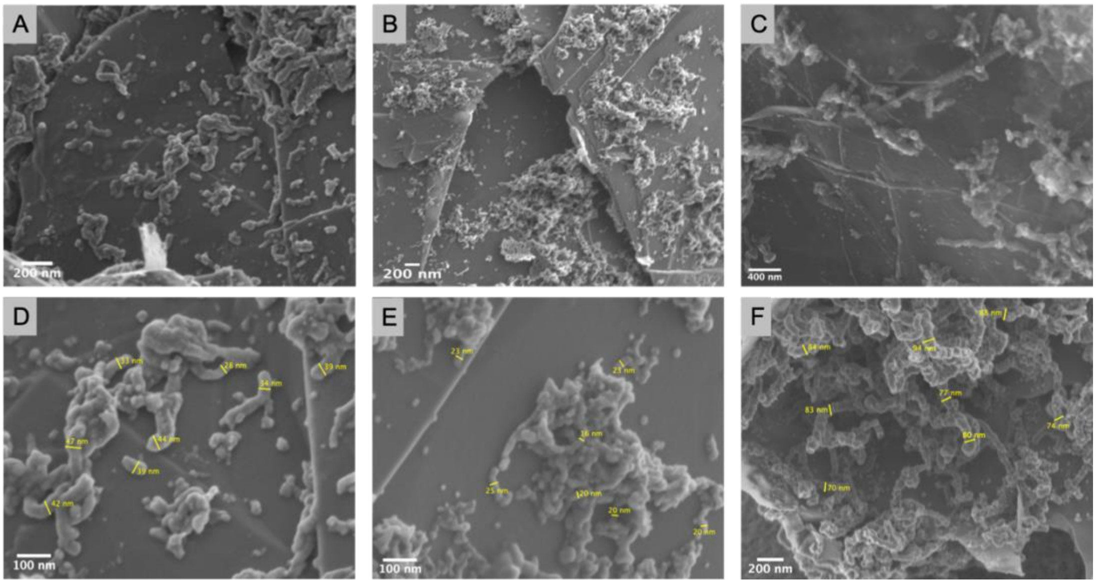

Figure 4.12 SEM images of FC-700(a,d), FC-800 (b,e), and FC-900 (c,f) samples indicating the CNFs distribution and diameter.

The FC-700 and FC-900 samples indeed have smaller surface area due to higher CNFs diameter compared to the 800°C sample. The improved surface are also confirms the avoidance of major re-stacking of FLG flakes. As seen in **Figure 4.12**, it is apparent that the thinnest CNFs are obtained at 800°C with a width less than 25 nm which is in tandem to its larger surface area in comparison to the samples prepared at 700°C and 900°C. The FC composites at 700°C have CNFs ranging from 30-50nm in diameter whereas the composites prepared at 900°C have CNFs ranging from 60-100nm. With the multi-fold increase in the thickness of CNFs at 900ºC it forms lesser amount of fibres in comparison to FC-800 and FC-700 samples where a large dispersed fibre cover is visible on the FLG flakes. This in-turn neutralizes the efficiency of the composite because the surface areas decreases (despite higher CNFs weight compared to those grown at 700ºC and 800ºC) as well as makes favourable pathway for deposition of Ni on FLG flakes after CNFs edge saturation.

Sample	**Amount of CNF(%)**		**Diameter of CNF ^{b} (nm)**	**T_{max} – IH (ºC)**	**C/O ratio^c**	**% of sp^2 carbon^c**
	Weight	TGA^a				
FC-700-NA	25	33	33-45	344	31	71
FC-800-NA	32	38	18-23	331	27	72
FC-900-NA	47	53	85-95	324	29	70

*Table 4.4 Properties of FLG-CNF support materials. *a- obtained from TGA; *b- Average diameter obtained from SEM analysis; *c- Obtained from XPS (have approximative character)*

Additionally, as mentioned earlier, higher Ni loading makes larger aggregates causing inhomogeneous heating distribution. The heating limits for each support under IH setup is listed in **Table 4.4**. All support materials are able to heat which gives the inference that there is no direct impact of the support morphology on the heating capacity. The support materials have almost the same C/O ratio with FC-800-NA being the lowest. Comparing FC-800-NA and FC-700-NA of similar weight, it can be seen that the ratio of edge-to-surface is higher in FC-800-NA attributed to lower diameter of CNFs in this sample, also confirmed by S_{BET} (CNFs can be longer or higher in quantity). Since there is no direct effect of FLG-CNFs morphology on the heating capacity, the IH heating is influenced by support interactions with the Ni NPs and their morphology, distribution and amount of loading.

4.1.4 Conclusion

A series of catalysts with varying diameter CNFs grown on FLG flakes subjected to impregnation with different loadings of Ni have been prepared. Further calcination and reduction steps rendered Ni NPs of diameter 6-8 nm or higher on the CNFs depending on the CNFs structure and size. Majority of the Ni NPs on FLG flakes were arranged along edges of carbon, *i.e.* edges of CNFs and also edges of FLG, with enhanced 2D aspects. A larger Ni loading gave rise to flattening of Ni NPs as platelets which further formed clusters. The samples were studied for their reactivity towards CO_2 methanation reaction in an Inductive heating setup which heats magnetically active catalyst. This mode of heating is found to be essentially beneficial in reducing the reaction temperature as well as to improving the efficiency. It also helps avoid the heat loss caused in reacting the entire reactor found in case of conventional Joule heating method. The CNFs grown at 800ºC have shown the best reactivity with a loading of ~10% Nickel. The role of FLG-CNF support for methanation in IH Setup has been studied in detail which helps identify the key parameters for structure designing of supports. The 800ºC grown CNFs had the lowest diameter in the range of 17-23 nm which allowed them for better dispersion of nanoparticles. The decrease in diameter goes with higher surface area and higher number of active sites (edges) to attach and stabilize NPs. More Ni NPs of lower dimension and higher dispersion is then obtained and thus higher efficiency. It was interesting to note that although FC-700-10 Ni and FC-700-20-Ni were prepared from the same batch of FLG-CNF composite, the 20% Ni loading maxed out the heating equipment but could not rise to a temperature suitable for methanation. Similar was the case for the FC-900 samples, although a high loading for FC-800 samples could be heated easily by the same setup. This indicates the fact that CNFs diameter beyond a certain limit when loaded with a larger amount Ni creates interaction and morphology which degrade its specific heat absorption capacities thereby making them unable to heat under same heating conditions. The reason for such behaviour can be studied further via magnetic properties analysis and specific absorption rate studies. Further, it was also proved that the Ni NPs dispersion on such supports stays stable for a long time in a thermodynamic regime and doesn't produce CO as by-product in a kinetic regime. To conclude, conversion of 85% with selectivity of 99.6% at a temperature of 360ºC was achieved for the FC-800-10Ni sample in an Inductive Heating setup. Above this temperature, the drop of conversion and selectivity suggest presence of parallel reactions.

References

[1] A. A. Balandin, S. Ghosh, W. Bao, I. Calizo, D. Teweldebrhan, F. Miao, C. N. Lau, *Nano Lett.*, 2008, Vol. 8, 902-907

[2] Global Carbon Project, Historical carbon dioxide emissions from global fossil fuel combustion and industrial processes from 1757 to 2017 (in million metric tons), Statista, https://www.statista.com/statistics/264699/worldwide-co2-emissions/ (accessed: August, 2020)

[3] A. Maroufmashat, M. Fowler, *Energies,* 2017, Vol. 10, 8, 1089

[4] I. G.–García, U. Izquierdo, V. L. Barrio, P. L. Arias, J. F. Cambra, *Int. J. Hydrog Energy*, 2016, Vol. 41, 43, 19587-19594

[5] A. Antenucci, G. Sansavini, *Renew. Sus. Energ. Rev.*, 2019, Vol. 100, 33-43

[6] F. D. Meylana, F. -P. Piguetab, S. Erkmana, *J. Energy Storage*, 2017, Vol. 11, 16-24

[7] C. Vogt, M. Monai, G. J. Kramer, B. M. Weckhuysen , *Nat. Catal.*, 2019, Vol. 2, 188-197

[8] R. M. Navarro, M. C. S.-Sánchez, M. C. A.-Galvan, F. del Vallea, J. L. G. Fierro, *Energy Environ. Sci.*, 2009, Vol. 2, 35-54

[9] I. Dincer, C. Acar, *Int. J. Hydrog. Energy*, 2015, Vol. 40, 34, 11094-11111

[10] Z. Yan, J. L. Hitt, J. A. Turner, T. E. Mallouk, *PNAS*, 2020, Vol. 117, 23, 12558-63

[11] X. Jia, X. Zhang, N. Rui, X. Hu, C.-j. Liu, *Appl. Catal. B*, 2019, Vol. 244, 159-169

[12] R.-P. Ye, Q. Li, W. Gong, T. Wang, J. J. Razink, L. Lin, Y.-Y. Qin, Z. Zhou, H. Adidharma, J. Tang, A. G. Russell, M. Fan, Y.-G. Yao, *Appl. Catal. B*, 2020, Vol. 268, 118474

[13] C. Italiano, J. Llorca, L. Pino, M. Ferraro, V. Antonucci, A. Vita, *Appl. Catal. B*, 2020, Vol. 264, 118494

[14] J. Lin, C. Ma,Q. Wang, Y. Xu, G. Ma,J. Wang, H. Wang, C. Dong, C. Zhang, M. Ding, *Appl. Catal. B*, 2019, Vol. 243, 262-272

[15] G. Garbarino, C. Wang, T. Cavattoni, E. Finocchio, P. Riani, M. F.-Stephanopoulos, G. Busca, *Appl. Catal. B*, 2019, Vol. 248, 286-297

[16] J. Wu, Z. Jin, B. Wang, Y. Han, Y. Xu, Z. Liang, Z. Wang , *Ind. Eng. Chem. Res.*, 2019, Vol. 58, 45, 20536-20542

[17] R. Zhou, N. Rui, Z. Fan, C.-j. Liu, *Int. J. Hydrog. Energy*, 2016, Vol. 41, 47, 22017-22025

[18] C. Wang, P. Zhai, Z. Zhang, Y. Zhou, J. Zhang, H. Zhang, Z. Shi, R. P. S. Han, F. Huang, D. Ma, *J. Catal.*, 2016, Vol. 334, 42-51

[19] J. Kirchner, J. K. Anolleck, H. Lösch, S. Kureti, *Appl. Catal. B*, 2018, Vol. 223, 47-59

[20] M.-D. Lee, J.-F. Lee, C.-S. Chang, *J. Chem. Eng. Japan.*, 1990, Vol. 23, 2, 130-136

[21] Z. Baysal, S. Kureti, *Appl. Catal. B*, 2020, Vol. 262, 118300

[22] Q. Liu, B. Bian, J. Fan, J. Yang, *Int. J. Hydrog. Energy*, 2018, Vol. 43, 10, 4893-4901

[23] P. Riani, G. Garbarino, T. Cavattoni, F. Canepa, G. Busca, *Int. J. Hydrog. Energy*, 2019, Vol. 44, 50, 27319-27328

[24] J. D.-Ramírez, P. Sánchez, V. Kyriakou, S. Zafeiratos, G. E. Marnellos, M. Konsolakis, F. Dorado, *J. CO_2 Util.*, 2017, Vol. 21, 562-571

[25] T. Franken, J. Terreni, A. Borgschulte, A. Heel, *J. Catal.*, 2020, Vol. 382, 385-394

[26] L. Falbo, C. G.Visconti, L. Liettia, J. Szanyi, *Appl. Catal. B*, 2019, Vol. 256, 117791

[27] A. C.-Arenas, A. Quindimil, A. D.-Quiñonero, E. B.-García, D. L.-Castelló, U. D.-L.-Torre, B. P.-Ayo, J. A. G.-Marcos, J. R. G.-Velasco, A. B.-López, *Appl. Catal. B*, 2020, Vol. 265, 118538

[28] B. Mutz, M. Belimov, W. Wang, P. Sprenger, M.-A. Serrer, D. Wang, P. Pfeifer, W. Kleist, J.-D. Grunwaldt, *ACS Catal*. 2017, Vol. 7, 10, 6802-6814

[29] J. Branco, P. E. Brito, A. C. Ferreira, *Chem. Eng. J.*, 2020, Vol. 380, 122465

[30] Y. R. Dias, O. W. P.-Lopez, *Energy Convers. Manag.*, 2020, Vol. 203, 112214

[31] G. Zhou, H. Liu, Y. Xing, S. Xu,H. Xie, K. Xiong, *J. CO_2 Util.*, 2018, Vol. 26, 221-229

[32] W. Li, Y. Liu, M. Mu, F. Ding, Z. Liu, X. Guo, C. Song, *Appl. Catal. B*, 2019, Vol. 254, 531-540

[33] W. Li, K. Wang, J. Huang, X. Liu, D. Fu, J. Huang, Q. Li, G. Zhan, *ACS Appl. Mater. Interfaces*, 2019, Vol. 11, 36, 33263-33272

[34] O. E. Everett, P. C. Zonetti, O. C. Alves, R. R.de Avillez, L. G. Appela, *Int. J. Hydrog. Energy*, 2020, Vol. 45, 11, 6352-6359

[35] M. Li, H. Amari, A. C.van Veen, *Appl. Catal. B*, 2018, Vol. 239, 27-35

[36] W. L. Vrijberg, J.W. A. van Helden, A. Parastaev, E. Groeneveld, E. A. Pidko, Emiel J. M. Hensen, *Catal. Sci. Technol.*, 2019, Vol. 9, 5001-5010

[37] X. Guo, H. He, A. Traitangwong, M. Gong, V. Meeyoo, P. Li, C. Li, Z. Peng, S. Zhang, *Catal. Sci. Technol.*, 2019,9, 5636-5650

[38] E, Truszkiewicz, K. Kowalczyk, A. Dębska, D. Wojda, E. Iwanek, L. Kępiński, B. Mierzwa, *Int. J. Hydrog. Energy*, 2020, Vol. 45, 56, 31985-31999

[39] A. Petala, P. Panagiotopoulou, *Appl. Catal. B*, 2018, Vol. 224, 919-927

[40] X. Wang, Y. Hong, H. Shi, J. Szanyi, *J. Catal*, 2016, Vol. 343, 185-195

[41] F. Wang, S. He, H. Chen, B. Wang, L. Zheng, M. Wei, D. G. Evans, X. Duan, *J. Am. Chem. Soc.*, 2016, Vol. 138, 19, 6298-6305

[42] N. M. Martin, F. Hemmingsson, A. Schaefer, M. Ek, L. R. Merte, U. Hejral, J. Gustafson, M. Skoglundh, A.-C. Dippel, O. Gutowski, M. Bauerf, P.-A. Carlsson, *Catal. Sci. Technol.*, 2019, Vol. 9, 1644-1653

[43] D. Heyl, U. Rodemerck, U. Bentrup, *ACS Catal.* 2016, Vol. 6, 9, 6275-6284

[44] A. Karelovic, PatricioRuiz , *J. Catal.*, 2013, Vol. 301, 141-153

[45] H. Muroyama, Y. Tsuda,T. Asakoshi, H. Masitah, T. Okanishi, T. Matsui, K. Eguchi, *J. Catal.*, 2016, Vol. 343, 178-184

[46] Y. Zhan, Y. Wang, D. Gu, C. Chen, L. Jiang, K. Takehira, *Appl. Surf. Sci.*, 2018, Vol. 459, 74-79

[47] Q. Liu, B. Bian, J. Fan, J. Yang, *Int. J. Hydrog. Energy*, 2018, Vol. 43, 10, 4893-4901

[48] A. Quindimil, U. D.-L.-Torre, B. P.-Ayo, J. A. G.-Marcos, J. R. G.-Velasco, *Appl. Catal. B*, 2018, Vol. 238, 393-403

[49] W. L. Vrijburg, E. Moioli, W. Chen, M. Zhang, B. J. P. Terlingen, B. Zijlstra, I. A. W. Filot, A. Züttel, E. A. Pidko, E. J. M. Hensen, *ACS Catal.*, 2019, Vol. 9, 9, 7823-7839

[50] J. Li, Y. Zhou, X. Xiao, W. Wang, N. Wang, W. Qian, W. Chu, *ACS Appl. Mater. Interfaces*, 2018, Vol. 10, 48, 41224-41236

[51] W. Zhen, F. Gao, B. Tian, P. Ding, Y. Deng, Z. Li, H. Gao, G. Lu, *J. Catal.*, 2017, Vol. 348, 200-211

[52] C. Hu, J. Qu, Y. Xiao, S. Zhao, H. Chen, L. Dai, *ACS Cent. Sci.*, 2019, Vol. 5, 3, 389-408

[53] W. Wang, C. D.-Viet, H. Ba, W. Baaziz, G. Tuci, S. Caporali, L. N.-Dinh, O. Ersen, G. Giambastiani, C. P.-Huu, *ACS Appl. Energy Mater.*, 2019, Vol. 2, 2, 1111-1120

[54] A. Primo, J. He, B. Jurca, B. Cojocaru, C. Bucur, V. I. Parvulescu, H. Garcia, *Appl. Catal. B*, 2019, Vol. 245, 351-359

[55] I. Janowska, M.-S. Moldovan, O. Ersen, H. Bulou, K. Chizari, M. J. Ledoux, C. P.-Huu, *Nano Res.*, 2011, Vol. 4, 511–521

[56] H. Vedala, D. C. Sorescu, G. P. Kotchey, A. Star, *Nano Lett.*, 2011, Vol. 11, 6, 2342-2347

[57] D. Mateo, J. Albero, H. García, *Appl. Catal. B*, 2018, Vol. 224, 563-571

[58] F. Hu, S. Tong, K. Lu, C.-M. Chen, F.-Y. Su, J. Zhou, Z.-H. Lu, X. Wang, G. Feng, R. Zhang, *J. CO_2 Util*, 2019, Vol. 34, 676-687

[59] W. Wang, G. Tuci, C. D.-Viet, Y. Liu, A. Rossin, L. Luconi, J.-M. Nhut, L. N.-Dinh, C. P.-Huu, G. Giambastiani. *ACS Catal*., 2019, Vol. 9, 7921-7935

[60] S. R. Yassine, Z. Fatfat, G. H. Darwisha, P. Karam, *Catal. Sci. Technol.*, 2020, Vol. 10, 3890-3896

[61] D. D. Masi, J. M. Asensio, P.-F. Fazzini, L.-M. Lacroix, B. Chaudret, *Angew. Chem. Int. Ed.*, 2020, Vol. 59, 15, 6187-6191

[62] W. Wang, C. D.-Viet, Z. Xu, H. Ba, G. Tuci, G. Giambastiani, Y. Liu, T. T.-Huu, J.-M. Nhut, C. P.-Huu, *Catal. Today*, 2019, DOI : 10.1016/j.cattod.2019.0

[63] W. Wang, C. D.-Viet, G. Tuci, Y. Liu, A. Rossin, L. Luconi, L., J.-M. Nhut., L. N.-Dinh, G. Giambastiani, C. P.-Huu, *ChemSusChem*, 2020, Vol. 13, 5468

[64] H. Ba, L. T.-Phuoc, C. P.-Huu, W. Luo, W. Baaziz, T. Romero, I. Janowska, *ACS Omega*, 2017, Vol. 2, 12, 8610-8617

[65] A. Mohanty, W. Baaziz, M. Lafjah, V. D. Costa, I. Janowska, *FlatChem*, 2018, Vol. 9, 15-20

[66] X. Lin, S. Wang, W. Tu, Z. Hu, Z. Ding, Y. Hou, R. Xu, W. Dai, *Catal. Sci. Technol.*, 2019, Vol. 9, 731-738

[67] Y. Zhang, Y. Shen, X. Xie, W. Du, L. Kang, Y. Wang, X. Sun, Z. Li, B. Wang, *Mater. Des.*, 2020, Vol. 196, 109111

[68] X. Guo, A. Traitangwong, M. Hu, C. Zuo, V. Meeyoo, Z. Peng, C. Li, *Energy Fuels*, 2018, Vol. 32, 3, 3681-3689

[69] K. Stangeland, D.Y. Kalai, H. Li, Z. Yu, *Appl. Energy*, 2018, Vol. 227, 206-212

[70] F. Koschany, D. Schlereth, O. Hinrichsen, *Appl. Catal. B*, 2016, Vol. 181, 504-516

[71] M. Frey, T. Romero, A.-C. Roger, D. Edouard, *Catal. Today*, 2016, Vol. 273, 83-90

[72] A. Yamaguchi, E. Iglesia, *J. Catal.*, 2010, Vol. 274, 52-63

[73] K. A. -Petersen, J.-H. B. Hansen, T. S. Christensen, I. Dybkjaer, P. S. Christensen, C. S. Nielsen, S. E. L. W. Madsen, J.R. R.-Nielsen, *Appl. Catal. A*, 2001, Vol. 221, 379-387

[74] U. Tozar, A. K. Avci, *Chem. Eng. Process.*, 2020, Vol. 151, 107914

[75] S. E. Olesen, K. J. Andersson, C. D. Damsgaard, I. Chorkendorff, *J. Phys. Chem. C*, 2017, Vol. 121, 29, 15556-15564

[76] C. Mebrahtua, S. Abate, S. Perathoner, S. Chen, G. Centi, *Catal. Today*, 2018, Vol. 304 , 181-189

[77] J. Gao, Y. Wang, Y. Ping, D. Hu, G. Xu, F. Gu, F. Su, *RSC Adv*., 2012, Vol. 22358-2368

[78] A. A. Balandin, *Nat. Mater*., 2011, Vol. 10, 569-581

[79] S. Ghosh, W. Bao, D. L. Nika, S. Subrina, E. P. Pokatilov, C. N. Lau, A. A. Balandin, *Nat. Mater.*, 2010, Vol. 9, 555-558

Supporting Information

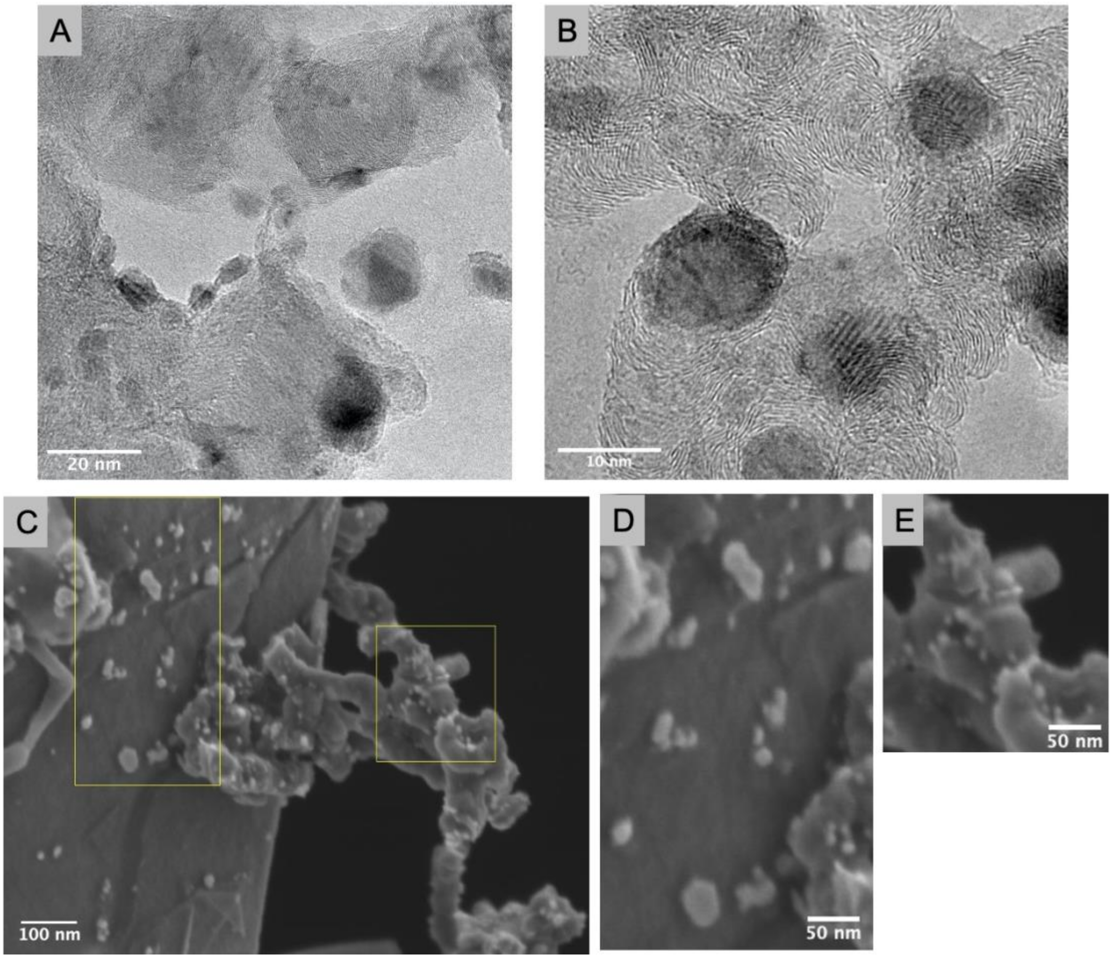

Figure SI 4.1 TEM images of FC samples showing the CNF morphology(a ,b); SEM images of FC sample (c), enlarged slices of image C (d)&(e), (d) showing lesser and smaller Ni particles on graphene surface compared to graphene edges, and (e)showing smaller particles on CNFs with homogenous dispersion.

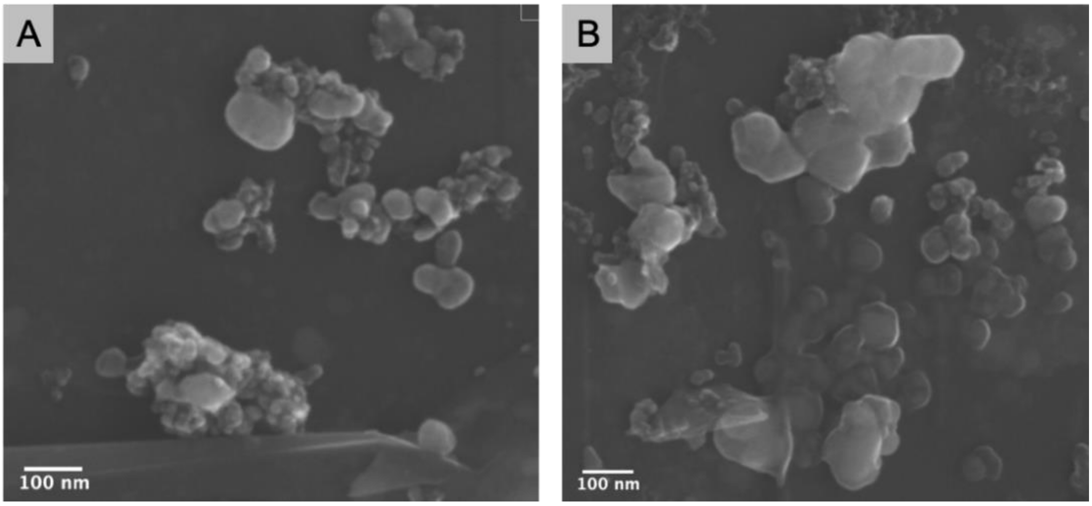

Figure SI 4.2 Flattening of Ni NPs under high loading.

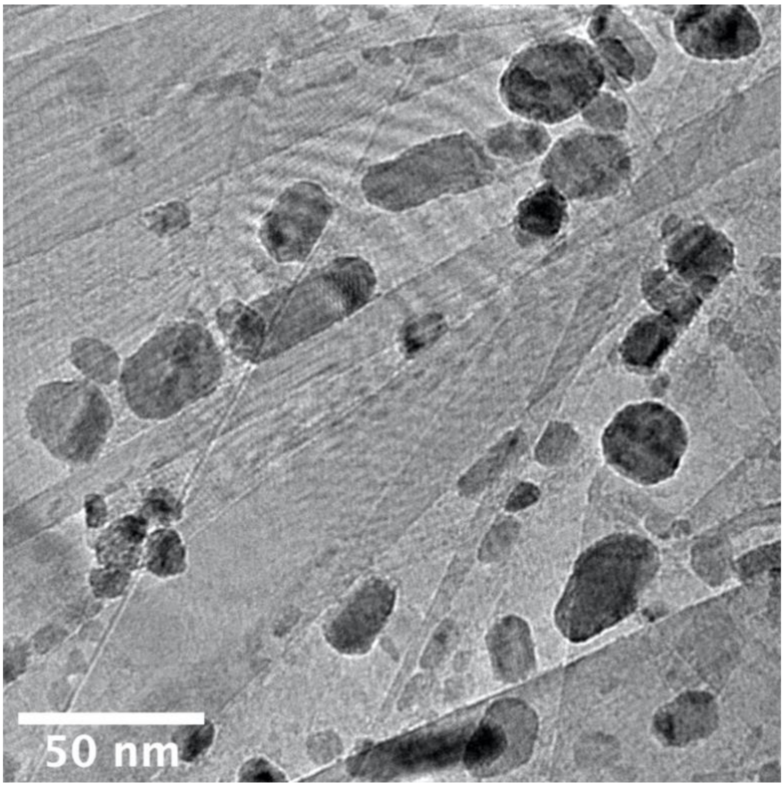

Figure SI 4.3 Agglomeration and elongation of particles along FLG edges.

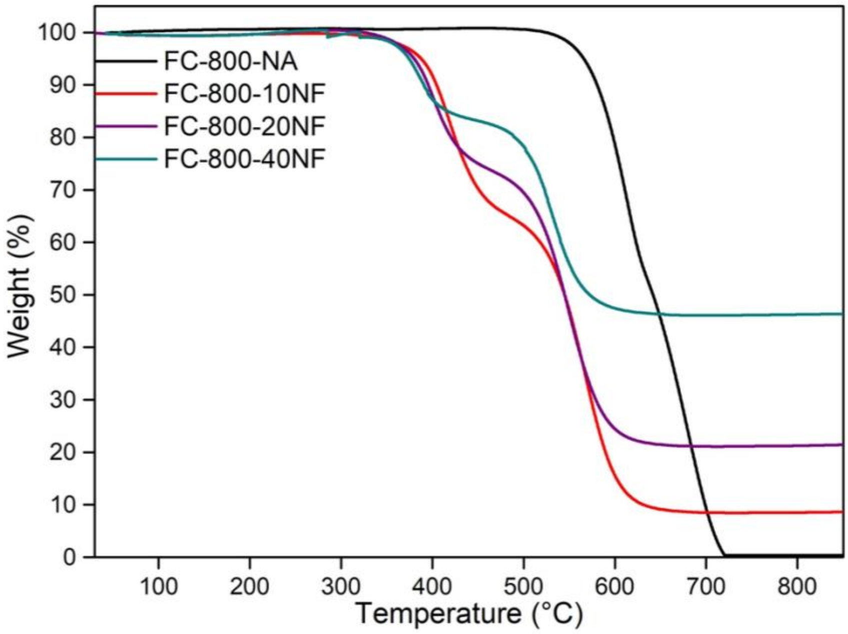

Figure SI 4.4 TGA of FC-800 samples

Sample	**sp^2 (284.4 ± 0.2 eV)**	**sp^3 (285.2 ± 0.2 eV)**	**C-OR (286 ± 0.2 eV)**	**C=O (287.2 ± 0.2 eV)**	**COO (288.7 ± 0.2 eV)**	***π-π**** **(291.01 ± 0.2 eV)**
FC-800-NA	71.5	7.2	7.6	4.5	4.6	4.6
FC-800-10Ni-F	69.9	8.8	8.1	4.2	4.4	4.6
FC-800-20Ni-F	69.9	9.9	7.7	4.4	4.5	3.6
FC-800-40Ni-F	69.3	9.5	7.4	4.8	4.5	4.5
FC-700-NA	70.6	8.9	6.8	3.8	4.6	5.3
FC-700-10Ni-F	68.2	10.9	8.7	4.2	3.9	4.1
FC-700-20Ni-F	69.3	8	8.4	5	4.6	4.7
FC-900-NA	69.2	8.9	8	4.2	4.8	4.9
FC-900-10Ni-F	66	9	8.3	7.7	6.2	4.8
FC-900-20Ni-F	68.7	12	5.9	4.1	4.7	4.6

Table SI 4.1 Percentage approximation of different kinds of Carbon according to XPS deconvolution.

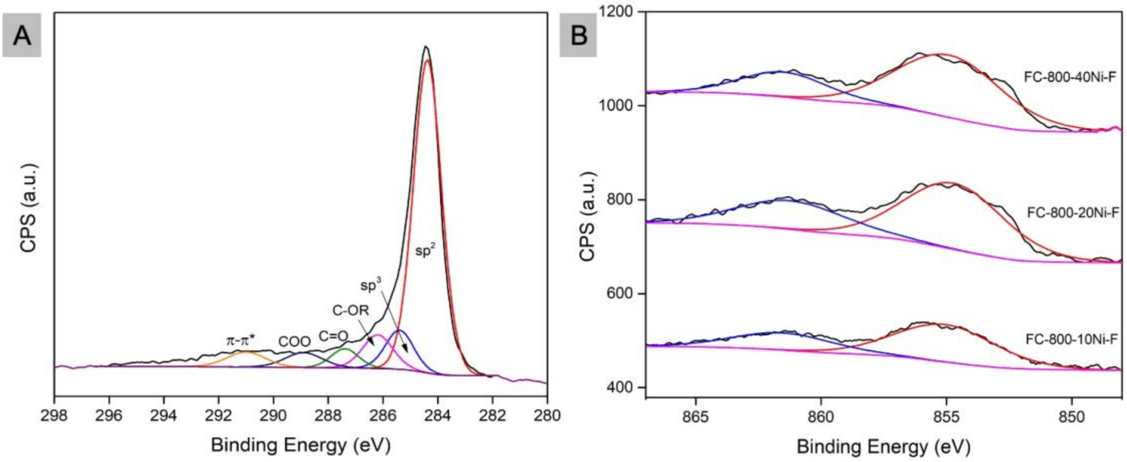

Figure SI 4.5 a)C1s spectra of FC-800-10Ni, b) Ni 2p spectra of FC-800 samples

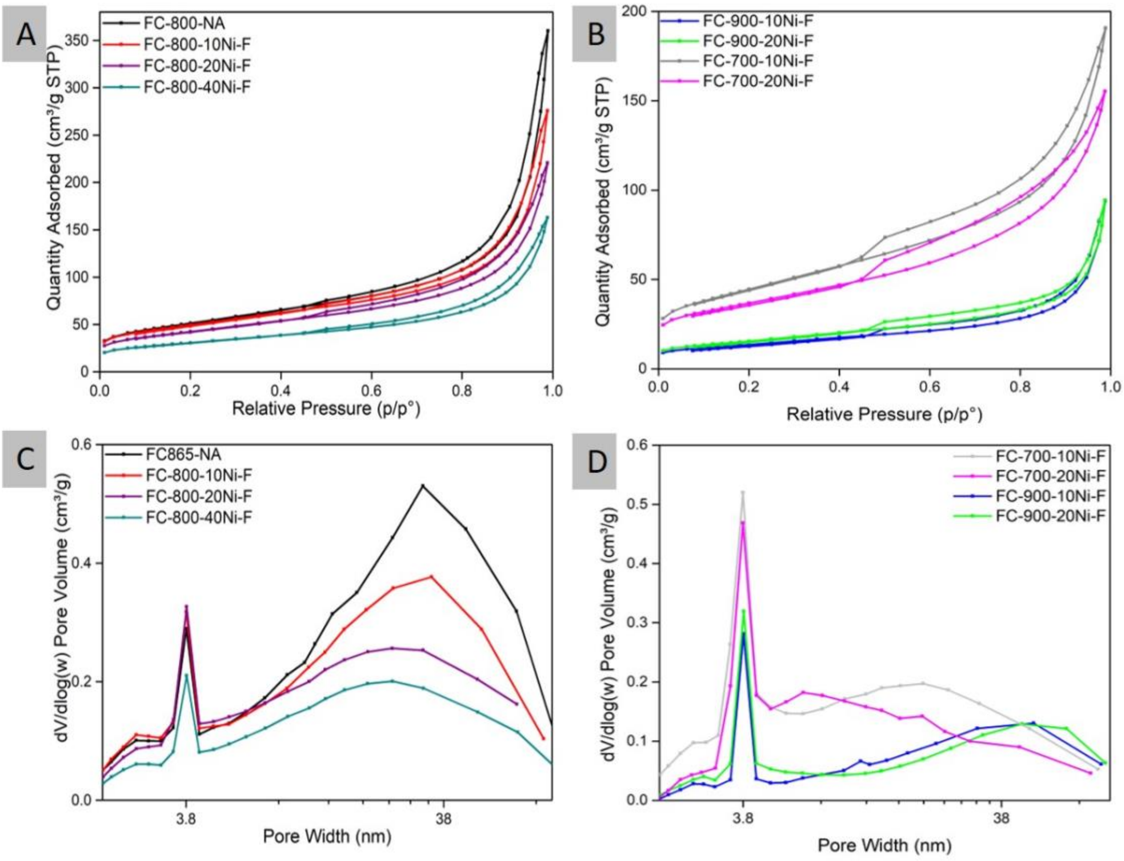

Figure SI 4.6 BET Surface area measurements (a,b), and pore size distribution(c,d) of FLG-CNF samples.

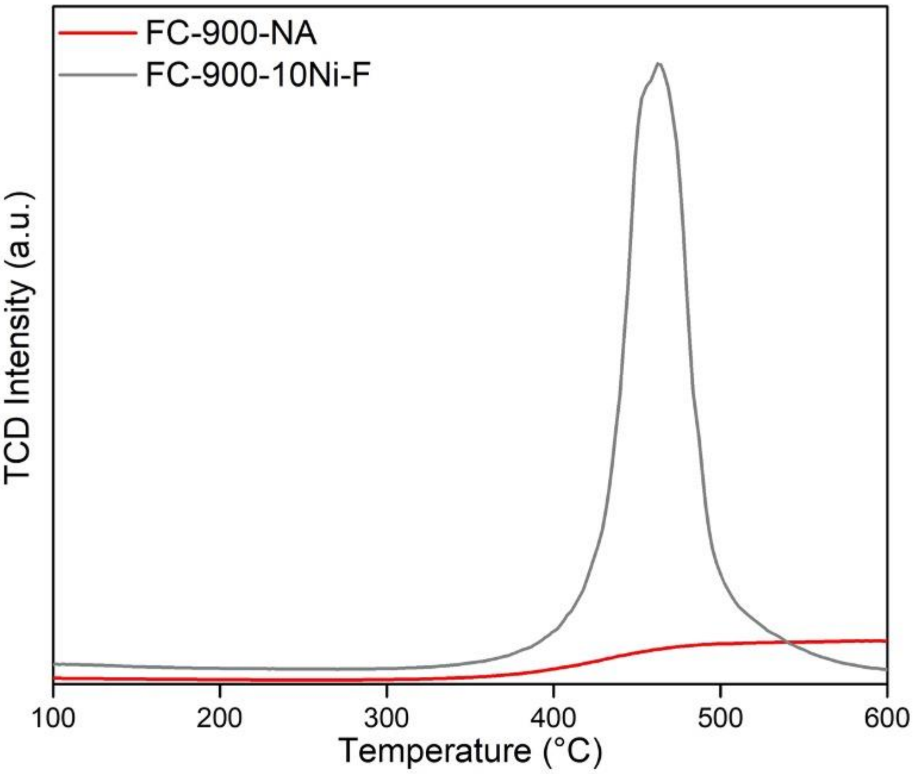

Figure SI 4.7 CO_2-TPD Intensity comparison between support with and without Ni loading.

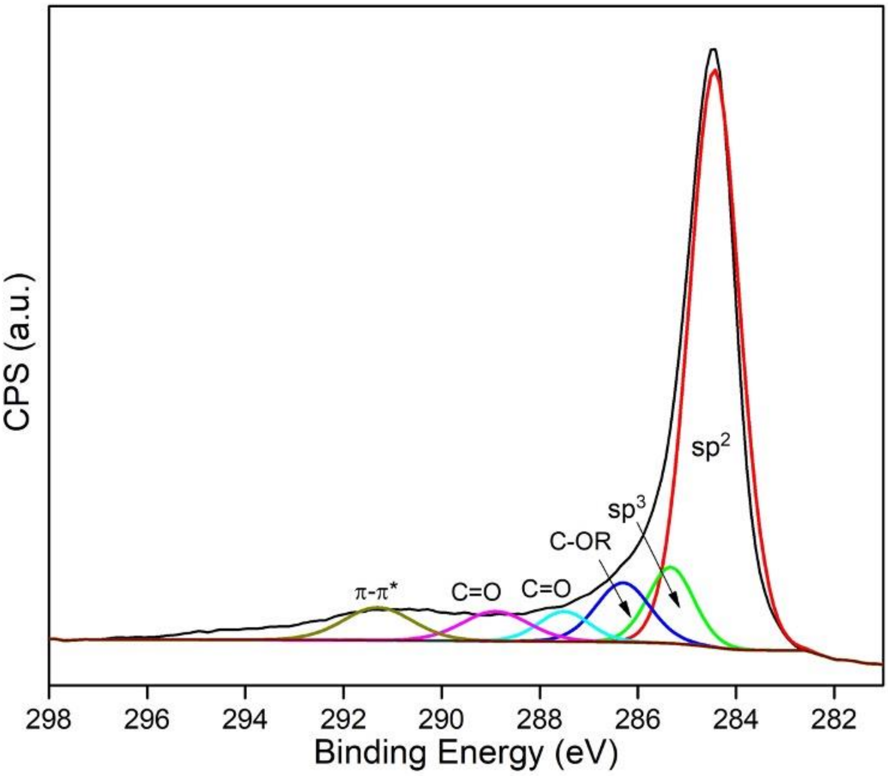

Figure SI 4.8 C1s XPS Spectra for FC-800-10Ni after 100 h stability test.

Chapter 5

Conclusion & Perspectives

5.1 Conclusions

The global energy trends have demanded for better, cleaner, greener and more sustainable energy solutions. The idea is not just to find a solution but to make it viable for future generations. This would help decrease the incessant degradation of fossil fuels as well as avoid its collateral consequences like global warming and wildfires. The Kyoto Protocol and the Copenhagen Accord have been able to solve some of the issues but lacked in implementation to a larger extent [1].So, the task is now in the hands of researchers to find solutions like renewable energies(REs) and be able to bring them to your palmtop. As discussed, the major problem concerning the use of REs is their intermittency and geo-accessibility. To achieve a dominating percentage of energy usage derived from REs, the world needs better storage systems that can help store large amount of energy as and when received from REs and be able to release them in a well-structured manner. Thus, there is a need for better storage systems like electro-chemical energy storage which is the new platform for energy storage today.

The global climate change has also been a major issue disturbing the balance in the current ecosystem. A large part of it is because of the increased CO_2 concentrations in the atmosphere. Carbon capture, and utilisation of CO_2 has been the major driving concept for efficient removal of CO_2 [2]. Industrial carbon dioxide capture and utilization is essential in order to decrease the final subsidy and to help improve the global impacts of increased CO_2 levels [3]. Catalytic hydrogenation of CO_2 to methane is considered to be one of the most efficient methods for removal of CO_2 as it can both reduce CO_2 and convert it into a useful gas fuel via the Power-to-Gas technology [4]. The need here is to find suitable metal-support catalyst combination that can handle high gas flows observed in industries. Besides, the heating method can be further optimised according to the catalyst so as to reduce the energy loss in heating the entire reactor.

Herein, the thesis focuses on appropriate structuration of few-layer-graphene based materials that can be used in energy storage as supercapacitors and in catalytic hydrogenation of carbon dioxide as high thermally conductive support material. FLG has also been used to act as template for synthesis of flat metal-based nanoplatelets. Further emphasis has been given on advantages of inductive heating system over conventional Joule heating system and their consequent ease of reactivity with graphene based materials.

5.1.1 FLG/C composites for supercapacitors

The work describes a greener, cleaner and cost-effective method for synthesis of highly aligned few-layer-graphene composites. Herein, h-HLB (high hydrophilic lipophilic balance) materials are used for exfoliation of expanded graphite to FLG. But, unlike earlier reports using it in low dosages [4], the current study uses it in large excess and retains its carbonized forms in the final composite. The idea underlying the design of the experiment was to maximize the use of the inherent high specific surface area of graphene arising from its basal plane and edges. Further, the goal was to achieve alignment of the layers so as to achieve higher capacitance.

The synthesis process is a no-waste method which involves instantaneous freeze drying of the materials obtained from exfoliation followed by high temperature gas treatment which helped retain alignment in some of the composites to a large extent. The usage of the such h-HLB exfoliants not only helps in de-stacking of graphene layers but also brings in unique ultra-microporosity and higher density to the composites which helps in improving the overall volumetric capacitance of the supercapacitors. Out of the various precursors used,it was observed that the composite containing only FLG and BSA derived carbon had a high volumetric capacitance of 467 F cm^{-3} at 0.5A g^{-1}. Additionally, theoretical approximation was also carried out to understand the contributions of different types of capacitance in the energy storage. It was found that these composites indeed have a larger pseudocapacitance courtesy to their large percentage of h-HLB precursor usage during exfoliation.

To summarize, it can be said that graphene based aligned supercapacitor electrode materials have been prepared. The prepared materials have a high volumetric capacitance, a large portion of which is attributed to the relatively compact and aligned structure aided by ultramicroporosity.

5.1.2 FLG as template for metal based nanoplatelets

FLG structuration is not only restricted to providing access to its edges and layers for electrochemical applications but also in acting as a template for obtaining more efficient metal nanoparticles. Two different synthesis strategies based on high temperature annealing were employed for obtaining flat metal nanoplatelets.

The first method involved in-situ synthesis of Fe NPs over FLG by a solvothermal method whereas the second method was based on wetness impregnation with Fe precursors. Both samples were subjected to high temperature annealing treatments via traditional heating or under µ–wave. The major outcome of the annealing process is the formation of two-faceted flattened Fe NPs with some coalescence but still high dispersion and homogenous distribution of NPs over FLGs. Both the samples indicate the idea of FLG acting as a template for well-defined metal nanoplatelets, esp. in case of µ–wave treated sample. The high-temperature annealing treatment causes graphitization thereby reducing the defects from the FLG surface.

These defect sites later turn into stabilizing centres for the metal NPs. Upon graphitization, the defects recover which leads to the partial separation and rising up of the metal NPs from the FLG plane thereby forming two-faceted nanoplatelets. The tilting of the Fe NPs on FLG provides a special advantage as not only one but two active surfaces might be utilised as active sites for reactions. The weakened reactions between the FLG support and metal NPs were also confirmed by growing carbon nanofibers (CNF). The CNFs were found to be formed on the sides of the metal NPs proving its dual active faces. Thus it was proved that graphene based material can be used as template for growing double-faceted flat metal NPs.

5.1.3 FLG/CNF support for Ni based Methanation of CO_2

This research work focused on two aspects of catalytic hydrogenation of carbon dioxide. First, it solidified the idea of using graphene based materials as support. Second, it proved that Inductive Heating is better suited than Joule Heating for the methanation reaction for the optimized samples (with low Ni loading and high surface area) which are sufficiently magnetically active to work in that current regime.

Seven FLG-CNF composites were prepared wherein CNFs was grown via CVD process onto FLG flakes (obtained via exfoliation with h-HLB precursor). The “herring-bond” type of CNFs were found to grow which had planes parallel to the FLG sheets and perpendicular to the main support axis suggesting that the Ni NPs over FLG had flat morphology during the CNFs synthesis. It was found that the growth temperature of CNFs defines its thickness and guides the dispersity of the Ni NPs formed by wetness impregnation method. It was observed that there were larger amount of Ni NPs docking on the nanofibers compared to the surface of graphene flakes. Further the NPs that are formed on the nanofibers are smaller in size compared to those on the graphene surface where it is largely formed around the edges. The Ni loading dominates the size of NPs formed and their consequent agglomeration. Flattening of Ni NPs was observed with increase in Ni loading over FLG. Inductive heating has been found to help reduce the temperature required for high conversion of CO_2 by direct heating of the active phase. Besides, it was also proved that the maximum efficiency was obtained for the thinnest CNFs grown at 800°C with a lower loading of Ni, as low as 10%. The conversion and selectivity is not stable after 360°C. It rather decreases slowly because of possible parallel. The after-test analysis revealed that the size of Ni NPs did not grow a lot and still have the maximum population in the range of 5-10 nm.

Contrarily, in conventional Joule heating setup, similar conversion was observed at a higher temperature, although with a very good selectivity which may be considered because of the high temperature reactor which does not allow for any water condensation near the catalytic bed. Besides, few samples which could not heat in the IH setup were able to work in the JH setup but with lower rate of conversion compared to the best set of catalysts. The direct heating of catalyst in case of IH is especially helpful in saving energy lost in heating the entire setup, but it needs optimization in terms of catalyst design so as to have high selectivity and conversion at a lower temperature.

To put in a nutshell, it can be said that this project confirmed that inductive heating is dependent on the structure of catalyst, both support and active phase. The structure determines the interactions and final morphology which also influences the magnetic properties (the IH capacity was different depending on the CNFs structure and Ni loading).

5.2 Perspectives

The current work present some ideas of tailoring the structure of graphene based materials for energy storage and conversion applications. Having verified the preliminary concepts as to how structuration of graphene can be done, following studies are delineated to better understand the optimization needed for a better tomorrow:

- Performing magnetic studies of FLG-CNFs/Ni composites to correlate with their structure and activity in IH setup with in-depth understanding of the role of support for inductive heating.
- Synthesis and study of flat Ni NPs for methanation and supercapacitor applications.
- Investigation of flat metallic NPs of Fe for methanation applications in both inductive heating and joule heating setup.
- Synthesis of Fe-Ni bimetallic alloy based NPs for methanation to finetune the selectivity and conversion simultaneously to a value >90% with a decrease in reaction temperature.

References

[1] L. C. Lau, K. T. Lee, A. R. Mohamed, *Renew. Sust. Energ. Rev.*, 2012, Vol. 16, 7, 5280-5284

[2] P. Markewitz, W. Kuckshinrichs, W. Leitner, J. Linssen, P. Zapp, R. Bongartz, A. Schreibera, T. E. Müller, *Energy Environ. Sci.*, 2012, Vol. 5, 7281-7305

[3] W. Gao, S. Liang, R. Wang, Q. Jiang, Y. Zhang, Q. Zheng, B. Xie, C. Y. Toe, X. Zhu, J. Wang, L. Huang, Y. Gao, Z. Wang, C. Jo, Q. Wang, L. Wang, Y. Liu, B. Louis, J. Scott, A.-C. Roger, R. Amal, H. Heh, S.-E. Park, *Chem. Soc. Rev.*, 2020, DOI: 10.1039/d0cs00025f

[4] A. Antenucci, G. Sansavini, *Renew. Sust. Energ. Rev.*, 2019, Vol. 100, 33-43

Publications & Communications

Publications

- Polyvinyl Alcohol-Few Layer Graphene Composite Films Prepared from Aqueous Colloids. Investigations of Mechanical, Conductive and Gas Barrier Properties; B. Van der Schueren, H. El Marouazi, A. Mohanty, P. Lévêque, C. Sutter, T. Romero, I. Janowska, *Nanomaterials*, 2020, 10, 85; DOI: 10.3390/nano10050858
- Tuning the structure of in-situ synthesized few layer graphene/carbon composites into nanoporous vertically aligned graphene electrodes with high volumetric capacitance; A. Mohanty, I. Janowska, *Electrochim. Acta*, 2019, Vol. 308, 206-216; DOI: 10.1016/j.electacta.2019.04.016
- Few layer graphene as a template for Fe-based 2D nanoparticles; A. Mohanty, W. Baaziz, M. Lafjah, V. Da Costa, I. Janowska, *Flatchem*, 2018, Vol. 9, 15-20 DOI: 10.1016/j.flatc.2018.04.002

Communications

- Structure Tailoring of Graphene based materials for energy applications; A. Mohanty, **ICPEES 2nd C&M Scientific Day**, ECPM, Strasbourg, 6th November, 2019 (Oral)
- Water mediated synthesis of ultra-microporous Few-Layer-Graphene/carbon electrodes for high volumetric capacitance; A. Mohanty, I. Janowska, **E-MRS,** Warsaw, Poland, 16th September 2019 (*Oral*)
- In-situ prepared few layer graphene/carbon composite electrodes for energy storage; A. Mohanty, I. Janowska, **CARBOCAT VIII,** Porto, Portugal, 26th June, 2018 (*Poster*)
- Tailoring of Fe-based NPs over few layer graphene (FLG) system, by and for catalysis; A. Mohanty, M. Lafjah, W. Baaziz, I. Janowska, **GECAT** Bretagne, France, 22nd May, 2018 (*Poster*)

Anurag MOHANTY

Structuration de matériaux à base de graphène pour l’énergie durable

Résumé

La production et le stockage des énergies renouvelables sont les deux facteurs clés de la durabilité de l'écosystème dans lequel nous vivons. Ce projet de thèse porte sur les modifications structurelles des matériaux à base de graphène multi-couches (FLG) pour le stockage électrochimique de l'énergie sous forme de supercondensateurs et la conversion chimique de l'énergie par la réaction de méthanation du CO_2. L’utilisation de h-HLB utilisé pour l'exfoliation initiale de graphite expansé a permis d’obtenir des matériaux avec un alignement élevé et un accès aux bords du FLG pour les supercondensateurs. Une approche théorique a été réalisée afin de distinguer et quantifier le type de capacitance. Des nanoplaquettes métalliques avec un double accès sur les faces ont été synthétisées à haute température en utilisant les FLG comme matrice. Une croissance de nanofibres de carbone (CNFs) a aussi été réalisée sur FLG, afin d’obtenir un composite à forte teneur en nanoparticules de nickel bien dispersées, permettant une conversion et une sélectivité élevées pour la réaction de méthanation du CO_2.

Mots-clés: graphène multi-couche, supercondensateur, méthanation du CO_2, chauffage par induction

Abstract

Renewable energy production and storage are the two key factors driving the sustainability of the ecosystem we dwell in. This thesis project deals with structural modifications of FLG based materials for electrochemical energy storage as supercapacitors and chemical energy conversion in the form of CO_2 methanation. Different zero-waste processes have been developed for specific applications. High alignment and edge access of FLG for supercapacitor has been achieved by retention of large excess of h-HLB materials used for initial exfoliation of graphite. A theoretical approach has been studied to distinguish and quantify the type of capacitance. Flat metal nanoparticles with double sided access has been synthesized by high temperature annealing processes with FLG as template. CNFs of various edge access have been grown on FLG flakes to obtain a high Ni NP dispersed composite suitable for high conversion and selectivity towards methanation reaction.

Keywords: Few-layer-graphene (FLG), supercapacitor, CO_2 methanation, Inductive Heating